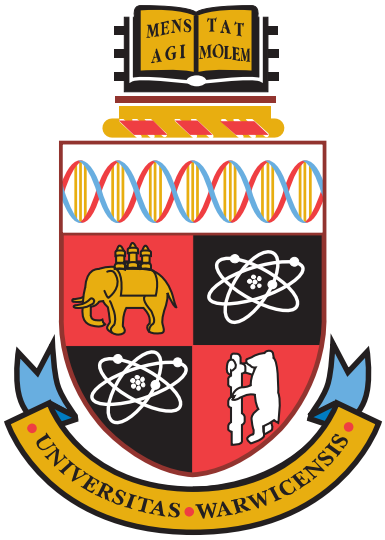

Colour Centres on Demand in Diamond

by

Matthew W. Dale

Thesis

Submitted to the University of Warwick

for the degree of

Doctor of Philosophy

Department of Physics

October 2015

Contents

List of Tables

List of Figures

Acknowledgments

First and foremost I would like to thank Prof Mark Newton for his excellent supervision and support throughout all of my years at Warwick. I would also like to thank Dr Chris Welbourn for insightful discussions and assistance over the last four years.

I am very grateful to the team at De Beers Technologies for their financial and technical support. In particular I would like to thank Dr Brad Cann, Dr David Fisher and Dr Philip Martineau. I also wish to thank the iMR-CDT for funding and all of the opportunities it has afforded me. I mustn't forget to thank the Physics Department mechanical workshop staff; without their assistance many of the experiments in this thesis would not have been possible.

My thanks go to the members of the Warwick EPR and Diamond group past and present, especially Ben, Chris, Mika, BenTwo, Anton, Sinead, Claudio, Angelo and Colin, for help, support, encouragement and coffee.

One of the highlights of my PhD was spending three weeks in Japan at the Japanese Atomic Energy Agency in Takasaki. I would like to thank Prof Junichi Isoya, Dr Shinobu Onoda, Dr Takeshi Ohshima, and their postdocs and students for their incredible hospitality and generosity in hosting me and my experiments.

My time at Warwick would not have been the same without my participation in the University of Warwick Archery Club. It provided both an escape from my studies and research and took me to distant lands such as Korea and Scotland. I am indebted to all members for the opportunities and enjoyment it gave me.

I wish to thank my family, for all of your love and support from across the Channel. I think that when I left home all those years ago, no one quite realised how long it was possible to stay a student! My thanks also go to Felicity's family for looking after me while I am away from home.

Last but certainly not least my thanks go to Felicity for her constant love and for supporting me through this adventure. I could not have made it without her.

Declaration and published work

I declare that the work presented in this thesis is my own except where stated otherwise, and was carried out entirely at the University of Warwick, during the period of October 2011 to October 2015, under the supervision of Prof. Mark Newton and Dr. Chris Welbourn. The research reported here has not been submitted, either wholly or in part, in this or any other academic institution for admission to a higher degree.

Some parts of the work reported and other work not reported in this thesis have been published, as listed below. It is anticipated that further parts of this work will be submitted for publication in due course.

Published papers

1. B. L. Green, M. W. Dale, M. E. Newton, D. Fisher, *Physical Review B* **92**, 165204 (2015)

2. D. I. Woodward, R. Dittmer, W. Jo, D. Walker, D. S. Keeble, M. W. Dale, J. Rödel, P. A. Thomas, *Journal of Applied Physics* **115**, 114109 (2014)

Conference presentations

1. 65th Diamond Conference, University of Warwick, presentation 'In-situ uniaxial stressed electron paramagenetic resonance'

2. 65th Diamond Conference, University of Warwick, poster presentation 'Pho-

tochromism in irradiated and annealed Ib diamond'

3. iMR-CDT research conference, University of Dundee, presentation 'GPa uniaxial stress of single crystal samples'

4. 47th Royal Society of Chemistry ESR Conference, University of Dundee, poster presentation 'GPA uniaxial stress of single crystal samples'

5. 64th Diamond conference, University of Warwick, poster presentation 'Neutron irradiation and the production of the negative nitrogen-vacancy centre'

6. 18th Hasselt Diamond Workshop 2013, Hasselt, Belgium, poster presentation 'Neutron irradiation and the production of the negative nitrogen-vacancy centre'

7. 46th Royal Society of Chemistry ESR Conference, University of Warwick, poster presentation 'Improving the accuracy of quantitative EPR'

8. 63rd De Beers Diamond conference, University of Warwick, poster presentation 'Investigation into the production of the negative nitrogen-vacancy centre in type Ib diamond'

Abstract

This thesis reports research on point defects in single crystal synthetic diamond. A number of techniques have been used including electron paramagnetic resonance (EPR), infrared (IR) absorption, ultraviolet-visible (UV-Vis) absorption and photoluminescence (PL) spectroscopies. The effect of perturbations by uniaxial stress on defect formation and migration have been investigated.

Photo- and thermo-chromic effects have been investigated in irradiated and annealed type-IaA diamond. Charge transfer between nitrogen and di-nitrogen vacancy defects together with quantification in their negative charge states has allowed their calibration constants to be determined. Improvements have been made in the ^{13}C hyperfine parameters for N_2V^- and its observation in diamond of natural isotopic abundance has allowed its ^{14}N quadrupole parameters to be determined.

Defects in neutron irradiated diamond have been studied by annealing isochronally up to 1600 °C. The majority of nitrogen could be accounted for through all annealing stages in a variety of defects including a maximum of 72(7) ppm of NV^-. The annealing behaviour strongly supports the involvement of interstitials in interstitial mediated nitrogen aggregation in addition to vacancy assisted nitrogen aggregation. A model of the mechanisms has been proposed and simulated with chemical kinetics, the result of which agrees well with experiment.

The effect of applying up to 3.0 GPa ⟨0 0 1⟩ uniaxial stresses to type-IIa samples during electron irradiation has been investigated. The treatment caused very little preferential orientation of the single interstitial and nearest neighbour di-interstitial, however it caused significant preferential orientation of 3H, believed to be the next nearest neighbour di-interstitial. The production rate of both di-interstitials was also increased by stress.

Irradiated samples have been annealed under [0 0 1] uniaxial stresses. The annealing successfully created preferentially oriented populations of the ⟨0 0 1⟩-split self interstitial with up to 93(1) % efficiency. Preferentially oriented interstitials have been annealed in situ in an EPR spectrometer allowing the site populations to be determined throughout the anneal.

Abbreviations

Definitions

[X]	Concentration of X
CVD	Chemical vapour deposition
CW	Continuous wave
CW-EPR	Continuous wave electron paramagnetic resonance
DFT	Density functional theory
E_A	Activation energy
EM	Electromagnetic
ENDOR	Electron nuclear double resonance
EPR	Electron paramagnetic resonance
FT-IR	Fourier transform infrared
FFT	Fast Fourier transform
FWHM	Full width at half maximum
$\hbar\omega$	Energy of a photon
HPHT	High pressure high temperature
IR	Infrared
λ	Wavelength of light
LVM	Local vibrational mode
μ_B	Bohr magneton

μ_N	Nuclear magneton
PL	Photoluminescence
ppb	Parts per billion atomic density
ppm	Parts per million atomic density
T_d	Threshold displacement energy
UV-Vis	Ultraviolet-visible
ZPL	Zero-phonon line

Crystalographic notation

$[h\,k\,l]$	a specific hkl direction
$\langle h\,k\,l\rangle$	a general hkl direction
$(h\,k\,l)$	a specific hkl plane
$\{h\,k\,l\}$	a general hkl plane

Common defects

V	Vacancy
C_I	Interstitial carbon
$C_{I_{001}}$	Interstitial carbon in the $\langle 0\,0\,1\rangle$-split configuration
N_S^0	Neutral substitutional nitrogen
N_{2S}	Di-substitutional nitrogen (also called A-centre)
NV	Nitrogen vacancy
N_2V	Di-nitrogen vacancy
N_{2I}	Di-nitrogen split interstitial

1

Introduction

Carbon is able to form a large number of allotropes [1], the most familiar being graphite and diamond. Other more exotic forms include graphene [2] and the fullerenes: carbon nanotubes [3] and Buckminsterfullerene [4]. Outside of its allotropes it is of course the basis of organic chemistry and life on Earth. The significance of carbon is a consequence of its ability to form bonds so readily with itself and to other elements.

The carbon atom has six electrons with the ground state configuration $1s^2 2s^2 2p^2$ where the two $2p$ electrons are unpaired in $2p_x$, $2p_y$ orbitals [5]. The energy required to excite an electron from the $2s$ orbital to the $2p_z$ state is easily provided by the energy released in bonding. Once in the excited state the lowest energy is achieved if four equivalent bonds are formed and so the $2s$ and three $2p$ orbitals hybridise into four sp^3 orbitals. The four equivalent bonds cause the tetrahedral coordination of the atoms in the diamond lattice. If one of the $2p$ orbitals is occupied in a π bond the remaining $2s$ and two $2p$ orbitals hybridise into three sp^2 orbitals, as found in many of the allotropes of carbon. Diamond is not the lowest energy configuration of carbon and will, given enough energy to overcome a barrier, revert into graphite [6].

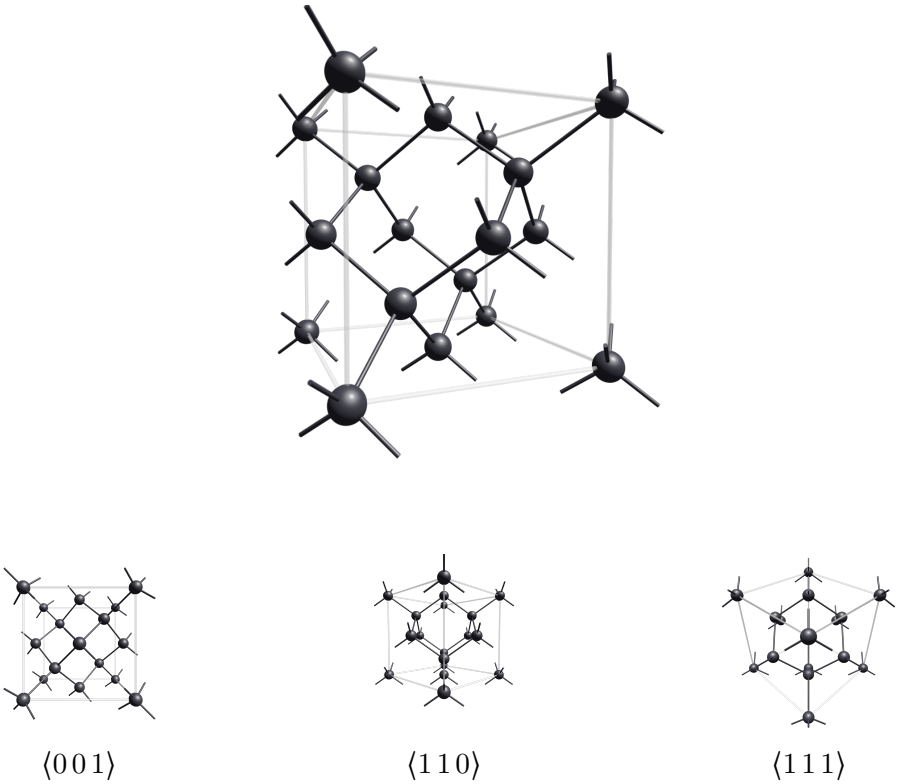

Figure 1-1 Unit cell of diamond viewed off-axis and down the three crystallographic directions showing four-fold, two-fold and three-fold symmetries. The unit cell has length 357 pm and the C-C bond length is 154 pm [7].

1.1 Structure, properties and applications

Diamond is a homonuclear cubic crystal consisting of two interpenetrating face-centred cubic (FCC) lattices, one displaced from the other by $a_0(\frac{1}{4}, \frac{1}{4}, \frac{1}{4})$, where a_0 is the lattice constant. The diamond structure is shown in figure 1-1. The short sp^3 C-C bonds are 154 pm giving a lattice constant 356.7 pm [7]. The density of diamond is $3.52\,\mathrm{g\,cm^{-3}}$ giving it an atomic density of $1.76 \times 10^{23}\,\mathrm{cm^{-3}}$, the highest of any solid, although denser allotropes of carbon are predicted to be feasible [8]. The diamond structure is in the $\mathrm{Fd\bar{3}m}$ space group and is shared by other group IV elements, silicon, germanium and α-tin. The analogous zincblende structure, where the two FCC lattices are composed of different elements, is the structure of many compound semiconductors.

At $2300\,\mathrm{W\,m^{-1}\,K^{-1}}$, pure diamond has the highest thermal conductivity at room

temperature of any material [9] (for comparison the thermal conductivity of copper is 390 $\mathrm{W\,m^{-1}\,K^{-1}}$ and of silicon is 150 $\mathrm{W\,m^{-1}\,K^{-1}}$ [9]) and can be increased further with ^{12}C isotopic enrichment [10]. It is extremely resistant to compressive forces with a bulk modulus of 443 GPa [11] and is the hardest of all natural materials [12] (only surpassed by synthetic nano polycrystalline diamond [13]). Diamond occurs naturally at high purity and has a band gap of 5.47 eV, making it optically transparent over a very broad range of energies [14]. It is also biologically compatible and chemically inert [15].

Due to its exceptional hardness diamond has long been used as an abrasive for the cutting and grinding of many materials. Its outstanding thermal conductivity makes it an excellent heat spreader, but the combination of its broad transparency, resulting from its large band gap, together with its thermal properties make it an excellent optical window for high power lasers and gyrotron windows [16, 17]. In the last two decades significant progress has been made in using defects in diamond, in particular the negatively charged nitrogen-vacancy centre (NV^-), for quantum information processing (QIP) [18–20] and nanoscale magnetometry [21–25]. Fundamental to these applications are the ability to optically detect magnetic resonance of NV^- [26] and its long spin coherences, even at room temperature ($T_2 > 1$ ms) [27–29]. Diamond is of course also highly valued as a gem for both its hard wearing and optical properties.

When diamond was first studied by IR absorption spectroscopy it was noted that specimens could be categorised into different types according to their absorption spectra [30], as summarised in table 1-1. It was observed that some diamonds had distinct absorptions in the IR and ultraviolet (UV) ranges, whilst in others the absorptions were not present. The former was labelled type-I and the latter type-II. It later transpired that the absorptions were caused by nitrogen impurities [31, 32]. Type-I was further divided according to the aggregation state of nitrogen [33], and type-II by electrical conductivity [34].

Type	Subtype	Characteristics
I		Nitrogen is detectable by the one-phonon IR absorption spectrum (approximately [N] > 1 ppm)
	Ia	Nitrogen is in aggregated forms
	IaA	Nitrogen is mainly in the form of the A-centre – two nearest neighbour substitutional nitrogen atoms [35]
	IaB	Nitrogen is mainly in the form of the B-centre – four substitutional nitrogen atoms surrounding a vacancy [36, 37]
	IaA/B	Contains a combination of A- and B-centres
	Ib	Nitrogen in mainly in the form of single substitutional centres [38]
II		Neither nitrogen nor boron is detectable in the IR absorption spectrum
	IIa	Nitrogen is not detectable in the IR absorption spectrum
	IIb	Boron is present in greater concentration than nitrogen [39, 40]

Table 1-1 Type classifications of diamond according to their IR absorption spectra.

1.2 Motivation for study

The driving force for this thesis is the ability to engineer defects in diamond. To engineer a defect it must ultimately be created with the desired properties: orientation, location, and environment. For applications such as magnetometers, quantum spin registers and hybrid quantum systems it is beneficial or critical that all defects are identical. Because of its symmetry, there are four orientations an NV centre can occupy in the lattice and so for all defects to be identical they must be created in one orientation. This has been achieved in grown-in NV^-, where the defect is incorporated during sample growth [41, 42], however this does not currently enable control over location and the resulting yield is low. The location of defects has successfully been predetermined by using ion implantation [43, 44], but the resulting defects are not created in alignment and their environment is damaged by the implantation and contains parasitic impurities.

1.3 Thesis outline

An outline of the remainder of this thesis is as follows:

- Chapter 2 reviews the relevant literature on the defects relevant to this thesis. These include the defects created from the irradiation of both type-IIa and type-Ib diamond and the products of the annealing of irradiated type-Ib diamond with an emphasis on the aggregation of nitrogen.
- Chapter 3 gives an account of the relevant theory for the spectroscopic techniques, radiation damage and annealing kinetics.
- Chapter 4 details the experimental techniques and apparatus which are used throughout the thesis.
- Chapter 5 discusses optical absorption and quantitative EPR techniques and presents new fitting software for accurate deconvolution and integration of spectra.
- Chapter 6 reports a study of the photo- and thermo-chromism of defects in irradiated type-Ib diamond. Calibration constants for a number of important defects are deduced.
- Chapter 7 presents a detailed annealing study of neutron irradiated type-Ib diamond including the quantification and annealing curves of a number of defects. Radiation damage is simulated and compared to the experimental data. A model of the annealing mechanisms is proposed and simulated.
- Chapter 8 reports on the results of electron irradiating type-IIa diamond whilst held under uniaxial stress. The production rates and relative site populations of a number of defects are altered by the applied stress. Insights are drawn into the production mechanisms of defects during irradiation.
- Chapter 9 investigates the annealing of irradiated type-IIa diamond under uniaxial stress, in particular the preferential orientation of single interstitials.

References

1. A. Hirsch, *Nature Materials* **9**, 868–871 (2010).
2. A. K. Geim, K. S. Novoselov, *Nature Materials*, 183–191 (2007).
3. S. Iijima, T. Ichihashi, *Nature* **363**, 603–605 (1993).
4. H. Kroto et al., *Nature* **318**, 162–163 (1985).
5. L. Pauling, *Journal of American Chemical Society* **53**, 1367–1400 (1931).
6. F. P. Bundy et al., *Carbon* **34**, 141–153 (1996).
7. H. Holloway et al., *Physical Review B* **44**, 7123–7126 (1991).
8. Q. Zhu et al., *Physical Review B* **83**, 193410 (2011).
9. Y. Yamamoto et al., *Diamond and Related Materials* **6**, 1057–1061 (1997).
10. J. R. Olson et al., *Physical Review B* **47**, 14850–14856 (1993).
11. H. J. McSkimin, *Journal of Applied Physics* **43**, 985 (1972).
12. V. V. Brazhkin, A. G. Lyapin, R. J. Hemley, *Philosophical Magazine A* **82**, 231–253 (2002).
13. K. Harano, T. Satoh, H. Sumiya, *Diamond and Related Materials* **24**, 78–82 (2012).
14. C. D. Clark, P. J. Dean, P. V. Harris, *Proceedings of the Royal Society of London. Series A* **277**, 312–329 (1964).
15. R. J. Narayan, R. D. Boehm, A. V. Sumant, *Materials Today* **14**, 154–163 (2011).
16. A. Kasugai et al., *Nuclear Fusion* **48**, 054009 (2008).
17. P. Maquet et al., *Fusion Engineering and Design* **88**, 2641–2645 (2013).
18. S. Prawer, I. Aharonovich, *Quantum Information processing with Diamond: Principles and Applications* (Elsevier, 2014).
19. T. D. Ladd et al., *Nature* **464**, 45–53 (2010).
20. J. Wrachtrup, F. Jelezko, *Journal of Physics: Condensed Matter* **18**, S807–S824 (2006).
21. S. J. DeVience et al., *Nature Nanotechnology* **10**, 129–134 (2015).
22. R. Schirhagl et al., *Annual review of physical chemistry* **65**, 83–105 (Jan. 2014).
23. M. Loretz et al., *Applied Physics Letters* **104**, 10–15 (2014).

24. D. Le Sage et al., *Nature* **496**, 486–489 (Apr. 2013).
25. S. Hong et al., *MRS Bulletin* **38**, 155–161 (2013).
26. A. Gruber et al., *Science* **276**, 2012–2014 (1997).
27. H. S. Knowles, D. M. Kara, M. Atatüre, *Nature materials* **13**, 21–25 (Jan. 2014).
28. N. Bar-Gill et al., *Nature communications* **4**, 1743 (2013).
29. G. Balasubramanian et al., *Nature materials* **8**, 383–7 (May 2009).
30. R. Robertson, J. J. Fox, A. E. Martin, *Philosophical Transactions of the Royal Society of London. Series A* **232**, 463–535 (1934).
31. W. Kaiser, W. L. Bond, *Physical Review* **115**, 857–863 (1959).
32. W. V. Smith et al., *Physical Review* **115**, 1546–1552 (1959).
33. R. M. Chrenko, R. E. Tuft, H. M. Strong, *Nature* **270**, 141–144 (1977).
34. J. F. H. Custers, *Physica* **18**, 489–493 (1952).
35. G. Davies, *Journal of Physics C: Solid State Physics* **9**, L537 (1976).
36. J. Loubser, J. A. Van Wyk, *Diamond conference*, Reading (unpublished), 1981.
37. R. Jones, P. R. Briddon, S. Öberg, *Philosophical Magazine Letters* **66**, 67–74 (1992).
38. R. M. Chrenko, H. M. Strong, R. E. Tuft, *Philosophical Magazine* **23**, 313–318 (1971).
39. A. T. Collins, A. W. S. Williams, *Journal of Physics C: Solid State Physics* **4**, 1789–1800 (1971).
40. R. M. Chrenko, *Physical Review B* **7**, 4560 (1973).
41. M. Lesik et al., *Applied Physics Letters* **104** (2014).
42. J. Michl et al., *Applied Physics Letters* **104**, 102407 (Mar. 2014).
43. S. Sangtawesin et al., *Applied Physics Letters* **105**, 063107 (2014).
44. J. O. Orwa et al., *Journal of Applied Physics* **109**, 083530 (2011).

2

Literature review

To date hundreds of defects have been observed in diamond [1], although it is often the case that the picture is incomplete with few known properties and only speculative models. Through different spectroscopic techniques we can start to build a picture by learning about the symmetry, constituent atoms and configuration of those atoms, and annealing behaviour and reaction mechanisms. In addition, ab initio calculations can be used to support models and help investigate candidate models.

This chapter aims to review the point defects significant to this thesis. Point defects are those which are localised in space, typically limited to several lattice points. For each defect discussed, emphasis has been given to the properties important to this thesis, such as its symmetry and what is known about its creation and destruction by irradiation and/or annealing. The reader is directed to section 3.3 for a brief discussion of the role of defect symmetry and its notation.

All diamond studied was synthetic type-I or type-IIa material grown by the high pressure high temperature (HPHT) and chemical vapour deposition (CVD) methods, respectively. Section 2.1 reviews the radiation damage products in intrinsic diamond relevant to chapters 8 and 9, section 2.2 reviews the products of radiation damage and subsequent annealing of type-I diamond relevant to chapters 6 and 7 and section 2.3 summarises nitrogen aggregation, providing background for chapter 7.

It is worth making a note at this point about the different naming conventions of defects in diamond. It is common for a spectral feature to be named prior to it being associated with a specific defect, often leading to confusing and inconsistent names. A few names have already been discussed in section 1.1 for some defects observed in IR absorption. For defects observed by a zero-phonon line (ZPL) in optical absorption and/or luminescence a convention (summarised in table 2-1) was used in early investigations to signify which treatment created the feature. This convention applies to a number of defects important to this thesis.

Category	Abbreviation	Meaning
Natural	N	Found in natural diamond
General radiation	GR	All diamond types after irradiation
Radiation	R	Type-I diamond after irradiation
Type-II radiation	TR	Type-II diamond after irradiation
Heated	H	Annealed diamond which was previously irradiated

Table 2-1 Naming convention and categorisation for ZPLs in diamond reproduced from Walker [2].

It is common for EPR defect spectra to be named with letters signifying the institution at which it was observed, followed by a number. For example the W15 spectrum is named after the University of Witwatersrand, although since its identification it is almost ubiquitously referred to the negatively charged nitrogen-vacancy centre, often abbreviated to NV^- or just NV (although the latter causes confusion with the neutral nitrogen vacancy centre, NV^0).

In this thesis, wherever possible, an abbreviation based on the atomic constituents of the defect is used, important examples of which are given in the abbreviations section at the front of the thesis. The original abbreviation is only used if the defect remains unidentified, or sometimes if the spectrum is specifically being referred to, rather than the corresponding defect.

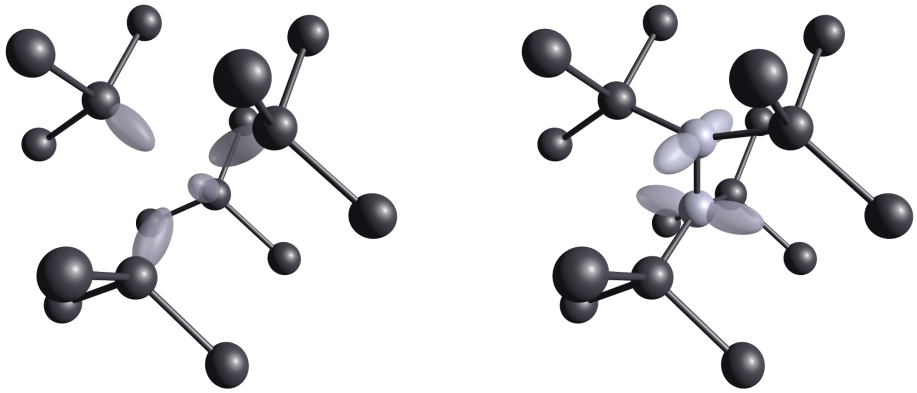

(a) Vacancy **(b)** ⟨0 0 1⟩-split interstitial

Figure 2-1 The vacancy and single ⟨0 0 1⟩ split-interstitial in diamond. The two central carbon atoms in the interstitial are sp^2 bonded, each having a p orbital normal to the symmetry axis. The interstitial atoms are indicated in light grey.

2.1 Radiation damage in type-IIa diamond

With sufficient energy, irradiating particles such as electrons, neutrons and ions can displace atoms from the carbon lattice. The primary radiation damage products in type-IIa diamond are Frenkel pairs of displaced atoms on interstitial sites and the corresponding vacant lattice sites. If a significant amount of energy is transferred from an irradiating particle, a cascade of damage can result [3]. Different configurations and complexes of interstitial and vacancy related defects have been proposed and identified in a variety of spectroscopies. The defects which result from electron and neutron damage of intrinsic diamond are reviewed here.

2.1.1 Vacancy

The GR1 absorption is observed in the majority of irradiated diamond [4]. Uniaxial stress measurements experimentally determined the symmetry of GR1 to be $\mathscr{T}_\mathrm{d}$, constraining it to either be a vacancy or $\mathscr{T}_\mathrm{d}$ interstitial [5]. The absorption has a ZPL at 1.673 eV (741.1 nm) corresponding to a transition from a $^1\mathrm{E}$ to $^1\mathrm{T}_2$ state as well as a weaker line at 1.653 eV (750.1 nm) corresponding to a transition from

a ^{1}A state to the $^1T_2$ state [5], consistent with previous theoretical analysis of the vacancy [6]. When electron donors are present in the lattice a ZPL at 3.150 eV (393.6 nm), known as ND1, is also observed. Davies argued that GR1 and ND1 must be the neutral (V^0) and negative vacancies (V^-) respectively by considering their symmetry, charge transfer between the two, and their production in different types of diamond [7]. The series of lines from 2.880–3.010 eV, labelled GR2-8 are also transitions from V^0 [8]. The structure of the vacancy is shown in figure 2-1a.

Charge transfer between V^0 and V^- allowed the ratio of the oscillator strengths to be determined as $f_{ND1}/f_{GR1} = 4.0(2)$ (where f relates the concentration to the integrated absorption coefficient by $A = f[X]$), which is corroborated by the annealing in of NV and N_2V [9]. The ground state of the neutral vacancy is diamagnetic and so the defect cannot be quantified by EPR, however upon illumination with UV light it can be excited to a $^5A_2$ state [10]. It was proposed that the production of this excited state was a result of the ionisation of V^-, rather than directly from V^0. The ground state of V^- is spin $\frac{3}{2}$, allowing its observation and quantification by EPR [11]. By relating the ND1 absorption to the quantification from EPR, the calibration constant for the optical absorption was determined to be $f_{ND1} = 4.8(2) \times 10^{-16}$ meVcm^2 and consequently $f_{GR1} = 1.2(3) \times 10^{-16}$ meVcm^2 [12].

With the ability to quantify the vacancy the radiation damage rates can be determined. A range of damage rates are reported in the literature, a result of the dependence on diamond type (e.g. nitrogen content; natural, CVD- or HPHT-grown). Twitchen et al. determined the production rate at room temperature from 1.9 MeV electrons to be 0.50(5) cm^{-1} in HPHT-grown type-Ib diamond (9(1) ppm N_S^0) [12]. Hunt et al. performed irradiation with 2 MeV electrons at 100 K and 350 K and concluded the production rate of vacancies in type-IIa HPHT diamond was 1.53(10) cm^{-1} at both temperatures [13]. The two production rates measured by Twitchen et al. and Hunt et al. were calculated using the aforementioned calibration constant for GR1.

The migration energy of V^0 was determined to be 2.3(2) eV by isothermal annealing experiments [9, 14]. A small proportion of V^0 is seen to anneal out at

$\approx 400\,^{\circ}\mathrm{C}$ (when interstitials are mobile), consistent with some interstitials having been created trapped within a barrier near vacancies recombining [15, 16].

2.1.2 ⟨001⟩-split interstitial

An EPR spectrum, labelled R2, was first reported in 1962 in electron irradiated type-IIa diamond [17]. After some dispute over the assignment of R2 to either the compressed vacancy or an isolated interstitial, it was much later identified as the neutral ⟨0 0 1⟩-split self interstitial ($C^0_{I_{001}}$), with symmetry $\mathscr{D}_{2d}$ [13]. The structure of the defect is depicted in figure 2-1b. The two central carbon atoms are sp^2 bonded, each having a p orbital normal to the symmetry axis.

The assignment of R2 as $C^0_{I_{001}}$ is supported by ab initio calculations using local-density-functional pseudopotential theory, which found the only stable structure of the single interstitial in the neutral, −1, +1, and +2 charge states to be $C_{I_{001}}$ [18]. The tetrahedral, 'hexagonal', bond-centred and ⟨1 1 0⟩-split interstitial were all found to be unstable. Later calculations using the plane-wave pseudopotential approach also concluded $C_{I_{001}}$ to be the most stable structure [19].

The EPR signal arises from an $S = 1$ excited state, 50 meV above a diamagnetic ground state. The centre has a very large axial zero field splitting with $D = \pm 4173(3)$ MHz. As well as the large D another distinctive feature of the R2 EPR spectrum is its very broad lines – up to 8 mT depending on the orientation with the external magnetic field. A typical linewidth of other radiation damage centres is 20 µT. The angular variation of the linewidth is consistent with a distribution of values of D [13].

The narrow forbidden EPR transitions of R2 rule out short relaxation times as causing the broadening. A possible mechanism is motional averaging. Such a broadening would be expected to have a temperature dependence, but none has been found between 77 K and 650 K. Since R2 is seen from a thermally excited state, measurements at lower temperatures cannot be made and so motional averaging cannot be ruled out. The lines are about 40 % broader in type-Ib diamond containing 300 ppm N^0_S, suggesting that a component of the broadening is related

to internal strain. In type-IIa diamond, internal strains near interstitials could be accounted for by nearby vacancies [13].

The production rate of R2 from 2 MeV electrons was measured to be $0.10(5)\,\mathrm{cm}^{-1}$ at 350 K but increased to $1.1(1)\,\mathrm{cm}^{-1}$ when the temperature was lowered to 100 K [20]. The production of R2 is the same in all three sites regardless of the direction of the irradiation [21]. $\mathrm{C}_{\mathrm{I}_{001}}$ has been observed to anneal out with activation energy 1.6(2) eV with an attempt frequency of 10^8 Hz [21, 22].

Further irradiation experiments over the temperature range 90–900 K led to the conclusion that annealing of interstitial atoms during irradiation is different to the thermal annealing of $\mathrm{C}^0_{\mathrm{I}_{001}}$ [16]. It was proposed that a highly mobile interstitial species with migration energy 0.3 eV, labelled I*, is produced by charge transfer or electronic excitation during irradiation. If I* is created within a capture radius R_C of a vacancy then it still needs to overcome a barrier to recombine with it or escape R_C. During irradiation below about 120 K, I* is immobile and the production of interstitials and vacancies is approximately equal. From 150–200 K, I* outside R_C can anneal out but those inside are still trapped. Only at temperatures above 400 K can the interstitials within R_C annihilate with the vacancy or escape to other traps.

The R2 defect is associated with a number of optical lines at 1.685 eV (735.8 nm) and 1.859 eV (666.9 nm) [23]. The 1.859 eV line originates in a forbidden transition made allowed by mixing with the 1.685 eV line [24]. Uniaxial stress measurements are consistent with $\mathrm{C}_{\mathrm{I}_{001}}$ in its ground state tunnelling between equivalent $\mathscr{D}_2$ configurations, and in its excited state between $\mathscr{C}_{2\mathrm{v}}$ configurations to give the observed $\mathscr{D}_{2\mathrm{d}}$ symmetry [25].

2.1.3 Di-⟨001⟩-split interstitial

The R1 EPR centre was first observed at the same time as R2 in electron irradiated type-IIa diamond [17]. It has been observed in type-I and type-II diamond by electron and neutron irradiation indicating it is an intrinsic defect, although its production rate appears to be reduced in type-I diamond [26, 27]. It was identified

more than thirty years later as being the di-$\langle 0\,0\,1\rangle$-split self interstitial by study of its ^{13}C hyperfine interactions [28]. A model of the defect is shown in figure 2-2a. The centre has $\mathscr{C}_{1h}$ symmetry with a $\{1\,1\,0\}$ mirror plane.

R1 has two electrons in parallel non-bonding $2p_x$ orbitals, perpendicular to the $\{1\,1\,0\}$ plane of the defect, giving an effective spin $S = 1$. It has a large near axial zero field splitting with $D = 4208(6)$ MHz. In contrast to R2 the lines are very narrow making the spectrum exceptionally sensitive to misalignment of the applied Zeeman field.

The production rate of R1 was found to be the same at $0.014(1)\,\mathrm{cm}^{-1}$ for irradiation of samples at both 100 K and 350 K with 2 MeV electrons [20]. In that study the production was proportional to dose up to the maximum dose of $4 \times 10^{18}\,\mathrm{e}^{-}\mathrm{cm}^{-2}$. The formation of R1 at 100 K means that a form of interstitials must be mobile at 100 K, under the conditions of irradiation. In contrast to [20], a previous study found that production saturated at a dose of $10^{18}\,\mathrm{e}^{-}\mathrm{cm}^{-2}$ and did not detect any production of R1 at 100 K [29].

Assignment of R1 to the di-$\langle 0\,0\,1\rangle$-split self interstitial was disputed by Lea-Wilson and Lomer who claimed that the only explanation of the saturation of its production involved an impurity [29]. The assignment was however reaffirmed by Baker, Twitchen and Newton who explained that the production saturation could be obtained by the defect having a large interaction cross section with incident electrons causing its destruction as well as its creation [30]. The structure is supported by ab initio calculations, from which good agreement between the measured and calculated D tensor was found [31].

A detailed isothermal annealing study was carried out by Twitchen et al., who found R1 to anneal out at about 300 °C. R1 is therefore less stable than R2 and cannot be created by annealing. By fitting to an Arrhenius relationship the activation energy was determined to be 0.6(1) eV with an associated attempt frequency $\approx 10^{3}\,\mathrm{s}^{-1}$ [32]. The low activation energy was argued to correspond not to dissociation of R1, but rather to its transformation into a next nearest neighbour pair of interstitials.

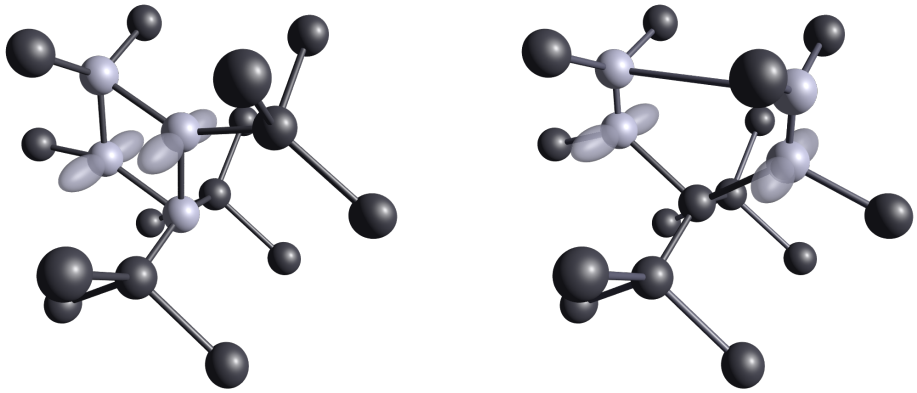

(a) R1 **(b)** Humble

Figure 2-2 Two configurations of the di-⟨0 0 1⟩-split self interstitial in diamond. The nearest neighbour interstitial R1 defect is $S = 1$ and was identified in EPR [28]. The $S = 0$ next nearest neighbour interstitial configuration of the Humble structure is calculated to be lower in energy than R1 and is postulated to correspond to the 3H optical system [31]. The interstitial atoms are indicated in light grey.

Lea-Wilson and Lomer observed six satellites to R1 in electron irradiated type-IIa diamond [29]. By studying ^{12}C enriched diamond to reduce the intensity of the ^{13}C hyperfine lines, a total of twelve satellite centres, labelled R1A–L, were identified [33]. The satellites are also $S = 1$ and have $\mathscr{C}_{1h}$ symmetry, however D is $\leq 4\%$ smaller and E is significantly larger than for R1. The satellites are explained as pairs of R1 and a vacancy in its $\{1\,1\,0\}$ plane. Separate to the R1 satellites are a set of lines, apparently very similar to R1 but with slightly smaller g [28].

Spin polarisation of R1 has been observed when the sample was cooled to approximately 60 K (concentration dependent) and illuminated with energy greater than 1.7(1) eV [34]. To explain the spin polarisation it was suggested that spin-orbit coupling with a ^1B_u state mediates selective excitation from the ^3B_u ground state.

2.1.4 3H

The 3H ZPL at 2.463 eV (not to be confused with the H3 ZPL at 2.464 eV) is produced by electron irradiation of all types of diamond; it is however created more readily in type-Ib diamond [35]. Walker reported that although the intensity

of 3H generally increases with dose, it does so somewhat erratically [23].

The production of 3H from electron irradiation (at room temperature) increases linearly with A-centre concentration and decreases linearly with B-centre concentration [15]. It is interesting to note that increasing the A-centre concentration reduces the production of R1 [27]. An increase in the concentration of B-centres decreases the production of 3H [15]. The centre is produced by irradiation at 80 K, but more readily at room temperature [2]. The centre was confirmed by uniaxial stress measurements to have $\mathscr{C}_{2v}$ symmetry and a $\langle 1\,1\,0 \rangle$ dipole [36].

Annealing up to 400 °C can increase the concentration of 3H – hotter anneals reduce it. The increase is believed to be a charge transfer effect since illumination with UV light was found to return the concentration up to 1000 °C [27]. Similar behaviour is reported with the 5RL optical system.

3H has been found to be bleached by UV or intense blue laser irradiation [37]. Although an enhancement of TR12 was also seen, these processes were not correlated as time constants for the defects differed. Since it is possible to either bleach or enhance 3H, there should be an EPR active charge state, although none has yet been identified. It was found in [38] that 3H emission can be quenched by GR1, thus changes in 3H luminescence do not necessarily correspond to changes in concentration.

Two models of the di-$\langle 0\,0\,1 \rangle$-split interstitial exist, the R1 EPR defect and the Humble interstitial, diagrams of which are in figure 2-2. Density functional theory (DFT) calculations found the $S = 0$ Humble interstitial to be 0.7 eV lower in energy than R1, thus its production is expected [31]. It was postulated that the decreased production of R2 relative to vacancy production between irradiation at 100 K and 300 K could correspond to an increased production of the Humble interstitial [20]. It was concluded by Goss et al. [31] that the positively charged Humble defect is compatible with 3H.

The 5RL system, observed in optical absorption and cathodoluminescence, is characterised by a ZPL at 4.582 eV (270.6 nm) which couples to local vibrational modes (LVMs) of energies much higher than the lattice phonon energies [39]. Isotopic

substitution has shown that the vibration involves a pair of carbon atoms [40]. Uniaxial stress measurements have shown the centre to have $\mathscr{C}_{2v}$ symmetry [39]. This together with photochromic changes involving 3H and 5RL led to it being suggested that 5RL is a different charge state of 3H [27].

2.1.5 TR12

The strongest features of the TR12 centre are its ZPL at 2.637 eV (470.2 nm) and an LVM at 2.437 eV (508.8 nm), however there are also a number of other modes [41]. Walker determined the symmetry by uniaxial stress measurements to be monoclinic I [23], however further measurements by Davies, Foy and O'Donnell were inconclusive with the authors disputing the original assignment [41]. They concluded that the stress data was incompatible with any transition at any centre of fixed symmetry.

The centre is produced by irradiation of type-IIa and type-IIb diamond, but not of type-I diamond [23]. Although created from irradiation at room temperature, its absorption and luminescence intensity was found to increase by annealing the sample up to 800 °C; higher temperatures destroy it. The production rate of TR12, relative to that of vacancies, was found to increase by a factor of four when irradiating with 1.5 MeV electrons compared to 0.6 MeV electrons [41]. The evidence suggests that the defect is a complex of interstitial carbon and possibly vacancies. It has been proposed from modelling that the defect consists of an interstitial carbon atom on a hexagonal site [42].

Iakoubovskii and Adriaenssens reported a ZPL between 2.648 and 2.654 eV that is stable at temperatures over 1400 °C, which they attributed to stressed TR12 centres. More recently, Naydenov et al. created arrays of TR12 centres by implantation of carbon ions and demonstrated single centre detection by their photoluminescence [43]. They showed TR12 to have photostable emission in the blue spectral region and proposed its use as a single photon source. The intensity of TR12 can be enhanced by UV or intense blue laser irradiation [37].

2.1.6 Other radiation damage complexes

As well as the distinctive R1 and R2 spectra caused by irradiation of type-IIa diamond there are a number of systems with overlapping lines in the centre field region. These lines are difficult to study and consequently not a great deal is known about them. Of note are the R3 and R14 defects [44]. Both centres are low symmetry with $S = 1$ and both increase on annealing before they anneal out. The lines of R14 do not appear to have a simple pattern of intensities.

If an irradiating particle has enough energy to displace multiple atoms from the diamond lattice then it is possible to create di-vacanacies [45]. The neutral charge state of the di-vacancy, known as R4/W6 in EPR, is $S = 1$ and the spin Hamiltonian has been well characterised [46]. At room temperature the centre has $\mathscr{D}_{3d}$ symmetry, but on cooling to low temperatures it distorts to $\mathscr{C}_{1h}$ symmetry. Although it can be produced directly by irradiation of type-IIa diamond, the di-vacancy increases in concentration significantly on annealing up to temperatures when the vacancy is mobile before annealing out by 1000 °C [45]. The TH5 optical system exhibits the same annealing behaviour [45] and is therefore thought to originate at the di-vacancy. A system of two vacancies separated by two bond carbon atoms has also been calculated to be stable [47, 48]

O3 is a paramagnetic defect with $S = 1$ and $\mathscr{C}_{2v}$ symmetry [49]. The preferred model which is consistent with the spin Hamiltonian parameters is a complex involving three parallel carbon interstitials. This assignment is corroborated by DFT calculations, which found the calculated D tensor to be in close agreement with the measured values [31]. O3 is created by irradiation at low temperature, but can be increased by annealing to temperatures where R1 and R2 anneal out.

2.2 Radiation damage in type-I diamond

The presence of nitrogen in the diamond lattice affects the outcome of radiation damage in a number of ways: neutral substitutional nitrogen (N_S^0) readily donates an electron to other intrinsic radiation damage defects such as V^0 [50]; after an-

nealing, and during irradiation, it will form complexes with intrinsic defects [51, 52]; and the strain induced by nitrogen impurities reportedly affects the dynamics of vacancy interstitial recombination changing damage rates [53]. The aggregation state of nitrogen is important to the outcome of subsequent annealing, creating different traps for mobile defects [27]. For example, in type-Ib diamond V is trapped by N_S to create NV; in type-IaA diamond V is trapped by di-substitutional nitrogen (N_{2S} – also known as the A-centre) to create the di-nitrogen vacancy (N_2V); and in type-IaB diamond V is trapped by N_4V (also known as the B-centre) to create N_4V_2.

2.2.1 Damage rates in type-IaA and type-Ib diamond

In HPHT type-IIa diamond, relatively free from dislocations, the damage rates (formation of interstitials and vacancies) have been well characterised [13], but for type-I diamond damage rates are not nearly so well understood. Charge compensation from nitrogen creates the negative vacancy (V^-) along with positive substitutional nitrogen (N_S^+). Although V^- can be quantified from its ZPL at 3.150 eV [12], if the concentration of N_S^0 is high, the background absorption [54] at 3.150 eV makes measurement difficult. Negative vacancies can also be quantified by EPR, however a similar problem exists with the signal being hidden under the N_S^0 signal [11]. An alternative to directly measuring vacancy concentrations is to assume that there are no other acceptors and so for every N_S^+ there is a corresponding V^-, then one only needs to measure N_S^+ from its one-phonon absorption [50].

A review was made by Palmer [55], but published in 1994 before the calibration constants were determined for V^0 and V^- [12]. He concluded that there was clear evidence that vacancy production is much higher in type-IaA diamond. Davies et al. found that the linewidth of the V^0 ZPL at 1.673 eV decreased upon annealing, leading to the suggestion that a large number of vacancies are created in strained regions near nitrogen aggregates [9].

A study was made of the damage rates in different growth sectors of a thin slice

of HPHT-grown diamond irradiated with 3 MeV to a dose of 2×10^{18} $e^- cm^{-2}$ [53]. The nitrogen concentration in each sector was 75 ppm in {1 1 1}, 25 ppm in {1 1 3} and ≤ 2 ppm in the {1 1 5} sectors. The corresponding vacancy production was 29 ppm, 22 ppm and 8 ppm in each sector respectively, showing increased damage rates for higher concentrations of N_S^0. It was argued that the mechanism responsible was the trapping of self interstitials by nitrogen to make nitrogen interstitial complexes. This is supported by EPR imaging of interstitials, which found that the R1 di-interstitial defect is produced preferentially in low nitrogen sectors [26].

2.2.2 Nitrogen interstitials

Compared to the self interstitial and interstitial complexes, very little is known about nitrogen interstitials in diamond. A number of LVMs, ZPLs and EPR lines have been attributed to nitrogen interstitials however the only one unambiguously identified is the di-nitrogen ⟨0 0 1⟩-split interstitial [56]. The annealing in of H1a in type-Ib diamond requires that other nitrogen interstitial defects exist [57].

2.2.2.1 Di-nitrogen ⟨001⟩-split interstitial

The di-nitrogen ⟨0 0 1⟩-split interstitial (N_{2I}), shown in figure 2-3, has been unambiguously identified [56]. The defect has an LVM at 1450.8 cm^{-1}, known as H1a, that is one of the strongest features in the IR spectra of type-IaA diamonds that have been irradiated and annealed [58]. Uniaxial stress experiments showed that the LVM originates from a defect with $\mathscr{D}_{2d}$ symmetry [56]. This, together with an excellent agreement of calculated piezospectroscopic parameters for N_{2I} with those experimentally determined for H1a were the basis of the assignment.

From isotopic substitution experiments it was determined that the 1450 cm^{-1} LVM occurs at one nitrogen [59] and two carbon atoms [60]. As a historical point this led to the incorrect assignment to a bond-centred nitrogen interstitial [51]. With the restriction that the defect involved only one nitrogen atom, ab initio calculations favoured the nitrogen ⟨0 0 1⟩-split interstitial over a bond-centred interstitial [61]. With the correct assignment [56], the previous confusion was explained by the

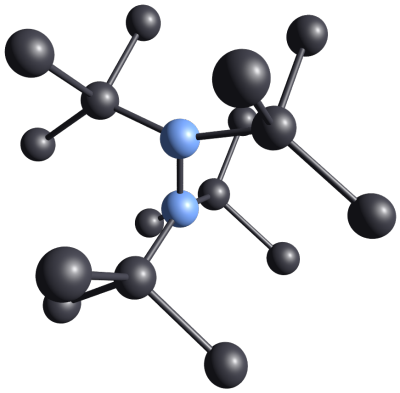

Figure 2-3 Model of the di-nitrogen ⟨0 0 1⟩-split interstitial. The defect has an LVM at 1450.8 cm^{-1} known as H1a.

vibration originating from a pair of degenerate modes, each involving a nitrogen and two carbon atoms.

H1a can be observed immediately after irradiation in type-I diamond and strengthened by annealing type-IaA diamond above 250 °C [59]. Type-Ib diamond requires annealing above 600 °C to create H1a. This suggests that there are two mechanisms for its production. From the low annealing temperature, one probably involves C_I migrating to N_{2S}:

$$C_I + N_{2S} \rightarrow N_{2I} \,. \tag{2-1}$$

The other first requires the creation of a nitrogen interstitial, N_I, which then migrates to N_S:

$$C_I + N_S \rightarrow N_I + C \tag{2-2}$$

$$N_I + N_S^0 \rightarrow N_{2I} + C \,. \tag{2-3}$$

The annealing in of N_{2I} in type-Ib diamond complements the annealing out of lines at 1424 cm^{-1} and 1564 cm^{-1} [62]. The annealing in of 1502 cm^{-1} correlates with a shoulder in the annealing in of H1a [58]. H1a is stable to about 1100 °C and is significantly reduced by annealing at 1400 °C [63]. The annealing out of H1a coincides with the annealing out of H1b and the annealing in of H2, possibly corresponding to H2 being created by the dissociation of H1b [63].

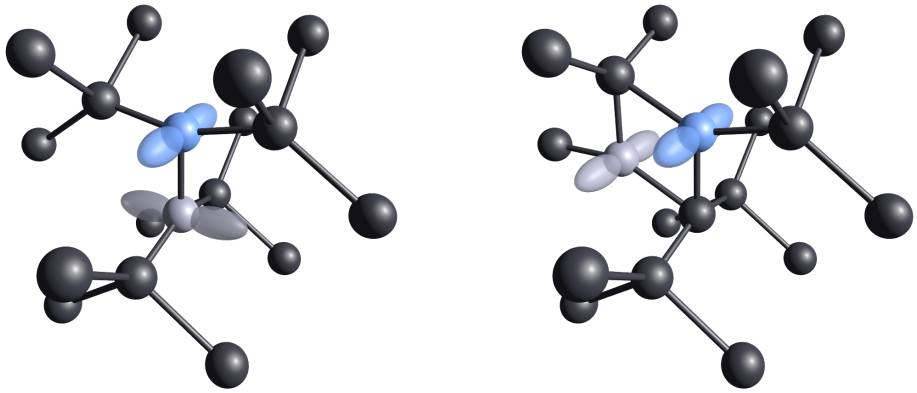

(a) N_I **(b)** $N_I - C_I$

Figure 2-4 Two nitrogen interstitial defects identified by EPR spectroscopy [52]. The proposed structures are the single nitrogen ⟨0 0 1⟩-split interstitial (a) and the ($N_I - C_I$) interstitial with the R1 structure (b). The interstitial nitrogen and carbon atoms are indicated in light blue and grey respectively, however they are interchangeable.

2.2.2.2 EPR of nitrogen interstitials

Two nitrogen interstitial defects, labelled WAR9 and WAR10 have been identified in EPR [52]. The proposed models are the single nitrogen ⟨0 0 1⟩-split interstitial (figure 2-4a), and the nitrogen-carbon di-⟨0 0 1⟩-split interstitial respectively, both in the neutral charge state (figure 2-4b). The assignment was based on the presence of $I = \frac{1}{2}$ hyperfine interactions (the diamond studied was ^{15}N doped), comparison with similar defects and their symmetries being $\mathscr{C}_{2v}$ for WAR9 and $\mathscr{C}_{1h}$ for WAR10.

The sample studied was HPHT-grown with ^{15}N isotopic substitution, facilitating the detection of the signals due to the absence of the central ^{14}N hyperfine. Both defects were only seen in the low nitrogen sectors of the diamond. It was suggested that they are both acceptors and are negatively charged when N_S is in excess. In the negative charge state both would be diamagnetic and so not detected by EPR.

Both defects were found after annealing at 827 °C and are stable up to at least 1527 °C [52]. Unfortunately it would be difficult to detect the defects prior to annealing to 600 °C due to the overlap with the signal from V^-. The calculated migration barrier for N_I in the neutral charge state is 1.7 eV, and 0.8 eV and 2.4 eV in the positive and negative charge states respectively [61]. The 1.7 eV and 2.4 eV

migration barriers corresponds to activation below 500 °C and 700 °C respectively, at odds with the observed stability at 1527 °C. The thermal stability of WAR9 and WAR10 is discussed by Atumi et al. [57] and alternative models considered. No stable structure could be found that fitted the parameters and it was suggested that WAR9 and WAR10 could be larger aggregates.

2.2.2.3 Other nitrogen interstitials

Numerous other LVMs and ZPLs have been attributed to nitrogen interstitial defects without an unambiguous identification. The assignment has often been made by the observation of a feature only in type-Ib diamond and annealing behaviour at temperatures where the carbon interstitial is known to be mobile.

The absorption spectra resulting from radiation damage in type-Ib diamond are markedly different to those in type-IIa diamond. Many differences can be accounted for by charge compensation by N_S, such as the presence of ND1 from V^- but lack of GR1 from V^0. In type-IIa diamond the 1.859 eV (666.9 nm) transition at $C^0_{I_{001}}$ is present after irradiation and stable until it anneals out; in (single growth-sector HPHT-grown) type-Ib diamond, its intensity increases significantly by annealing at 350 °C, then anneals out as expected [27].

Collins and Dahwich investigated ZPLs in irradiated type-Ib diamond at 2.367 eV and 2.535 eV (523.8 nm and 489.1 nm) which show interesting annealing behaviour [62]. To overcome the high background absorption in irradiated type-Ib diamond a 200 µm thick sample was used. The 2.367 eV line is present after irradition and anneals out at 250 °C, at which point the 2.535 eV line anneals in. The 2.535 eV line then anneals out as the increase in $C^0_{I_{001}}$ is seen. In a previous study of the systems [64] it was suggested they consisted of nitrogen and an interstitial. Also in that study, complementary photochromism was observed between the 2.367 eV line and another at 1.979 eV (626.5 nm), but without any corresponding photoconductivity. The authors suggested that the transitions were from the same defect but in a configuration of different symmetry. It was argued that the increase of $C^0_{I_{001}}$ is from carbon interstitials being released as the 2.535 eV nitrogen-interstitial complex anneals out [62].

An LVM has been found at 1612 cm^{-1} which anneals in gradually with annealing up to 400 °C then anneals out as $C^0_{I_{001}}$ anneals out, at which point LVMs at 1424 cm^{-1} and 1564 cm^{-1} anneal in [62]. They are then stable until approximately 600 °C when they anneal out as N_{2I} anneals in. This annealing behaviour and observation only in type-Ib diamond led to it being postulated that they are LVMs at a precursor to N_{2I}, presumably N_I [62], however no shift was detected in the 1424 cm^{-1}, 1564 cm^{-1} and 1612 cm^{-1} LVMs with isotopic substitution of nitrogen [62]. Annealing to about 600 °C creates LVMs at 1502 cm^{-1} and 1706 cm^{-1}, which both anneal out at around 900 °C. A line at 1856 cm^{-1} anneals in as 1706 cm^{-1} anneals out. With 50 % ^{15}N substitution the 1502 cm^{-1} and 1706 cm^{-1} LVMs each have another mode associated with them [60] whereas 1856 cm^{-1} has two additional modes [65]. It has been postulated from agreement of modes with simulations that the 1706 cm^{-1} and 1856 cm^{-1} modes are at the Humble and R1 forms of nitrogen interstitials respectively [61].

2.2.3 594 nm defect, H1b and H1c

The 594 nm defect has a ZPL at 2.086 eV (594.4 nm) and is observed in type-Ia and type-Ib diamond after irradiation and is enhanced by annealing, attaining a maximum at around 800 °C and annealing out by 1000 °C [66]. A uniaxial stress study has shown the line to be from a trigonal E to E transition [67]. Another ZPL at 2.916 eV (425.2 nm) correlates in intensity with the 2.086 eV ZPL [67] and has been shown to be an E to A transition at a trigonal centre [68]. It is suggested they originate at the same defect where the ground E state is common to both transitions [67].

As the 594 nm defect anneals out the H1b and H1c defects, at 0.6124 eV (2024 nm) and 0.6408 eV (1934 nm) respectively, anneal in [66]. The symmetry of both H1b and H1c is $\mathscr{C}_{1h}$ [66]. The amount of H1b and H1c created is proportional to the amount of N_{2S} and N_4V in the diamond [58, 66], leading to the suggestion that the defects are formed by the 594 nm defect being trapped at N_{2S} and N_4V. This probably stems from the similar scenario with H3 and H4 being formed by a vacancy being trapped at N_{2S} and N_4V respectively [69]. As H1b anneals out at

1600 °C H2 anneals in [63].

2.2.4 Nitrogen vacancy defects

The negatively charged nitrogen-vacancy centre (NV^-) is one of the most studied defects in diamond, owing to its potential for applications in quantum information processing and sensing, arising from the ability to perform optically detected magnetic resonance (ODMR) on bulk defects and single centres [70]. An overview of the properties relevant to this thesis is given here. For extensive detail of its properties see the review by Doherty et al. [71]. A model of the defect is shown in figure 2-5a.

NV^- was first detected by its ZPL at 1.945 eV (637.5 nm) in PL and absorption, identified as a transition between an A ground state and E excited state of a trigonal defect [72, 73]. The symmetry, together with the observed correlation between its annealing in and the annealing out of GR1 and ND1, led to its identification [73]. The assignment was confirmed by observation of its EPR signal (also known as W15) [74].

When the defect is excited to its ^3E state, it can relax to the ground state by emission of a $\lesssim 1.945$ eV photon, or by a non-radiative pathway via intermediate dark states [75]. The rate of the relaxation through the non-radiative pathway depends on the spin state, leading to a net polarisation into the $m_S = 0$ state. The dependence of the non-radiative decay rate on the spin state leads to the ODMR signal.

The NV centre is also present in the neutral charge state (NV^0) identified by its ZPL at 2.156 eV (575 nm) determined by uniaxial stress to be an E to A transition at a trigonal centre [68]. It was determined that the defect responsible was NV^0 by the correlation between the increase of 2.156 eV and decrease of 1.945 eV after annealing with increasing neutron irradiation [76]. Charge transfer can be driven between NV^0 and NV^- [77] with the relative concentrations of each determined approximately by the concentration of N_S donors [78].

Despite NV^0 having an $S = \frac{1}{2}$ ground state an EPR signal has not been observed

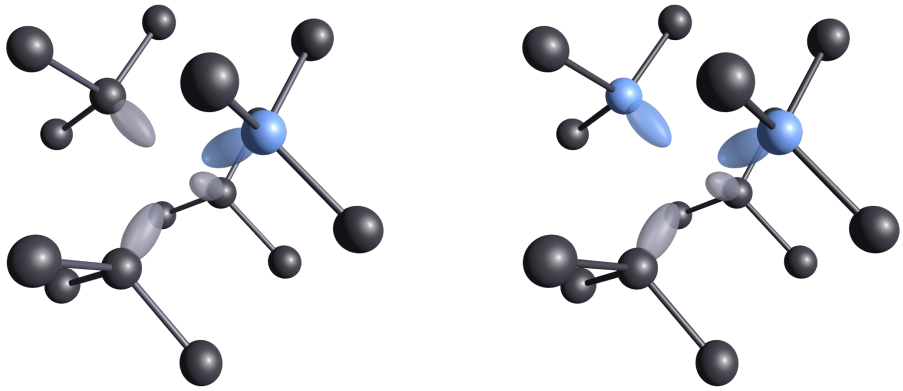

(a) NV **(b)** N_2V

Figure 2-5 Models of the nitrogen-vacancy (NV) and di-nitrogen-vacancy (N_2V) defects. The nitrogen atoms are indicated in light blue.

for it [79]. The lack of a detectable EPR signal for the ground state is reasoned to be the result of dynamic Jahn-Teller coupling broadening the lines, reducing detection sensitivity [79]. NV^0 does however exhibit an EPR signal from an excited $^4A_2$ state when illuminated with light of energy $\geq 2.2\,\text{eV}$ [79].

The single nitrogen-vacancy defect is part of a family of multi-nitrogen-vacancy defects (N_nV). The H2 and H3 ZPLs at 1.257 eV (986 nm) and 2.463 eV (503 nm) respectively had long been believed to correspond to the negative and neutral charge states of the di-nitrogen vacancy (N_2V) from their $\mathscr{C}_{2v}$ symmetry [73, 80]. A model of the defect is shown in figure 2-5b. Both ZPLs were known to occur from different charge states of the same defect from studies of their photochromism [81, 82], however an unambiguous identification was only made by the recent identification of the EPR signal of the $S = \frac{1}{2}$ ground state of N_2V^- [83].

2.3 Nitrogen aggregation in diamond

The most noticeable result of annealing to high temperature, usually at high pressure and typically over 2000 °C, is the aggregation of single substitutional nitrogen into complexes such as N_{2S} [84] and at higher temperature N_4V [85].

This process is depicted in the simplest form as

$$4N_S \rightleftharpoons 2N_{2S} \rightleftharpoons N_4V + C_I \,, \tag{2-4}$$

where each step is the result of a more complex set of mechanisms and the reverse process also occurs. The rate of $Ns \rightarrow N_{aggregates}$ compared to $N_{aggregates} \rightarrow N_S$ is determined by temperature; at lower temperatures equation (2-4) is weighted further to the right but the process takes longer. The extent of aggregation can be used to estimate time spent and temperature experienced of a natural diamond in the mantle, and help distinguish natural from synthetic diamond [86].

The characteristic spectroscopic features of N_{2S} and N_4V are one-phonon absorptions. The defects are also commonly called the A-centre and B-centre respectively, names originating from the original identification of two types of diamond by the one-phonon absorption of the defects. The one-phonon absorption for N_{2S} does not have any sharp features but a somewhat broad peak at 1280 cm^{-1} with a shoulder at 1215 cm^{-1} [84]. The one-phonon absorption of N_4V has a broad absorption at 1175 cm^{-1} followed by a plateau from 1230–1310 cm^{-1} and a peak at the Raman frequency 1332 cm^{-1} [85].

When studying the aggregation of nitrogen in irradiated diamond Collins found that the presence of radiation damage caused significant aggregation of N_S into N_{2S} at the relatively low temperature of 1500 °C [87]. The resulting concentration of aggregated nitrogen was found to be approximately a factor of 100 greater than the vacancy concentration. It was proposed that N_S is a much more efficient trap than N_{2S} for V. The resulting NV diffuses through the lattice at high temperatures, combining with N_S to create N_2V. N_2V then releases V to leave behind N_{2S}. The V can then be recycled to repeat the process. In this way a small concentration of vacancies can dramatically enhance the aggregation rate.

The proposal of vacancy-enhanced aggregation was supported by early theoretical calculations showing its activation energy to be 4.5 eV and for direct movement of N_S by concerted exchange to be somewhat higher at 6.3 eV [88]. Later calculations found the activation energy for concerted exchange to be higher at 8.4 eV [89]. A theoretical investigation into the diffusion of NV determined the migration barrier

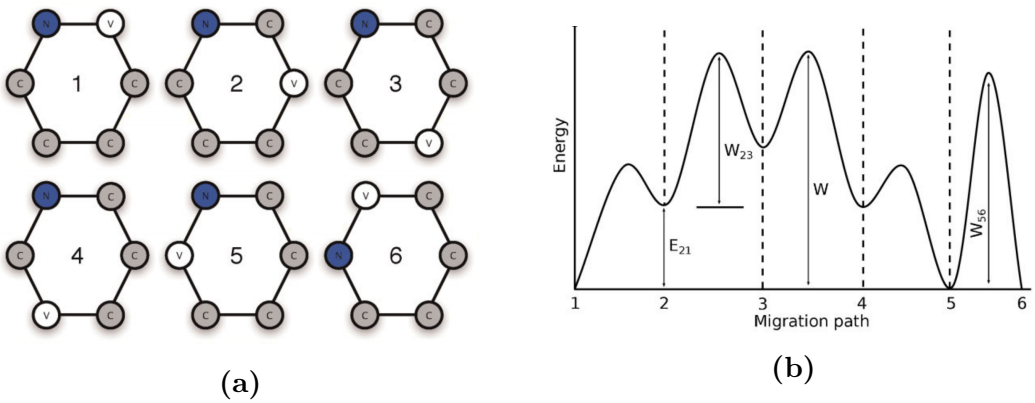

(a) (b)

Figure 2-6 The proposed mechanism for migration of NV [90]. The vacancy trajectory 1-6 in (b) corresponds to the configurations depicted in (a). Figures reproduced from [90].

to be 4.9 eV and the dissociation barrier to be higher at 5.8 eV [90]; the mechanism proposed for migration of NV is shown in figure 2-6. A recent publication has compiled experimental and theoretical data on processes related to nitrogen aggregation and concluded that, although vacancy assisted aggregation can be important, the formation of N_{2S} at lower temperatures is mediated by interstitials [91].

Nitrogen aggregation in HPHT-grown type-Ib diamond has been observed to follow second order kinetics with a measured activation energy of 5.5(7) eV at 6 GPa, with an increase in rate with lower pressure [92]. The incorporation of Co and Ni also affects the aggregation rate leading to a range of rate constants [93, 94]. It is thought that the effect of substitutional Ni and Co is to release interstitials which mediate aggregation [95].

The formation mechanisms of N_4V and platelets are disputed. Platelets have been shown to be monolayers of interstitial defects which are not solely composed of but can incorporate nitrogen [96]. Platelets are most readily identified by a large peak in the IR absorption spectrum at approximately 1365 cm^{-1} (sometimes referred to as B′) [97]. It was proposed that platelets are formed as a by-product of the aggregation of N_{2S} to N_4V [97]. Calculations have since suggested the formation of N_4V to be too slow to provide the interstitials necessary for platelets [98]. Instead it was proposed that platelets are partial dislocations which grow to

release vacancies. These vacancies are then trapped at N_{2S} to make N_2V which can migrate to another N_{2S} to create N_4V.

References

1. A. M. Zaitsev, *Optical Properties of Diamond* (Springer, Berlin Heidelberg, 2001).
2. J. Walker, *Reports on Progress in Physics* **42**, 1605–1659 (1979).
3. J. T. Buchan et al., *Journal of Applied Physics* **117**, 245901 (2015).
4. C. D. Clark, R. W. Ditchburn, H. B. Dyer, *Proceedings of the Royal Society of London. Series A* **234**, 363–381 (1956).
5. C. D. Clark, J. Walker, *Proceedings of the Royal Society of London A* **334**, 241–257 (1973).
6. C. A. Coulson, M. J. Kearsley, *Proceedings of the Royal Society of London. Series A* **241**, 433–454 (1957).
7. G. Davies, *Nature* **269**, 498–500 (1977).
8. J. E. Lowther, *Physical Review B* **48**, 11592 (1993).
9. G. Davies et al., *Physical Review B* **46**, 13157–13170 (Nov. 1992).
10. J. A. van Wyk et al., *Physical Review B* **52**, 12657–12667 (Nov. 1995).
11. J. Isoya et al., *Physical Review B* **45**, 1436–1439 (Jan. 1992).
12. D. Twitchen et al., *Diamond and Related Materials* **8**, 1572–1575 (Aug. 1999).
13. D. C. Hunt et al., *Physical Review B* **61**, 3863–3876 (Feb. 2000).
14. S. Lawon et al., *Journal of Physics: Condensed Matter* **4**, L125–131 (1992).
15. I. Kiflawi et al., *Journal of Physics: Condensed Matter* **19**, 046216 (Jan. 2007).
16. M. E. Newton et al., *Diamond and Related Materials* **11**, 618–622 (2002).
17. E. A. Faulkner, J. N. Lomer, *Philosophical Magazine* **7**, 1995 (1962).
18. S. Breuer, P. Briddon, *Physical Review B* **51**, 6984–6994 (Mar. 1995).
19. L. H. Li, J. E. Lowther, *Journal of Physics and Chemistry of Solids* **58**, 1607–1610 (1997).
20. D. J. Twitchen et al., *Physica B* **273-274**, 628–631 (1999).
21. D. Hunt, PhD thesis, University of Oxford, 1999.
22. L. Allers, A. T. Collins, J. Hiscock, *Diamond and Related Materials* **7**, 228–232 (1998).

23. J. Walker, *Journal of Physics C: Solid State Physics* **10**, 3031–3037 (Aug. 1977).
24. G. Davies, H. Smith, H. Kanda, *Physical Review B* **62**, 1528–1531 (2000).
25. H. Smith et al., *Physical Review B* **69**, 045203 (Jan. 2004).
26. G. A. Watt, M. E. Newton, J. M. Baker, *Diamond and Related Materials* **10**, 1681–1683 (2001).
27. K. Iakoubovskii et al., *Physica B* **340-342**, 67–75 (Dec. 2003).
28. D. J. Twitchen et al., *Physical Review B* **54**, 6988–6998 (1996).
29. M. A. Lea-Wilson, J. N. Lomer, *Philosophical Magazine A* **74**, 685–695 (1996).
30. J. Baker, D. Twitchen, M. Newton, *Philosophical Magazine Letters* **76**, 57–62 (July 1997).
31. J. P. Goss et al., *Physical Review B* **63**, 195208 (Apr. 2001).
32. D. J. Twitchen et al., *Journal of Physics: Condensed Matter* **13**, 2045–2051 (2001).
33. K. Iakoubovskii, J. M. Baker, M. E. Newton, *Physica Status Solidi (a)* **201**, 2516–2520 (2004).
34. D. J. Twitchen et al., *Diamond and Related Materials* **8**, 1101–1106 (1999).
35. G. Davies, *Proceedings of the Royal Society of London. Series A* **336**, 507–523 (1974).
36. H. E. Smith, PhD thesis, King's College London, 2004.
37. I. I. Vlasov, V. G. Ralchenko, E. Goovaerts, *Physica Status Solidi (a)* **193**, 489–493 (2002).
38. K. Iakoubovskii, G. J. Adriaenssens, *Physica Status Solidi (a)* **181**, 59–64 (Sept. 2000).
39. A. T. Collins, P. M. Spear, *Journal of Physics C: Solid State Physics* **19**, 6845–6858 (1986).
40. A. Collins et al., *Diamond and Related Materials* **2**, 136–141 (1993).
41. G. Davies, C. Foy, K. O'Donnell, *Journal of Physics C: Solid State Physics* **14**, 4153–4165 (1981).
42. A. Mainwood, A. T. Collins, P. Woad, *Materials Science Forum* **143**, 29–34 (1994).

43. B. Naydenov et al., *Applied physics letters* **95**, 181109 (Nov. 2009).

44. M. A. Lea-wilson, J. N. Lomer, J. A. Van Wyk, *Philosophical Magazine Part B* **70**, 101–107 (1994).

45. M. A. Lea-wilson, J. N. Lomer, J. A. Van Wyk, *Philosophical Magazine B* **72**, 81–89 (July 1995).

46. D. J. Twitchen et al., *Phys. Rev. B* **59**, 12900–12910 (May 1999).

47. D. Hyde-Volpe, B. Slepetz, M. Kertesz, *The Journal of Physical Chemistry C* **114**, 9563–9567 (June 2010).

48. B. Slepetz, M. Kertesz, *Physical chemistry chemical physics : PCCP* **16**, 1515–21 (2013).

49. D. C. Hunt et al., *Physical Review B* **62** (2000).

50. S. C. Lawson et al., *Journal of Physics: Condensed Matter* **10**, 6171–6180 (1999).

51. I. Kiflawi et al., *Physical Review B* **54**, 16719–16726 (1996).

52. S. Felton et al., *Journal of Physics: Condensed Matter* **21**, 364212 (2009).

53. A. T. Collins, A. Dahwich, *Journal of Physics: Condensed Matter* **15**, L591–L596 (2003).

54. K. Iakoubovskii, G. J. Adriaenssens, *Journal of Physics: Condensed Matter* **12**, L77–L81 (2000).

55. D. W. Palmer, in *Properties and Growth of Diamond*, ed. by G. Davies (INSPEC, Exeter, 1994), chap. 5.1, pp. 143–153.

56. S. Liggins et al., *Physical Review B* **81**, 085214 (Feb. 2010).

57. M. K. Atumi et al., *Journal of Physics: Condensed Matter* **25**, 065802 (2013).

58. G. S. Woods, *Philosophical Magazine Part B* **50**, 673–688 (1984).

59. G. S. Woods, A. T. Collins, *Journal of Physics C: Solid State Physics* **15**, L949–L952 (1982).

60. A. T. Collins et al., *Journal of Physics C: Solid State Physics* **21**, 1363–1376 (1988).

61. J. Goss et al., *Physical Review B* **70**, 235208 (2004).

62. A. Collins, A. Dahwich, *Diamond and Related Materials* **13**, 1959–1962 (Nov. 2004).

63. A. T. Collins et al., *Journal of Applied Physics* **97**, 083517 (2005).

64. A. T. Collins, S. Rafique, *Proceedings of the Royal Society of London A* **367**, 81–97 (1979).

65. A. T. Collins, G. S. Woods, *Journal of Physics C: Solid State Physics* **20**, L797–L801 (1987).

66. A. T. Collins, G. Davies, G. S. Woods, *Journal of Physics C: Solid State Physics* **19**, 3933 (1986).

67. G. Davies, M. H. Nazare, *Journal of Physics C: Solid State Physics* **13**, 4127–4136 (Aug. 1980).

68. G. Davies, *Journal of Physics C: Solid State Physics* **12** (1979).

69. G. Davies, *Journal of Physics C: Solid State Physics* **5**, 2534–2542 (Sept. 1972).

70. A. Gruber et al., *Science* **276**, 2012–2014 (1997).

71. M. W. Doherty et al., *Physics Reports* **528**, 1–45 (July 2013).

72. C. D. Clark, C. A. Norris, *Journal of Physics C: Solid State Physics* **4**, 2223 (1971).

73. G. Davies, M. F. Hamer, *Proceedings of the Royal Society of London A* **348**, 285–298 (1976).

74. J. H. H. Loubser, J. A. van Wyk, *Diamond Research* **1**, 11 (1977).

75. M. W. Doherty et al., *New Journal of Physics* **13**, 025019 (Feb. 2011).

76. Y. Mita, *Physical Review B* **53**, 11360–11364 (May 1996).

77. N. Manson, J. Harrison, *Diamond and Related Materials* **14**, 1705–1710 (Oct. 2005).

78. A. T. Collins, *Journal of Physics: Condensed Matter* **14**, 3743–3750 (Apr. 2002).

79. S. Felton et al., *Physical Review B* **77**, 081201 (Feb. 2008).

80. S. C. Lawson et al., *Journal of Physics: Condensed Matter* **4**, 3439–3452 (1992).

81. Y. Mita et al., *Journal of Physics: Condensed Matter* **2**, 8567–8574 (1990).

82. Y. Mita et al., *Diamond and Related Materials* **2**, 768–772 (Apr. 1993).

83. B. L. Green, PhD thesis, University of Warwick, 2013.

84. S. R. Boyd, I. Kiflawi, G. S. Woods, *Philosophical Magazine Part B* **69**, 1149–1153 (June 1994).

85. S. R. Boyd, I. Kiflawi, G. S. Woods, *Philosophical Magazine Part B* **72**, 351–361 (1995).

86. T. Evans, Z. Qi, *Proceedings of the Royal Society of London. Series A* **381**, 159–178 (1982).

87. A. T. Collins, *Journal of Physics C: Solid State Physics* **13**, 2641–2650 (1980).

88. A. Mainwood, *Physical Review B* **49**, 7934–7941 (1994).

89. S. Papagiannidis, PhD thesis, University of Newcastle upon Tyne, 2003.

90. H. Pinto et al., *Physica Status Solidi (A) Applications and Materials Science* **209**, 1765–1768 (2012).

91. R. Jones et al., *Diamond and Related Materials* **53**, 35–39 (2015).

92. I. Kiflawi et al., *Diamond and Related Materials* **6**, 1643–1649 (1997).

93. D. Fisher, S. C. Lawson, *Diamond and Related Materials* **7**, 299–304 (Feb. 1998).

94. Y. V. Babich et al., *Inorganic Materials* **38**, 464–467 (2002).

95. V. a. Nadolinny et al., *Diamond and Related Materials* **9**, 883–886 (2000).

96. P. J. Fallon et al., *Philosophical Magazine A* **72**, 21–37 (1995).

97. G. S. Woods, *Proceedings of the Royal Society of London A* **407**, 219–238 (1986).

98. J. P. Goss et al., *Physical Review B* **67**, 165208 (2003).

3

Theory

3.1 Electron paramagnetic resonance

Electron paramagnetic resonance (EPR) is a powerful technique for the investigation of energy levels, structure and environment of point defects. For a species to have an EPR signal it must be paramagnetic (having one or more unpaired electrons). Molecules with unpaired electrons, also called radicals, are usually highly reactive and generally short lived; radicals are hence rare, making EPR a very selective technique. This same selectivity can however be of particular advantage as it dramatically reduces background signals and simplifies spectra.

Point defects in semiconductors are often electrically active, with more than one charge state having levels in the band gap. If one electron is either added or removed from a diamagnetic point defect, one charge state must have an odd number of electrons. A point defect with an odd number of electrons must be paramagnetic and hence it is likely (although not certain) that an EPR signal will be observed. Many point defects in diamond have EPR signals making EPR a particularly relevant tool to this thesis.

A brief account of the EPR theory necessary for this thesis will be given here. Further details can be found in an excellent treatise by Weil and Bolton [1] and a particularly thorough treatise by Abragam and Bleaney [2]. For more concise discussions specific to defects in semiconductors see Watkins [3] or Lannoo and

Bourgoin [4].

3.1.1 Resonance

First, to understand the origin of the EPR signal it is useful to understand what is meant by the term resonance. A magnetic dipole moment $\boldsymbol{\mu}$ in a fixed magnetic field $\boldsymbol{B}$ has energy

$$W = -\boldsymbol{\mu} \cdot \boldsymbol{B} \,, \tag{3-1}$$

and precesses with angular velocity

$$\omega_L = -\gamma \, |\boldsymbol{B}| \,, \tag{3-2}$$

where γ is the gyromagnetic ratio. This precession of the dipole is illustrated in figure 3-1.

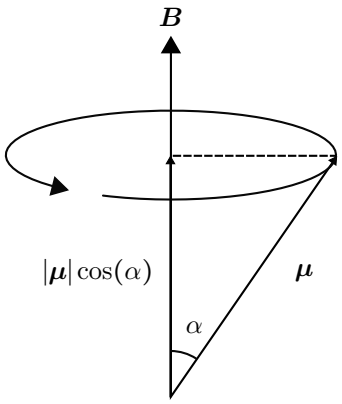

Figure 3-1 Precession of a magnetic dipole $\boldsymbol{\mu}$ in a magnetic field $\boldsymbol{B}$. The angle between $\boldsymbol{B}$ and $\boldsymbol{\mu}$ is denoted by α.

When a magnetic field $\boldsymbol{B_1} = |\boldsymbol{B_1}| \cos(\omega t)$ oscillating normal to $\boldsymbol{B}$, interacts with the precessing dipole, and the resonance condition $\omega = \omega_L$ is met, it alters the component of the dipole along the direction of $\boldsymbol{B}$. From equation (3-1), its energy thus changes.

The magnetic dipole is the angular momentum of the electron, $\hat{\boldsymbol{J}}$. $\hat{\boldsymbol{J}}$ is the sum of the orbital angular momentum $\hat{\boldsymbol{L}}$ and the spin angular momentum $\hat{\boldsymbol{S}}$. The angular momentum is quantised and described by the quantum number J. It takes the values $m_J = -J, -J+1, ...J$, giving rise to $J(J+1)$ discrete energy levels.

In EPR of solids, and in particular diamond, we can approximate $\hat{\boldsymbol{J}} = \hat{\boldsymbol{S}}$, where m_S takes the values $m_S = -S, -S+1, ...S$. The number of values, $S(S+1)$ is the spin multiplicity. Transitions between these levels can be excited by quanta of electromagnetic radiation (EM) $\hbar\omega$.

3.1.2 Hamiltonian

The spin Hamiltonian, $\hat{\mathscr{H}}$, describes all of the interactions with and between nuclear and electron spins. The Hamiltonian can be presented in different forms; a form appropriate to this thesis is as follows:

$$\hat{\mathscr{H}} = \underbrace{\mu_B \boldsymbol{B}^T \cdot \boldsymbol{g} \cdot \hat{\boldsymbol{S}}}_{\text{Zeeman}} + \underbrace{\hat{\boldsymbol{S}}^T \cdot \boldsymbol{D} \cdot \hat{\boldsymbol{S}}}_{\text{zero field}} + \sum_i^n \Big[\underbrace{-\mu_N g_{n_i} \boldsymbol{B}^T \cdot \hat{\boldsymbol{I}}_i}_{\text{nuclear Zeeman}} + \underbrace{\hat{\boldsymbol{S}}^T \cdot \boldsymbol{A}_i \cdot \hat{\boldsymbol{I}}_i}_{\text{hyperfine}} + \underbrace{\hat{\boldsymbol{I}}_i^T \cdot \boldsymbol{P}_i \cdot \hat{\boldsymbol{I}}_i}_{\text{quadrupole}} \Big] , \tag{3-3}$$

where $\hat{\boldsymbol{S}}$ and $\hat{\boldsymbol{I}}$ are the electron and nuclear spin operators respectively and the sum is over nearby nuclei. In the following sections each component of $\hat{\mathscr{H}}$ will be briefly explained.

3.1.3 Zeeman interaction

The Zeeman interaction of an unpaired electron is given by

$$\hat{\mathscr{H}}_{\text{EZ}} = \hat{\boldsymbol{\mu}} \cdot \boldsymbol{B} , \tag{3-4}$$

where $\hat{\boldsymbol{\mu}}$ is the electronic magnetic dipole moment arising from $\hat{\boldsymbol{S}}$ and $\hat{\boldsymbol{L}}$:

$$\hat{\boldsymbol{\mu}} = -\mu_B (\hat{\boldsymbol{L}} + g_e \hat{\boldsymbol{S}}) , \tag{3-5}$$

μ_B is the Bohr magneton given by $\mu_B = \frac{e\hbar}{2m}$ and g_e is the electron g-factor (a dimensionless constant). For point defects in solids the orbital momentum is strongly quenched by the interaction with electrical charges of nearby atoms. Therefore, the primary contribution to the total angular momentum is from $\hat{\boldsymbol{S}}$. The spin however can introduce a small orbital magnetic momentum in its environment through spin-orbit coupling. For isotropic spin-orbit coupling $\hat{\mathscr{H}}_{\text{SO}} = \lambda_{SO} \hat{\boldsymbol{L}} \cdot \hat{\boldsymbol{S}}$.

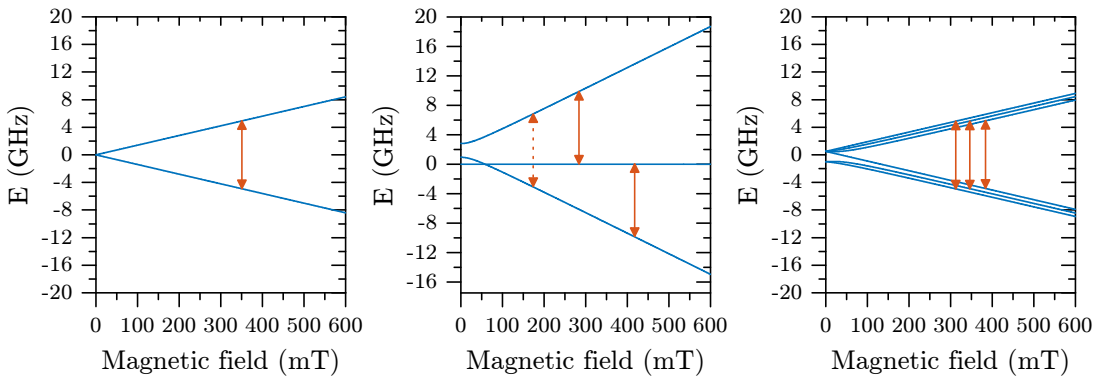

Figure 3-2 Examples of the effect on the energy levels of (a) the Zeeman interaction with $S = \frac{1}{2}$, (b) Zeeman interaction and zero-field splitting with $S = 1$, and (c) hyperfine interaction with $S = \frac{1}{2}, I = 1$. Transitions at 9.8 GHz are indicated.

The orbital and spin-orbital terms are approximated by $\boldsymbol{g} = g_e\mathbf{1} + \lambda_{SO}\boldsymbol{\Lambda}$, where $\boldsymbol{\Lambda}$ is the spin-orbit coupling matrix. Hence the Zeeman term is given by

$$\hat{\mathscr{H}}_{\mathrm{EZ}} = \mu_B \boldsymbol{B}^T \cdot \boldsymbol{g} \cdot \hat{\boldsymbol{S}} \,, \tag{3-6}$$

where $\boldsymbol{g}$ is a tensor, accounting for the symmetry of the local environment of the electron.

Since S takes integer or half-integer values, the energy difference between two adjacent levels is

$$\Delta W = \mu_B \boldsymbol{B}^T \cdot \boldsymbol{g} \cdot \hat{\boldsymbol{S}} \,, \tag{3-7}$$

and can be excited by EM radiation with energy $\hbar\omega = \Delta W$. A transition between energy levels separated by Zeeman splitting is illustrated in figure 3-2a.

3.1.4 Nuclear Zeeman

Analogous to the electron Zeeman interaction, the nuclear spin couples with the applied magnetic field, causing a further splitting of energy levels. The Hamiltonian describing the interaction is

$$\hat{\mathscr{H}}_{\mathrm{NZ}} = -\sum_i \mu_N g_{n_i} \boldsymbol{B}^T \cdot \hat{\boldsymbol{I}}_i \,. \tag{3-8}$$

Since the nuclear mass is much larger than the electron mass $\mu_N \ll \mu_B$ and so the nuclear Zeeman interaction is significantly smaller than the electronic Zeeman interaction.

3.1.5 Zero-field interaction

Local fields can lift the degeneracy of the spin states when there is no external magnetic field. The effect arises from spin-orbit coupling and couplings to other spins in dipole-dipole interactions. In the case that two or more electron spins are coupled together the effective spin $S \geq 1$. The zero-field splitting is represented by the tensor $\boldsymbol{D}$ and its Hamiltonian is written as follows:

$$\hat{\mathscr{H}}_{\mathrm{ZF}} = \hat{\boldsymbol{S}}^T \cdot \boldsymbol{D} \cdot \hat{\boldsymbol{S}} \ . \tag{3-9}$$

In the coordinates of the interaction and defining D_z as the principle value, we can write

$$\hat{\mathscr{H}}_{\mathrm{ZF}} = D\left\{\hat{S}_z^2 + \tfrac{1}{3}S(S+1)\right\} + E(\hat{S}_x^2 + \hat{S}_y^2) \ , \tag{3-10}$$

where, with $D_x \geq D_y$,

$$D = \tfrac{3}{2}D_z \ , \tag{3-11}$$

$$E = \tfrac{1}{2}(D_x - D_y) \ . \tag{3-12}$$

If $D_x - D_y = 0$, $E = 0$ and the interaction is axial. If $E \neq 0$ the interaction is rhombic. An example of the effect of the zero-field interaction on the energy levels is shown in figure 3-2b.

3.1.6 Hyperfine interaction

The hyperfine interaction originates from the coupling between electron and nuclear spins, with the usual effect of a smaller secondary splitting of the energy levels. An illustration of the effect of the hyperfine interaction can be seen in figure 3-2c. The analysis of hyperfine interactions at defects is exceptionally powerful, providing information on their constituent atoms, symmetry and spin localisation. Nuclei can be identified by relative isotopic abundances or by g_N through

electron-nuclear double resonance (ENDOR) spectroscopy or the observation of forbidden transitions. The most common isotopes leading to hyperfine interactions in diamond are ^{13}C, ^{14}N, ^{15}N and ^{1}H. The Hamiltonian for the total hyperfine interaction is given by

$$\hat{\mathscr{H}}_{\mathrm{HF}} = \sum_i \hat{\boldsymbol{S}}^T \cdot \boldsymbol{A}_i \cdot \hat{\boldsymbol{I}}_i \ , \tag{3-13}$$

where $\hat{\boldsymbol{I}}_{\boldsymbol{i}}$ is the i^{th} coupled nucleus and $\hat{\boldsymbol{A}}_{\boldsymbol{i}}$ is its hyperfine coupling tensor. The hyperfine interaction can be separated into an isotropic component and an anisotropic component. Unless there is strong $\boldsymbol{g}$ anisotropy, $\boldsymbol{A}$ is approximately symmetric and we can write

$$\boldsymbol{A}_{\mathrm{diag}} = A_0 \mathbf{1} + \boldsymbol{T} \ , \tag{3-14}$$

where A_0 is the isotropic hyperfine coupling constant and $\boldsymbol{T}$ is the dipolar coupling tensor.

The isotropic component, also called the Fermi contact interaction, arises from non-zero unpaired electron probability density at the nucleus. This only results from electrons in s-orbitals, making it isotropic. It is given by

$$A_0 = \frac{2\mu_0}{3} g_e g_n \mu_B \mu_N \left|\psi(0)\right|^2 \ , \tag{3-15}$$

where $|\psi(0)|^2$ is the electron spin density at the nucleus. In the principal axes of the interaction, and neglecting $\boldsymbol{g}$ anisotropies and spin-orbit couplings, $\boldsymbol{T}$ is approximately described by

$$\boldsymbol{T} = \frac{\mu_0}{4\pi} \frac{g_e g_n \mu_B \mu_N}{\langle r^3 \rangle} \begin{pmatrix} -1 & & \\ & -1 & \\ & & 2 \end{pmatrix} = \begin{pmatrix} -T & & \\ & -T & \\ & & 2T \end{pmatrix} , \tag{3-16}$$

where $\langle r^3 \rangle$ is the mean third power of the electron distance from the nucleus, tabulated in standard references [5]. Details on the calculation of the unpaired electron probability density from the hyperfine interaction can be found in §6.4.1.

3.1.7 Quadrupole interaction

A nucleus with $I \geq 1$ has a quadrupole moment and interacts with the local electric field gradient. The field gradient is normally caused by the electron distribution

in the immediate neighbourhood. Since they are spherical, the *s*-orbitals of the atom do not contribute to the field gradient and thus the quadrupole interaction mainly arises from the *p*-orbitals, however *s*-orbitals from neighbouring defects can contribute to the field gradient. The quadrupole Hamiltonian is given as

$$\hat{\mathscr{H}}_{\mathrm{Q}} = \sum_{I>1/2} \hat{\boldsymbol{I}}_i^T \cdot \boldsymbol{P} \cdot \hat{\boldsymbol{I}}_i \ . \tag{3-17}$$

Analogously to equation (3-10), $\hat{\mathscr{H}}_{\mathrm{Q}}$ can be written as

$$\hat{\mathscr{H}}_{\mathrm{Q}} = P_{\parallel} \left[\left\{ \hat{I}_z^2 + \tfrac{1}{3} I(I+1) \right\} + \tfrac{1}{3} \eta (\hat{I}_x^2 + \hat{I}_y^2) \right] \ . \tag{3-18}$$

As with the zero-field splitting, $P_{\parallel} = \frac{3}{2} P_z$ and $\eta = (P_x - P_y)/P_z$. Since an isotropic component would cause an equal shift to all energy levels $\boldsymbol{P}$ is traceless.

3.1.8 EPR intensity

The EPR intensity is determined by the transition rate, $M_{uv}(\boldsymbol{B}_1)$, the spin polarisation factor, β_{uv}, and, as a result of the field-swept experiment, the frequency-field conversion factor, γ_{uv}. The intensity of a transition between states u and v can be written:

$$A_{uv}(\boldsymbol{B}_1) \propto |M_{uv}(\boldsymbol{B}_1)|^2 \, \beta_{uv} \gamma_{uv} \ . \tag{3-19}$$

Each term will be briefly defined here.

3.1.8.1 Transition probability

The transition probability between the states u and v is proportional to the square of the matrix elements

$$|M_{u \to v}(\boldsymbol{B}_1)|^2 = \left| \langle v | \, \hat{\mathscr{H}}_{\mu w} \, | u \rangle \right|^2 \ , \tag{3-20}$$

where $\hat{\mathscr{H}}_{\mu w}$ is the Hamiltonian describing the interaction with the microwaves given by

$$\hat{\mathscr{H}}_{\mu w} = -\hat{\boldsymbol{\mu}} \cdot \boldsymbol{B}_1 \ . \tag{3-21}$$

3.1.8.2 Spin polarisation

The intensity also depends on the polarisation factor which is proportional to the population difference between u and v. At thermal equilibrium the population difference is determined by the Boltzmann distribution:

$$\beta_{uv} = \frac{e^{-\alpha E_u} - e^{-\alpha E_v}}{\sum_q e^{-\alpha E_q}} , \quad \alpha = 1/k_B T , \tag{3-22}$$

where the denominator is the partition function. Except at very low temperatures, $k_B T \gg E_q$ and so β_{uv} is proportional to $W_{uv} = E_v - E_u$. In a field swept experiment $W_{uv} = \nu_{\mu w}$ and hence is the same for every transition. Non thermal equilibrium populations can be introduced for example by microwave power saturation or optical spin polarisation.

3.1.8.3 Frequency-field conversion

The frequency-field conversion factor results from the experiment being field-swept rather than frequency-swept [6, 7]. For a transition between states u and v it is given by

$$\gamma_{uv} = \left| \frac{\partial B}{\partial W_{uv}} \right| , \tag{3-23}$$

where W_{uv} is the energy difference between states u and v. It can be interpreted as originating from the different times it takes for $W_{uv}(B)$ to sweep through the fixed microwave bandwidth, dependent on the rate of splitting of the energy levels.

For a $\Delta m_S = \pm 1$ transition, γ_{uv} is proportional to $1/g$. Thus, in most instances, when comparing two defect spectra it will approximately cancel and can safely be ignored. However, if $S \geq 1$, $\Delta m_S = \pm 2$ transitions can be allowed. For a $\Delta m_S = \pm 2$ transition, away from anticrossings, $\gamma_{uv} \approx \frac{1}{2g}$; a factor of $1/2$ compared to the $\Delta m_S = \pm 1$ transitions. This is seen for NV^- as shown in figure 3-3. Additionally, the presence of anticrossings complicates the matter by making γ_{uv} field dependent. If a broad resonance is near to an anticrossing, γ_{uv} can change significantly as the field is swept through the resonance giving rise to an asymmetric lineshape [8].

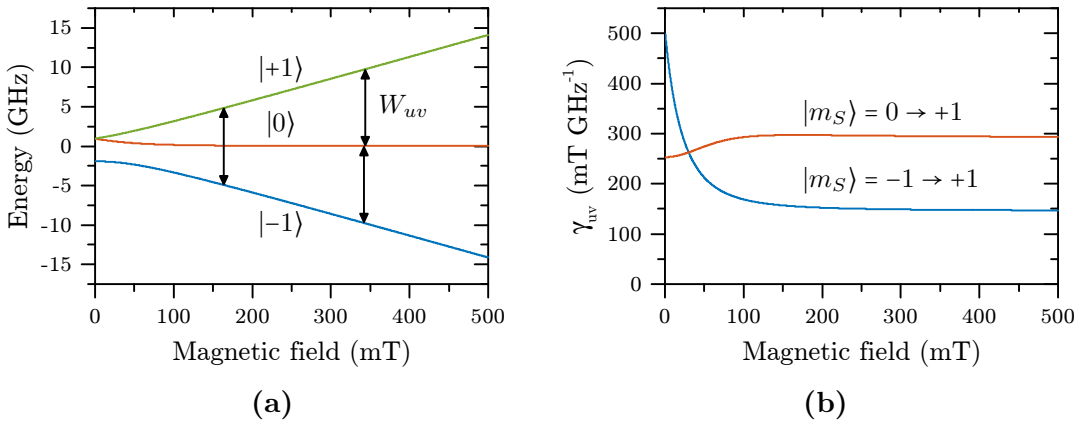

Figure 3-3 (a) Energy levels of NV^- with $\boldsymbol{B} \parallel \langle 0\,0\,1 \rangle$ and 9.75 GHz transitions indicated. (b) Frequency-field correction factor for $|m_S\rangle = -1 \rightarrow +1$ and $|m_S\rangle = 0 \rightarrow +1$ transitions.

3.2 Optical absorption and luminescence

The interaction of light with defects in semiconductors can tell us a wealth of knowledge about their atomic structure, including their chemical composition and symmetry, electronic and vibrational properties. Although the word optical is often only related to that which can be detected by the human eye (400–700 nm), here it will also be used to encompass wavelengths from the IR to the UV range.

As for EPR in section 3.1, a brief account will be given of the optical theory for this thesis. For an overview of the optical properties of solids the reader is directed towards Fox [9]. For more specific treatments of the optical properties of defects in semiconductors see Davies [10] and Pajot and Clerjaud [11].

3.2.1 Electric dipoles

An electric dipole consists of separated positive and negative charges. In an atom the positively charged nucleus and negatively charged electron form such a dipole. When the dipole oscillates it emits EM radiation, the frequency of which, ω, is determined by the frequency of oscillation. For small displacements the natural resonant frequency, ω_0, of a dipole is determined by its reduced mass, μ and a

restoring force. For an electron and nucleus $\mu \approx \mathrm{m}_e$ and so

$$\omega_0 \approx \sqrt{\frac{k}{m_e}}\,, \tag{3-24}$$

where k is a spring constant. When the atom receives energy sufficient to excite oscillations it emits radiation at frequency ω_0. When EM radiation is incident on an atom the reverse is also true; the electric field can couple with the atomic dipole driving it at ω. If the electric field is at frequency ω_0 then the dipole resonates and absorbs energy. Since the electron is bound to the atom its energy is quantised and only certain transitions are allowed. Only a photon of the correct energy $\hbar\omega = E_2 - E_1$ can be absorbed, promoting the electron into an excited state.

Instantaneous dipole moments between atoms can also oscillate when the atoms move relative to one another, however due to the increased mass of nuclei over electrons, ω_0 is lower. Rather than causing electronic transitions, the dipole excites phonons in the lattice.

The transition probability between the states u and v is given by Fermi's golden rule:

$$W_{u\to v} = \frac{2\pi}{\hbar}\left|M_{u\to v}\right|^2 g(\hbar\omega)\,, \tag{3-25}$$

where

$$M_{u\to v} = \langle u|\,\hat{\mathscr{H}}_{opt}\,|v\rangle\,, \tag{3-26}$$

and

$$\hat{\mathscr{H}}_{opt} = -\boldsymbol{p}\cdot\boldsymbol{\epsilon}\,, \tag{3-27}$$

where $\boldsymbol{p}$ is the dipole moment and $\boldsymbol{\epsilon}$ is a plane wave given by $\boldsymbol{\epsilon} = \boldsymbol{\epsilon_0} e^{\pm i\boldsymbol{k}\cdot\boldsymbol{r}}$. In equation (3-25) $g(\hbar\omega)$ is the density of states.

3.2.2 Intrinsic absorption of diamond

Intrinsic diamond has a wide indirect band gap of 5.47 eV [12] making it transparent for wavelengths longer than 227 nm, except for a band from 2.6–6.2 µm due to multi-phonon absorption. There is no one-phonon absorption in intrinsic diamond or other tetrahedrally-bonded homonuclear crystals such as silicon and germanium due to their inversion symmetry. The vibrations of nuclei are countered by equal

and opposite movements of neighbours, such that no dipole moment is induced to which EM radiation can couple.

The maximum frequency of a single phonon is $1332\,\mathrm{cm}^{-1}$, corresponding to the Brillouin zone-centre and Raman frequency [13]. The limits of multi-phonon absorption correspond to integer multiples of this frequency. The two phonon absorption peaks at $2159\,\mathrm{cm}^{-1}$ with an absorption coefficient of $14.5\,\mathrm{cm}^{-1}$; three-phonon and higher order absorptions decrease in intensity due to the reduced probability of the required combination of phonons. Due to the large number of possible phonon modes the multi-phonon absorption is relatively smooth; it has been reproduced with reasonable accuracy by a joint-density-of-states calculation [14]. Further details can be found in an overview of the intrinsic optical properties of diamond by Mildren [15].

3.2.3 Defect induced transitions

3.2.3.1 Electronic transitions

A point defect can introduce spatially and energetically localised electronic states into the band gap. Transitions between such a localised in-gap state and the continuum of the valence or conduction band results in broad spectral features. If a defect has two such states however, transitions between them are observed as a sharp characteristic spectral feature called a zero-phonon line (ZPL).

In addition to the zero-phonon transitions, electron-phonon coupling allows mixed transitions creating a so-called vibronic sideband to the ZPL. The strength of the coupling is characterised by the Huang-Rhys factor [4]. In absorption a photon can provide energy for the zero-phonon transition and a vibrational mode in the excited state, leading to the observation of the absorption sideband at higher frequency than the ZPL in the spectrum. In luminescence the emitted photon energy is the difference between the zero-phonon transition and the vibrational mode in the ground state, leading to the luminescence sideband at lower frequency than the ZPL. The resulting absorption and luminescence spectra of a defect approximately mirror each other. Absorption and luminescence transitions between two electronic

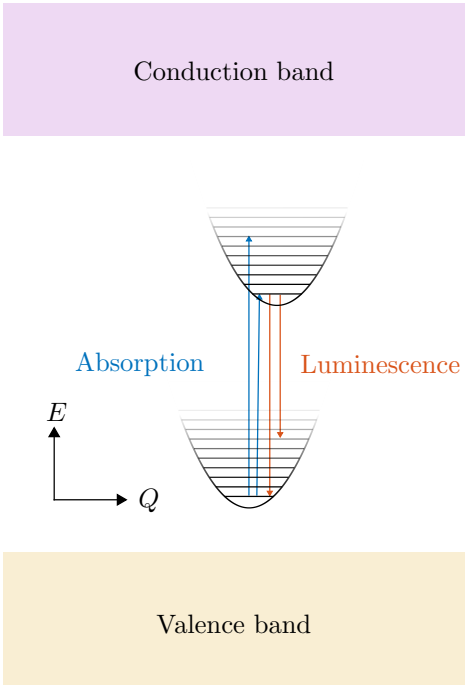

Figure 3-4 Zero-phonon and phonon-coupled transitions between ground and excited states of a defect in the band gap. Absorption and emission both occur from the lowest vibration sublevel. E is the energy and Q is the configuration coordinate.

states of a defect are shown diagrammatically in figure 3-4.

The energy of a ZPL in diamond can be determined to approximately meV resolution in absorption and photoluminescence spectroscopy making it possible to distinguish between the ZPLs of many different defects. The ratio of the ZPL to phonon sideband is dependent on temperature; since at lower temperature the occupancy of higher energy vibrational states decreases, intensity moves from the phonon sideband into the ZPL. Spectra are therefore usually recorded with the sample at 77 K to increase sensitivity.

By balancing absorption and luminescence processes, the intensity of an absorption (including ZPL and sideband) can be related to the concentration by

$$\int \mu(E)dE = \frac{g_e}{g_g}\frac{\pi^2}{9}\frac{\hbar^3 c^2}{\tau E^2}\frac{(n^2+2)^2}{n^2}[N]\,, \tag{3-28}$$

where g_e and g_g are the degeneracies of the excited and ground states, τ is the radiative lifetime of the transition and n is the refractive index [10].

3.2.3.2 Vibrational modes

One-phonon absorption is permitted by the introduction of defects into the lattice which destroy the local symmetry. The vibration of a substitutional atom lighter than the intrinsic atoms, or a tightly bound atom, is at a higher frequency than the Raman frequency. This vibration will not propagate through the lattice and hence is a local vibrational mode (LVM); LVMs are often IR active.

Such vibrations are modelled well by a simple diatomic model of two masses, the impurity m_a and the host atom M, separated by a spring with spring constant k. The frequency of the vibration is then given by

$$\omega_a = \sqrt{\frac{k}{\chi M + m_a}} \,. \tag{3-29}$$

where the empirical constant χ accounts for the vibrations of host atoms [16]. If m_a is replaced by m_b the ratio of frequencies is

$$\frac{\omega_b}{\omega_a} = \sqrt{\frac{\chi M + m_b}{\chi M + m_a}} \,. \tag{3-30}$$

If an atom is present in more than one isotope an LVM involving the atom will be split into a number of modes dependent on the isotopes and origin of the vibration. Knowing the isotopic content can allow the atoms involved in an LVM to be identified.

When the defect has a mass larger than the intrinsic atoms, or is loosely bound, vibrations are at a frequency lower than the Raman frequency. Such modes are referred to as resonant modes and can propagate some distance from the defect. Such modes are created by the nitrogen impurities which led to the early type classification of diamond.

3.2.4 Photoluminescence

Photoluminescence (PL) is the emission of a photon after absorbing a photon of equal or higher energy. When an electron at a defect absorbs a photon of appropriate energy, it is raised in energy to an excited state, which relaxes either radiatively or non-radiatively. For diamond, the radiative lifetime is typically on

the order of tens of nanoseconds [17]. PL spectroscopy is a very sensitive technique, enabling detection of defects at sub ppb concentrations, and single centre detection in confocal microscopy [18].

Since the emission of a photon depends on the energy relaxation mechanism in the solid, involving radiative and non-radiative processes, luminescence processes are more complicated than absorption. Although PL intensity can be used as an indication of defect concentration, such assessment should be made very cautiously; the technique should not be used for any quantitative measurements.

As well as photoluminescence, defects in diamond can undergo phosphorescence. Phosphorescence is a similar process to photoluminescence except that after absorption of a photon, the excited state undergoes intersystem crossing to a metastable state of higher spin multiplicity, usually a spin triplet. Forbidden transitions are then required to return to the ground state, often occurring at a much slower rate compared to photoluminescence.

3.3 Symmetry and defect sites

Crystals can be categorised by their point group, which contains the geometric symmetry operations under which the crystal is invariant. A consequence of the invariance is that any macroscopic physical property is also invariant with respect to the same symmetry operation; this is known as Neumann's principle. A lattice site in diamond belongs to the tetrahedral point group or $\mathscr{T}_\mathrm{d}$ in the Schoenflies notation. A defect must belong to a point group which is a subgroup of the lattice point group. A number of common subgroups of $\mathscr{T}_\mathrm{d}$ are listed in table 3-1.

Group theory can be used to relate the physical properties of an object to its symmetry and is important in the study of the electron orbitals of molecules or point defects. For an excellent introduction in the context of molecular orbitals the reader is directed to Atkins and Friedman [19]. Although group theory is not discussed in detail here, some additional notation must be defined.

For each point group there exists a character table which gives the result of the

Symmetry	Schoenflies notation	Symmetry related sites
Tetrahedral	$\mathscr{T}_{\mathrm{d}}$	1
Tetragonal	$\mathscr{D}_{\mathrm{2d}}$	3
Trigonal	$\mathscr{C}_{\mathrm{3v}}$	4
Rhombic I	$\mathscr{C}_{\mathrm{2v}}$	6
Monoclinic I	$\mathscr{C}_{\mathrm{1h}}$	12

Table 3-1 Common point groups of defects in diamond with the corresponding Schoenflies notation.

symmetry operations of the group on the symmetry species. The symmetry species are given by irreducible representations (irreps) and identified by Mulliken symbols. **A** is a one-dimensional state (singly degenerate), **E** is a two-dimensional state (doubly degenerate) and **T** is a three-dimensional state (triply degenerate). The subscripts g and u signify whether the group is symmetric or antisymmetric with inversion respectively. The subscripts 1 and 2 indicate whether the state is symmetric or antisymmetric respectively with rotation about a secondary axis. For the symmetry of electron orbitals, superscripts prefixing the Mulliken symbol indicate the spin multiplicity of the state

$\mathscr{C}_{\mathrm{3v}}$	E	$2\mathrm{C}_3$	$3\sigma_{\mathrm{v}}$
$\mathbf{A_1}$	1	1	1
$\mathbf{A_2}$	1	1	−1
E	2	−1	0

Table 3-2 Character table for the $\mathscr{C}_{\mathrm{3v}}$ point group.

For context, the character table for the $\mathscr{C}_{\mathrm{3v}}$ point group is shown in table 3-2. The first row gives the point group and the symmetry operations under which it is geometrically invariant, the first column contains the irreps and the value is the character and gives the result of the operation on the irrep.

Of particular relevance to the results of this thesis is symmetry in the context of EPR of point defects. EPR is sensitive to the orientation of any anisotropic interactions and thus allows us to identify the symmetry of defects. The EPR spectrum consists of a superposition of the spectra from the defect in inequivalent

sites. Depending on the orientation of the sample to the external magnetic field, $\boldsymbol{B}$, sites may or may not be degenerate with one another.

Take for example the $S = \frac{1}{2}$ defect N_S^0. The defect has an anisotropic nitrogen hyperfine interaction, with its axis along $\langle 1\,1\,1 \rangle$, creating a spectrum with three approximately equally spaced lines. From equation (3-13), the splitting between the outer lines depends on the relative orientation of $\boldsymbol{B}$ and the hyperfine tensor, $\boldsymbol{A}$. The symmetry of N_S^0 is $\mathscr{C}_{3v}$ and as such it has four inequivalent sites. If $\boldsymbol{B}$ is oriented along $\langle 0\,0\,1 \rangle$ then the angle between $\boldsymbol{B}$ and $\boldsymbol{A}$ is the same for every site at 54.7° and the spectra overlap. If $\boldsymbol{B}$ is oriented along $\langle 1\,1\,0 \rangle$, two sites make 90° and two make 35.3° giving two sets of lines with the intensity ratio 2:2. If $\boldsymbol{B}$ is oriented along $\langle 1\,1\,1 \rangle$, one site makes 0° and the other three make 70.6°, giving two sets of lines with the intensity ratio 1:3.

3.4 Irradiation damage

3.4.1 Interaction

To understand the process of defect production by irradiation damage we must approach the problem formally. The treatment given here is similar to that given by Lannoo and Bourgoin [4, p. 218]. The flux of incident particles

$$\phi = nv, \tag{3-31}$$

where n is the concentration of particles and v their velocity, causes a rate of defect production

$$\nu = \sigma N \phi, \tag{3-32}$$

with σ the effective cross section dependent on the radiation causing the displacement and the target, and N the concentration of nuclei in the solid. The cross section must be defined more explicitly as

$$\sigma = \int_\theta d\sigma(\theta) \tag{3-33}$$

to encompass the angular distribution of scattered particles, $d\sigma$.

The number of particles reaching x decreases according to the probability that they have already made a collision. The number collisions in a thin slice between x and $x + dx$ is proportional to the probability of having reached x, $p(x)$, the thickness of the slice, dx, and the density of scattering centres, σN. Thus the change in probability between reaching x and $x + dx$ is given by

$$-dp = p(x)\sigma N dx. \tag{3-34}$$

Solving for $p(x)$ with the boundary condition that $p(0) = 1$ gives the exponential decay

$$p(x) = e^{-\sigma N x}. \tag{3-35}$$

If the scattering cross section is small, or the material is thin, the distribution of interactions can be considered constant through the material and the approximation made that the rate is σN.

3.4.2 Energy transfer

The simplest treatment of two particles interacting is to suppose they are hard spheres that collide elastically, as would two billiard balls. The dynamics of mass m incident on mass M is described in the following. Prior to the collision, in the rest frame of M, m has kinetic energy E. After the collision M is scattered at an angle θ to the original direction of m with kinetic energy T. The mass m is scattered at the angle ϕ to its original direction with kinetic energy $(E - T)$. A diagrammatic representation of the collision is shown in figure 3-5. The conservation equations for momentum and energy for the collision are as follows:

$$mv_0 = mv\cos\phi + MV\cos\theta \tag{3-36a}$$

$$0 = -mv\sin\phi + MV\sin\theta \tag{3-36b}$$

$$\frac{1}{2}mv_0 = \frac{1}{2}mv^2 + \frac{1}{2}MV^2 \tag{3-36c}$$

where v_0 and v are the velocity of m before and after the collision respectively. The velocity of M after the collision is given by V. Solving equations (3-36) we can express the transferred energy T in terms of E, m, M and θ:

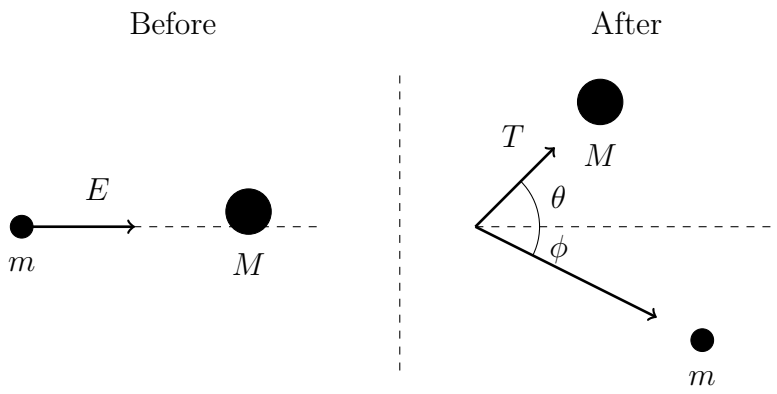

Figure 3-5 Diagram showing the collision between a particle of mass m and kinetic energy E incident on a stationary particle of mass M. After the collision mass M is scattered at the angle θ and mass m scattered at the angle φ. The kinetic energy transferred to mass M is T.

$$T = \frac{4mM}{(m+M)^2}\cos^2\theta \cdot E. \tag{3-37}$$

3.4.3 Special cases

There are several important cases to consider in which equation (3-37) is simplified. A useful quantity to know is the maximum energy that m can transfer to M. Maximum energy transfer will occur when m collides with M directly such that $\theta = 0$. Equation (3-37) then simplifies to

$$T_{max} = \frac{4mM}{(m+M)^2} \cdot E. \tag{3-38}$$

Notice that it is only possible for m to transfer all of its energy when $m = M$. If it were less it will rebound backwards, any more and it will continue forward after the collision. Thus another important case is when $m = M$ and we have

$$T = \cos^2\theta \cdot E. \tag{3-39}$$

If $m \ll M$ we can make the approximation that

$$T = \frac{4m}{M}\cos^2\theta \cdot E \tag{3-40}$$

and conversely if $m \gg M$

$$T = \frac{4M}{m}\cos^2\theta \cdot E. \tag{3-41}$$

It is seen that the transfer efficiency of the collision is dependent on the matching of the masses. For instance, an electron colliding with a carbon ion can transfer a maximum of 0.0046 % of its energy.

Particle	Mass (u)	Energy at 0.1 c (eV)
Electron	1/1823	2.56×10^3
Neutron	1	4.71×10^6
Carbon ion	12	5.60×10^7

Table 3-3 Masses and relativistic energies for typical irradiating particles. The data indicates at what particle energies a relativistic treatment becomes necessary. It can be seen that MeV electrons certainly require a relativistic treatment but for neutrons and carbon ions such corrections are not absolutely necessary.

3.4.4 Relativistic corrections

The classical treatment is usually adequate for ions and neutrons but given that a 180 keV electron is required to cause a displacement in diamond [20], referring to table 3-3, it is seen that relativistic effects must be considered for electrons. The kinetic energy of a relativistic particle is given by $E = m_0\gamma c^2 - m_0 c^2$, where m_o is the rest mass and γ is the Lorentz factor, and so the conservation equations for momentum and energy become

$$m_0\gamma_0 v_0 = m_0\gamma v\cos\phi + MV\cos\theta \tag{3-42a}$$

$$0 = -m_0\gamma v\sin\phi + MV\sin\theta \tag{3-42b}$$

$$m_0\gamma_0 v_0 = m_0\gamma v^2 + \frac{1}{2}MV^2. \tag{3-42c}$$

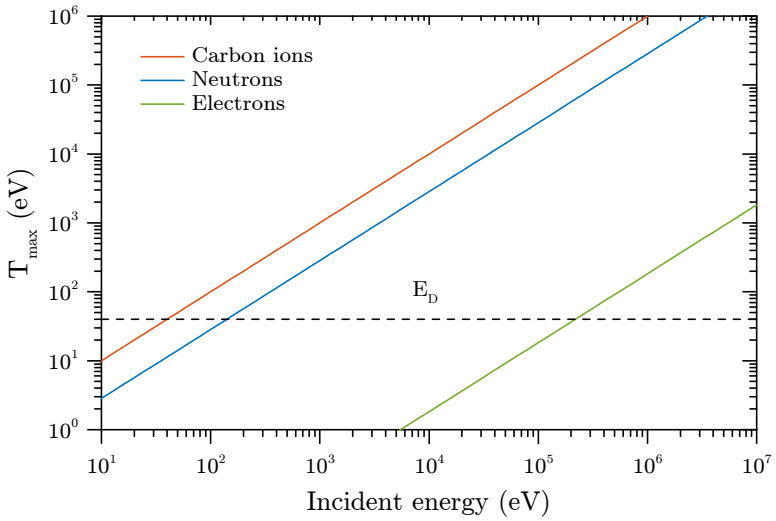

Figure 3-6 Maximum energy transmitted to a carbon atom by incident carbon ions, neutrons and electrons calculated from equations calculated from equations (3-38) and (3-43). To cause a displacement it is necessary to overcome the energy binding an atom to its lattice site. The displacement threshold energy for diamond is about 40 eV [20].

Since $m_0 \ll M$ an electron's energy transfer efficiency is very low and we can approximate that $v = v_0$. Equations (3-42) can then be solved to give

$$T_{max} = 2\frac{m_0}{M}E\left(2 + \frac{E}{m_0c^2}\right). \tag{3-43}$$

3.5 Chemical kinetics

The probability of a particle being in a state with energy E_a is given by the Boltzmann distribution,

$$p_i = \frac{e^{-E_a/k_BT}}{Z}\ , \tag{3-44}$$

where the partition function

$$Z = \sum_i^N e^{-E_a/k_BT}\ , \tag{3-45}$$

T is the temperature of the system and k_B is Boltzmann's constant. Suppose that for a mechanism to succeed a particle must be in a state with energy greater than an activation energy, E_a. The mechanism does not become successful at a distinct temperature, but rather the probability of success increases with temperature.

For an ensemble of particles, the overall rate of a process is proportional to the frequency at which it is attempted and the probability of it succeeding. These factors can be combined into a rate constant:

$$k = \nu \cdot e^{-E_a/k_B T} \,, \tag{3-46}$$

where ν is the attempt frequency. This equation is known as the Arrhenius equation and is commonly used to characterise the temperature dependence of chemical reactions. It is an empirical relationship which can be applied to many different thermally-induced processes, examples relevant to this thesis are the annealing of defects, the reorientation of defects and charge transfer between defects.

3.5.1 Kinetic order

As well as being proportional to the rate constant the rate of a process is proportional to the number (or concentration) of particles participating. For a process involving one particle, for example $[X] \rightarrow [Y]$, the rate is proportional to $[X]$ with proportionality constant k:

$$\frac{d[X]}{dt} = -k[X] \,. \tag{3-47}$$

This is a first order process and has the simple solution

$$[X] = [X_0]e^{-kt} \,. \tag{3-48}$$

An example of a first order process is the dissociation of a point defect in a semiconductor. The rate of the process depends only on its concentration and first order kinetics will accurately describe it. Other processes in a semiconductor are the recombination of a Frenkel pair and the formation of complexes. In both instances the process depends on the concentration of two defects. In the approximation that one defect is very much more abundant than the other, first order kinetics can be applied, albeit with an additional proportionality constant. Otherwise higher order kinetics are needed. The example $[X] + [X] \rightarrow [Y]$ is the simplest second order process. The change in $[X]$ is given by

$$\frac{d[X]}{dt} = -k_2[X]^2 \,, \tag{3-49}$$

which has the solution

$$[X] = \frac{[X_0]}{1 + [X_0]k_2 t}. \tag{3-50}$$

If two different species combine, for example $[X] + [Y] \rightarrow [Z]$ where $[X]$ and $[Y]$ change as

$$\frac{d[X]}{dt} = \frac{d[Y]}{dt} = -k_2[X][Y]\,, \tag{3-51}$$

the process is described as mixed second order.

The change in concentration of one defect can depend on the concentration of others, with multiple processes having different activation energies. The resulting set of equations which describe all of the processes is a system of coupled differential equations. Systems of coupled differential equations can be solved numerically. If defects are not homogeneously distributed throughout the system, annealing kinetics do not provide an accurate description of their interactions.

For a first order process the rate of change is proportional to the concentration, so the percentage change is the same for any concentration. For a second order process the change is proportional to the square of the concentration and so the percentage change is faster at higher concentrations and slower at lower concentrations. The result is that for one concentration a given second order process might occur at a lower temperature than a different first order process. At lower concentrations the first order process will occur at the same temperature but the second order process might now happen at a higher temperature than the first order process.

3.5.2 Time, temperature and pressure

Higher temperatures increase the probability or success of attempts at overcoming a barrier; time allows more attempts at overcoming the barrier. According to kinetic theory an identical result can be achieved by annealing for a longer time at a lower temperature. This is demonstrated in figure 3-7 which shows the completion of 1.6 eV and 2.3 eV second order processes as functions of both time and temperature. The colour in the figure represents the equivalent anneal in terms of the completion of the process.

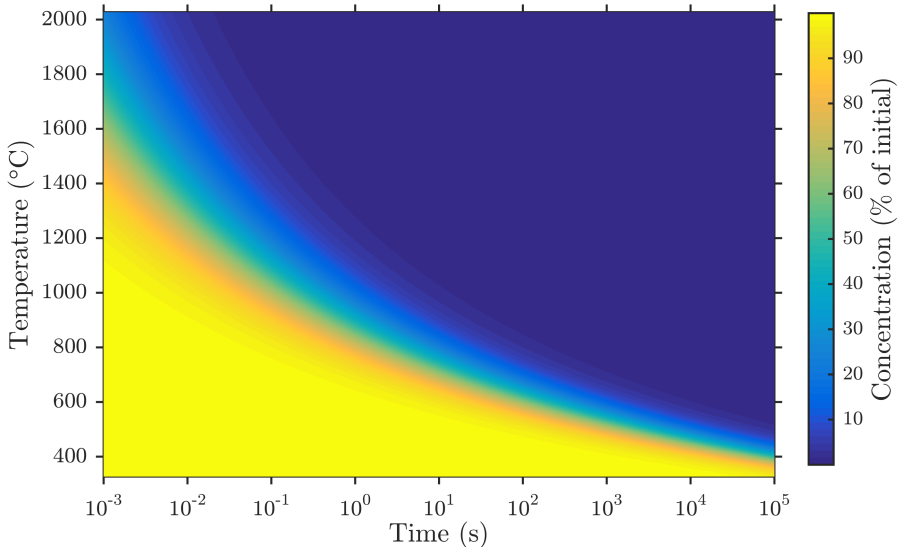

(a) $E_a = 1.6\,\text{eV}$

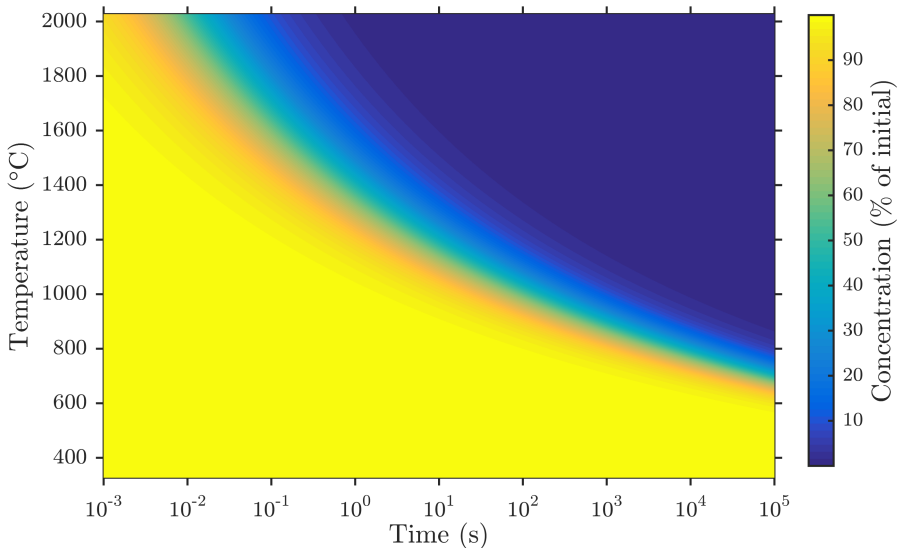

(b) $E_a = 2.3\,\text{eV}$

Figure 3-7 Result of equation (3-50) over a range of times and temperatures with activation energies of 1.6 eV (a) and 2.3 eV (b). The starting concentration was 100 ppm and the attempt frequency was 10^{11} Hz. The change in colour represents the annealing out of a species, starting at 100 % and finishing at 0 %.

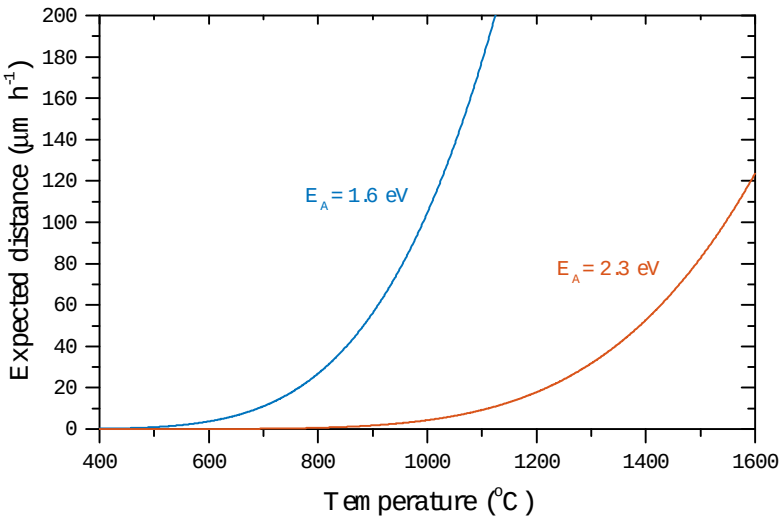

Figure 3-8 Approximate migration distance of interstitials and vacancies in an unimpeded random walk with the activation energies 1.6 eV and 2.3 eV respectively, an attempt frequency $\nu = 1 \times 10^{11}\,\mathrm{s}^{-1}$.

In reality figure 3-7 is only an approximation as the annealing of defects depends on the precise mechanism of the process. If different mechanisms respond differently to a short hot anneal versus a long cooler anneal we potentially have a way of controlling their relative rates. If a process requires a short diffusion distance but has a large barrier a rapid, higher temperature anneal might be very effective at selectively completing it. Rapid annealing with laser pulses has been demonstrated to heal lattice damage caused by ion implantation [21].

For a particle on a random walk the expected distance it travels from its origin is approximately $d\sqrt{N}$, where d is the size of each step and N is the number of steps. For a defect in an otherwise empty lattice, the number of steps per second is approximately given by the Arrhenius equation (equation (3-46)) and thus the approximate expected migration distance can be calculated. The result of the calculation is displayed in figure 3-8. Of course, once a defect starts moving it will most likely become trapped at another forming a new complex. However, if that complex dissociates at a higher temperature the defects could then perhaps migrate further.

The effect of pressure on annealing is less commonly explored. The aggregation rate of nitrogen is known to decrease with increasing hydrostatic pressure when HPHT treating diamond [22]. Hydrostatic pressure causes a uniform compression

of the lattice, the size of which is determined by the bulk modulus. This increases the energy barrier for the migration of defects. A uniaxial stress has a similar effect but will affect the different symmetry determined sites of a defect differently, depending on the axis of the stress. Thus the relative energies of sites can be altered, creating a preferential population of defects in a set of sites [23]. If a defect is limited to a subset of its sites its migration through the lattice will also be hindered.

References

1. J. A. Weil, J. R. Bolton, *Electron Paramagnetic Resonance* (John Wiley & Sons, Inc., Hoboken, NJ, USA, Second, Dec. 2006).
2. A. Abragam, B. Bleaney, *Electron Paramagnetic Resonance of Transition Metal Ions* (Oxford University Press, Oxford, 1970).
3. G. D. Watkins, in *Identification of Defects in Semiconductors*, ed. by M. Stavola (Academic Press, 1998), pp. 1–41.
4. M. Lannoo, J. Bourgoin, *Point Defects in Semiconductors I* (Springer, Berlin Heidelberg, 1983).
5. J. R. Morton, K. F. Preston, *Journal of Magnetic Resonance (1969)* **30**, 577–582 (1978).
6. R. Aasa, T. Vänngård, *Journal of Magnetic Resonance (1969)* **19**, 308–315 (1975).
7. S. Stoll, A. Schweiger, *Journal of Magnetic Resonance* **178**, 42–55 (Jan. 2006).
8. J. Pilbrow et al., *Journal of Magnetic Resonance (1969)* **52**, 386–399 (1983).
9. M. Fox, *Optical Properties of Solids* (Oxford University Press, Oxford, 2001).
10. G. Davies, in *Identification of Defects in Semiconductors*, ed. by M. Stavola (Academic Press, 1998), pp. 2–89.
11. B. Pajot, B. Clerjaud, *Optical Absorption of Impurities and Defects in Semiconducting Crystals* (Springer Berlin Heidelberg, Berlin, Heidelberg, 2013), vol. 169.
12. C. D. Clark, P. J. Dean, P. V. Harris, *Proceedings of the Royal Society of London. Series A* **277**, 312–329 (1964).
13. C. V. Raman, *Proceedings of the Indian Academy of Sciences - Section A* **19**, 189–198 (1944).
14. R. Wehner et al., *Solid State Communications* **5**, 307–309 (1967).
15. R. P. Mildren, in *Optical Engineering of Diamond* (Wiley-VCH Verlag GmbH & Co. KGaA, Weinheim, Germany, Mar. 2013), pp. 1–34.
16. M. D. McCluskey, *Journal of* **87**, 3593–3617 (2000).
17. G. Davies et al., *Physical Review B* **46**, 13157–13170 (Nov. 1992).

18. A. Gruber et al., *Science* **276**, 2012–2014 (1997).

19. P. W. Atkins, R. S. Friedman, *Molecular Quantum Mechanics* (OUP Higher Education Division, Oxford, Fifth edit, 2010), p. 560.

20. J. Koike, D. M. Parkin, T. E. Mitchell, *Applied Physics Letters* **60**, 1450–1452 (1992).

21. M. G. Allen et al., *Applied Physics Letters* **63**, 2062 (1993).

22. I. Kiflawi et al., *Diamond and Related Materials* **6**, 1643–1649 (1997).

23. C. A. J. Ammerlaan, E. A. Burgemeister, *Physical Review Letters* **47**, 954–957 (1981).

4

Experimental techniques

4.1 Optical spectroscopy

4.1.1 Dispersive and Fourier transform spectroscopy

A dispersive spectrometer with a single point detector detects only one narrow band of wavelengths at a time, which is selected by a monochromator either before or after the light enters the sample (figure 4-1b). To record a spectrum the diffraction grating/s in the monochromator is/are incrementally rotated, scanning through the wavelengths, and the signal recorded at each interval. High sensitivity and resolution can be achieved however acquisition time is slow. Alternatively the diffraction grating can remain fixed and an array of detectors used such as a charge coupled device (CCD) (figue 4-1a). An array detector makes acquiring a spectrum much faster, however sensitivity and resolution are reduced.

A Fourier transform infrared (FT-IR) spectrometer creates an interferogram of a broadband source, usually with a Michelson interferometer. The digitised interferogram is then Fourier transformed to construct the spectrum in the frequency domain. A diagram of an FT-IR spectrometer with a Michelson interferometer is shown in figure 4-2.

In the interferometer a beam splitter separates the light from the source into two beams each directed at mirrors. One mirror is fixed in position whilst the other

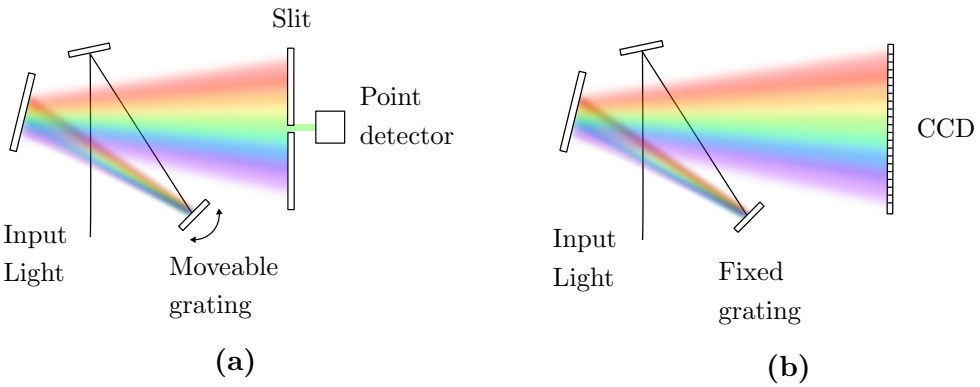

Figure 4-1 Diagrams of two types of dispersion spectrometer. (b) uses a fixed grating and detects different wavelengths with spatially separated pixels of a CCD. (a) Has a moveable diffraction grating allowing diffracted light to be scanned over a slit. A high sensitivity detector such a PMT collects light at one spatial position.

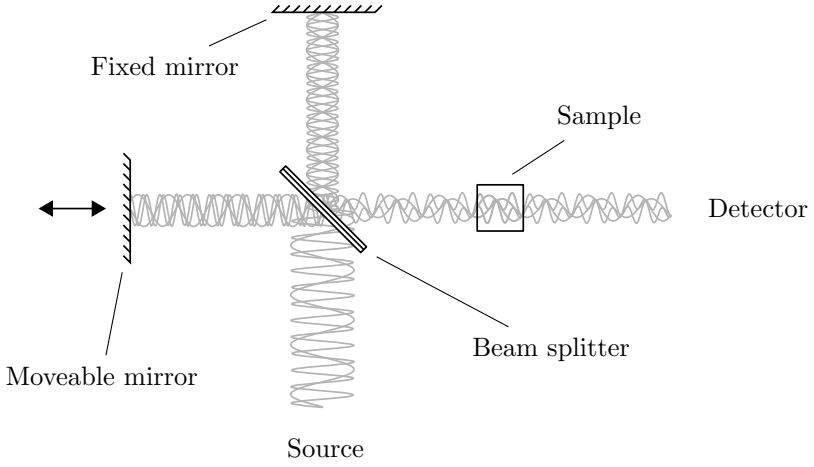

Figure 4-2 Diagram of an FT absorption spectrometer employing a Michelson interferometer. The light from a broadband source is split between two paths by a beam splitter. The length of one of the paths is changed by moving a mirror causing interference when the light recombines. The interferogram is recorded after the light passes through the sample.

can be translated back and forth, allowing the relative path lengths to be changed. When the beams superimpose back at the beam splitter some wavelengths interfere constructively and others destructively. When the path lengths are equal all wavelengths interfere constructively giving rise to the centreburst in the interferogram. The spectrum is recorded with and without the sample in the beam, the difference being the sample spectrum.

An FT spectrometer has several advantages over a dispersive spectrometer:

- **Fellgett's advantage** – Broadband illumination is used rather than narrow band monochromated light, thus an FT-IR spectrometer collects light from all wavelengths simultaneously.
- **Jacquinot's advantage** – For a dispersive spectrometer the throughput is limited by the entrance and exit slits on the monochromator. An FT spectrometer can have a much higher throughput.
- **Connes' advantage** – The wavelength calibration in an FT spectrometer is very accurate as it can be constantly compared to a HeNe laser reference.

There are also potential disadvantages to an FT spectrometer. As well as collecting all light simultaneously, it also collects all source noise simultaneously. This is known as Fellgett's disadvantage and when the noise is source limited it precisely cancels Fellgett's advantage. This is often true for FT-visible spectrometers. The higher throughput of an FT spectrometer can be undesirable if the sample is photosensitive. This becomes an increasing problem for increasing light energy and is particularly relevant to diamond where defects can be photochromic.

A dual beam dispersive spectrometer has the advantage that the sample beam can be constantly compared to a reference beam. In an FT spectrometer any drift in the background will appear in the spectrum. The combination of advantages and disadvantages mean it is common to use an FT spectrometer for IR absorption spectroscopy, but a dual beam dispersive spectrometer for visible-UV absorption spectroscopy.

4.1.2 Experimental details

4.1.2.1 Infrared absorption measurements

Here, IR absorption spectra were recorded with a PerkinElmer Spectrum GX Fourier transform IR (FT-IR) spectrometer. The spectrometer can be configured for MIR measurements over the range 370–7800 cm^{-1} with a filament source, KBr beam splitter and an MIR optimised TGS detector, or for NIR measurements over the range 2700–12 000 cm^{-1} with a tungsten halogen lamp, Quartz beam splitter and an NIR optimised TGS detector. The spectrometer was operated at a resolution of 1 cm^{-1} for all measurements in this thesis.

For all operation, except that with a cryostat, a 5× beam condenser was used. With the beam condenser, and at a resolution of 1 cm^{-1}, the spot diameter was approximately 1 mm. It also conveniently rotates the beam allowing a sample to be easily mounted on top of an aperture with the beam travelling vertically through it.

4.1.2.2 Ultraviolet-visible absorption measurements

UV-vis absorption spectra were recorded with a PerkinElmer Lambda 1050 spectrometer. The spectrometer has two sources for covering a broad range of wavelengths: a tungsten filament halogen lamp for the NIR-visible range and a deuterium lamp for the UV range. Before entering the sample chamber the light is monochromated, depolarised with a Hanle depolariser and alternated between the sample beam and reference beam with a rotating mirror. After traversing the sample chamber both sample and reference beams are focused onto the detector.

An InGaAs detector is used for NIR measurements and a photomultiplier tube for visible-UV measurements. By synchronising the detection with the rotating mirror the absorption in the sample arm is determined relative to the reference arm. The ideal setup therefore is to have everything but the sample (e.g. optical windows) in the reference arm such that the only difference is the sample of interest.

Measurements were made with the sample at 80 K in an exchange gas Oxford

Instruments continuous flow cryostat with the sample mounted in an indium aperture. The temperature was regulated by a heater set by an Oxford Instruments intelligent temperature controller.

4.1.2.3 Photoluminescence spectroscopy

A dispersive Renishaw inVia Raman microscope spectrometer was used for the collection of PL spectra with 2.808 eV (441.6 nm) and 3.815 eV (325.0 nm) excitation from a HeCd laser and 1.959 eV (632.8 nm) excitation from a HeNe laser. The microscope operates in reflection mode and has an automated stage allowing reproducible positioning and mapping of large areas.

All measurements were made at approximately 80 K. For quick inspection of samples, spectra were recorded with the sample immersed in liquid nitrogen. For all results presented in this thesis, samples were mounted in a Linkam TMS600 microsope stage and cooled with liquid nitrogen to 80 K.

4.2 Electron paramagnetic resonance spectroscopy

When probing energy levels in a dispersive optical absorption spectrometer the energy of the light is swept through a range to find the energies of light which are absorbed. A similar approach can be applied with EPR. To characterise a simple Zeeman splitting a fixed magnetic field can be applied and the microwave frequency swept to find the energy difference between the spin levels. Alternatively, rather than sweeping the microwave frequency, it can remain static while the energy levels are changed by sweeping the magnetic field. From an experimental point of view it is much easier to accurately sweep the magnetic field (field-swept EPR) than to sweep the microwave frequency (frequency-swept EPR). Consequently field-swept EPR is the most common method for continuous wave (CW) EPR spectroscopy.

The frequency dependent atmospheric absorption of microwaves, mainly due to water vapour, determines the frequencies for which microwave technologies are

developed. The atmospheric microwave absorption spectrum is divided up into bands which have the best transmission. The most common bands used in EPR spectrometers are X-band at 8–12 GHz, Q-band at 33–50 GHz and W-band at 75–110 GHz. The majority of EPR spectra in this thesis were recorded at X-band with some Q-band measurements. The wavelengths of 10 GHz and 34 GHz microwaves are 3 cm and 0.9 cm respectively, convenient length scales to work with.

As well as CW-EPR a broadband microwave pulse can be applied to the system with a static magnetic field in so called pulsed EPR. The pulse perturbs the spins which emit microwaves as they relax back which can be monitored. The resulting spectrum in the time domain can be Fourier Transformed to provide a spectrum in the frequency domain. Pulsed EPR is a powerful tool for investigating the dynamics of spin systems.

The operation of CW-EPR spectrometers will be briefly described here. Pulsed EPR techniques were not used in this thesis so will not be discussed further. Further details on the operation and theory of CW and pulsed EPR can be found in one of the excellent texts on the subject [1–5].

4.2.1 The EPR spectrometer

Figure 4-3 shows a simplified diagram of the main components in a CW-EPR spectrometer. The microwave source (typically a gunn diode or a klystron) provides microwaves at a stable frequency and power. The transmission of microwaves is either through waveguide (rectangular pipe of dimension determined by the wavelength) or coaxial cable. An attenuator allows adjustment of the microwave power before being directed to the sample in the resonator by a circulator. Circulators allow the transmission of microwaves from one port to the next in rotation.

The resonator is impedance matched such that, in the absence of absorption, there is no reflected power. It is said to be critically coupled. Absorption of microwaves in the sample causes an impedance mismatch causing the reflection of microwaves back to the circulator. Before reaching the diode the microwaves are mixed with a phase matched reference signal from the source which biases the microwave

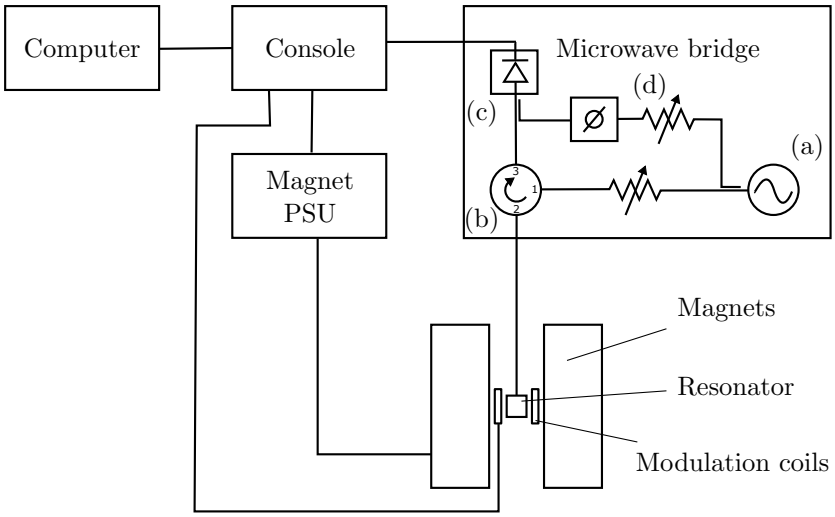

Figure 4-3 Diagram of the components making up a typical CW-EPR spectrometer. The labelled components of the microwave bridge are: (a) source, (b) circulator, (c) diode and (d) reference arm.

detector. The bias causes the detector to operate in its linear regime. Finally the current is converted to a digital signal with an analogue to digital converter.

The resonator enhances the sensitivity by increasing the microwave magnetic field (B_1), whilst minimising the microwave electric field (E_1), at the sample. The most common resonator is a cavity. A cavity resonator has a resonant frequency governed by its physical size. The frequency of the microwave source is tuned to the frequency of the resonator. A cavity is characterised by its Q-factor – the energy stored / energy lost per cycle. Q-factors of cavity resonators are typically several thousand.

To further improve sensitivity, phase sensitive detection is employed. The magnetic field is modulated by a small amount, usually at 100 kHz, causing modulations in the EPR signal. A lock-in amplifier de-modulates the signal, extracting only the component which has the same frequency and phase as the field modulation. The scheme is very effective at rejecting noise and unwanted signals. The signal amplitude at the modulation frequency is proportional to the slope of the EPR absorption. Consequently, for modulation amplitudes smaller than the linewidth, the signal is approximately a derivative of the absorption.

4.2.2 Experimental details

For the results in this thesis Bruker EMX and EMX-E CW-EPR spectrometers were used in conjunction with Bruker ER041XG and ER041X X-band microwave bridges and a ER053QRD Q-band microwave bridge. The ER041X bridge allowed up to 30 dB of additional attenuation to the ER041XG bridge, equating to microwave powers as low as 200 pW. Such low powers are sometimes required to avoid microwave power saturation of spin transitions in diamond.

The X-band bridges were coupled to either a Bruker ER4119HS cylindrical cavity or ER4122SHQ spherical cavity. Samples were mounted in the resonators in a single axis goniometer, either on a quartz rod or in a second axis goniometer. The dual axis set-up allowed accurate alignment of the field along any axis of the crystal. The Q-band bridge was coupled to a Bruker 5102QT cavity with samples mounted on a Rexolite® rod held in a single axis goniometer.

For high temperature measurements a Bruker variable temperature system was employed. Nitrogen gas was heated by a long filament before entering the resonator through a quartz insert and flowing past the sample. A thermocouple is positioned below the sample, just outside the resonator. The cavity was kept at a constant temperature by flowing RT nitrogen through it.

Quantitative measurements were made by comparing the intensity of the particular defect spectrum in the sample to that of N_S^0 in a reference sample. Separate reference samples were used for slow passage and rapid passage quantitative measurements. For slow passage measurements a type-Ib diamond was used, determined by FT-IR spectroscopy to have 270(14) ppm of N_S^0. The sample was prepared from a single homogeneous sector of an HPHT-grown diamond and had a mass of 2.68 mg. For rapid passage measurements a type-IIa diamond was used, determined by slow passage quantitative EPR to have 41(4) ppb of N_S^0. The sample was grown by CVD and had a mass of 88.5 mg. Intensities of spectra were determined by fitting of a lineshape convolved with simulated resonances. A detailed description of the methods used can be found in §5.2.1.

4.2.3 Loop-gap resonators

A loop-gap resonator (LGR) provides an alternative to the standard cavity resonator [6]. An LGR is a lumped-element resonator, that is, the regions of high electric and magnetic field are identifiable and spatially separated [7]. In an LGR the loops act as inductors and the gaps as capacitors, and as such they can be modelled as LCR circuits.

The frequency of an LGR with n identical gaps is given by

$$\nu = \frac{1}{2\pi\sqrt{LC}} , \tag{4-1}$$

where

$$L = \frac{\mu_0 \pi r^2}{z} \quad \text{and} \quad C = \epsilon_r \epsilon_0 \frac{wz}{nt} , \tag{4-2}$$

where r is the radius of the loops, z is the height of the structure, w is the gap length and t is the gap thickness [6]. Further terms can be added to account for fringing effects [7].

To increase the filling factor the size of the loop can be decreased, however maintaining the frequency requires that capacitance be increased. Capacitance can be increased by increasing the area of the gaps or decreasing their width, or by filling the gaps with a dielectric, however this is usually impracticable for low temperature operation. The frequency of the LGR is approximately independent of its height (ignoring corrections for fringing effects), allowing the design of LGRs much thinner than cavities, which are confined by the wavelength.

The advantages of LGRs are listed by Rinard and Eaton [7]. Those which are pertinent to their use here are as follows:

- Large filling factor
- Good SNR for small samples
- Confinement of E_1 to gaps
- Operation from 1–18 GHz with minimal design changes
- Relatively small size

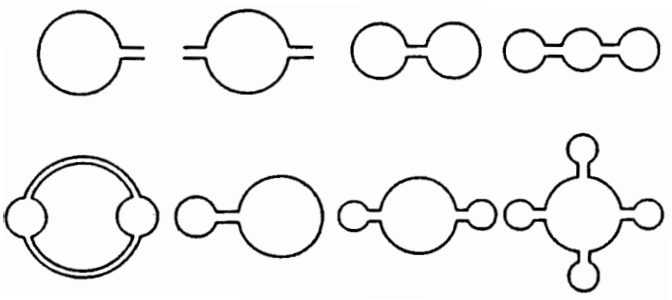

(a)

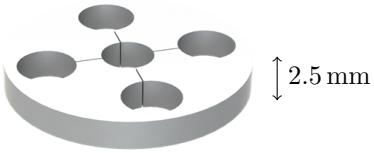

(b)

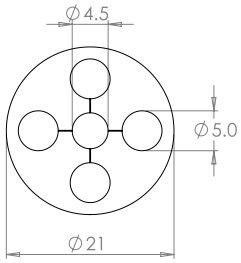

(c)

Figure 4-4 (a) Cross sections of a number of LGR geometries given by Hyde and Froncisz [9]. (b) Image of the LGR used here. (c) The dimensions of the LGR used here.

Some disadvantages are:

- lower Q-factor than cavity
- careful positioning of sample required
- frequency shifts as coupling is changed

Many different geometries of LGR are possible from the simple one-loop one-gap split ring design [6] to a seventeen-loop sixteen-gap rising sun structure [8]. Diagrams of a range of designs are shown in figure 4-4a.

At microwave frequencies LGRs radiate lowering the Q-factor and so it is necessary to use a shield. The Q-factor is inversely proportional to electrical resistance, hence it is favourable to construct LGRs from low resistivity materials such as silver. The confinement of E_1 to the gaps makes LGRs particularly appropriate for studying lossy samples [10].

In this work a four-gap five-loop "rising sun" LGR was used with a resonant frequency of 9.83 GHz, constructed from the glass ceramic Macor® and electroplated

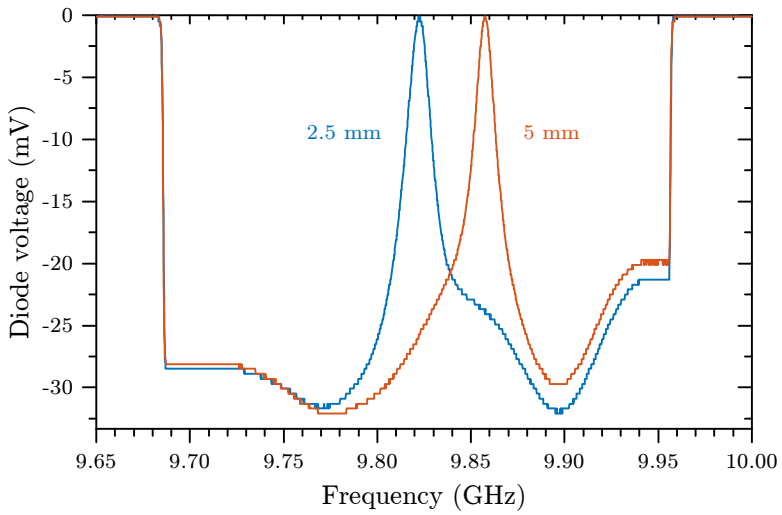

Figure 4-5 Critically coupled resonator modes of the rising sun LGR used here. The modes for two LGRs are shown with heights of 2.5 mm and 5.0 mm.

in silver. The silver layer was thin enough to allow penetration by the 100 kHz modulation field. The geometry of the LGR is shown in figure 4-4. Microwaves were capacitively coupled to the centre loop of the LGR by a coupling loop on the end of a semi-rigid coaxial cable. Coupling was tuned by adjusting the distance between the LGR and coupling loop. The critically coupled mode of the LGR is shown in figure 4-5. The Q-factors are in the range 500–1000. Although the Q-factor is lower than that achievable with a cavity resonator, the product ηQ is similar.

4.3 Uniaxial stress

For irradiating under stress and annealing under stress, optical stress probes were used modified with the addition of water cooling. For uniaxially stressed EPR a new probe design was implemented but the principle used for generating stress is the same as for the optical stress probes. Both designs use compressed gas (typically nitrogen) for generating pressure. Gas pressure was regulated using a computer controlled Bronkhorst El-Press 602CV mass flow controller. Pressures could be regulated up to approximately 2 MPa with an accuracy of 0.3 kPa.

The regulated gas fills a cylinder with a piston of area 3805 mm^2, which pushes

down on the sample through a series of rods and anvils. The pressure on the sample is given by

$$P_{\text{sample}} = P_{\text{gas}} \cdot \frac{A_{\text{piston}}}{A_{\text{sample}}} \,. \tag{4-3}$$

The large amplification of pressure by the ratio of areas of the piston and sample make pressures of several GPa easily achievable with typical sample areas of 1 mm^2.

To ensure that the sample is subjected to a homogeneous uniaxial stress, it must be prepared with pairs of carefully polished parallel faces and have a constant cross-sectional area. The samples must also be free from cracks and inclusions which could otherwise act as fracture sources. The smaller the stressed area of the sample the higher the potential stress that can be applied to it, however preparation is more difficult for smaller samples and spectroscopy might become difficult. A good compromise is a sample having a stressed face of area 1–2 mm^2 and a length of at least 2 mm along stress axis. For stressed EPR a higher aspect ratio is desirable to fill the resonator and keep anvils away from it.

4.3.1 Optical stress probes

A number of optical stress probes were used for the work in this thesis, all of which were constructed in-house by previous group members [11, 12]. The design of the probes is shown in figure 4-6. Their construction is of grade 316 stainless steel and brass. The probes are designed to be compatible with commercial cryostats allowing low temperature experiments.

Great care must be taken when mounting samples to ensure that the interface between the sample and the anvil is free from dirt and that, once under pressure, the sample is not subjected to any torque. To account for small imperfections in the sample and anvil surfaces, which might otherwise act as force intensifiers, a layer of aluminium foil is applied to the surfaces of the anvils. The foil is relatively soft and will flow into any gaps.

The pre-tensioner screws down inside the cylinder onto the piston, allowing samples to be held firmly in place before pressure is applied. The pre-tensioner does not form a gas tight seal inside the cylinder so the pressure is always the same

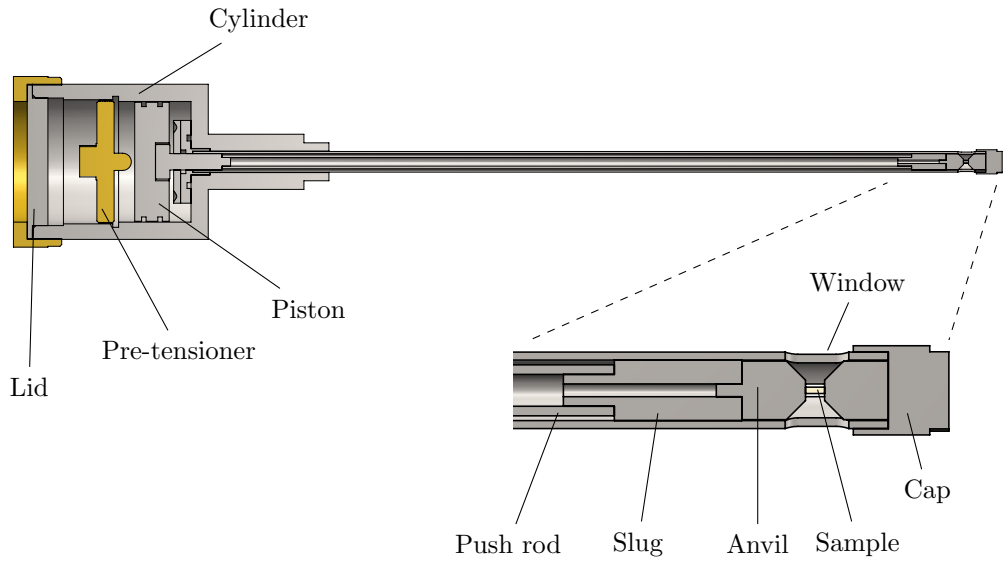

Figure 4-6 Cross section diagram of the optical stress probe showing how force is applied to the sample.

either side of it. Once samples are mounted the lid is placed on and fastened, forming a gas tight seal to 2 MPa. Nitrile o-rings are used to form the gas seals for the lid and the piston.

Regulated gas enters the cylinder through a fitting in the lid, filling the cylinder to a predetermined pressure and creating a force on the piston proportional to gas pressure and piston area. The piston forces down a push rod which in turn pushes a slug. The slug forms a sliding fit with the support tube, ensuring force is applied along the intended axis. The slug pushes directly on to a replaceable anvil, which in turn pushes on the sample. On the other side of the sample is another anvil and the removable end cap. The pressure on the sample is inversely proportional to its area.

4.3.2 EPR stress probe

A new EPR probe has been developed which allows uniaxial stress to be applied to the sample in situ. The probe is specifically designed for the GPa stresses and sensitivity to small samples required for studying diamond. A photo and cross section diagram of the probe are shown in figure 4-7.

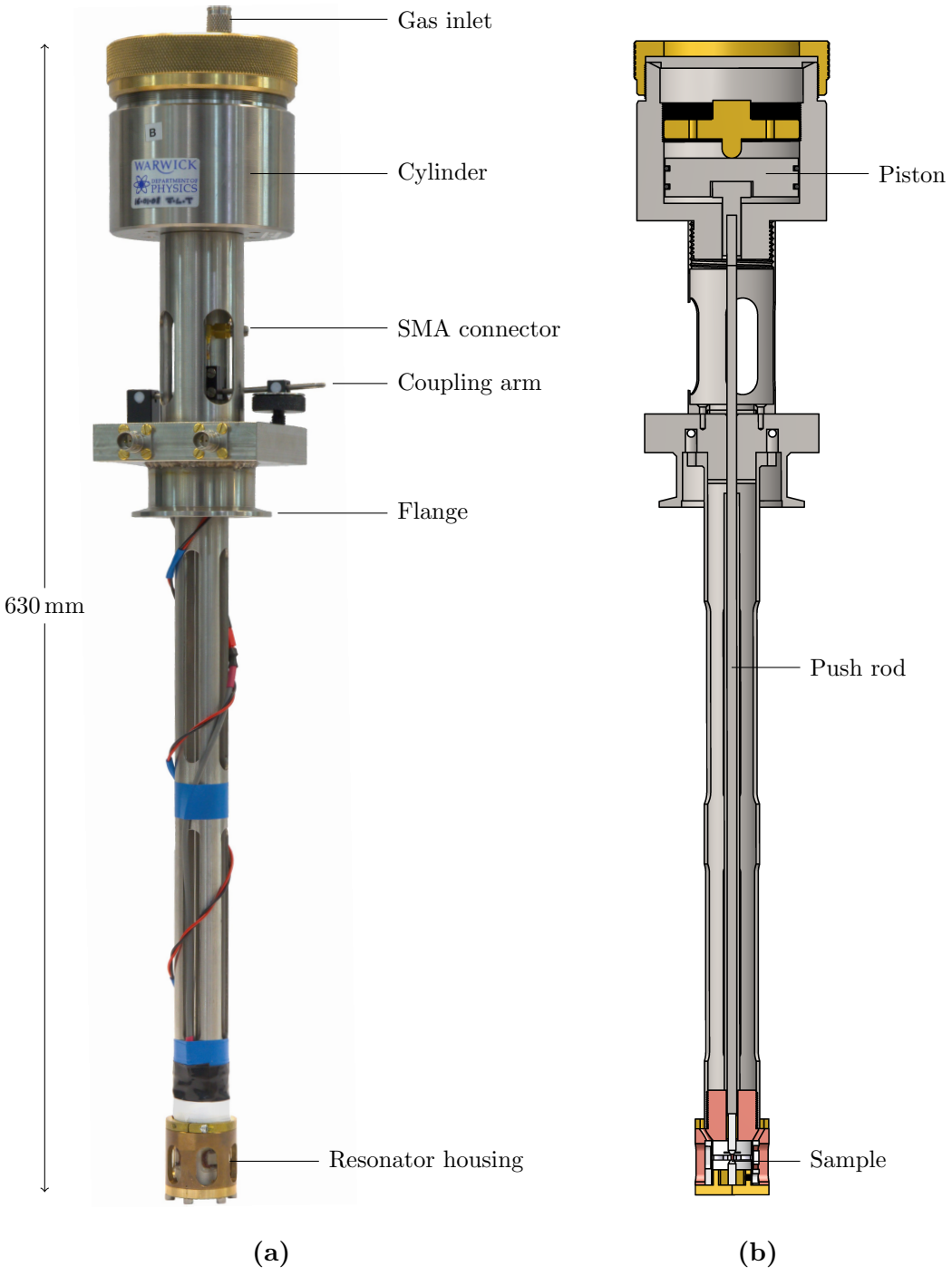

Figure 4-7 Photo (a) and cross-section diagram (b) of the unixial stress EPR probe with the main components labelled.

Initial design and construction of the probe was undertaken by previous group members. As with the optical stress probe the EPR stress probe uses a pneumatic piston and push rod to stress the sample, but also incorporates a microwave resonator. In this work the construction was completed with several small modifications to the design. Once completed and tested the probe was demonstrated on the N_S^0 and NV^- defects in diamond.

The greatest challenge is that of applying force to the sample whilst it is in a resonator. One solution is to have the sample extend through the entire resonator allowing anvils to remain outside, an approach which has been very successful for studying silicon [13]; however, the requirement for sample sizes similar to the wavelength makes it impractical for studying diamond at X-band frequencies. To use force transmitting components inside the resonator necessitates that they have low dielectric constants, do not contribute a background EPR signal and have excellent compressive strength – a very limiting set of requirements.

Central to the design here is the use of an LGR (§4.2.3). LGRs can be made a few mm thick allowing small samples to extend through their entire height. In addition they allow large filling factors with small samples and confine E_1 to the gaps. The five-loop four-gap LGR used here is described in §4.2.3 and shown in figure 4-4. Its position in the resonator housing is shown in figure 4-8. The fringing fields of the LGR mean that conductive materials should still be avoided nearby; therefore short pieces of fused-quartz and diamond anvils are used to transmit force between a steel push rod and the sample.

The LGR is held in place by Rexolite® inserts, which are also covered in 20 µm aluminium foil to create the resonator shield. The inserts slot inside a Rexolite® holder, into which modulation coils are mounted, which in turn slots into the resonator housing. The resonator housing is constructed from beryllium copper and brass. Non-magnetic materials must be used so as to not spoil the homogeneity of B_0. Further from the sample the probe is almost entirely constructed from grade 316 stainless steel. The resonator housing can be accessed by removing the bottom brass plate by undoing six brass screws.

The probe is compatible with commercial cryostats allowing operation down to

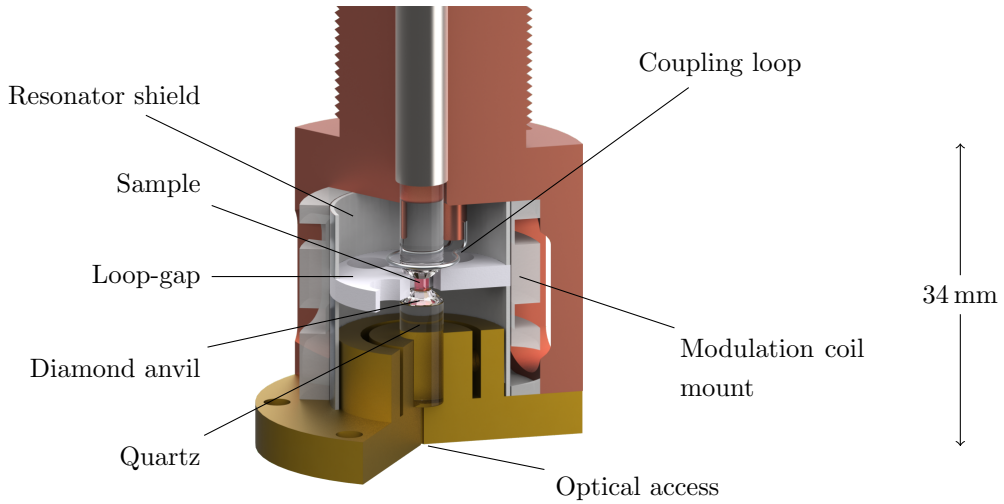

Figure 4-8 Cut-away diagram of the resonator housing. Microwaves are coupled to the resonator by a coupling loop, the position of which can be adjusted vertically. Metal components are kept away from the loop-gap by using quartz push rods inside the resonator housing.

4 K. In the cryostat the sample can be illuminated by a fibre optic cable inserted into the bottom of the brass plate. Light enters the diamond through the quartz rod and diamond anvil.

4.4 Annealing

There are two methods for studying the annealing behaviour of defects. The simplest is isothermal annealing: the concentration of a defect is monitored over time at a fixed temperature. This usually involves annealing in small steps between which measurements can be taken, but ideally annealing would be performed in situ and data recorded continuously. The method can be accurate in measuring activation energies and determining reaction order, however it is often time consuming and can only investigate a narrow range of activation energies limited by the Boltzmann distribution. One isothermal anneal will only provide the rate constant, from which the attempt frequency and activation energy cannot be distinguished. To separate the two variables a number of isothermal anneals are required over a range of temperatures. An Arrhenius plot can then be made by plotting $\log(k)$ against $1/T$ (see equation (3-46)). This should show a linear relationship, the gradient of which is the activation energy.

The other method is isochronal annealing. In an isochronal annealing experiment the sample is heated to a desired temperature for a set time and then characterised. For the next anneal the temperature is increased by a fixed step. The process is repeated for the desired number of steps. Isochronal annealing can explore a large range of activation energies but can only really estimate what the activation energy of a process is. Isochronal annealing would typically be used to investigate a poorly understood system, after which isothermal annealing could be used to accurately determine an activation energy.

4.4.1 Tube furnace annealing

Unless stated otherwise annealing and charge transfer treatments were performed in an Elite Thermal Systems horizontal tube furnace at atmospheric pressure. The furnace consists of an alumina tube, into which the sample is loaded, surrounded by heating elements in an insulating block. Alumina radiation shields are inserted into each end of the tube. The tube was continuously purged with nitrogen boil off to maintain a non-oxidising atmosphere.

For each anneal the furnace was heated to the anneal temperature, then the sample was loaded to the centre of the hot zone in an alumina boat over a period of a few minutes to prevent thermal shock. For anneals at 1000 °C and over samples were buried in the alumina boat in sacrificial diamond grit. When unloading, samples were moved out of the hot zone but remained in the furnace to cool whilst it was still purged.

4.4.2 Laser annealing

For annealing under uniaxial stress a CW LIMO 1.261 eV (983 nm) diode laser was focussed onto the diamond. A coat of silicone thermal grease on the diamond was found to effective at absorbing the laser power at its surface – pure diamond has very low absorption at 1.261 eV. The laser was capable of operating continuously at an output power of up to 40 W. It was coupled directly into an armoured fibre optic cable, the output of which was coupled, in an enclosed housing, to a lens

with a focal length of 55 mm. The focused spot had a diameter of ≈ 1 mm. Safety was greatly increased by not needing to collimate the beam in free space. The experiment was also contained inside a metal enclosure with interlocks on the door that when tripped turned off the laser.

References

1. G. R. Eaton et al., *Quantitative EPR* (Springer Vienna, New York, 2010).
2. J. A. Weil, J. R. Bolton, *Electron Paramagnetic Resonance* (John Wiley & Sons, Inc., Hoboken, NJ, USA, Second, Dec. 2006).
3. C. P. Poole, *Electron Spin Resonance* (John Wiley & Sons, Inc., New York, 1967).
4. A. Abragam, B. Bleaney, *Electron Paramagnetic Resonance of Transition Metal Ions* (Oxford University Press, Oxford, 1970).
5. A. Schweiger, G. Jeschke, *Principles of Pulse Electron Paramagnetic Resonance* (Oxford University Press, Oxford, 2001).
6. W. Froncisz, J. S. Hyde, *Journal of Magnetic Resonance (1969)* **47**, 515–521 (1982).
7. G. A. Rinard, G. R. Eaton, in *Biomedical EPR, Part B: Methodology, instrumentation, and Dynamics*, ed. by L. J. B. Sandra R. Eaton, Gareth R. Eaton (Springer US, 2005), chap. 2, pp. 19–52.
8. N. M. Atherton, *Magnetic Resonance in Chemistry* **28**, 737–737 (Aug. 1990).
9. J. Hyde, W. Froncisz, in *Electron Spin Resonance*, ed. by M. C. R. Symons, chap. 7, pp. 175–184.
10. M. Tamski et al., *Phys. Chem. Chem. Phys.* **17**, 23438–23447 (2015).
11. S. Liggins, PhD thesis, The University of Warwick, 2010.
12. B. L. Green, PhD thesis, University of Warwick, 2013.
13. G. D. Watkins, J. W. Corbett, *Physical Review* **121**, 1001–1014 (1961).

5

Defect quantification in diamond

Many of the subsequent results in this thesis required the quantification of defect concentrations by IR and UV-vis absorption and EPR spectroscopies. This chapter discusses methods used and developed. This includes experimental methodology and the analysis of resulting data, for which software has been written.

5.1 Analysis of optical absorption spectra

5.1.1 SpectrumManipulator

A large number of optical spectra were analysed for this thesis. To aid the analysis a graphical program, by name SpectrumManipulator, was written in MATLAB[1]. MATLAB provides access to powerful functions allowing fast development of functional, platform independent software tools. A potential limitation of using MATLAB is the requirement for the MATLAB runtime and compatibility with future MATLAB versions. Although no individual capability of the program was unique, the program streamlined a number of tasks and allowed the flexibility to add new features as required and automate bulk tasks.

The original purpose of SpectrumManipulator was the calibration of IR absorption spectra (converting absorbance into absorption coefficient) and concentration

[1]MATLAB version 8.5, The MathWorks, Inc., 2015

determination by fitting calibrated characteristic spectra to the experimental spectrum. The user interface during deconvolution of a spectrum is shown in figure 5-1.

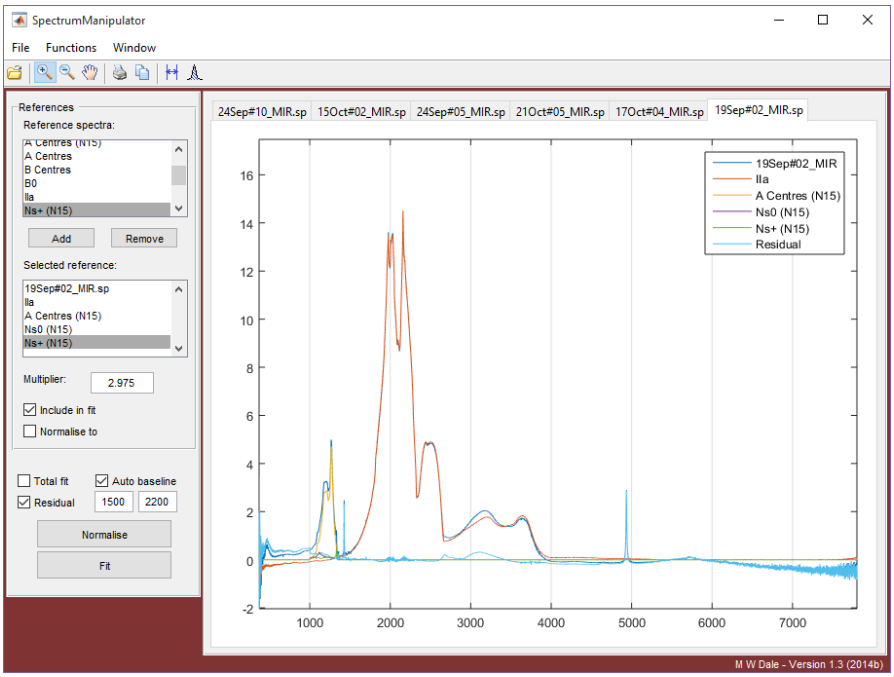

Figure 5-1 Screen-shot of SpectrumManipulator being used to normalise an IR absorption spectrum and deconvolve the one-phonon spectrum into its constituent components.

Normalisation of spectra was achieved by minimising the sum of squares

$$\mathbf{R}^2 \equiv \sum_i [ay_i - f_i - b]^2 \,, \tag{5-1}$$

where a is the scaling of the experimental spectrum, y_i is the i^{th} element of the experimental spectrum, f_i is the i^{th} element of a normalised intrinsic spectrum and b is the constant baseline. The intrinsic diamond spectrum was calibrated to have an absorption coefficient of $12.3\,\text{cm}^{-1}$ at $2000\,\text{cm}^{-1}$. The parameter a can alternatively be determined by $\log(10)/d$ where d is the sample thickness in cm, however this neglects reflections and differences in aperture sizes.

An experimental spectrum can be saved as a reference spectrum and fitted to another spectrum. When adding component spectra they are interpolated to the same resolution as the experimental spectrum. Each new experimental spectrum is opened in a tab allowing comparisons to be made between multiple spectra.

In addition to the ability to calibrate a spectrum and deconvolve it into components, other features of SpectrumManipulator include the ability to change the units (e.g. from cm^{-1} to meV), stitch together spectra from different spectral ranges, smooth spectra, apply a band-stop filter for effective removal of beating, linear and spline baselines, subtraction of spectra, and fitting of Voigt lineshapes.

5.1.2 Absorption coefficient

The attenuation of light through a thin slice of thickness dz due to absorption is given by

$$dI(z,\omega) = -\mu(\omega)I(z,\omega)dz \,, \tag{5-2}$$

where $\mu(\omega)$ is the frequency dependent absorption coefficient – the fraction of light absorbed per unit length. Solving this differential equation yields the transmittance through a medium of depth z as

$$T(\omega) = \frac{I(z,\omega)}{I(0,\omega)} = e^{-\mu(\omega)z} \,. \tag{5-3}$$

Since T is not linearly dependent on $\mu(\omega)$ it is often preferable to measure the optical density, or absorbance, defined by

$$A(\omega) = -\log_{10}(T(\omega)) \,. \tag{5-4}$$

Substituting T and rearranging provides us with the relationship between the measured absorbance and the absorption coefficient

$$\mu(\omega) = \frac{\log(10)}{z} A(\omega) \,, \tag{5-5}$$

which allows us to relate the measurement to the concentration of absorbing centres. Thus IR and UV-vis absorption are quantitative techniques.

From figure 5-2 however, a fraction of light experiences multiple reflections and passes through the sample several times. Where a significant proportion of light is absorbed in one pass the reflection terms are small, but if the absorption is small they are potentially significant. Considering reflections at each interface, the total

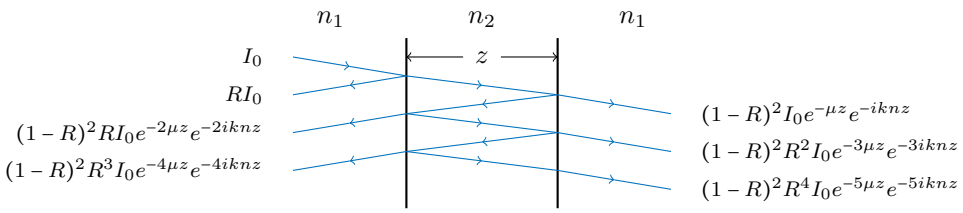

Figure 5-2 Multiple reflections of light when travelling through a medium of refractive index n_2, depth z and absorption coefficient μ, from a medium of refractive index n_1.

transmitted light is then more accurately given by

$$T = (1-R)^2\left(e^{-\mu z}e^{-iknz} + R^2e^{-3\mu z}e^{-3iknz} + ...\right) \tag{5-6}$$

$$= \frac{(1-R)^2\,e^{-\mu z}}{1 + R^2e^{-2\mu z} - 2Re^{-\mu z}\cos(2knz)}\,. \tag{5-7}$$

The detected signal is the sum of reflected components with increasing path lengths and phase-shifted by differing amounts. The periodic term is caused by interference and is often observed experimentally in the IR spectra of thin parallel plates of diamond as a periodic beating. Since the beating is at a fixed frequency appropriate filtering of the signal can be effective in removing it.

5.1.3 Nitrogen in diamond

Several forms of nitrogen in diamond, namely N_S^0, N_S^+, N_{2S} and N_4V, all have characteristic one-phonon absorption spectra, originally leading to the type classification of diamond. The calibrations relating the strength of absorptions to concentrations have previously been determined for all of these defects and are given in table 5-1.

SpectrumManipulator was used to quantify nitrogen from the one-phonon absorption. One-phonon spectra of each of the defects were calibrated, using the constants in table 5-1, to correspond to 1 ppm of nitrogen in the form of each defect. The calibrated spectra are shown in figure 5-3. When the calibrated spectra are fitted the required scaling factor corresponds to the concentration.

Fitting spectra with a single type of nitrogen is straightforward and can normally be accurately achieved by performing a least squares fit. This is often also true

Defect	Wavenumber (cm^{-1})	Calibration (ppm / cm^{-1})	Reference
N_S^0	1344	37	[1]
N_S^0	1130	25(2)	[2]
N_S^+	1332	5.5(10)	[3]
N_{2S}	1282	16.5(10)	[4]
N_4V	1282	79.4(80)	[5]

Table 5-1 One-phonon calibration definitions for nitrogen defects with a spectrometer resolution of $1\,cm^{-1}$. Where the defect comprises more than one nitrogen atom the constant is for nitrogen in the form of the defect. It is often more appropriate to fit N_S^+ by its feature at $1040\,cm^{-1}$.

when nitrogen is in two or more forms, for example a mixed type-IaA/B diamond. When there are unknown features in the one-phonon spectrum a least squares fit cannot be relied upon. In this case it is best to scale each defect manually paying careful attention to their most distinctive features, such as the N_S^0 LVM at $1344\,cm^{-1}$, the N_{2S} peak at $1282\,cm^{-1}$ and the N_4V peak at $1170\,cm^{-1}$.

Particular care must be taken when fitting N_S^+. The calibration constant is given for the $1332\,cm^{-1}$ peak however, being the maximum phonon frequency in intrinsic diamond, other defects such as N_4V and nickel defects also cause absorption at $1332\,cm^{-1}$. It is therefore best to fit N_S^+ by accounting for the absorption at $1040\,cm^{-1}$. N_{2S} can also be tricky to deconvolve due to the lack of sharp features. In this case the broad absorption at $480\,cm^{-1}$, which does not overlap with other defect spectra, can aid in achieving a reliable fit.

5.1.4 Electronic transitions

A large number of defects in diamond have electronic transitions which are observed in their absorption spectra (a thorough review of observed absorptions at defects, many of which have not been identified, is given by Zaitsev [6]). The total integrated intensity of an electronic absorption (in $meVcm^{-1}$) is proportional to the concentration of the defect, thus, with knowledge of the oscillator strength determining the absorption coefficient from the concentration, the defect can be quantified.

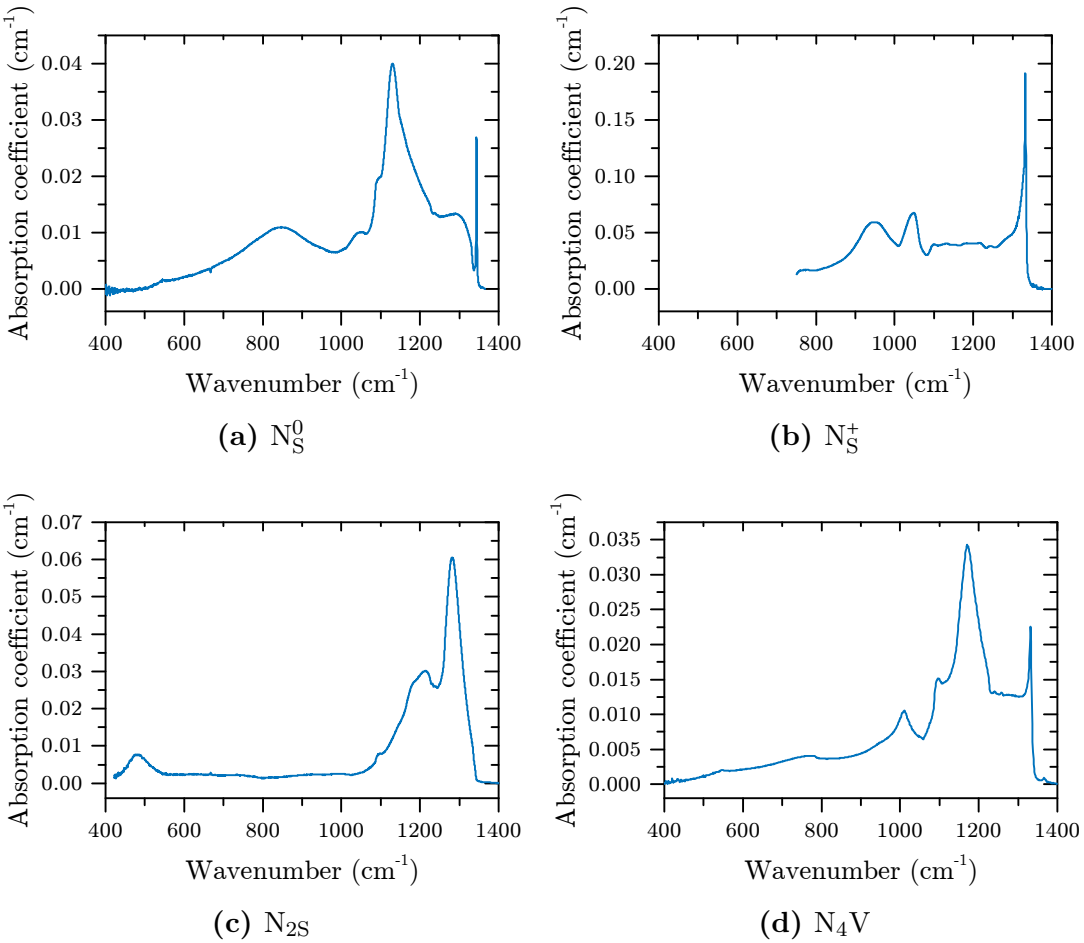

Figure 5-3 One phonon absorption spectra of common nitrogen containing defects in diamond. Each spectrum represents a concentration of 1 ppm of nitrogen in the form of the defect. The characteristic features of N_S^+ at 950 cm^{-1} and 1040 cm^{-1} and N_{2S} at 480 cm^{-1} can aid in achieving a reliable fit.

The precise shape of the absorption can change between samples and at room temperature features are very broad making integration challenging. When the sample is cooled the intensity of the absorption shifts from the phonon sideband to the ZPL, along with a narrowing of the ZPL. The strength of the absorption in the phonon sideband is characterised by the electron-phonon coupling constant (also called the Huang Rhys factor); for a definition and a good example see [7].

At low temperature ZPLs are sharp and can usually be fitted by a single Voigt lineshape after the background and edge of the phonon side-band have been accounted for with an appropriate baseline. An example of a fit of a Voigt lineshape to a baselined ZPL is shown in figure 5-4. If the line is significantly asymmetric,

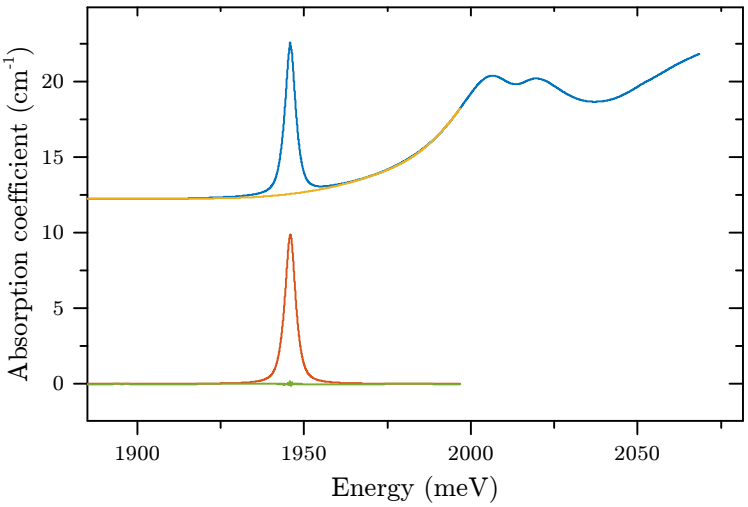

Figure 5-4 An example of a fit to the ZPL of NV^- at 1.945 eV recorded at 77 K. Top: the experimental spectrum (consisting of the ZPL on the side of the phonon sideband) along with the baseline. Bottom: the fit to the baselined ZPL and the resulting residual.

for example GR1, a split function should be used instead. For this reason it is standard practice to measure the intensity of the ZPL at 77 K. The intensity of the absorption, A, is related to the concentration by

$$A = f[X] \tag{5-8}$$

where f is the calibration constant in meVcm^{-1} and $[X]$ is the concentration of the defect in cm^{-3}. A number of calibration constants were determined in this thesis and are tabulated along with others in table 6-3.

5.2 Analysis of EPR spectra

5.2.1 Signal intensity

In the absence of microwave power saturation the CW-EPR double integrated intensity is proportional to several factors as follows

$$\text{EPR signal} \propto \chi'' \eta Q_L \sqrt{P}\,, \tag{5-9}$$

where χ'' is the magnetic susceptibility, η is the filling factor, Q_L is the loaded resonator Q-factor and P is the microwave power. Each factor will be discussed

briefly in the following section. For further details see Eaton et al. [8] or Weil and Bolton [9].

5.2.1.1 Magnetic susceptibility

The magnetic susceptibility, χ'', represents the absorption by the magnetic resonance transitions (the parameter which we are trying to measure). The intensity of χ'' is spread over all of the transitions between the spin energy levels and so the whole spectrum must be considered. It is also inversely proportional to temperature.

5.2.1.2 Filling factor

The filling factor represents the extent of the overlap between B_1 and the sample and is given by

$$\eta = \frac{\int_{\text{sample}} B_1^2 dV}{\int_{\text{cavity}} B_1^2 dV} \,. \tag{5-10}$$

If B_1 were uniform then η would simply be the ratio between the sample and cavity volumes. For small samples (so that B_1 is approximately constant over the sample), η can be approximated as being proportional to the sample volume. In the case of a sample of uniform density this is proportional to the mass, m.

5.2.1.3 Q-factor

The Q-factor is the ability of a resonator to store energy, often defined as the ratio of the energy stored to energy dissipated per cycle. In CW-EPR the signal is reflected power resulting from a change in Q-factor. The loaded Q-factor, Q_L, has a number of contributions but can mainly be accounted for by

$$\frac{1}{Q_L} = \frac{1}{Q_{\text{u}}} + \frac{1}{Q_{\text{r}}} + \frac{1}{Q_\epsilon} \,, \tag{5-11}$$

where Q_{u} is the Q-factor of the unloaded resonator, Q_{r} results from energy lost in the resonator structure, and Q_ϵ is the effect of dielectric losses from the interaction of E_1 with a non-vanishing imaginary component in the complex dielectric constant $\epsilon_r = \epsilon'_{\text{r}} - i\epsilon''_{\text{r}}$.

5.2.1.4 Microwave power

The proportionality to $\sqrt{P}$ is only true when the spin transition is not saturated, that is the spin populations are approximately in thermal equilibrium. With sufficient power it is possible that the signal intensity reduces with increasing power. An example of this can be seen later in this chapter in figure 5-12b. The behaviour of the signal with P can be fitted to the following expression

$$\text{Signal} = \frac{\alpha\sqrt{P}}{\left(1+\frac{P}{\beta}\right)^{\alpha/2}}\,, \tag{5-12}$$

where α and β are constants.

5.2.2 Quantitative measurements

The EPR intensity is proportional to the spin concentration in addition to many other parameters. By properly accounting for all of the parameters, either experimentally or in subsequent analysis of data, accurate quantitative measurements can be made.

Although it is possible to perform an absolute spin quantification with a calibrated spectrometer [10], it is in practice more reliable to compare the signal of the sample under investigation (hereafter called sample) with that of a reference sample (hereafter called reference) for which the spin concentration is known. A number of different references can in principle be used with the requirement that they are stable. To minimise errors the reference should be as close as possible in size and dielectric properties to the sample, such that differences in η and Q_ϵ are minimised. For the results of this thesis the N_S^0 spectrum in a type-Ib diamond was used as a reference.

With the subscripts s and r denoting sample and reference parameters respectively, the concentration of a defect is given by

$$[X_\mathrm{s}] = [X_\mathrm{r}]\frac{I_\mathrm{s}c_\mathrm{s}}{I_\mathrm{r}c_\mathrm{r}}\,, \tag{5-13}$$

where I is the intensity of the complete spectrum and c is a factor accounting for potential differences in the sample size, defect studied and experimental parame-

ters. The signal can depend on many different parameters which must be included in c, but a definition which was satisfactory for most experiments in this thesis is

$$\frac{1}{c} = \sqrt{P} \cdot B_{\mathrm{mod}} \cdot Q \cdot \underbrace{[G \cdot N \cdot t]}_{\text{scan}} \cdot \underbrace{\left[g^2 \cdot S(S+1) \cdot m\right]}_{\text{sample}}, \tag{5-14}$$

where the parameters are:

- P microwave power
- B_{mod} the modulation amplitude
- Q cavity Q-factor
- G detector gain
- N number of scans
- t acquisition time per scan
- g the electron g-factor
- S the total effective spin
- m sample mass

The best practice is to keep as many parameters as possible constant between the reference and sample scans such that the number of parameters in c is kept to a minimum.

One of the largest potential errors in quantitative EPR results from inconsistencies in sample and reference placement. An EPR cavity resonator is usually designed such that the sample sits in the centre of the cavity at a maximum in B_1 and a minimum in E_1. Any movement of the sample from this position will change B_1 and E_1 at the sample. This causes a change in η and Q_ϵ leading to differences in signal intensity [8, chapter 11.2]. Another error relating to sample positioning is caused by non-uniformity in the B_{mod} field [11]. It is therefore important to use design and procedure to make sample placement as reproducible as possible. Comparing a reference and sample of different sizes and/or shapes can introduce similar errors as those from sample positioning.

Once spectra of the sample and reference have been recorded the intensities corresponding to different defects must be determined. This is the subject of the next section.

5.2.3 The advantages of fitting

An EPR spectrum of one defect can consist of many individual resonances all with the same linewidth. A notable exception is when dynamic effects occur on the EPR timescale leading to motional broadening. With knowledge of the spin Hamiltonian parameters and in the absence of microwave power saturation the experimentally observed positions and intensities of transitions can be computed. The only parameters of the spectrum that change from one sample to another are the total intensity and linewidth of each component spin system.

Because of the use of magnetic field modulation and lock-in detection, an EPR spectrum usually has a derivative lineshape. The intensity of the spectrum can be determined by a double numerical integration. This can be performed on the experimental spectrum, however has the following significant disadvantages:

1. Overlapping spectra cannot be deconvolved.
2. Any background signals, for example from other defects or the cavity, will be included in the integral.
3. Any assymetry in the derivative lineshape (caused for example by incorrect phase) will cause a baseline in the first integral leading to significant errors in the double integral.
4. Noise on the spectrum is summed over every data point causing large errors.

As a result direct integration is only successful when there is only one defect, signal to noise is very large and backgrounds are insignificant.

Fitting the lineshape and amplitude of a simulated spectrum to the experimental spectrum mitigates the problems with integrating non-zero baselines, and significantly reduces the errors from integrating noise. A simulation can be numerically integrated, however, if there are insufficient data points numerical integration of

a non-centred derivative lineshape can create significant errors. An alternative to numerical integration is fitting a normalised lineshape with the result that the intensity is a parameter of the fit. Other advantages of fitting simulated spectra are that it allows the deconvolution of multiple spectra and the extrapolation of the intensity of one part of the spectrum to the whole spectrum.

5.2.4 Lorentzian, Gaussian and Voigt profiles

The unmodulated EPR lineshape can usually be deconvolved into Lorentzian and Gaussian components. The Lorentzian component is characteristic of the lifetime of a resonance; the longer lived and more defined, the narrower the Lorentzian component. Since the broadening is not caused by variations in the magnetic field or spin parameters it is called homogeneous broadening.

Gaussian distributions result from the sum of a large number of independent, identically distributed variables. A Gaussian component to the lineshape easily arises from many sources but is often caused by unresolved hyperfine couplings and field inhomogeneities. Since it results from variation in field or spin parameters, Gaussian broadening is known as inhomogeneous broadening.

Both the Lorentzian and Gaussian distributions have normalised analytic functions. The normalised Lorentzian distribution is given by

$$L(x;\gamma) = \frac{1}{\pi\gamma}\left[\frac{\gamma^2}{x^2+\gamma^2}\right], \tag{5-15}$$

where the full width at half maximum (FWHM) is related to γ by

$$L_{\mathrm{FWHM}} = 2\gamma\,. \tag{5-16}$$

The normalised Gaussian distribution is given by

$$G(x;\sigma) = \frac{1}{\sigma\sqrt{2\pi}} e^{-\frac{1}{2}\left(\frac{x}{\sigma}\right)^2}, \tag{5-17}$$

where the FWHM is related to σ by

$$G_{\mathrm{FWHM}} = 2\sqrt{2\log(2)}\cdot\sigma\,. \tag{5-18}$$

The Gaussian and Lorentzian distributions can be convolved together to give the Voigt profile:

$$V(x;\gamma,\sigma) = \int_{-\infty}^{\infty} L(s;\gamma)G(x-s;\gamma)ds \tag{5-19}$$

The Voigt profile is also normalised since it is the convolution of two normalised components. Due to its physical significance the Voigt profile has many applications in spectroscopy. Since a convolution is computationally expensive an approximation known as the pseudo-Voigt, the linear sum of a Gaussian and Lorentzian, is sometimes used.

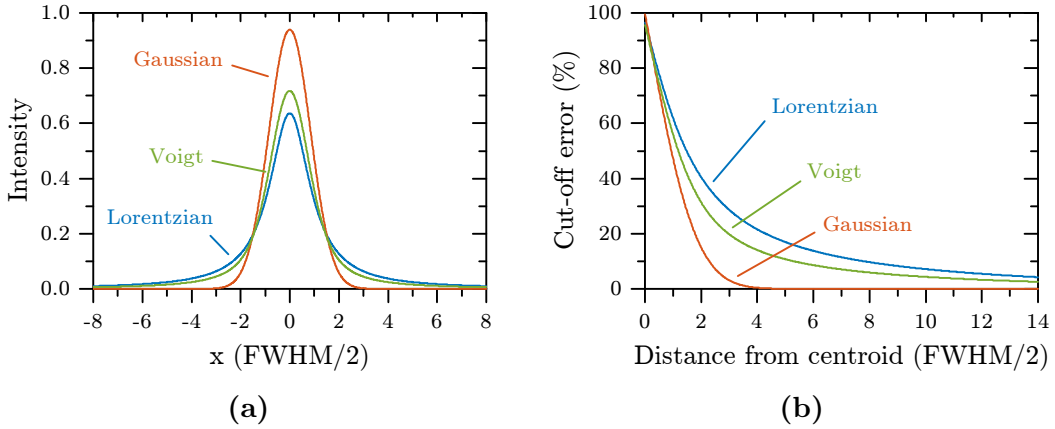

Figure 5-5 (a) Comparison between normalised Lorentzian, Gaussian and Voigt lineshapes of the same width (the Lorentzian and Gaussian components of the Voigt are of equal width). (b) Percentage of intensity of Lorentzian, Gaussian and Voigt lineshapes in (a) within distance from centroid.

An important property of the Gaussian and Lorentzian lineshapes is that

$$\lim_{x\to\infty} G(x;\sigma) = 0\,. \tag{5-20}$$

whereas

$$\lim_{x\to\infty} L(x;\gamma) \neq 0\,, \tag{5-21}$$

hence a significant portion of a Lorentzian line is in its tails, thus a large baseline is required either side for accurate fitting. This is demonstrated in figure 5-5, which shows a comparison between the lineshapes and the cumulative intensity from the centre. For a Gaussian 85 % of the intensity is within two FWHM and for a Lorentzian only 60 %.

5.2.5 Pseudomodulation

It is possible to fit Voigt profiles to the first integral of the experimental data, however this will most likely introduce baselines and does not take account of modulation broadening. Instead it is better to fit the modulated line directly, using a pseudomodulated lineshape as outlined by Hyde et al. [12]. It can be shown that the first harmonic pseudomodulated line with modulation amplitude B_m is given by

$$f_1(B; B_m) = \int_{-\infty}^{\infty} \hat{f}(s) J_1(B_m s/2) e^{iBs} ds \,, \tag{5-22}$$

where $\hat{f}(s)$ is the Fourier transform of the absorption lineshape, J_1 is the Bessel function of the first kind and s is a dummy variable.

The EPR spectrum is then constructed from the convolution of the stick spectrum $S(B)$, determined by matrix diagonalisation or perturbation theory from the Spin Hamiltonian, with the pseudomodulated lineshape. Since the Voigt-profile also requires a convolution, it is most efficient to construct the lineshape in one convolution of all of the components as, computationally, fewer FFTs are required:

$$\hat{f}_{\mathrm{mod}}(s; B_m) = \mathrm{FFT}(S(B)) \cdot \mathrm{FFT}(L(x)) \cdot \mathrm{FFT}(G(x)) \cdot J_1(x, B_m) \tag{5-23}$$

$$f_{\mathrm{mod}}(B; B_m) = -\mathrm{Im}(\mathrm{iFFT}(\hat{f}_{\mathrm{mod}}(B; B_m))) \,. \tag{5-24}$$

In this way, using the Voigt lineshape rather than for example a pseudo-Voigt requires little extra expense. If care is taken to ensure that each component is normalised $f_{\mathrm{mod}}(B; B_m)$ will also be normalised, and the scaling factor determined from fitting corresponds to the integrated intensity.

Figure 5-6 shows a Lorentzian line which has been pseudomodulated with a range of modulation amplitudes. The figure demonstrates the increase in signal, approximating the derivative lineshape, and subsequent modulation broadening which occurs when increasing the modulation amplitude.

From figure 5-6 it is apparent that, although the signal height increases initially with modulation amplitude, once the amplitude is greater than twice the linewidth the signal height starts to decrease. Despite the signal intensity increasing linearly with modulation amplitude the SNR is not best at the greatest modulation ampli-

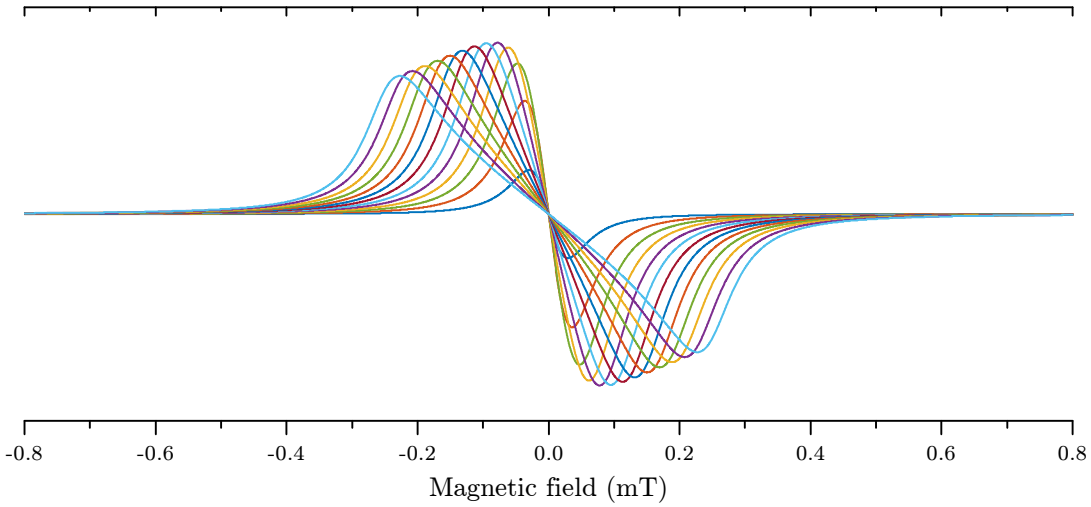

Figure 5-6 Pseudomodulation of a Lorentzian line with FWHM of 0.10 mT with modulation amplitudes from 0.02–0.50 mT in 0.04 mT increments.

tude. Figure 5-7 shows the relationship between modulation amplitude and signal height and linewidth.

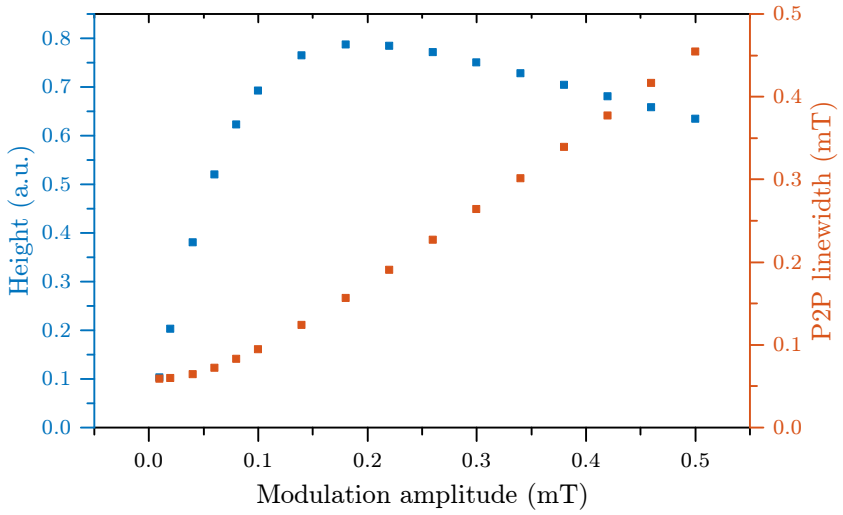

Figure 5-7 Variation of signal height and peak-to-peak linewidth with increasing pseudomodulation of a 0.10 mT Lorentzian line.

5.2.6 EPRsimulator

EPRsimulator was written in MATLAB[2] to accurately fit and deconvolve single crystal EPR spectra into constituent defects with a fast and easy to use inter-

[2]MATLAB version 8.5, The MathWorks, Inc., 2015

face. The program builds on and replaces EPR Wizard [13], written by a previous group member, providing several advantages, namely access to the powerful programming environment of MATLAB and spectral simulation with EasySpin.[3]

EasySpin is a well documented, supported and continually developed MATLAB toolbox for simulating and fitting EPR spectra. For simulation of solid state spectra EasySpin uses matrix diagonalisation and energy level diagram modelling [14]. Although EasySpin also simulates lineshapes and provides facilities for spectral fitting it is not by itself ideally suited to routine analysis and comparison of spectra for quantitative EPR.

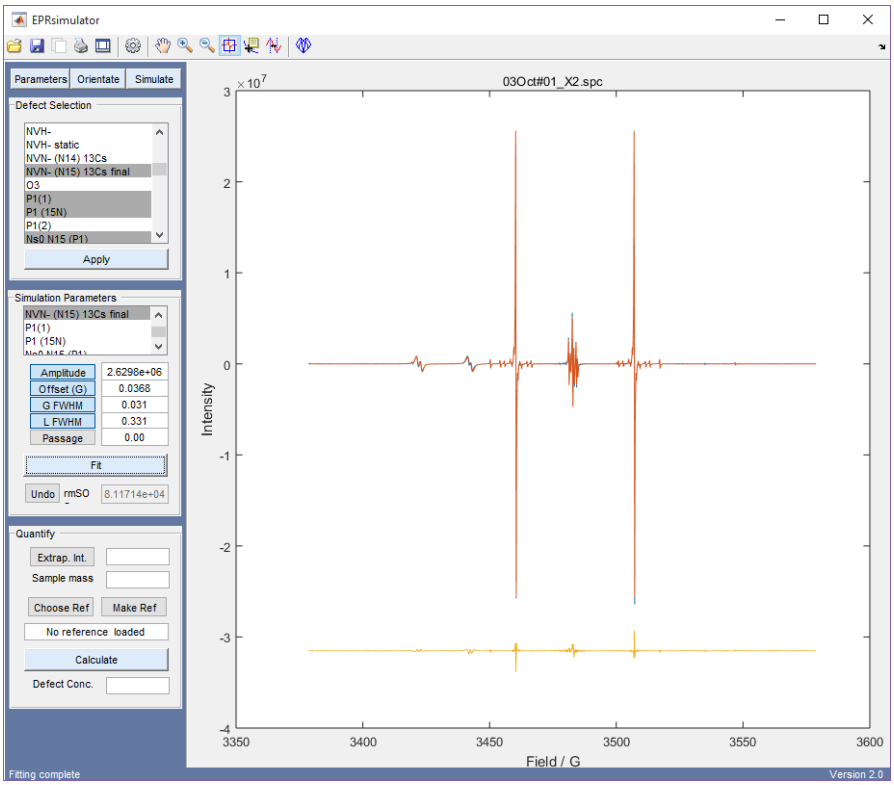

Figure 5-8 Screen-shot of EPRsimulator showing the main user interface for fitting spectra.

The main features of EPRsimulator are:

- Loading Bruker data files with EasySpin and displaying of experimental spectra and parameters
- Determining the magnetic field orientation to the crystal from anisotropic hyperfine interactions

[3] EasySpin 4.5.5, www.easyspin.org

- Simulating resonances of predefined defects with EasySpin
- Applying a normalised pseudomodulated Voigt lineshape to the resonances
- Optimisation of the lineshape parameters of multiple defect spectra to an experimental spectrum
- Quantification of defects by comparison with a reference spectrum
- Simulation of EPR 'roadmaps' showing the spectral orientation dependence

5.2.6.1 Simulating, fitting and quantification

Parameters are stored for each defect in a MATLAB '.mat' file, a binary file which can include variables in a number of types. The file can contain multiple spin systems, required for example when describing defects with isotope mixes. Each spin system includes a symmetry and the parameters required by EasySpin for simulating resonances. For example: spin, nuclei, isotopic abundances, and Zeeman, hyperfine, quadrupole, and zero-field tensors.

To simulate a spectrum for a defect, the spin system is input into EasySpin, along with a set of orientations to specify each symmetry related defect site (see §3.3). The orientations are determined by the defect symmetry and the angles between the crystal and $\boldsymbol{B}$. For each symmetry a set of rotation matrices are defined relating the orientation of each subsequent site to the first. These rotation matrices are used to determine the orientation between each site and $\boldsymbol{B}$. Each site is effectively treated in EasySpin as a separate spin system.

The resulting resonance positions and amplitudes output from EasySpin are converted into a normalised stick spectrum. A lineshape is then applied to the stick spectrum using the protocols in section 5.2.4 and section 5.2.5 to give a normalised spectrum. The lineshape can then be least squares fitted to the experimental spectrum using a trust-region reflective algorithm with the fit parameters amplitude, Lorentzian FWHM, Gaussian FWHM and a field offset. On every iteration of the least squares fitting a new lineshape is created with new parameters.

EPRsimulator allows the simulation and fitting of multiple defect spectra to the

experimental spectrum, each with different fit parameters, with the option to exclude any parameters from the fit. To ensure that there are no errors from using too low a resolution, EPRsimulator doesn't allow fitting of a linewidth causing fewer than a specified number of data points per FWHM.

A caveat of the protocol for simulation of the spectrum is that each resonance has the same lineshape. This is a very good approximation for most defects in diamond, particularly when the sweep width is narrow. Using different lineshapes for different resonances would be computationally very expensive as a different convolution would be required for each and it would also dramatically increase the number of fit parameters required.

A reference sample file can be saved including experimental parameters, parameters from the fit of a defect, the concentration of the defect and the sample mass. The concentration of paramagnetic defects in another sample can then be quantified from equation 5-13 using the parameters of a new fit and the reference sample parameters. When quantifying defects a correction is made to allow for any resonances outside of the experimental sweep width. This allows, for example, for the quantification of defects from half-field spectra, or using only one symmetry related site.

5.2.7 Other considerations

5.2.7.1 Orientation determination

The usual procedure when making quantitative measurements on single crystals is to align the crystal in the magnetic field such that a number of sites are degenerate. This has the advantage of simplifying the spectrum, facilitating identification of different transitions, and allowing a simulation to be created at the same, predefined orientation. The usual procedure for aligning samples is to perform fast scans of an anisotropic defect such as N_S^0 or R1 using the modulation coils, such that changes in orientation can be seen in real time. This of course requires sufficient signal to noise.

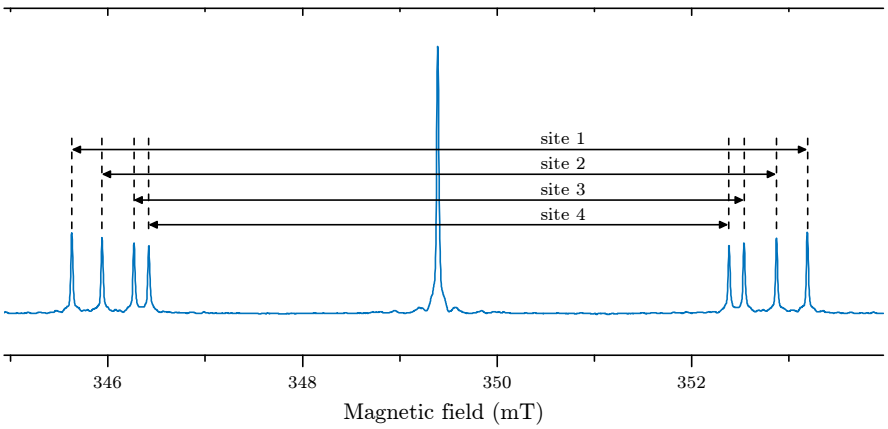

Figure 5-9 Example of a rapid passage N_S^0 spectrum with the crystal at a random orientation. The distance between the transitions of each defect site can be used to determine the orientation.

Rather than aligning the sample to a specific orientation, the orientation of the simulation can be fitted to the experiment. This is particularly effective for routine measurements of N_S^0. A method for determining the sample orientation from its N_S^0 spectrum was initially created by Ben Green, a former group member, and is employed in EPRsimulator. The off-orientation peak positions of the N_S^0 spectrum are automatically detected. The separation between the transitions with $m_I = -1$ and $m_I = +1$ are then compared with a look-up table to determine one of a number of degenerate orientations. The error in orientation determination depends on the rate of movement of transitions, $\frac{dB}{d\theta}$. For a defect such as R1 with a very large zero-field splitting and narrow linewidth the accuracy of orientation can be $< 0.01°$.

The quantification of N_S^0 from off-orientation spectra has been shown to provide consistent results with a similar standard deviation to oriented spectra. For routine measurements the increase in throughput is potentially large, since time is not required to align the sample. Although at present only the spectrum of N_S^0 has been used to determine the orientation of the crystal, any defect with an anisotropic Hamiltonian could be used.

5.2.7.2 Multiple sector fitting

The defect incorporation rate during sample growth is not necessarily homogeneous, for example the incorporation of N_S^0 depends on the growth sector. An

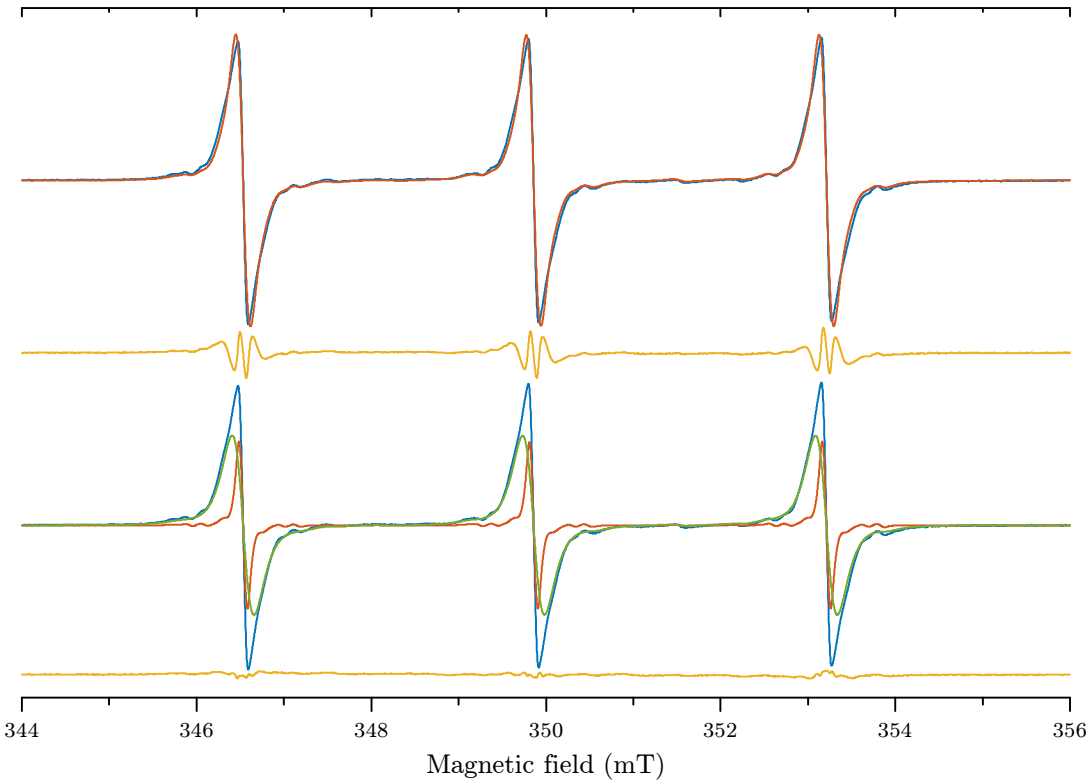

Figure 5-10 Comparison of fitting of an example N_S^0 spectrum with one linewidth (top) and two linewidths (bottom). The experimental spectrum is shown along with each component. The residuals are shown beneath. The concentrations of the two sectors are estimated to be 90 ppm and 230 ppm calculated from equation (5-27).

HPHT-grown diamond will usually be composed of multiple growth sectors unless specific care is taken to ensure that it is prepared from a single sector of a diamond. In the $\{1\,1\,1\}$, $\{0\,0\,1\}$, $\{1\,1\,0\}$ and $\{1\,1\,\bar{3}\}$ sectors nitrogen is usually incorporated in the approximate ratios 100:50:10:1 [15], although this can vary depending on the sample growth conditions such as temperature and pressure.

Since the EPR lineshape depends on concentration [16], it is sometimes necessary to use multiple lineshapes, representative of each sector, to obtain a good fit. An example is shown in figure 5-10 where the fitting of a spectrum to one and two N_S^0 lineshapes is compared. The local concentration in each sector can be estimated using the relation by Van Wyk et al. (equation (5-27)), or the average concentration over growth sectors can be determined from the total intensity. Improving a fit by accounting for sectors can be particularly useful to help deconvolve other components.

5.2.7.3 Quantification from $\Delta m_S = \pm 2$ transitions

There are two reasons why errors are reduced when quantifying from $\Delta m_S = \pm 2$ transitions. Firstly, the field positions of the $\Delta m_S = \pm 1$ transitions can be very sensitive to crystal orientation due to the anisotropic dipolar interaction. This is clear from the roadmap for NV^- shown in figure 5-11. Rotating off the [0 0 1] direction about the $[1\,\bar{1}\,0]$ axis, the $\Delta m_S = \pm 1$ transitions move at a rate of 2490 µT per degree, whereas the $\Delta m_S = \pm 2$ transitions move at only 23 µT per degree. To be able to fit the spectrum well, and obtain accurate intensities from the $\Delta m_S = \pm 1$ transitions, the sample must be aligned to within 0.05°.

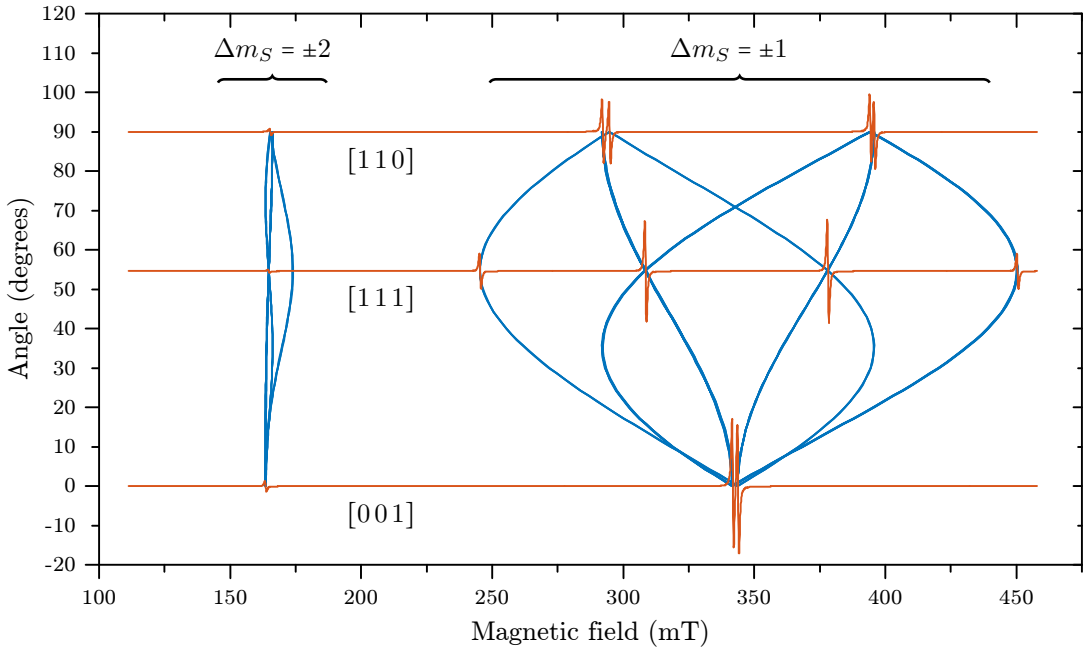

Figure 5-11 Roadmap of NV^- in {1 1 0} plane and spectra along the principle axes showing the orientation dependence of the spectrum. The angle is from the [0 0 1] direction.

Secondly, the $\Delta m_S = \pm 1$ transitions saturate very easily (see figure 5-12), requiring very low microwave powers for quantitative measurements. In contrast it takes approximately 30 dB less attenuation to saturate the $\Delta m_S = \pm 2$ transitions. The ability to run at higher power more than makes up for their smaller relative intensity. The orientation sensitivity and saturation behaviour of the $\Delta m_S = \pm 1$ transitions both lead to underestimates in concentrations when quantifying from the $\Delta m_S = \pm 1$ transitions making it beneficial to use the $\Delta m_S = \pm 2$ transitions.

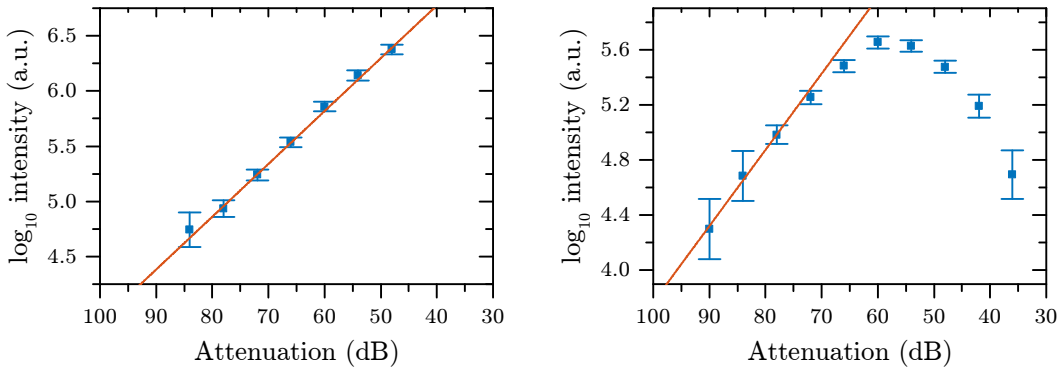

(a) $\Delta m_s = \pm 2$ **(b)** $\Delta m_s = \pm 1$

Figure 5-12 Saturation curves for NV^- in an HPHT grown diamond. The $\Delta m_S = \pm 1$ transitions saturate more easily than the $\Delta m_S = \pm 2$ transitions. Linear fits are shown to the four lowest power points in (a) and three lowest power points in (b).

If a scan is made of the half field spectrum, consisting only of $\Delta m_S = \pm 2$ transitions, the intensity of the total spectrum, including the $\Delta m_S = \pm 1$ transitions, must still be accounted for in the spin quantification. If the ratio between the half field and centre field spectra is known accurately the total intensity can be extrapolated from the half field spectrum. The spectrum can be simulated to obtain this ratio, however the frequency-field conversion factor, γ_{uv}, must be accounted for for each resonance (see §3.1.8.3). The measured intensity is proportional to γ_{uv}, which differs by approximately a factor of two between the $\Delta m_S = \pm 1$ and 2 transitions.

By default, EasySpin accounts for γ_{uv} for each resonance [17]. Simulating the NV^- spectrum with $\boldsymbol{B} \parallel \langle 0\,0\,1 \rangle$, the ratio between the intensities of the $\Delta m_S = \pm 2$ transitions in the half field spectrum and the $\Delta m_S = \pm 1$ transitions in the centre field spectrum is

$$\frac{I_{CF}}{I_{HF}} = 25.8\,. \tag{5-25}$$

To confirm this, experimental spectra were recorded of NV^-, using low powers to avoid saturation and with very careful alignment of the sample. The ratio was experimentally determined to be

$$\frac{I_{CF}}{I_{HF}} = 26(4)\,, \tag{5-26}$$

in very good agreement with that calculated. For comparison, without the γ_{uv} correction the simulated ratio is 14.0.

5.2.7.4 Defect concentration and signal to noise ratio

In the absence of microwave power saturation, the EPR signal integrated intensity is proportional to spin concentration, [X]. One would therefore expect that the higher the spin concentration the higher the SNR, however there are several other factors that need to be considered. According to Van Wyk et al., for N_S^0 concentrations above approximately 10 ppm, the EPR linewidth increases linearly [16]. An expression for the peak-to-peak linewidth of the first derivative, δ, was derived as follows:

$$\delta([\mathrm{X}]) = (1.2 \times 10^{-6}[\mathrm{X}]^2 + 1.4 \times 10^{-4})^{\frac{1}{2}} \text{ mT} , \tag{5-27}$$

where [X] is the concentration in ppm. For first derivative Lorentzian and Gaussian lines,

$$\text{peak height} \propto \frac{1}{\delta^2} , \tag{5-28}$$

so for a line of fixed intensity, as the linewidth increases the peak height decreases. For a fixed linewidth the intensity of the line is proportional to its height. Factoring together the increase in height and the corresponding increase in width, the EPR signal height has the following dependence on concentration

$$\text{EPR height}([\mathrm{X}]) \propto \frac{[\mathrm{X}]}{(\delta([\mathrm{X}]))^2} \tag{5-29}$$

$$\propto \frac{[\mathrm{X}]}{1.2 \times 10^{-6}[X]^2 + 1.4 \times 10^{-4}} . \tag{5-30}$$

As a result the signal to noise ratio peaks at approximately 10 ppm, for fixed experimental parameters. Of course though, with an increase in linewidth the modulation amplitude can be increased while maintaining good lineshape (figure 5-6). For small modulation amplitudes signal intensity is proportional to modulation amplitude as shown in figure 5-7. If, for example, the modulation amplitude is kept proportional to linewidth then the signal height is constant after 10 ppm. This behaviour is depicted in figure 5-13. In reality signal can be further improved as concentration increases, since spectra can be recorded at a high microwave power without saturating the transitions.

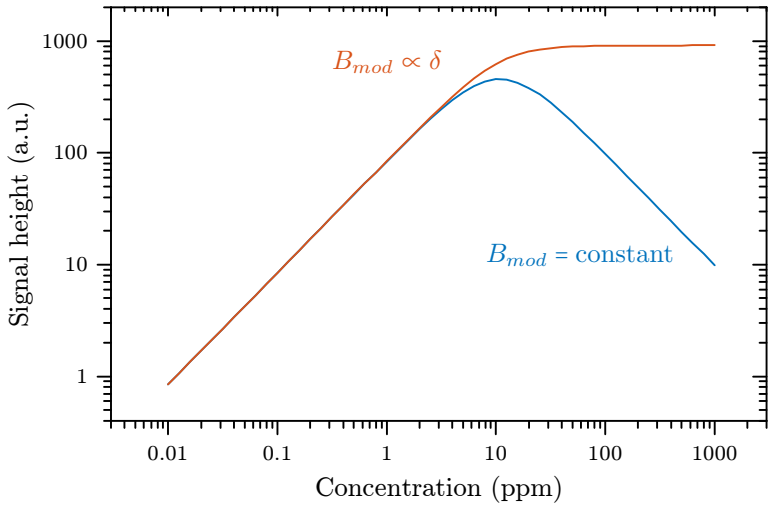

Figure 5-13 Change in signal height of N_S^0 with concentration for fixed modulation amplitude and modulation amplitude proportional to linewidth calculated from equation (5-30).

5.3 Conclusions

Techniques for the quantification of defects by IR and UV-visible absorption and EPR spectroscopies, particularly relating to the analysis and fitting of spectra, have been improved. The software SpectrumManipulator and EPRsimulator have been developed to analyse optical and EPR spectra respectively. EPRsimulator improves on previous software by fitting a normalised pseudo-modulated Voigt lineshape to spectra, using EasySpin to simulate resonance positions and intensities. The use of a normalised lineshape eliminates numerical integration errors. EPRsimulator can fit the orientation of a simulation to the experimental spectrum allowing quantitative measurements without tedious crystal alignment.

Fitting multiple linewidths to account for different concentrations in different sectors have been shown to dramatically improve fits. It has been confirmed that we can correctly quantify defects from their $\Delta m_S = \pm 2$ transitions, important for quantifying defects with large zero-field splittings such as NV^-.

References

1. S. Liggins, PhD thesis, The University of Warwick, 2010.
2. I. Kiflawi et al., *Philosophical Magazine Part B* **69**, 1141–1147 (June 1994).
3. S. C. Lawson et al., *Journal of Physics: Condensed Matter* **10**, 6171–6180 (1999).
4. S. R. Boyd, I. Kiflawi, G. S. Woods, *Philosophical Magazine Part B* **69**, 1149–1153 (June 1994).
5. S. R. Boyd, I. Kiflawi, G. S. Woods, *Philosophical Magazine Part B* **72**, 351–361 (1995).
6. A. M. Zaitsev, *Optical Properties of Diamond* (Springer, Berlin Heidelberg, 2001).
7. S. C. Lawson et al., *Journal of Physics: Condensed Matter* **4**, 3439–3452 (1992).
8. G. R. Eaton et al., *Quantitative EPR* (Springer Vienna, New York, 2010).
9. J. A. Weil, J. R. Bolton, *Electron Paramagnetic Resonance* (John Wiley & Sons, Inc., Hoboken, NJ, USA, Second, Dec. 2006).
10. N. D. Yordanov, *Applied Magnetic Resonance* **6**, 241–257 (1994).
11. R. Barklie, L. Sealy, *Journal of Magnetic Resonance (1969)* **97**, 611–615 (1992).
12. J. S. Hyde et al., *Applied Magnetic Resonance* **1**, 483–496 (1990).
13. A. M. Edmonds, PhD thesis, 2008.
14. S. Stoll, PhD thesis, Eidgenössische Technische Hochschule Zürich, 2003.
15. R. C. Burns et al., **104**, 257–279 (1990).
16. J. A. Van Wyk et al., *Journal of Physics D: Applied Physics* **30**, 1790–1793 (1997).
17. S. Stoll, A. Schweiger, *Journal of Magnetic Resonance* **178**, 42–55 (Jan. 2006).

6

Photo- and thermo-chromism

A photochromic process is usually defined as a reversible change in the optical absorption spectrum caused by the absorption of photons. If the energy of an absorbed photon is sufficient to excite an electron from a defect level into the conduction band, or from the valence band to a defect level, the electronic charge of defects can be changed. This charge transfer changes the electronic configuration of the defects involved and therefore the absorption bands and overall colour. Heating the sample in the dark can cause a thermochromic change in the opposite direction. Cycling between heating in the dark and illuminating can result in reversible changes in colour. This behaviour has been observed in a number of defects in diamond; notable examples are the vacancy [1], NV [2], NV : H [3], and N_2V [4], which will all accept an electron from N_S^0 to become negatively charged in a process that can be reversed with appropriate illumination, for example:

$$X^0 + N_S^0 \underset{\text{Light}}{\overset{\text{Heat}}{\rightleftharpoons}} X^- + N_S^+ \,. \tag{6-1}$$

Unlike in silicon where the charge states of defects are dictated by the position of the Fermi level, the large band-gap of diamond means the charge state is largely determined by the spatial proximity between donors and acceptors [5]. With NV for example, if $[N_S] \gg [NV]$, e.g. there is 100 ppm of N_S and 1 ppm NV, they will almost all accept an electron to become NV^- and the charge states are stable. With only 1 ppm N_S, although potentially all NV^0 could be converted to

NV^-, only a fraction will. This fraction is unstable and can be easily changed by illumination with appropriate energy light or heat treatment. Stability of charge states is important for applications of defects requiring specific charge states [2].

EPR is an invaluable tool for defect identification and characterisation providing information on their symmetry, electronic structure, constituent nuclei and quantity. Many defects are diamagnetic and cannot be observed by EPR. If however there are two possible charge states of a defect then at least one of them should be paramagnetic and observable in EPR (an exception would be a double-electron charge transfer process). The negative charge state of N_2V was predicted to be $S = \frac{1}{2}$ however it has not been irrefutably identified until very recently [6].

The H3 absorption at 2.463 eV (503.2 nm) was shown by uniaxial stress to be a $\langle 1\,1\,0 \rangle$ dipole at a $\mathscr{C}_{2v}$ centre [7], proposed to be N_2V^0 [8]. Photochromic measurements by Mita et al. suggested that the H2 absorption at 1.256 eV (986.3 nm) is from the same defect as H3 but in a different charge state. This was further supported by uniaxial stress data on H2 showing it to also have $\mathscr{C}_{2v}$ symmetry [9].

Here, detailed charge transfer experiments were performed to show the correlation between the EPR signal of N_2V^- with the H2 and H3 absorptions in ^{15}N isotopically enriched diamond. The spin Hamiltonian of N_2V^- has been refined with an experimentally determined ^{13}C hyperfine interaction and the observation of N_2V^- in ^{14}N diamond has allowed the quadrupole interaction to be characterised. Charge transfer between NV^0 and NV^- has enabled the determination of both of their oscillator strengths and further photochromic changes in the H1b and 594 nm centres has been investigated.

6.1 Sample details

The sample was HPHT-grown with isotopic enrichment of 95 % ^{15}N. After growth the concentration of N_S^0 was 110(5) ppm however it should be noted that nitrogen incorporation varies between the different growth sectors of diamond. The following treatments were then used after growth to create a relatively large concentration of N_2V^- to N_S^0:

1. HPHT anneal for 1 h at temperature $\gtrapprox$ 1900 °C to aggregate $\approx$ 85(5) ppm nitrogen into N_{2S}
2. Irradiation with 4.5 MeV electrons to create 5(1) ppm of vacancies
3. Anneal for 14 h at 800 °C to migrate vacancies to N_{2S} creating N_2V

Of the starting 110(5) ppm of nitrogen only 102(5) ppm is accounted for by N_S^0, N_S^+ and N_{2S}. H1a was present after irradiation with intensity 1.6(1) cm^{-2}. The loss of a small but significant amount of nitrogen by irradiation could be accounted for by the trapping of interstitials to form H1a, potentially amongst other complexes.

6.2 Experimental details

6.2.1 Spectroscopy

IR absorption measurements were made from 370–13 000 cm^{-1} at a resolution of 1 cm^{-1} using a Perkin Elmer Spectrum GX FT-IR spectrometer. Mid IR (MIR) measurements from 370–7800 cm^{-1} were made with a beam condenser reducing the spot size to a diameter of 1 mm on the sample. Near IR (NIR) measurements from 2700–13 000 cm^{-1} were taken with the sample mounted on the cold finger of a custom built cryostat cooled to a temperature of 90 K. Spectra were normalised for the intrinsic diamond two-phonon absorption at 2000 cm^{-1} to be 12.3 cm^{-1}. For quantification of N_S^0, N_S^+ and N_{2S} the calibration constants given in table 5-1 were used.

Optical absorption measurements were made on an Oxford Instruments Lambda 1050 dispersive spectrometer from 1100–200 nm using a 1 nm slit. The sample was mounted in an Oxford Instruments Optistat exchange gas cryostat and cooled to 77 K. FT-IR and UV-vis absorption measurements were made through the same section of the sample.

EPR measurements were made at room temperature on a Bruker X-band EMX spectrometer equipped with a 90 dB bridge and a Bruker spherical microwave cavity. Quantitative measurements of $\Delta m_s = \pm 1$ transitions were made with 12.6 nW

of microwave power to avoid their saturation. For NV^- the $\Delta m_s = \pm 1$ transitions are very anisotropic making alignment, and subsequent fitting, of spectra difficult. A reduction in errors is found by quantifying from the $\Delta m_s = \pm 2$ (also known as half-field) transitions, which also require a higher microwave power to saturate. The intensities of the component spectra were determined by fitting with spectra simulated from the spin Hamiltonians and convolved with a a normalised psuedo-modulated Voigt lineshape.

6.2.2 Heat treatment

Heat treatment to cause thermochromic changes was performed in the dark in a nitrogen purged tube furnace at 550 °C for 15 min. These conditions were chosen as they were previously shown to be sufficient to cause the maximum change [3]. This treatment did not cause any further annealing of the sample which had previously been annealed to 800 °C for 14 h. Where spectroscopic measurements were made after heat treatment, the sample was transferred to the appropriate sample holder or spectrometer in the dark with minimal light exposure to minimise photochromic changes. When light was required a red filter was used such that its energy was < 2 eV.

6.2.3 Photoexcitation

Photochromic changes were induced by illumination of the sample with a 3.061 eV (405 nm) diode laser at 100 mW of power. Near band-gap excitation with a HeAg laser at 5.528 eV (224.3 nm) was attempted but resulted in a significantly smaller photochromic change. The effect of the 3.061 eV illumination was apparent after exposure of < 1 s as a change in colour of the sample from purple to red (see figure 6-1). Further exposure did not cause any further colour change, hence an illumination of 5 s was used in experiments.

EPR measurements with in situ illumination were made with the sample affixed to a quartz rod and the laser incident on the sample through the rod. With the laser at 100 mW of power the heating effect was enough to cause the tuning

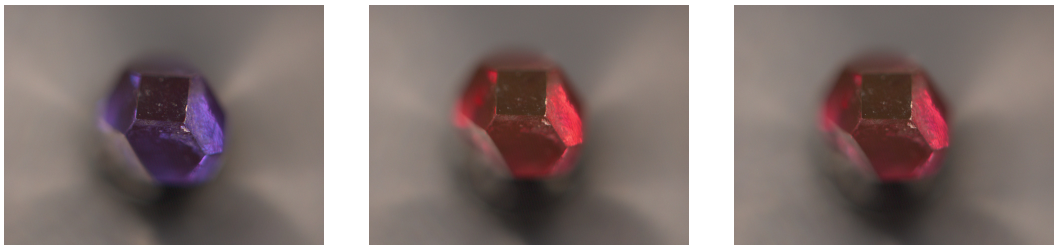

(a) (b) (c)

Figure 6-1 Photos of sample SYN339 taken in a DiamondView™, each with identical instrument settings, after heat treatment (left), two minutes after illumination (middle) and two hours after illumination (right) with 3.061 eV light at 100 mW. The DiamondView™ illumination intensity was set very low to minimise in situ photochromic changes and luminescence.

of the spectrometer to drift. This was stabilised by performing the experiment in a Bruker variable temperature system (ER 4141VT) with room temperature nitrogen gas flowing past the sample.

6.3 Results and discussion

6.3.1 Stability of charge states

Initial efforts focused on in situ illumination of the sample to quantify differences in the EPR and optical absorptions. Although in situ illumination causes the largest photochromic changes, it was unfortunately not reproducible in different spectrometers and proved difficult with UV-vis absorption measurements for two reasons: firstly, saturation of the detector was caused by scattering of the illumination source into the spectrometer, although this could be remedied by appropriate filtering; secondly the luminescence intensity from NV^- and N_2V^0 was so strong that it saturated the detector. Filtering would have been difficult since the luminescence was around a large range covering the regions of interest.

From the colour changes of the sample shown in figure 6-1, it was clear that a proportion of the photochromic changes were long lived at room temperature. To investigate this the sample was illuminated ex situ then immediately transferred

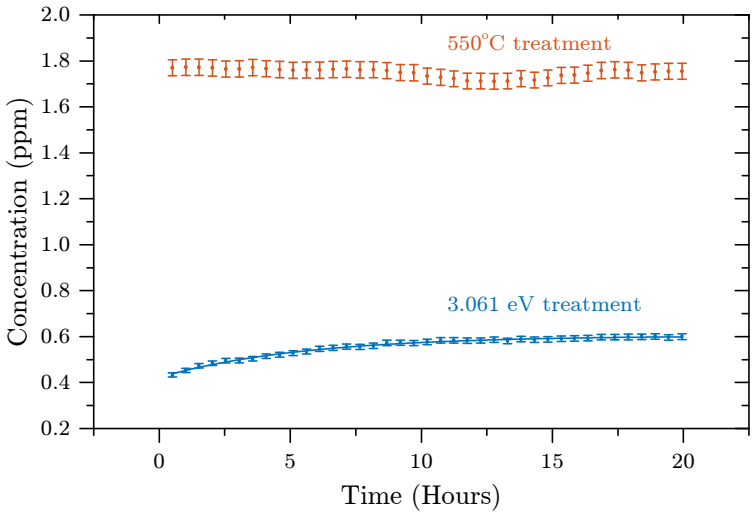

Figure 6-2 Concentration of N_2V^- determined by EPR over 20 h periods after heat treatment and after illumination with the sample in the dark. After heat treatment $[N_2V^-]$ is stable, however after illumination it slowly returns to an intermediate value. The solid line is fit to a single exponential with time constant 5.5(2) h.

in the dark to an EPR cavity where the N_2V^- concentration was monitored over time. The resulting time scans are shown in figure 6-2 where time zero corresponds to illumination. The concentration of N_2V^- plateaus at 0.6 ppm after 20 h (cf. 1.8 ppm after heat treatment). A single exponential fits well to this change with a longer time constant of $1.99(7) \times 10^4$ s. The stability of the heated state was also investigated but showed no significant change over a 20 h period. The small dip between 10–15 h is during night time and most likely due to the spectrometer tuning changing with the lab temperature.

From the stability of the illuminated state after a 20 h period it was clear that spectroscopy after ex situ illumination would be feasible for correlating optical absorptions with EPR spectra. To minimise errors in subsequent measurements, the sample was illuminated 24 h before spectroscopy and kept in the dark in the meantime. Since the heated state is stable, measurements could be made on the sample immediately after heat treatment.

6.3.2 Optical, infrared and EPR spectroscopy

Figure 6-3b shows UV-vis absorption spectra over the range 1.2–4.2 eV after heat treatment, 24 h after illumination treatment and the difference spectrum (heated subtracted from illuminated). A number of strong absorptions are seen, notably H2 and H3 ZPLs at 1.256 eV and 2.463 eV, NV^- and NV^0 at 1.945 eV and 2.156 eV and the 594 nm centre at 2.086 eV. In addition the H2 LVM at 1.424 eV is also observed. The dramatic change in the optical absorption spectrum gives insight into the origin of the colour change in figure 6-1.

The NIR absorption spectra recorded in an FT spectrometer are shown in figure 6-3a over the range 0.35–1.60 eV. It should be noted that for this measurement the 24 h period was not waited after illumination due to time constraints, therefore photochromic changes are slightly larger. The temperature was also slightly warmer at 90 K. The range of these measurements overlaps with the measurements made in the dispersive spectrometer showing the H2 absorption but in addition we see the H1b absorption.

All of the aforementioned systems underwent photo/thermochromic changes. With illumination H3 increases dramatically while H2 decreases, as previously reported [4]. NV^0 increases as NV^- decreases, the 594 nm centre increases and the H1b absorption decreases. As confirmation that the monochromated light source in the spectrometer did not cause any photochromic effects, each measurement was made twice consecutively with no discernible difference. All of the photochromic changes were reversed by heat treatment.

To quantify the changes the ZPLs were fitted to Voigt lineshapes after subtraction of a suitable baseline. The baselines were carefully chosen as splines through as few points as possible while minimising the residual from the Voigt fit; the process had good reproducibility. The intensities of the lines and their relative changes are given in table 6-1.

MIR spectra were also recorded at room temperature after heat treatment and 24 h after illumination, the one-phonon region of which is shown in figure 6-4. The spectra are dominated by absorption from N_{2S} and H1a, the di-nitrogen $\langle 0\,0\,1 \rangle$

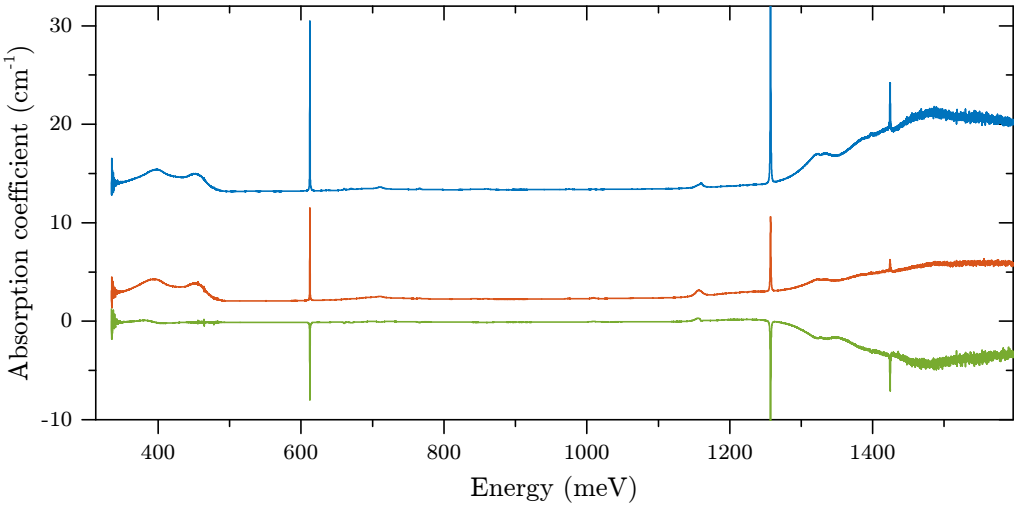

(a) NIR absorption spectra at 90 K after heat treatment (top), illumination (middle) and the heated spectrum subtracted from the illuminated spectrum (bottom). The feature on the left is the intrinsic diamond three-phonon absorption. In the spectrum after heat treatment the H2 absorption is clipped as it was too intense to measure.

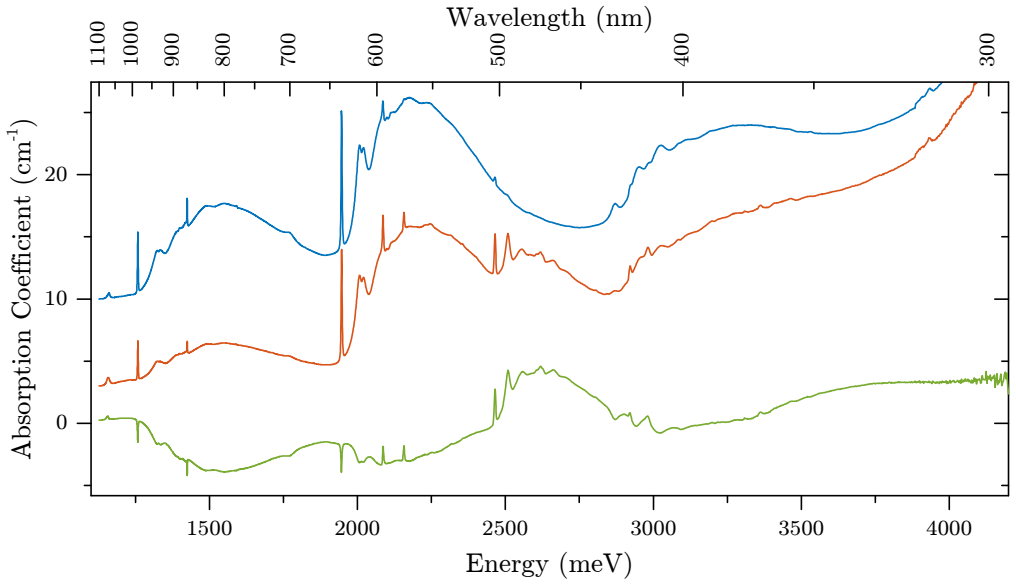

(b) UV-vis absoprtion spectra at 77 K after heat treatment (top), illumination (middle) and the heated spectrum subtracted from the illuminated spectrum (bottom).

Figure 6-3 Absorption spectra from 0.35–4.2 eV after heat treatment and illuminations treatment and the resulting difference spectra.

ZPL (eV)	Intensity after Heat treament ($meVcm^{-1}$)	Intensity after illumination treatment ($meVcm^{-1}$)	Percentage difference (%)
1.256 (H2)	24(1)	12.2(6)	−50(6)
1.424 (H2 LVM)	3.8(2)	1.9(1)	−55(6)
2.463 (H3)	3.2(2)	19(1)	500(40)
1.945 (NV^-)	53(3)	42(2)	−21(6)
2.156 (NV^0)	1.11(6)	6.9(3)	520(40)
2.086 (594 nm)	10.5(5)	13.9(7)	33(8)
0.612 (H1b)	9.6(5)	5.0(3)	−48(6)

Table 6-1 Intensities of ZPLs in figure 6-3b except H1b which is from the NIR spectra in figure 6-3a. The intensities are all determined by appropriate baselining and fitting a Voigt lineshape.

split interstitial [10]. It should be noted that in ^{15}N diamond the H1a LVM is at 1426.7 cm^{-1} whereas for ^{14}N it is at 1450.3 cm^{-1}. Smaller contributions from N_S^0 and N_S^+ are also observed. Despite the large N_{2S} absorption the difference spectrum on the right of figure 6-4 shows clear contributions from N_S^0 and N_S^+. By fitting the difference spectrum it is found that illumination caused an increase in N_S^0 of 1.6(8) ppm and a decrease of N_S^+ of 1.6(4) ppm. No photochromism or thermochromism was seen from N_{2S} or H1a.

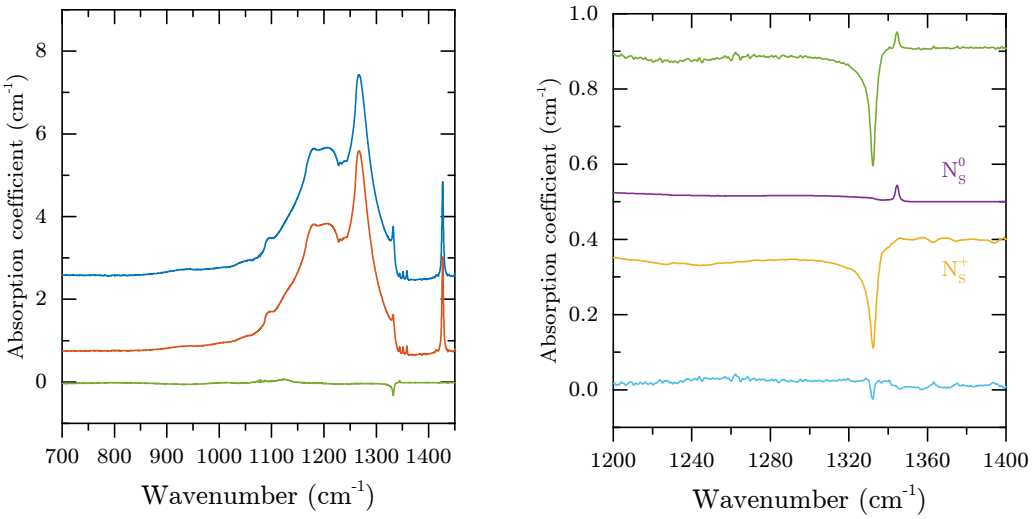

Figure 6-4 On the left: One phonon spectra of SYN339 after heat treatment (top); after illumination treatment (middle) and the first subtracted from the second (bottom). On the right: the difference spectrum (top); the deconvolved 1.6 ppm N_S^0 and 1.6 ppm N_S^+ component spectra (middle) and residual (bottom). All spectra were recorded at room temperature.

EPR spectra were recorded of N_S^0, NV^- and N_2V^- after the heat treatment and 24 h after illumination. The spectra were fitted to pseudomodulated Voigt lineshapes simulated from the spin Hamiltonian for each defect. The resulting quantification is given in table 6-2.

	Concentration after treatment (ppm)		
Defect	Heat	Illumination	Difference
N_S^0	5.0(3)	6.6(3)	1.6(4)
NV^-	1.6(1)	1.3(1)	−0.4(1)
N_2V^-	1.8(1)	0.6(1)	−1.2(1)

Table 6-2 Concentrations of defects determined by EPR after heat and illumination treatments.

The combined difference in NV^- and NV^0 is −1.6(1) ppm matching the 1.6(4) ppm difference in N_S^0. This is in agreement with the MIR data where changes of 1.6 ppm N_S^0 and −1.6 ppm N_S^+ account well for the one-phonon difference spectrum. Considering the errors it is still possible that there is 0.4 ppm of other defects accepting charge from N_S^0.

6.3.3 Oscillator strengths and calibration constants for NV and N_2V

In the absence of saturation, EPR signal is proportional to the number of spins. Thus if the signal is compared to a well characterised reference sample the technique can be quantitative. From Beer's law the optical absorption coefficient from a defect is linearly dependent on its concentration, hence only a calibration constant is required to determine the concentration from a ZPL. The absorption is then given by

$$A = f[\mathrm{X}]\,, \tag{6-2}$$

where f is the calibration constant in meV cm^2 and [X] the concentration in cm^{-3}. A number of calibration constants for ZPLs in diamond have been determined

previously by various authors, however some, including those for NV and H2/H3, were determined by indirect methods [11].

Where two ZPLs correspond to the same defect in differing charge states, for example the 1.945 eV and 2.156 eV lines of NV^- and NV^0, and that defect undergoes a photochromic change, a relative dipole moment can be determined. Making the assumption that

$$[NV^-] + [NV^0] = \text{constant} , \tag{6-3}$$

then for any photochromic change

$$\Delta[NV^-] + \Delta[NV^0] = 0 . \tag{6-4}$$

The ratio of the corresponding changes in ZPLs then gives the relative oscillator strengths of the two defects:

$$\frac{\Delta A_{1.945\,\mathrm{eV}}}{\Delta A_{2.156\,\mathrm{eV}}} = \frac{f_{1.945\,\mathrm{eV}}}{f_{2.156\,\mathrm{eV}}} . \tag{6-5}$$

If the calibration constant is determined for one then the other is also known.

To accurately determine the calibration constant for NV^-, quantitative EPR measurements were taken of NV^- and UV-vis absorption spectra were recorded for a number of irradiated and annealed HPHT-grown samples. The resulting data is shown in figure 6-5a. A fit through the data and the origin gives the calibration constant for NV^- as

$$f_{1.945\,\mathrm{eV}} = 1.70(8) \times 10^{-16}\,\mathrm{meV\,cm^2} . \tag{6-6}$$

This is in agreement with the previous value in the literature determined by indirect methods of $1.40(35) \times 10^{-16}\,\mathrm{meV\,cm^2}$, although it was not specified whether that value corresponded to NV^- or NV^0 [11].

Figure 6-5b compares the size of the 1.945 eV and 2.156 eV absorptions in sample SYN339. Different ratios correspond to different degrees of charge transfer obtained over several iterations of the experiment. Only a small spread in the ratio was measured after heat treatment of the sample since the state is stable. A larger deviation was obtained after illumination treatment by making the UV-vis

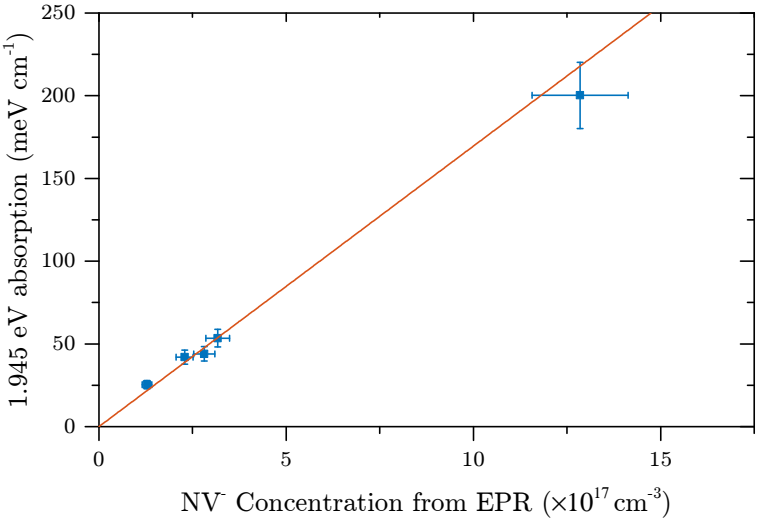

(a)

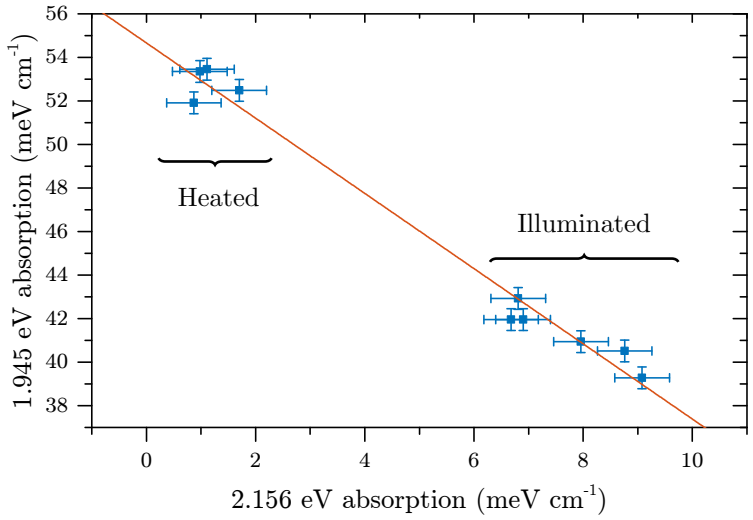

(b)

Figure 6-5 (a) Integrated intensities of the 1.945 eV ZPL measured at 77 K, against NV^- concentrations quantified by EPR spectroscopy for several ^{14}N and ^{15}N samples. The line is a linear fit to the data with gradient $1.70(8) \times 10^{-16}$ meV cm^2. (b) Relative intensities of the 1.945 eV and 2.156 eV absorptions at 77 K for sample SYN339 measured after repeated heating and illumination cycles as described in the text. A range of degrees of charge transfers were made by waiting different periods between illumination and cooling of the sample. The slope of the fit is −1.73(8).

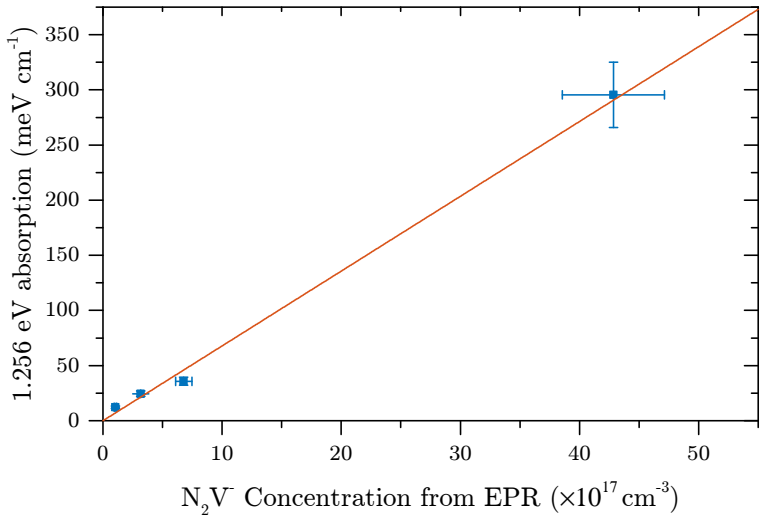

(a)

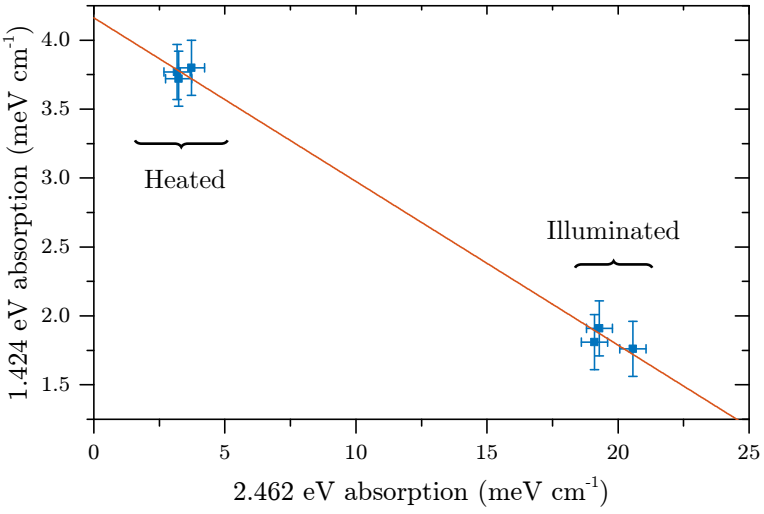

(b)

Figure 6-6 (a) Integrated intensities of the 1.256 eV ZPL measured at 77 K, against N_2V^- concentrations quantified by EPR spectroscopy for several ^{14}N and ^{15}N samples. The line is a linear fit to the data with gradient $6.8(10) \times 10^{-17}$ meV cm^2. (b) Relative intensities of the 1.424 eV and 2.462 eV absorptions at 77 K measured after repeated heating and illumination cycles as described in the text. The slope of the fit is –0.119(4).

measurement at varying times after treatment. The fit to the data gives the ratio of oscillator strengths as

$$\frac{f_{1.945\,\mathrm{eV}}}{f_{2.156\,\mathrm{eV}}} = 1.73(8)\,, \tag{6-7}$$

from which the calibration constant for NV^0 is

$$f_{2.156\,\mathrm{eV}} = 9.8(6) \times 10^{-17}\,\mathrm{meV\,cm^2}\,. \tag{6-8}$$

The calibration constant for N_2V^- was determined analogously to NV^- by analysis of several HPHT-grown samples. The data is shown in Figure 6-6. A fit through the data and the origin gives the calibration constant as

$$f_{1.256\,\mathrm{eV}} = 6.8(10) \times 10^{-17}\,\mathrm{meV\,cm^2}\,. \tag{6-9}$$

The spectrometer used a PMT above 1.425 eV and an InGaAs detector below, reducing the accuracy of comparisons between the 1.256 eV and 2.462 eV lines. The H2 absorption was instead determined by measuring the intensity of its 1.424 eV LVM. The 1.256 eV ZPL and 1.424 eV LVM of H2 have been shown to be related by the fixed ratio 0.135(4) at low temperature [9]. Thus it is possible to determine the intensity of the ZPL from the LVM. A drawback is that the LVM is difficult to fit because of the presence of a shelf underneath it due to the cut-off of the optic-mode contribution to the H2 vibronic band; nonetheless measurements of it proved consistent. The resulting comparison between the intensity of the 1.424 eV and 2.462 eV lines is shown in figure 6-6. The ratio between the lines is −0.119(4), hence

$$\frac{f_{1.256\,\mathrm{eV}}}{f_{2.465\,\mathrm{eV}}} = 0.88(4)\,, \tag{6-10}$$

and the calibration constant for N_2V^0 is

$$f_{2.462\,\mathrm{eV}} = 7.7(12) \times 10^{-17}\,\mathrm{meV\,cm^2}\,. \tag{6-11}$$

The calibration constants determined here are summarised and compared with previously determined constants in table 6-3.

Defect	ZPL (eV)	Calibration constant ($meV\,cm^2$)	Reference
V^-	3.150	$4.8(2) \times 10^{-16}$	[1]
V^0	1.673	$1.2(3) \times 10^{-16}$	[1]
NV^-	1.945	$1.70(8) \times 10^{-16}$	
NV^0	2.156	$9.8(6) \times 10^{-17}$	
N_2V^-	1.256	$6.8(10) \times 10^{-17}$	
N_2V^0	2.462	$7.7(12) \times 10^{-17}$	
N_3V^0	2.985	$8.6(20) \times 10^{-17}$	[11]

Table 6-3 Summary of calibration constants for vacancies and nitrogen vacancy defects, determined in this and other work where referenced.

6.3.4 NV and N_2V photochomism mechanism

To investigate the time constants associated with the photochromic changes, EPR time scans of N_S^0, NV^- and N_2V^- were made with in situ illumination. The sample was subjected to the heat treatment before being mounted on a quartz rod and transferred to the resonator in the dark. The EPR intensity was then monitored at a fixed field chosen to maximise the SNR for each defect. Whilst the EPR intensity was monitored the sample was illuminated for two minutes to allow an equilibrium of charge states to be reached. After switching off the light the recovery was monitored for a few hours. The time scan for each defect was recorded in a separate experiment under identical conditions and normalised to the quantification made previously after heat treatment (table 6-2). The resulting data is shown in figure 6-7.

As seen already, illumination caused $[N_s^0]$ to increase and $[NV^-]$ and $[N_2V^-]$ to decrease. A temporary increase in signal from NV^- during illumination due to optical spin polarisation [12] has been corrected for in the figure by scaling its intensity during the illumination period to match the intensity immediately after the light was switched off. The initial change in signal once the laser was switched on occurred over approximately 10 s before reaching an equilibrium.

When the light is switched on the sum of the concentrations of N_S^0, NV^- and N_2V^- seems to overshoot before returning to an equilibrium. This could be an

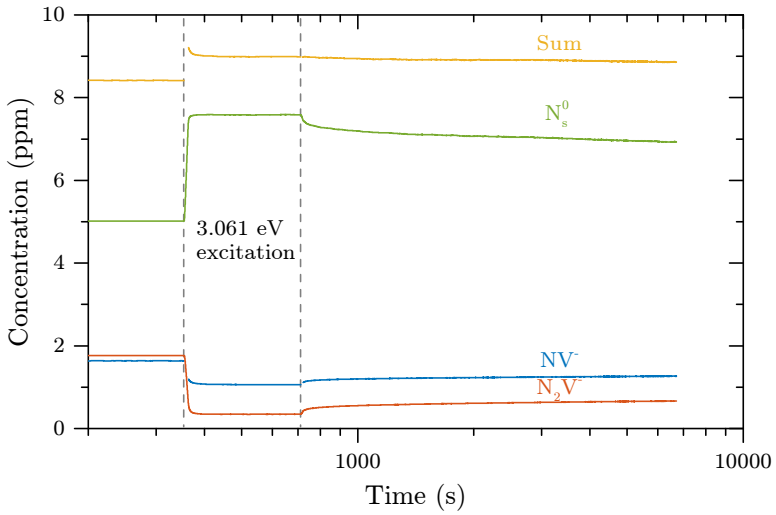

Figure 6-7 EPR time scans of N_S^0, NV^- and N_2V^- with in situ illumination between 360 s and 720 s. The NV^- signal during illumination has been corrected to account for spin polarisation. The sample was heat treated before each measurement. The signal for each defect after illumination is found to fit well to two exponentials.

artefact from the correction for the spin polarisation of NV^- or alternatively could correspond to there being an initial charge transfer to N_S resulting in unstable species, before a redistribution of charge with NV and N_2V. The thermal ionisation energy for N_S^0 is 1.7 eV [13], while the photoionisation energy is 2.2 eV [14].

When the light was switched off the EPR signal had a fast initial change which quickly slowed. For each defect the change in signal could be fitted accurately in the range 800–6700 s with the two exponential function

$$X(t) = X(0) + A_1 e^{-t/t_1} + A_2 e^{-t/t_2} \,, \tag{6-12}$$

where $t = 0$ is the time at which the light was switched off. Fitting between the range 720–800 s required an increasing number of exponential functions. The parameters resulting from the fits are given in table 6-4.

Mita et al. made a study of the recovery processes of H3 and H2 (which are now known to be N_2V^0 and N_2V^-) by their optical absorptions after illumination with 2.410 eV light [15]. Although N_S^0 was also studied by EPR, at the time it could not be directly correlated with N_2V^- due to the absence of an EPR signal. The recovery was faster with increasing temperature but the effect was much more

	t_1 (s)	t_2 (s)
N_S^0	243	5166
NV^-	281	3104
N_2V^-	285	2427

Table 6-4 Time constants resulting from fitting equation (6-12) to the 800–6700 s range of the time scans in figure 6-7.

dramatic above 147 °C. It was argued that the dominant recovery process was tunnelling below 147 °C and thermal ionisation above. The samples in that study had 17–69 ppm remaining N_S^0 giving a much smaller average donor to acceptor distance than with the 5 ppm N_S^0 here.

The fast and slow components to NV^- and N_2V^- in figure 6-7 could correspond to different mechanisms for charge transfer or to the same process in two sectors of different concentrations in the diamond. If the donors and acceptors exist in different concentrations in two sectors then we would expect to see a different time constant associated with each. If N_S^0 is acting as the donor for NV^- and N_2V^-, the time constants observed for NV^- and N_2V^- should also be observed for N_S^0. Since the time constants for NV^- and N_2V^- are similar it is not surprising that they are not individually resolved in N_S^0.

The fast process with time constant 240–280 s, where most of the change happens, is consistent with a charge transfer mechanism described by

$$NV^0 + N_S^0 \underset{\text{Light}}{\overset{\text{Heat}}{\rightleftharpoons}} NV^- + N_S^+ \tag{6-13}$$

$$N_2V^0 + N_S^0 \underset{\text{Light}}{\overset{\text{Heat}}{\rightleftharpoons}} N_2V^- + N_S^+ \ , \tag{6-14}$$

since we see a similar time constant for N_S^0, NV^- and N_2V^-. Since the slow component is described by different time constants for each defect it is most likely an observation of a more complicated process involving intermediate defects. Another effect that might be important is the transfer of charge and redistribution

of charge across multiple defects, for example

$$N_S^0 + N_S^+ \rightleftharpoons N_S^+ + N_S^0 \tag{6-15}$$

$$NV^0 + NV^- \rightleftharpoons NV^- + NV^0 \tag{6-16}$$

$$N_2V^0 + N_2V^- \rightleftharpoons N_2V^- + N_2V^0 \tag{6-17}$$

$$NV^0 + N_2V^- \rightleftharpoons NV^- + N_2V^0\ . \tag{6-18}$$

6.3.4.1 Photochromism of H1b and the 594 nm defect

The 594 nm defect is produced on irradiation of type-I diamond. Subsequent annealing of the diamond up to approximately 800 °C increases its intensity, after which it anneals out and H1b anneals in [16]. In figure 6-3a H1b is seen to decrease with illumination while the 594 nm defect increases. The effect is reversed by heating. Photochromism of the H1b and 594 nm defects has previously been reported by [17]. UV light drove the charge transfer one way and light from a 100 W halogen lamp had the reverse effect. Here heat treatment had the same effect as the UV illumination.

H1b and H1c are observed to anneal in with the same ratio as the concentration of N_{2S} to N_4V. From this the H1b and H1c defects are believed to be created by the 594 nm defect being trapped at N_{2S} and N_4V respectively [16]. Results in this thesis (chapter 7) have shown that H1b can be created without N_{2S} being previously present, suggesting that there is more that one route to its formation. This is seen with other defects, for example N_2V.

A possible conclusion to draw from the complementary charge transfer of H1b and the 594 nm defect in figures 6-3a and 6-3b, is that they are different charge states of the same defect. The apparent annealing out of the 594 nm defect with the annealing in of H1b could then in fact be a charge transfer process. It is possible that N_S^0 acts as a donor for this; as we saw there was room in the errors for up to an additional 400 ppb of acceptors. Alternatively the photochromism could be caused by a reconfiguration of the defects from one to the other without any charge transfer. It is of course also possible that the photochromism of H1b and the 594 nm defect are unrelated.

The symmetry of H1b is $\mathscr{C}_{1h}$ [16] whilst that of the 594 nm defect is $\mathscr{D}_{3d}$ [18], however it should be noted there was some uncertainty in the latter assignment. The $\mathscr{D}_{3d}$ symmetry considerably constrains possible structures of the 594 nm defect to either a bond-centred interstitial (nitrogen or carbon), a di-substitutional defect such as N_{2S}, a di-vacancy or impurity di-vacancy such as the silicon vacancy. Ab initio calculations have predicted the bond-centred carbon and nitrogen interstitials to be less stable than the alternative $\langle 0\,0\,1\rangle$-split configurations making them unlikely. Relative energies of interstitial configurations are given in table 6-5. N_{2S} is of course well characterised and unambiguously not the 594 nm defect.

	Charge state			
Interstitial	-1	0	+1	Reference
Carbon	4.45	4.05	3.04	[19]
Nitrogen	1.2	1.9	2.1	[20]

Table 6-5 Total energy in eV of bond-centred interstitials relative to the corresponding $\langle 0\,0\,1\rangle$-split interstitial. The energies of all charge states of the nitrogen and carbon interstitials are lower in the $\langle 0\,0\,1\rangle$-split interstitial configuration.

A negatively charged di-vacancy is an interesting candidate for the 594 nm defect. Since the defect is only seen in type-I diamond we would expect it to be negatively charged. The negative di-vacancy (V_2^-) has been identified in EPR (W29) [21] and has very similar annealing behaviour to the 594 nm defect [16, 22]. Difficulties with this assignment are that to be participating in charge transfer with N_S^0 it must be accepting an electron, and there was no sign of a defect associated with the negative di-vacancy in this work.

That H1b has appeared as such a strong feature here in electron irradiated diamond and much stronger still in neutron irradiation diamond (see chapter 7) implies it exists in a relatively high concentration. However both H1b and H1c have very low Huang-Rhys factors of $S \approx 0.1$ [16] with almost all of their absorption intensities in their ZPLs. It is therefore likely that we are extremely sensitive to their detection. If the photochromic change of H1b corresponded to a charge transfer of 400 ppb of $N_S^0 \rightarrow N_S^+$, as discussed above as the maximum possible, the corresponding calibration constant for H1b would be $\sim 6.5 \times 10^{-17}$ meV cm^2.

6.4 Improvements in the EPR parameters of N_2V^-

The use of ^{15}N-doped diamond was critical to the first correct identification of N_2V^- by EPR [6, 23]. The nuclear spin of ^{14}N is $I = 1$, resulting in a quadrupole interaction. The quadrupole causes mixing of the nuclear spin states, transferring intensity to forbidden transitions, increasing the number of observed transitions from 16 to 81. Together with the overlap of the central line of the $^{14}N_S^0$ spectrum, this precluded previous detection of N_2V^- in samples of natural isotopic abundance.

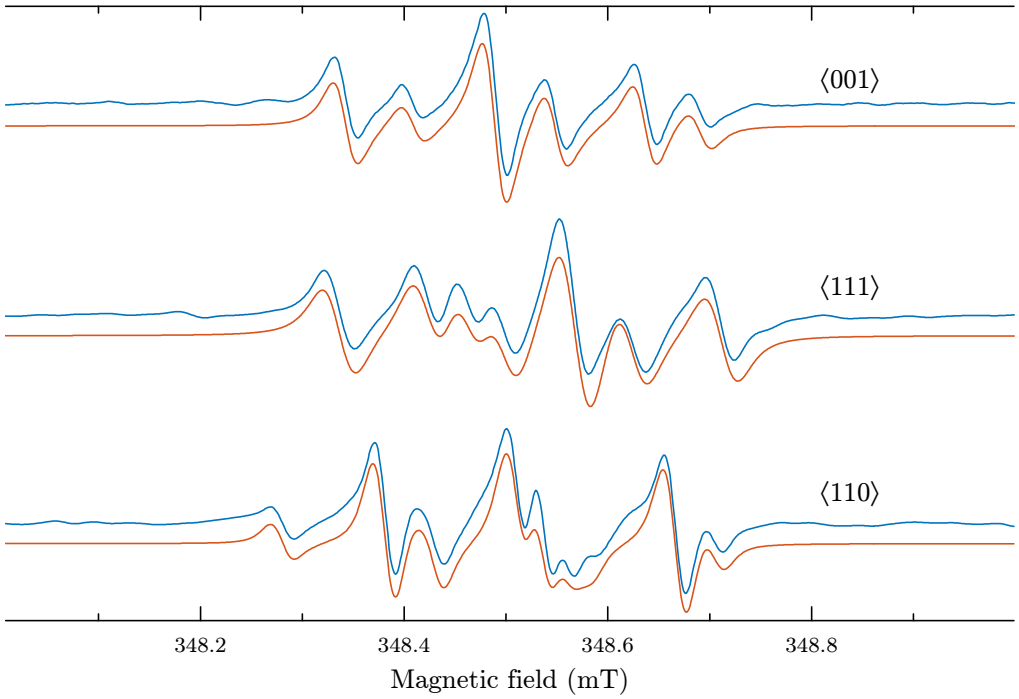

Figure 6-8 EPR spectra of N_2V^- in ^{15}N diamond with $\boldsymbol{B}$ along $\langle 0\,0\,1\rangle$, $\langle 1\,1\,1\rangle$ and $\langle 1\,1\,0\rangle$ directions. For each direction the experimental spectrum with $^{14}N_S^0$ subtracted is above while the N_2V^- simulation is below.

The ^{15}N nitrogen hyperfine was determined by Green to be non-axial with an isotropic component of +4.02 MHz [23], indicating effectively zero unpaired spin density in the nitrogen $2s2p$ orbitals. The dipolar component was found to have an interaction strength, b, of −0.46 MHz. This result is in remarkable agreement with the simple calculation of a dipolar interaction between the unpaired electron

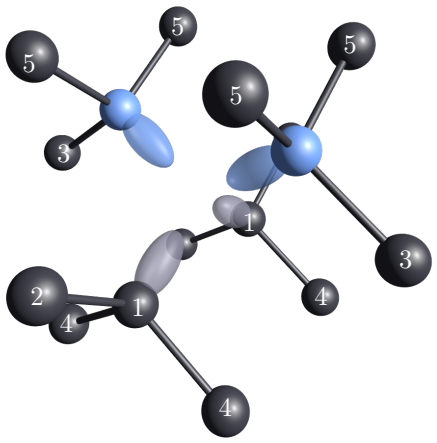

Figure 6-9 Diagram of N_2V in one of its six sites. Distinct carbon atoms are labelled.

spin and a ^{15}N nucleus at the next nearest neighbour distance, r, of 2.52 Å. The interaction is given by

$$b = \frac{\mu_0}{4\pi} \frac{g_e \mu_B g_n \mu_n}{h} \left\langle \frac{1}{r^3} \right\rangle \tag{6-19}$$

with the result $b = -0.50$ MHz for a nitrogen nucleus. Example experimental spectra of $^{15}N_2V^-$, compared with simulations from the derived values, are shown for the three principle axes in figure 6-8.

6.4.1 ^{13}C hyperfine interaction

In the work by Green an initial estimate of the strength of the nearest-neighbour (labelled 1 in figure 6-9) ^{13}C hyperfine interaction was made by considering the similar case of the vacancy [23]. For both V^0 and V^- the hyperfine interactions are along $\langle 1\,1\,1 \rangle$, and have a similar ratio between A_s and A_p of approximately 3 and 4 respectively, implying the same to be true for other vacancy cage-type defects. The hyperfine interaction from V^- was therefore taken and doubled to account for the spin density being localised over two atoms rather than the four in V^-.

The resulting N_2V^- simulation predicted the position of the transitions in the spectrum to be outside the $^{15}N_S^0$ transitions for the magnetic field along $\langle 1\,1\,1 \rangle$. A scan taken over approximately fourteen days with the magnetic field along $\langle 1\,1\,1 \rangle$

successfully resolved ^{13}C lines, identified by their 1:2:1 structure. Assuming the ratio between A_s and A_p to be the same as for V^- the hyperfine was estimated as $A_s \approx 214\,\text{MHz}$ and $A_p \approx 52\,\text{MHz}$.

The discovery of large thermochromic increases in the concentration of N_2V^- has since allowed improvements in EPR signal intensity. In the same sample, the SNR achieved after fourteen days was achieved in only two to three days after heat treatment. Spectra, which clearly resolved the ^{13}C hyperfines, were subsequently recorded with the magnetic field along the $\langle 0\,0\,1\rangle$ and $\langle 1\,1\,0\rangle$ directions allowing determination of the hyperfine anisotropy; the final Hamiltonian parameters, compared with the estimates, are given in table 6-6.

Parameter	Value (MHz)	Direction	Reference
$A_\parallel$	318	$[\bar{1}\,1\,1]$	[23]
$A_\perp$	162	$[\bar{1}\,\bar{1}\,1]$	
$A_\parallel$	317.5(50)	2.0(5)° from $[\bar{1}\,1\,1]$	This work
$A_\perp$	202.3(50)	$[\bar{1}\,\bar{1}\,1]$	

Table 6-6 Spin Hamiltonian parameters for the $^{13}C_1$ hyperfine interaction with N_2V^-.

Experimental scans along with the simulations of N_2V^- are shown in figure 6-10 where the ^{13}C transitions are visible, including those under the $^{15}N_S^0$ hyperfines. It should be noted that the symmetry of N_2V^- with a nearest-neighbour ^{13}C is $\mathscr{C}_{1h}$. This creates the site intensities $8, 4$ for the magnetic field along $\langle 0\,0\,1\rangle$, $6, 3, 3$ for $\langle 1\,1\,1\rangle$ and $4, 2, 4, 2$ for $\langle 1\,1\,0\rangle$. The nitrogen hyperfine anisotropy, however, is very small compared to that of the ^{13}C and as such we effectively see a $\mathscr{C}_{3v}$ symmetry with site intensities 4 for $\langle 0\,0\,1\rangle$, $1, 3$ for $\langle 1\,1\,1\rangle$ and $2, 2$ for $\langle 1\,1\,0\rangle$.

The unpaired electron probability density on each nearest-neighbour ^{13}C can be calculated from experimental results using standard tables and methods [24, 25]. The unpaired electron wave function can be written as the linear combination of atomic orbitals

$$\Psi = \sum_j \eta_j \psi_j \,, \quad \psi_j = \alpha_j \left(\phi_{2s}\right)_j + \beta_n \left(\phi_{2p}\right)_j \,,$$

where ψ_j is a hybrid $2s2p$ atomic orbital at the j^{th} site, α_j and β_j are the $2s$ and

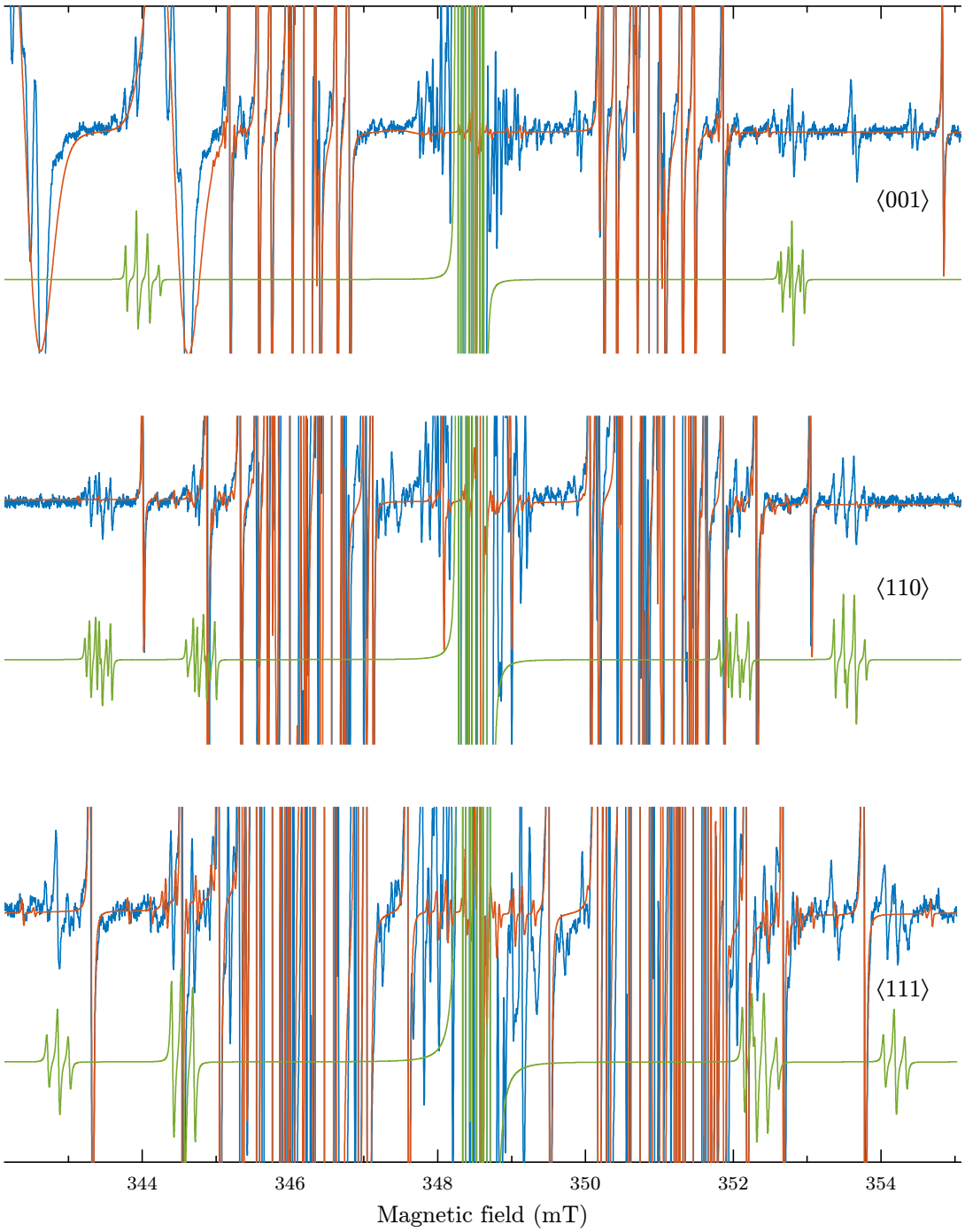

Figure 6-10 EPR spectra of SYN339 with a microwave frequency of approximately 9.74 GHz and $\boldsymbol{B}$ along ⟨0 0 1⟩, ⟨1 1 0⟩ and ⟨1 1 1⟩ directions highlighting the ^{13}C hyperfines of N_2V^-. A combined simulation of $^{14}N_S^0$, $^{15}N_S^0$, $^{15}N_S^0$, NV^- and N_2V^- is overlaid over the experiment and the simulation of N_2V^- offset below. The ⟨1 1 1⟩ spectrum was recorded by Green [23].

$2p$-type characters and η_j is the total electron localisation. Normalisation requires that

$$\alpha_j^2 + \beta_j^2 = 1$$
$$\sum \eta_j^2 = 1 \, .$$

The fraction of unpaired electron population on site j in a $2s$ orbital is given by $\alpha_j^2\eta_j^2$ and in a $2p$ orbital by $\alpha_j^2\eta_j^2$. The axial hyperfine parameters $A_\parallel$ and $A_\perp$ are related to s-type and p-type contributions, denoted a_j and b_j respectively, by

$$\begin{aligned} A_\parallel &= a_j + 2b_j \\ A_\perp &= a_j - b_j . \end{aligned} \tag{6-20}$$

a_j and b_j are determined by

$$a_j = a^* \alpha_j^2 \eta_j^2$$
$$b_j = b^* \beta_j^2 \eta_j^2 \, ,$$

where a^* and b^* are the isotropic and anisotropic hyperfine parameters respectively for the given nucleus. a^* and b^* are tabulated by Morton and Preston for the most common nuclei: for ^{13}C, $a^* = 3777\,\text{MHz}$ and $b^* = 107.4\,\text{MHz}$ [24]. From equation (6-20) and the ^{13}C hyperfine values in table 6-6, $a_C = 240.7\,\text{MHz}$ and $b_C = 38.4\,\text{MHz}$, giving $\alpha_C^2 = 15\,\%$, $\beta_C^2 = 85\,\%$ and for each nearest-neighbour carbon atom $\eta_C^2 = 42\,\%$. Thus the unpaired electron probability density is highly localised on the two carbon atoms.

Additional ^{13}C hyperfine interactions can be observed in figure 6-10 around the central structure. These correspond to the next nearest-neighbour sites indicated by labels 2-5 in figure 6-9. Although an attempt could have been made to fit these interactions from the current data, to accurately determine this interaction ENDOR experiments would be more appropriate.

6.4.2 ^{14}N Quadrupole interaction

With the ^{15}N and ^{13}C hyperfine parameters accurately determined for $^{15}N_2V^-$ it is straight forward to create a simulation for $^{14}N_2V^-$: the ^{15}N hyperfine parameters

only need scaling by the ratio of the isotopic nuclear g-values, leaving the ^{14}N quadrupole interaction as the only unknown parameter. A correlation has previously been shown between the size of the quadrupole interaction and the electron localisation in the $2p$ orbital on the ^{14}N nucleus for a number of defects in diamond [26]. Using an electron localisation of the $2p$ orbital of 0 % on the ^{14}N nucleus, the quadrupole of N_2V^- was estimated to have $P_\parallel = -5.2$ MHz. As is the case with similar defects, it is expected that this interaction is aligned along $\langle 1\,1\,1 \rangle$.

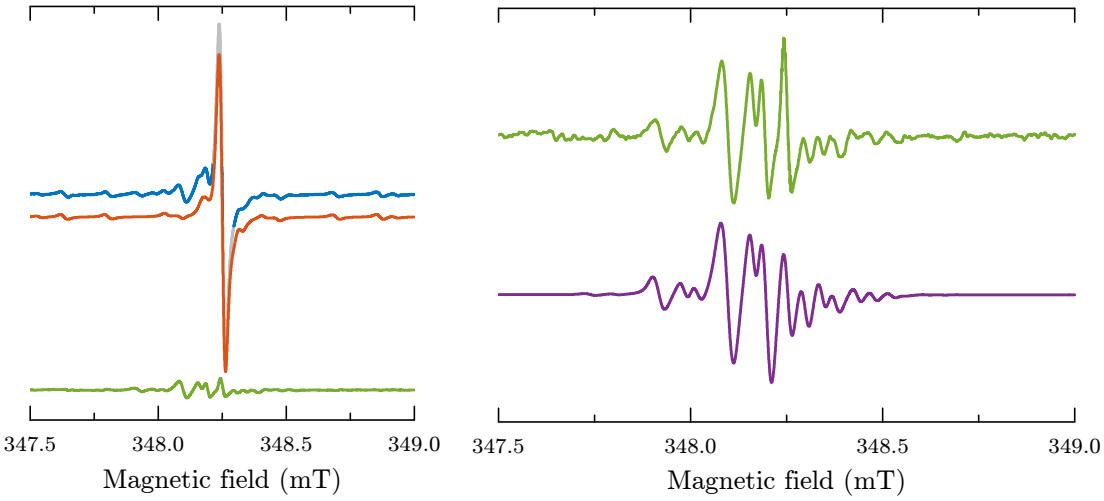

Figure 6-11 N_2V^- EPR in diamond with nitrogen in natural isotopic abundance. On the left is the experiment spectrum (top), a simulation of N_S^0 and a single line at $g = 2.002\,69$ (middle) and the corresponding residual (bottom). On the right is the residual (top) and N_2V^- simulation (bottom).

In an attempt to identify N_2V^- in diamond of natural nitrogen isotopic abundance, an HPHT-grown diamond, initially with approximately 80 ppm of N_S^0, was subjected to the treatment described in section 6.1. An EPR spectrum of the central hyperfine of N_S^0 with the magnetic field along $\langle 0\,0\,1 \rangle$ is shown in figure 6-11. To extract the N_2V^- spectrum one of the outer hyperfine lines of N_S^0 was subtracted from the central hyperfine, along with a single line at $g = 2.00269$.

Simultaneous fitting of the $\langle 0\,0\,1 \rangle$ spectrum and a $\langle 1\,1\,0 \rangle$ spectrum yielded a best-fit value of $P_\parallel = -5.0$ MHz, in close agreement with the previous estimate. The angle of the interaction was tilted from the $[1\,1\,1]$ axis while remaining in the $(1\,\bar{1}\,0)$ plane, but no improvement was found in the quality of the fit. The simulation of N_2V^- on the right in figure 6-11 clearly fits the experimental spectrum. The

ability to simulate N_2V^- allows its quantification in diamond of natural nitrogen isotopic abundance.

6.5 Conclusions

Charge transfer has been observed involving a large number of defects in irradiated and annealed diamond, including N_S, NV, N_2V, H1b and the 594 nm defects. There was a remarkable colour change of the diamond associated with the charge transfer. By HPHT treating type-Ib diamond to aggregate the majority of nitrogen into N_{2S} (85(5) ppm in N_{2S} out of 110(5) ppm), subsequent irradiation created a large concentration of N_2V (2.4(1) ppm of N_2V versus 3.9(1) ppm of NV). N_2V is a major product resulting from irradiating and annealing type-IaA diamond.

Charge transfer was driven one way by heating the sample at 550 °C, and reversed by illumination with 3.061 eV light. FT-IR, UV-vis and EPR spectroscopy experiments were performed after the heat and illumination treatments. With the sample kept in the dark the change induced by the heat treatment was found to be stable whilst that induced by the optical treatment was unstable, recovering over the course of hours.

The ZPL absorptions from NV^- and N_2V^- have been correlated with their EPR signals, allowing the determination of optical calibration constants. Furthermore, charge transfers between NV^0 and NV^- and between N_2V^0 and N_2V^- have been characterised to determine the ratios of oscillator strengths. Together with the calibration constants for NV^- and N_2V^-, this has allowed the determination of optical calibration constants for NV^0 and N_2V^0. All calibration constants determined here agree well with previous calibration constants arrived at by indirect methods.

The recovery rates of defects after illumination has been investigated with EPR spectroscopy. The recoveries of N_S^0, NV^- and N_2V^- could all be broadly described by two exponentials corresponding to a fast process and a slow process. The fast process agrees well with direct charge transfer with N_S but the slow process required a more complicated mechanism. The possible relationship between H1b

and the 594 nm defect have been discussed, although the structure of both defects remain unidentified.

Despite the observation of photochromism, likely corresponding to a charge transfer, no EPR signals were seen which could be attributed to either H1b or the 594 nm defect. Possible explanations for a paramagnetic defect to not be observed are that the defect motionally averages between two symmetries on the EPR timescale, significantly broadening the lineshape, or there is a very large zero-field splitting. Alternatively it is possible that the photochromism is due to a double charge transfer, with neither charge state EPR active, or there is no charge transfer and it is the result of a reconfiguration of the defect. The majority of charge transfer with N_S was accounted for by changes in NV and N_2V. Considering errors, of a 1.6(4) ppm change in N_S^0 between illumination and heat treatments, up to 0.4 ppm could correlate to changes in H1b and the 594 nm defect. A lower bound for the H1b calibration constant was estimated as $f_{\mathrm{H1b}} \sim 6.5 \times 10^{-17}\,\mathrm{meV\,cm^2}$.

Improvements have been made in the spin Hamiltonian of N_2V^-, mitigated by improvements in signal caused by driving charge transfer. The nearest neighbour ^{13}C hyperfine interaction for N_2V^- has been fully characterised allowing the unpaired electron density on the carbons adjacent to the vacancy (labelled '1' in figure 6-9) to be determined at $\approx 85\,\%$. With the nitrogen hyperfine parameters having previously been determined for $^{15}N_2V^-$, $^{14}N_2V^-$ has been identified in diamond of natural nitrogen isotopic abundance and the quadrupole interaction characterised.

6.6 Future work

Further investigation of H1b and the 594 nm defect is required. The energy dependence of their photochromism needs determining as does the dependence of their recovery on temperature. If a defect is present in more than one charge state at least one must be EPR active. If a charge state were to be identified by EPR a great deal of information about the structure could be discovered. A potential reason for the lack of an EPR signal is that the defects motionally average, significantly broadening their EPR resonances; motional averaging could be frozen out

by applying stress to the sample. Samples containing the optical lines should also be investigated at various temperatures, at higher frequencies and with optical excitation.

References

1. D. Twitchen et al., *Diamond and Related Materials* **8**, 1572–1575 (Aug. 1999).
2. N. Manson, J. Harrison, *Diamond and Related Materials* **14**, 1705–1710 (Oct. 2005).
3. R. U. A. Khan et al., *Journal of Physics: Condensed Matter* **21**, 364214 (Sept. 2009).
4. Y. Mita et al., *Journal of Physics: Condensed Matter* **2**, 8567–8574 (1990).
5. A. T. Collins, *Journal of Physics: Condensed Matter* **14**, 3743–3750 (Apr. 2002).
6. B. L. Green et al., *Physical Review B* **92**, 165204 (2015).
7. G. Davies, M. F. Hamer, *Proceedings of the Royal Society of London A* **348**, 285–298 (1976).
8. G. Davies, *Journal of Physics C: Solid State Physics* **9**, L537 (1976).
9. S. C. Lawson et al., *Journal of Physics: Condensed Matter* **4**, 3439–3452 (1992).
10. S. Liggins et al., *Physical Review B* **81**, 085214 (Feb. 2010).
11. G. Davies, *Physica B: Condensed Matter* **273-274**, 15–23 (1999).
12. N. R. S. Reddy, E. R. Manson, N B]Krausz, *Journal of Luminescence* **38**, 46–47 (1987).
13. R. G. Farrer, *Solid State Communications* **7**, 685–688 (1969).
14. J. Rosa et al., *Diamond and Related Materials* **8**, 721–724 (1999).
15. Y. Mita et al., *Diamond and Related Materials* **2**, 768–772 (Apr. 1993).
16. A. T. Collins, G. Davies, G. S. Woods, *Journal of Physics C: Solid State Physics* **19**, 3933 (1986).
17. E. Gaillou, E. Fritsch, F. Notari, *Diamond and Related Materials* **17**, 2029–2036 (2008).
18. G. Davies, M. H. Nazare, *Journal of Physics C: Solid State Physics* **13**, 4127–4136 (Aug. 1980).
19. S. Breuer, P. Briddon, *Physical Review B* **51**, 6984–6994 (Mar. 1995).
20. J. Goss et al., *Physical Review B* **70**, 235208 (2004).

21. J. Kirui, J. van Wyk, M. Hoch, *Diamond and Related Materials* **8**, 1569–1571 (Aug. 1999).

22. J. K. Kirui, J. a. Van Wyk, M. J. R. Hoch, *Diamond and Related Materials* **39**, 78–81 (2013).

23. B. L. Green, PhD thesis, University of Warwick, 2013.

24. J. R. Morton, K. F. Preston, *Journal of Magnetic Resonance (1969)* **30**, 577–582 (1978).

25. G. D. Watkins, J. W. Corbett, *Physical Review* **121**, 1001–1014 (1961).

26. O. D. Tucker, M. E. Newton, J. M. Baker, *Physical Review B* **50**, 15586–15596 (Dec. 1994).

7

Annealing of neutron irradiated type-Ib diamond

7.1 Introduction

Emerging applications of diamond for quantum information processing and sensing require that we engineer defects with optimised properties, such as location, orientation and an environment free of parasitic impurities [1, 2]. To engineer defects we must first understand their formation, migration, dissociation and aggregation into larger complexes. With the possible exception of hydrogen, the most common impurity in diamond is nitrogen and thus, over the years, a significant body of work has been devoted to understanding the annealing processes involved in the aggregation of nitrogen in diamond (see §2.3). Many of the defects important to nitrogen aggregation have been identified and can now be quantified by a combination of IR absorption, UV-vis absorption and EPR spectroscopies.

Ion implantation provides a route to creating addressable arrays of defects or shallow defects [3]. Ion implantation causes very different damage to the diamond lattice than irradiation with electrons. An incident high energy electron usually only has sufficient energy to displace one or two atoms, however for ion implantation the added mass of the ion increases the transfer efficiency, potentially creating a cascade of damage. This cascade might lead to an assortment of vacancy and

interstitial complexes along ion tracks.

Characterising the annealing of ion implantation damage presents challenges as the damage is not homogeneous through the bulk of the diamond. Rather, for example, the damage is concentrated in a layer less than 60 nm deep for 30 keV nitrogen ion implantation [4]. The effective 'damaged' sample volume is very small. One solution is to 'simulate' ion implantation damage with neutron irradiation. For a collision of two hard spheres of masses m and M, the maximum transfer energy from one to the other (in a head on collision) is given by equation (3-38). For a head on collision the transfer efficiency reaches 100 % when $m = M$. A typical neutron emitted from the fission of ^{235}U has energy 1 MeV [5], giving $T_{max} = 284$ keV for a collision with a carbon atom. The interaction cross section of neutrons with diamond is small, so that the effect of neutron irradiation is to create energetic carbon ions, and hence cascade damage, homogeneously through the diamond [6]. This bulk damage allows investigation by various spectroscopic techniques.

A second motivation for specifically studying neutron damage in diamond is that it makes very large concentrations of radiation damage defects, facilitating investigation by spectroscopic techniques. For electron irradiation at available fluxes a typical damage rate might be 0.5 ppm V h^{-1}, so creating large concentrations of the order of 100 ppm would be very expensive. Such concentrations are however easily possible with neutron irradiation. Thus, damage concentrations comparable to the nitrogen concentration in a typical ungettered HPHT-grown diamond are achievable.

7.2 Neutron damage of diamond

7.2.1 Neutron damage versus electron damage

To displace an atom from the lattice, an energy greater than the displacement threshold energy, T_d, must be supplied to it. T_d has been determined for diamond in a number of studies together giving a range of values, from low estimates of 32 eV

estimated from the carbon-carbon bond energies, to 80 eV by observing optical absorption spectra after irradiation [7]. Bourgoin and Massarani determined, by measuring conductivity after series of irradiations, that $T_d = 35(5)$ eV [8]. Koike, Parkin and Mitchell observed the formation of defect clusters during irradiation in a transmission electron microscope and determined that $T_d = 37.5(12)$ eV for electrons incident on $\langle 0\,0\,1 \rangle$, $T_d = 45.0(13)$ eV for electrons incident on $\langle 1\,1\,1 \rangle$ and $T_d = 47.6(13)$ eV for electrons incident on $\langle 1\,1\,0 \rangle$ [9]. In line with similar studies a value of 40 eV has been used here [10].

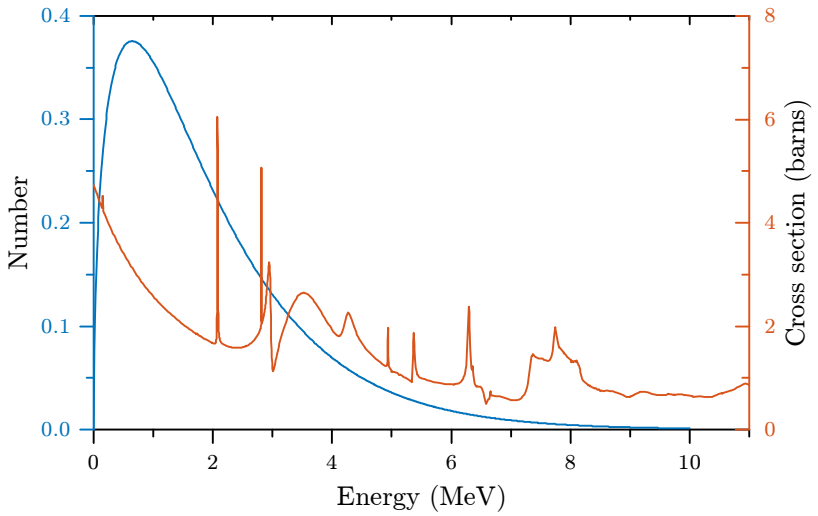

Figure 7-1 Energy spectrum of ^{235}U [5] and the elastic scattering interaction cross section with carbon [11].

When a high energy neutron interacts with a carbon atom it transfers a proportion of its energy to it, likely sufficient to displace it from its lattice site and leave it highly energetic. The neutron will most probably leave the crystal without further interaction; the carbon ion on the other hand is likely to be charged giving it a much larger interaction cross section. It will cause further knock-on displacements of more carbon atoms in the vicinity of the first interaction, which themselves cause further displacements and so on, giving rise to a cascade of damage. The interaction of a 1 MeV neutron in the diamond will on average result in 150 displacements [6], not considering interstitial-vacancy recombination during irradiation. The homogeneity of the damage through the whole diamond depends on the localisation of the cascade damage; whether there is a significant overlap in cascades or the damage exists in isolated clusters.

When a charged particle travels through a material it loses the majority of its energy to ionisation and the creation of electron-hole pairs [12]. This loss of energy causes charged particles to have a short range in solids. Neutrons have a much smaller interaction cross section than charged particles. Taking the interaction cross section of 2.5 barns for a 1 MeV neutron, from equation (3-35), 95.7 % of neutrons will pass through 1 mm of diamond without interacting. From those that do interact the distribution of interaction through the diamond will be nearly uniform. 1 MeV electrons on the other hand will typically penetrate only 1–2 mm into diamond [12], potentially giving rise to a very non-uniform interaction.

7.2.2 Modelling the damage

Neutron damage can be modelled as two separate parts: first, the interaction of the neutron with the lattice to create an energetic carbon ion; second, the cascade caused by that ion with the lattice. Ion damage is a well studied problem and can be modelled with SRIM (The Stopping and Range of Ions in Matter), software which has been in development since the 1980s [13]. SRIM is largely focused towards the analysis of ion beams incident on the surfaces of materials and does not directly support neutron beams. It does however allow the input of a list of energies, positions and vectors of ions resulting from interactions with particles in the bulk. The resulting cascade damage from each ion can then be evaluated.

Mainwood [6] used SRIM to calculate the distribution of the cascade damage for 1 MeV neutrons with a cross section of 2.5 barns. This was then convolved with the profile of the neutron interaction rate of 0.44 cm^{-1}, giving a total vacancy production rate of 68(7) $\mathrm{V\,n^{-1}\,cm^{-1}}$. The recombination of vacancy and interstitial pairs was argued to cause a significant reduction in the damage produced, which can be accounted for by atoms displaced with less than 173(30) eV recombining [14]. Adding 173 eV to the displacement threshold energy gave the vacancy production rate 16(7) $\mathrm{V\,n^{-1}\,cm^{-1}}$.

7.2.3 New simulations

A similar approach to Mainwood was used here, however the interaction of each individual neutron was considered independently. To handle the neutron-diamond interaction a program was written in the C programming language. The inelastic scattering cross section of fast neutrons (< 10 MeV) is relatively small and we can safely approximate the interaction as only consisting of the elastic cross section, thus modelling it as hard-sphere collisions. The program first created a particle with energy drawn from the probability distribution given in figure 7-1. It then sampled the energy dependent elastic cross section (also shown in figure 7-1) and used equation (3-35) to determine the depth at which an interaction occurred. A transverse position and scattering angle were then drawn from probability distributions. The scattering angle was used with equation (3-37) to calculate the energy transfer.

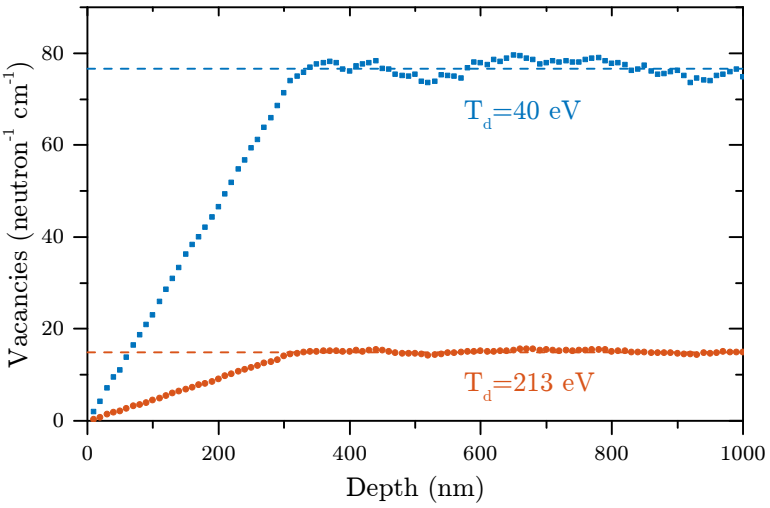

Figure 7-2 Simulated vacancy production rates versus depth from neutron irradiation of diamond. The increase for the first 300 nm corresponds to the length of individual damage cascades. T_d = 40 eV was used to calculate the number of initially displaced atoms, and T_d = 213 eV to calculate the number which are displaced with sufficient energy that they do not immediately recombine [6].

The resulting list of carbon ions created with their positions and velocity vectors was then input into SRIM-2013 which calculated the damage distribution for each ion individually. A displacement threshold energy of T_d = 40 eV was used to account for straight forward displacement; T_d = 213 eV was used to account

for the requirement for atoms to have at least 173 eV of kinetic energy after being displaced to not immediately recombine [6]. Figure 7-2 shows the vacancy distribution versus depth from 360 000 cascades simulated in SRIM. The vacancy production rates once constant are $77(10)\,\mathrm{V\,n^{-1}cm^{-1}}$ for $T_d = 40\,\mathrm{eV}$ and $15(2)\,\mathrm{V\,n^{-1}cm^{-1}}$ for $T_d = 213\,\mathrm{eV}$. For a dose of $10^{18}\,\mathrm{n\,cm^{-2}}$ the latter rate corresponds to a vacancy concentration of 85(11) ppm.

Each cascade consists of a few well separated events with the majority of damage at the end when the carbon ions have less energy and a higher cross section. For the moment though lets consider that the damage is homogeneously distributed through the volume of each cascade. The cascade volume can be approximated by a cone which, from the SRIM simulations, has height 300 nm and radius 30 nm, giving a volume of $2.8 \times 10^5\,\mathrm{nm^3}$. There are 3.5×10^{15} such volumes in $1\,\mathrm{cm^3}$. If neutrons interact at a rate of $0.44\,\mathrm{cm^{-1}}$ a dose of $10^{18}\,\mathrm{n\,cm^{-2}}$ creates 4.4×10^{17} cascades in a $1\,\mathrm{cm^3}$ volume. Thus there should be significant overlap between cascades. As the routine produces the three-dimensional distribution of vacancies, future analysis can characterise the inhomogeneity of the cascades and better assess the homogeneity of the total damage.

7.3 Experimental details

Three neutron irradiated type-Ib HPHT-grown diamonds have been subjected to an isochronal annealing study. IR absorption and EPR spectra were recorded of each sample after each annealing stage. UV-vis absorption spectroscopy was attempted, however nearly all absorptions of interest were too strong to obtain a sufficient signal. Type-IIa CVD-grown samples were also neutron irradiated, allowing a comparison to be made with the type-Ib diamonds.

7.3.1 Annealing

Samples were annealed in a tube furnace for four hours at each annealing stage. The furnace was continuously purged with dry nitrogen (boil off from liquid ni-

trogen storage) for all annealing stages to minimise graphitisation. For anneals of 1000 °C and above the samples were additionally buried in diamond grit as sacrificial protection. The final anneal of sample Ib-A at 1600 °C was made in an evacuated tube furnace at De Beers Technologies (UK).

7.3.2 IR absorption spectra

After each annealing step FT-IR spectra were recorded at room temperature over the range 370–12 000 cm^{-1}. The spectrometer was continuously purged with dry nitrogen to minimise the absorption from atmospheric water and carbon-dioxide. After mounting samples, at least five minutes were allowed for the spectrometer to purge sufficiently. Spectra over the range 370–4000 cm^{-1} were recorded with a glowbar source and KBr beamsplitter. Spectra over the range 4000–12 000 cm^{-1} were recorded with a tungsten filament source and quartz beamsplitter. A beam condenser was used to focus the light onto the sample with a spot diameter of approximately 1 mm.

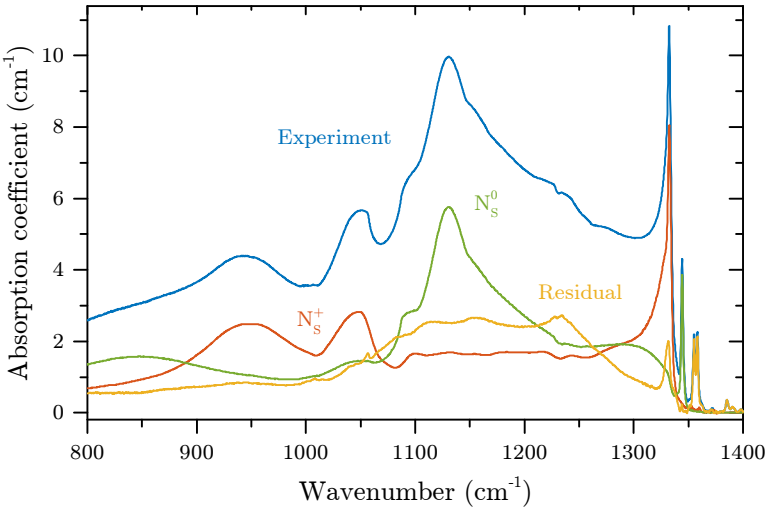

Figure 7-3 Example fit to one-phonon spectrum of sample Ib-A after 900 °C anneal. N_S^0 has been fitted to the 1344 cm^{-1} LVM and N_S^+ has been scaled to account for the distinctive absorptions at 950 cm^{-1} and 1040 cm^{-1}.

Spectra were analysed using the SpectrumManipulator software described in §5.1.1. The resulting spectra were calibrated by fitting to an intrinsic diamond spectrum which had previously been scaled to have an absorption coefficient of 12.7 cm^{-1} at

2000 cm^{-1}. The only baseline applied to IR absorption spectra as displayed was a flat offset. Concentrations from the one-phonon absorption were determined by fitting calibrated spectra to the experimental data, an example of which is shown in figure 7-3. Not all absorption in the one-phonon region could be accounted for with absorption from N_S^0, N_S^+ and N_{2S} so the fit was based on the minimisation of features rather than the sum of squares (§5.1.3). The intensity of LVMs and ZPLs were determined by fitting to a Voigt lineshape.

7.3.3 EPR spectra

EPR spectra were recorded of all samples at room temperature after each annealing step to quantify the N_S^0, NV^- and N_2V^- in the sample, as well as to look for and characterise other defects of interest. To quantify defects the signal intensity was compared with that of a previously characterised reference sample. The reference sample was a small diamond with 270(14) ppm of N_S^0, determined by FT-IR spectroscopy, cut from a single sector of a HPHT-grown diamond. The quantification of NV^- was made from the $\Delta m_s = \pm 2$ transitions for reasons discussed in §5.2.7.3.

7.3.4 Sample details

The type-Ib diamonds which were neutron irradiated were grown by the HPHT method resulting in $[N_S^0]_{initial} > 200$ ppm. They were cut and polished into cuboids of approximate dimension $4 \times 2 \times 1\,mm^3$. The optical measurements were made through the centre of the largest face which was approximately {0 0 1} oriented. The type-IIa diamonds were polished CVD plates of approximate dimension $4 \times 4 \times 0.5 mm^3$. The largest faces (the growth directions) were {0 0 1} oriented. The details of the samples are given in table 7-1.

Samples were neutron irradiated in the BigBeBe facility at Delft University of Technology. The source of neutrons at the facility is a pool-type research reactor using low-enriched ^{235}U as fuel. In BigBeBe the neutron flux is $1.5 \times 10^{13}\,n\,cm^{-2}\,s^{-1}$ over the range 1–1000 keV and $5.9 \times 10^{12}\,n\,cm^{-2}\,s^{-1}$ over the range 1–10 MeV. The

Name	Mass (mg)	$[N_s^0]_{initial}$ (ppm)	Dose (cm^{-2})	$[V]_{predicted}$ (ppm)
Ib-A	49	315(10)	1×10^{18} n	85(11)
Ib-B	52	268(10)	5×10^{17} n	43(5)
Ib-C	50	215(10)	2×10^{17} n	17(2)
IIa-A	47.1	0.093(9)	1×10^{18} n	85(11)
IIa-B	58.8	0.078(8)	1×10^{18} n	85(11)
IIa-C	34.6	0.038(4)	5×10^{17} n	43(5)
IIa-D	63.6	0.224(20)	2×10^{17} n	17(2)

Table 7-1 Samples used in this chapter with their masses for reference and irradiation details. The initial nitrogen concentrations were determined by the one-phonon absorption, except for the type-IIa samples for which rapid passage EPR was used. The predicted vacancy concentrations were deduced from the simulations in §7.2.3.

sample temperature during irradiation is approximated to have been 200 °C or less [15]. This is corroborated by no change being observed in optical spectra after annealing to 200 °C. After neutron irradiation the samples were completely opaque to the eye, except sample IIa-D, which was very dark green.

7.4 Results

A large number of spectra have been produced by this study, providing data on many defects. Some of the absorption features studied have previously been identified and, in the case of some defects, calibration constants are known. There are also a large number of features for which, although speculations have been made about their origin, the identity of the defects responsible are not known. Results from the IR and EPR spectroscopy are drawn together here to provide as complete a picture as possible about the processes occurring during annealing of these samples.

The largest irradiation damage to nitrogen content ratio was for sample Ib-A, causing its annealing curves to be clearest with the largest defect concentrations. Hence the results from that sample have been used whenever it is impracticable to display every annealing curve.

7.4.1 IR absorption

One-phonon absorptions in diamond have been well studied and characterised. Due to the symmetry of the lattice, one-phonon absorptions are not possible in intrinsic diamond - any one-phonon absorption must occur at a defect. One-phonon absorptions are seen in diamond for impurities which are heavier than the atoms of the host lattice and not tightly bonded. This includes N_S^0, N_S^+, N_{2S} and N_4V, all of which can also be quantified from the absorption from the calibration constants in table 5-1.

When the absorption occurs above the frequency $1332\,cm^{-1}$ the vibration responsible is above the phonon frequency range in diamond and localised in space and frequency. This occurs either as a result of the vibration being at a lighter atom than carbon (for example at a hydrogen atom), the bonding being tighter than that of the lattice (for example at an interstitial atom), or a combination of the two. Figure 7-4 shows example spectra of the one-phonon absorption and LVMs from sample Ib-A after each annealing stage.

Figure 7-5 shows the annealing curves for N_S^0, N_S^+, and N_{2S} for each sample. Before irradiation the only detectable one-phonon absorption was that from N_S^0, the quantification of which is given in table 7-1 for each sample.

7.4.1.1 One-phonon absorption

Irradiation created a significant concentration of vacancies. Nitrogen donates an electron to a vacancy in the charge transfer

$$N_S^0 + V^0 \rightarrow N_S^+ + V^-, \tag{7-1}$$

converting a significant proportion of the N_S^0 into N_S^+. It has previously been postulated that in an electron irradiated type-Ib diamond the concentration of N_S^+ is equivalent to the concentration of negative vacancies [16]. This assumes that there are no species other than single neutral vacancies accepting charge from N_S^0, an assumption which has not been tested in neutron irradiated diamond. The N_S^+ concentrations after irradiation were 134(20) ppm, 66(10) ppm and 26(4) ppm in

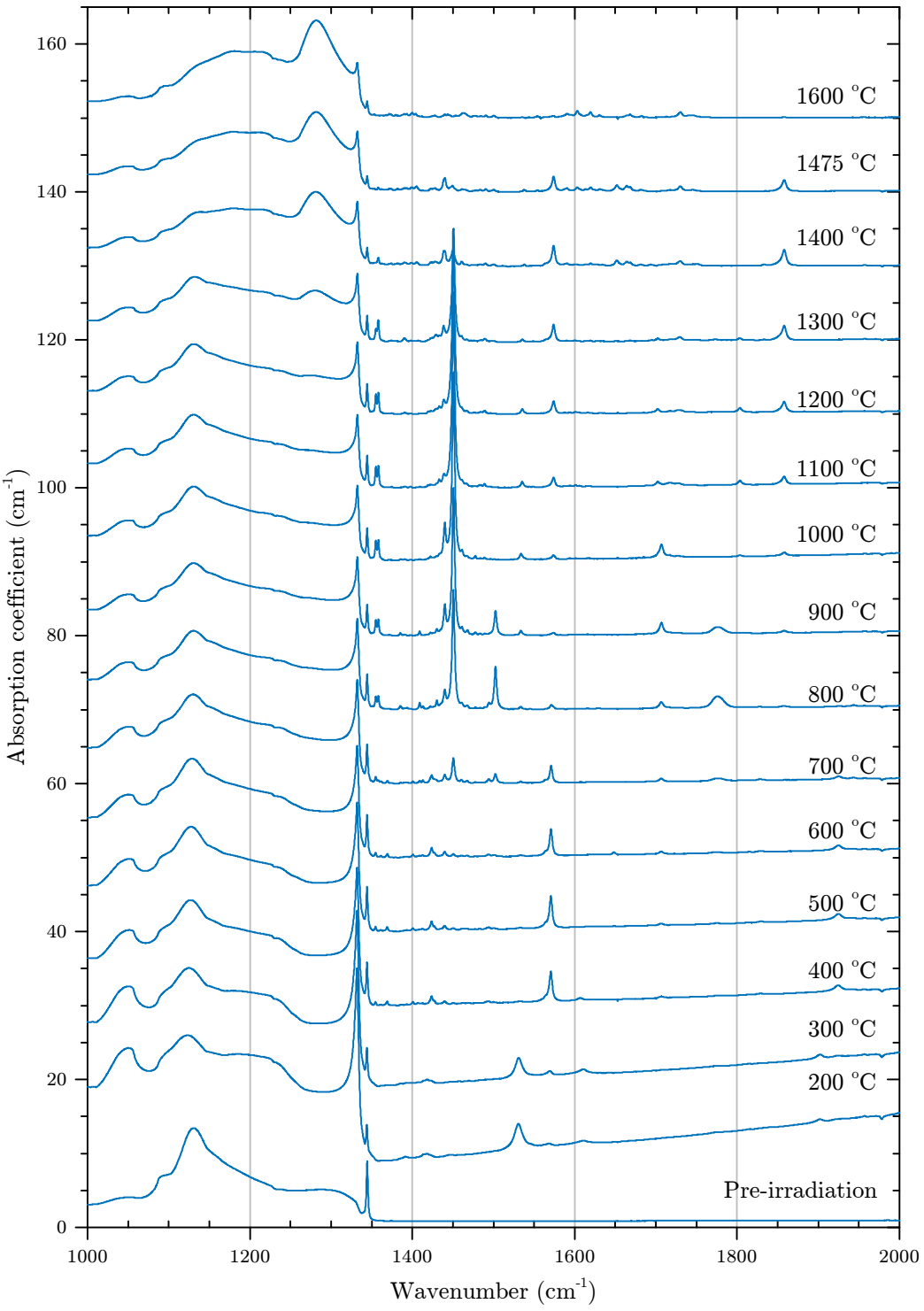

Figure 7-4 One- and two-phonon absorption for sample Ib-A after successive 4 h anneals from 200–1600 °C in 100 °C intervals. The intrinsic two-phonon diamond absorption has been subtracted and the spectra offset vertically.

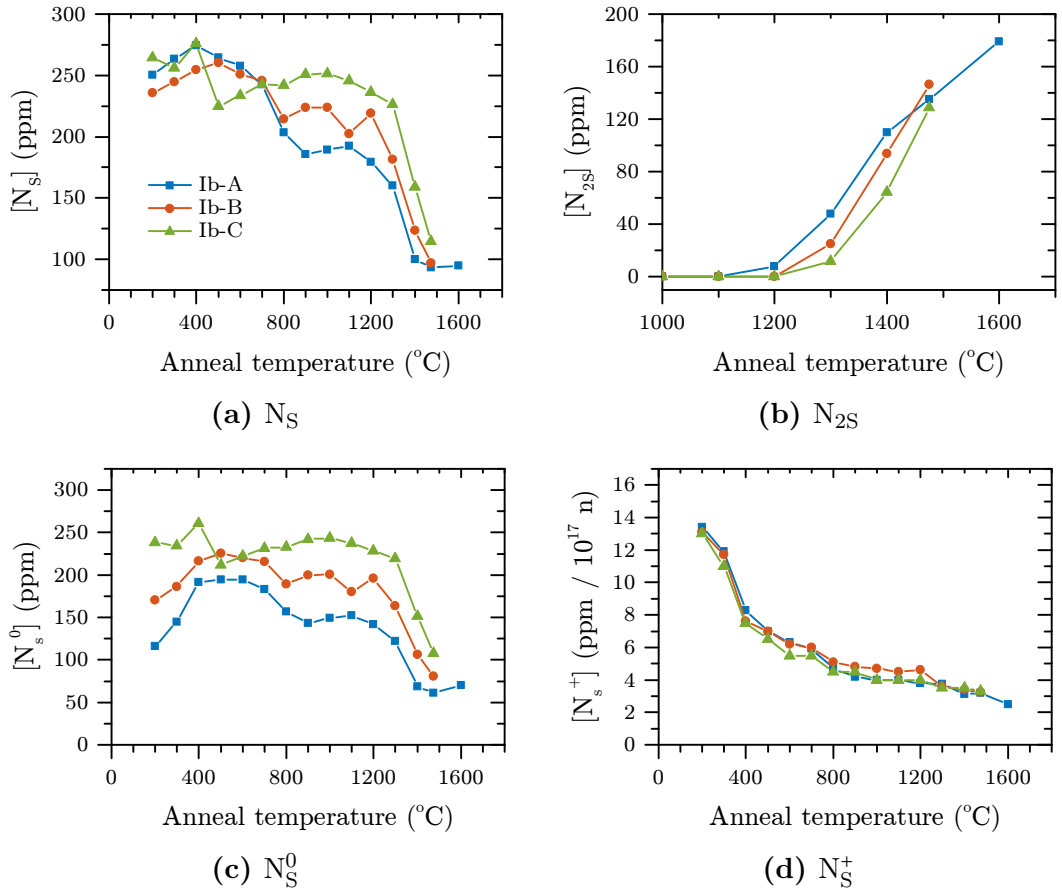

Figure 7-5 Concentration of nitrogen defects determined by one-phonon absorption. (a) is the sum of N_S^0 and N_S^+. (d) has been normalised to the neutron dose to illustrate the dose dependence. In (b) the initial increase is proportional to dose but then a different mechanism takes over.

samples Ib-A, Ib-B and Ib-C respectively. These concentrations scale well with the neutron dose. If they equate to the vacancy concentrations they are only a factor of 1.6 higher than those calculated in §7.2.3.

The changes in one-phonon absorption after annealing can be categorised as follows:

1. The first distinct change in the one-phonon absorption is after annealing to 400 °C, a temperature which would indicate the involvement of interstitials. A significant decrease (approximate halving) in $[N_S^+]$ is seen with a commensurate increase in $[N_S^0]$ in a charge transfer. The change in $[N_S^+]$ is proportional to the radiation dose.

2. The second change at 600–800 °C corresponds to the mobility of vacancies and the production of NV and N_{2I}. This is seen as a drop in total substitutional nitrogen (figure 7-5a); presumably the capture of vacancies and interstitials at N_S. A small drop occurs in $[N_S^+]$ implying a loss of acceptors.

3. The third significant change is the reduction in N_S^0, starting at 1300 °C, corresponding to the production of N_{2S}. The initial production of N_{2S} by annealing at 1300 °C was proportional to the irradiation dose. This dose dependence was lost in subsequent anneals, possibly with a shift to a dependence on N_S^0. In sample Ib-A, which was annealed to 1600 °C, although $[N_{2S}]$ increased, $[N_S]$ stayed constant.

The one-phonon spectrum could not be accounted for solely by N_S^0, N_S^+ and N_{2S}; there was a residual which had a consistent shape but reduced in intensity with each anneal. Neutron irradiation of type-IIa diamond creates a characteristic one-phonon spectrum [15] which has a different shape but similar annealing behaviour to the residual. An example of the residual after annealing at 900 °C can be seen in figure 7-3.

7.4.1.2 Local vibrational modes

To display the annealing behaviour and correlations between LVMs, the intensity plot in figure 7-6 has been constructed displaying the absorptions for sample Ib-A after each anneal. In the plot, colour denotes the logarithm to base 10 of the intensity of the absorption coefficient. Each spectrum has had the intrinsic diamond absorption removed and the data has been interpolated between annealing temperatures.

In neutron irradiated type-IIa diamond the strongest LVMs are at 1531 cm^{-1} and 1571 cm^{-1} [15]. In neutron irradiated type-Ib diamond they are joined by a host of other LVMs (For a review of previous work on LVMs important here see §2.2). The relative size of the LVMs can be seen in figure 7-4 where the 1450.8 cm^{-1} mode of N_{2I} dominates the spectra.

Immediately after irradiation 1531 cm^{-1} was the largest LVM until it annealed out

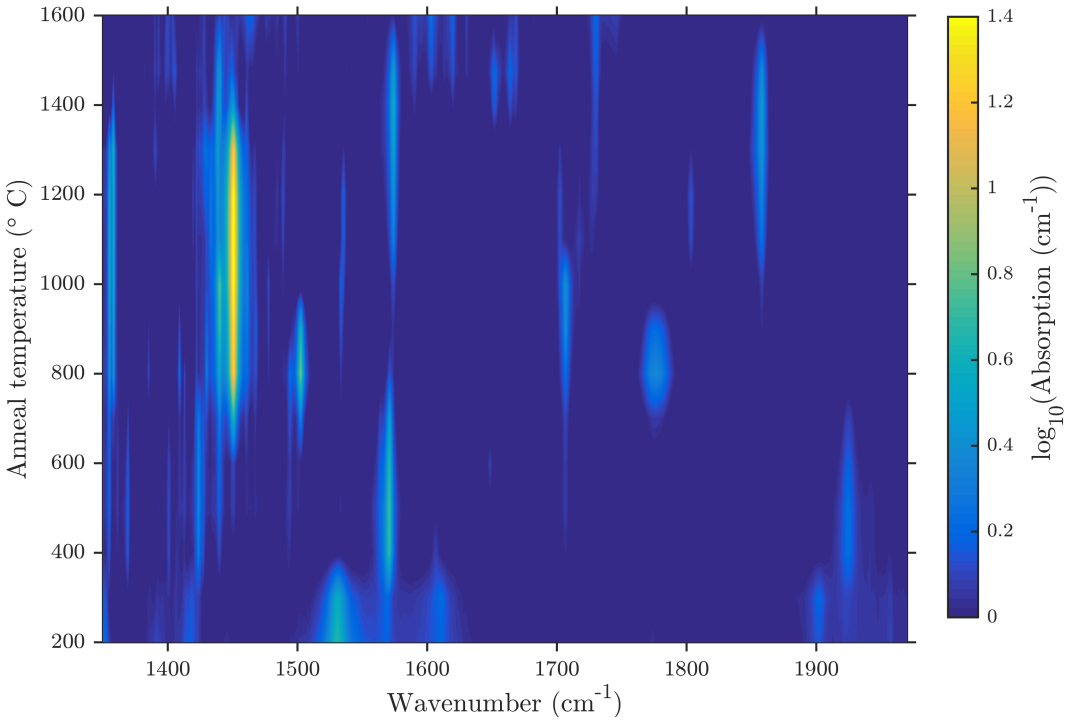

Figure 7-6 LVMs in sample Ib-A after successive 4 h anneals from 200–1400 °C in 100 °C intervals. The intrinsic two-phonon diamond absorption has been subtracted. Many LVMs can be seen annealing in and out allowing correlations between them to be made. The intensity gives the base 10 logarithm of the absorption coefficient.

during the 400 °C anneal. Since it is also seen in irradiated type-IIa diamond it does not involve nitrogen. Smaller modes at 1608 cm^{-1}, 1419 cm^{-1} and 1904 cm^{-1} also anneal out at the same temperature. As 1531 cm^{-1} anneals out the 1571 cm^{-1} mode anneals in, accompanied by a line at 1924 cm^{-1}, a cluster of lines between 1400 cm^{-1} and 1500 cm^{-1} (the strongest of which is 1424 cm^{-1}) and the beginning of the 1706 cm^{-1} LVM at a low intensity. All of the aforementioned lines anneal out between 600 °C and 800 °C, except 1706 cm^{-1}.

At around 700 °C, the 1706 cm^{-1} LVM starts to increase in intensity and new lines grow at 1450 cm^{-1}, 1502 cm^{-1} and 1776 cm^{-1}. The line at 1776 cm^{-1} is broader than all other LVMs with a FWHM of 17 cm^{-1} (compared to approximately 4 cm^{-1} for other lines). The lines at 1502 cm^{-1} and 1776 cm^{-1} are short lived, annealing out by 1000 °C. The 1706 cm^{-1} LVM continues to grow until it suddenly disappears after annealing at 1100 °C.

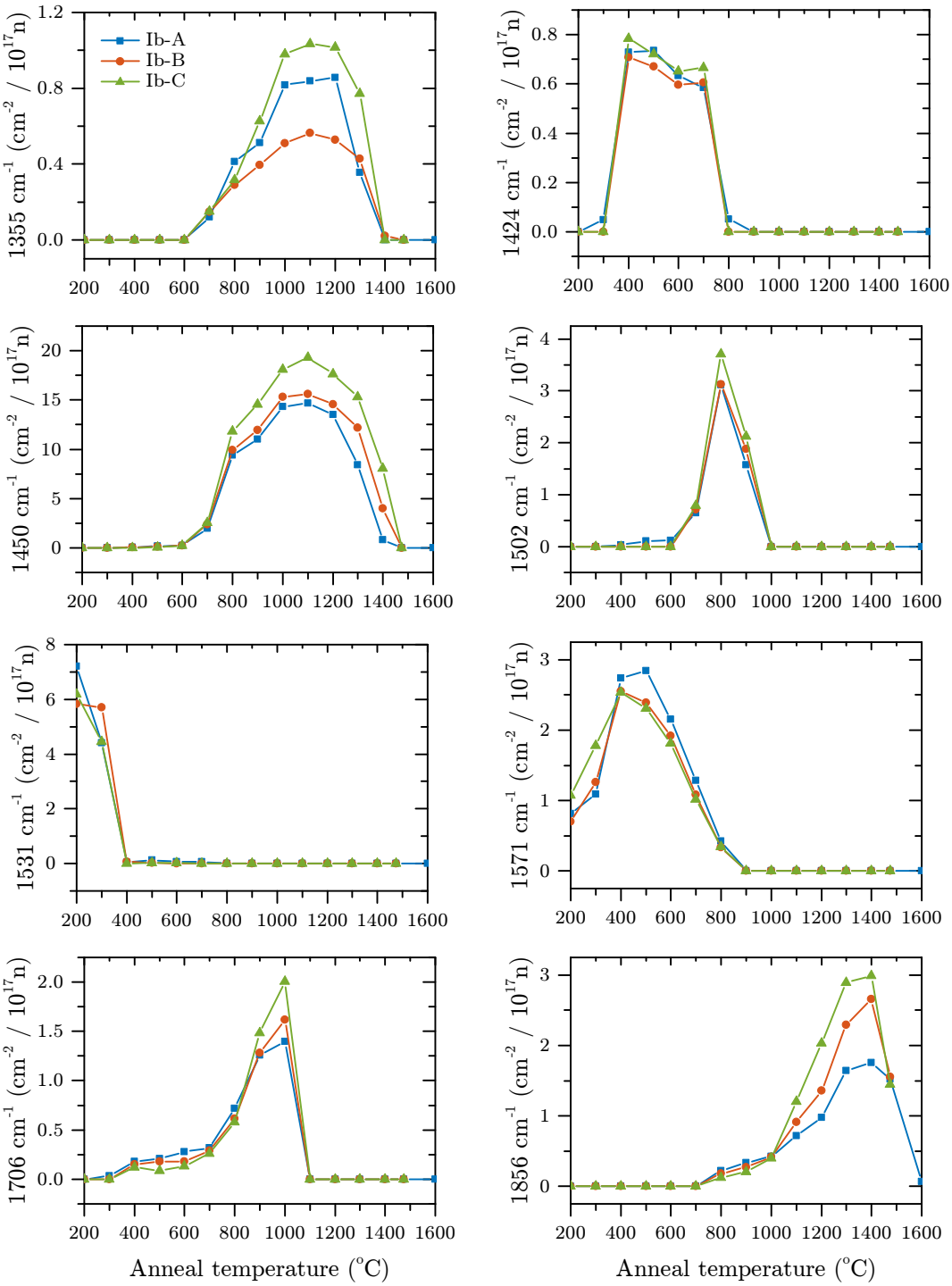

Figure 7-7 Annealing curves of the largest LVMs seen for the three neutron irradiated type-Ib samples. The data has been normalised to the neutron dose to distinguish processes which are radiation damage limited. Where there are more than one LVM with the same annealing curve (such as 1450 cm^{-1} and 1524 cm^{-1} and 1856 cm^{-1} and 1574 cm^{-1}) the weaker lines have been omitted.

The strongest LVM was the 1450 cm^{-1} mode of N_{2I}, which anneals in starting at 700 °C, attains its maximum at 1100 °C, and anneals out between 1400 °C and 1500 °C. It is accompanied by a ^{13}C shifted mode [17] at 1438 cm^{-1}. There is also an apparent doublet of lines at 1355 cm^{-1} and 1358 cm^{-1} [18] which anneal in and out at roughly the same temperatures as N_{2I}. On closer inspection the 1358 cm^{-1} mode follows the same annealing curve as 1450 cm^{-1}, but the 1355 cm^{-1} mode anneals in differently and out 100 °C earlier than 1358 cm^{-1}, indicating that it is a vibration at a different defect.

Lines at 1574 cm^{-1} and 1856 cm^{-1} anneal in gradually, attaining a maximum intensity after annealing at 1400 °C before annealing out at around 1500 °C. They appear to be joined by a third line at 1440 cm^{-1}. It is difficult to tell when it anneals in as it overlaps with the N_{2I} ^{13}C at 1438 cm^{-1}, but it persists longer than 1450 cm^{-1} and also anneals out at 1400 °C. As those lines anneal out, many small lines appear to anneal in between 1400 cm^{-1} and 1500 cm^{-1} and between 1600 cm^{-1} and 1700 cm^{-1}.

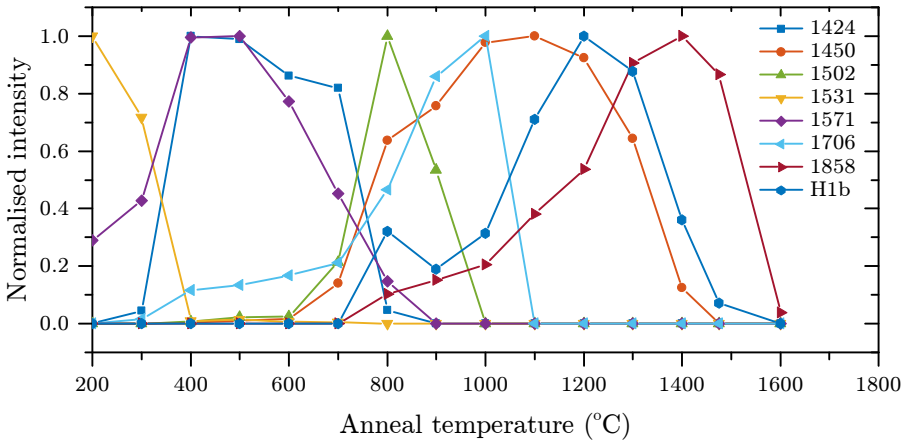

Figure 7-8 Combined annealing curves from figure 7-7 for sample Ib-A. The annealing curves have been normalised to have maximum intensity 1.

7.4.1.3 NIR absorption

The NIR spectra are shown in figure 7-9 for sample Ib-A after each annealing stage. After irradiation the absorption above 2000 cm^{-1} rose quickly to higher energy with a number of features, the most prominent of which is a very broad peak

(500 cm^{-1} wide) at approximately 3140 cm^{-1}. This structure diminished slowly with each anneal until it disappeared during the 800 °C anneal. A similar dramatic increase in absorption above 2000 cm^{-1} was also seen in the type-IIa samples after irradiation; however it was a monotonically increasing ramp without the broad 3140 cm^{-1} feature. For comparison the spectrum of a type-IIa diamond, irradiated to the same neutron dose, is shown in its as irradiated state in figure 7-9.

Annealing at 800 °C caused the appearance of the ZPL of the H1b absorption at 0.612 eV (4935 cm^{-1}). The annealing curve for H1b is shown in figure 7-10b. At RT the ZPL was difficult to integrate as it was asymmetric, probably the result of strain as has previously been observed [19]. The ZPL narrowed significantly, losing the asymmetry, after annealing at 1300 °C, at which point it also started to decrease in intensity annealing out completely during the 1600 °C anneal. The absorption to higher frequency of H1b appears to include its vibronic sideband. The sideband has previously been noted to be too small to be detected [19] but seems to be visible here at RT.

An interesting feature is the ZPL at 0.545 eV (4396 cm^{-1}) and associated sideband, which anneals in starting at 1200 °C. Its annealing curve is shown in figure 7-10a. This absorption has previously been studied by Mita, Kanehara and Nisida who found it to be photochromic [20]. The absorption increases after annealing at 1600 °C showing no sign of annealing out. The annealing of the 0.545 eV defect seems to complement the annealing out of NV^- and could therefore be related to NV or N_2V. It was proposed that the defect consists of two vacancies and a nitrogen, or is a nitrogen aggregate. A uniaxial stress study has previously been performed on the line and it was concluded to originate at a defect with $\mathscr{C}_{1h}$ symmetry with a dipole axis in the $\langle 1\,1\,\overline{3}\rangle$ direction, consistent with a model involving two nitrogen atoms and two vacancies (N-V-V-N or V-N-N-V) [15].

The photochromism of the 0.545 eV defect was investigated. Spectra were recorded of sample Ib-A after annealing to 1475 °C at 90 K with and without simultaneous illumination with a 3.061 eV laser at approximately 100 mW. The largest change in the spectrum was the 0.545 eV line along with changes in the one-phonon region and small changes in H1b and N_2V^-. Illumination decreased 0.545 eV and N_S^+ and

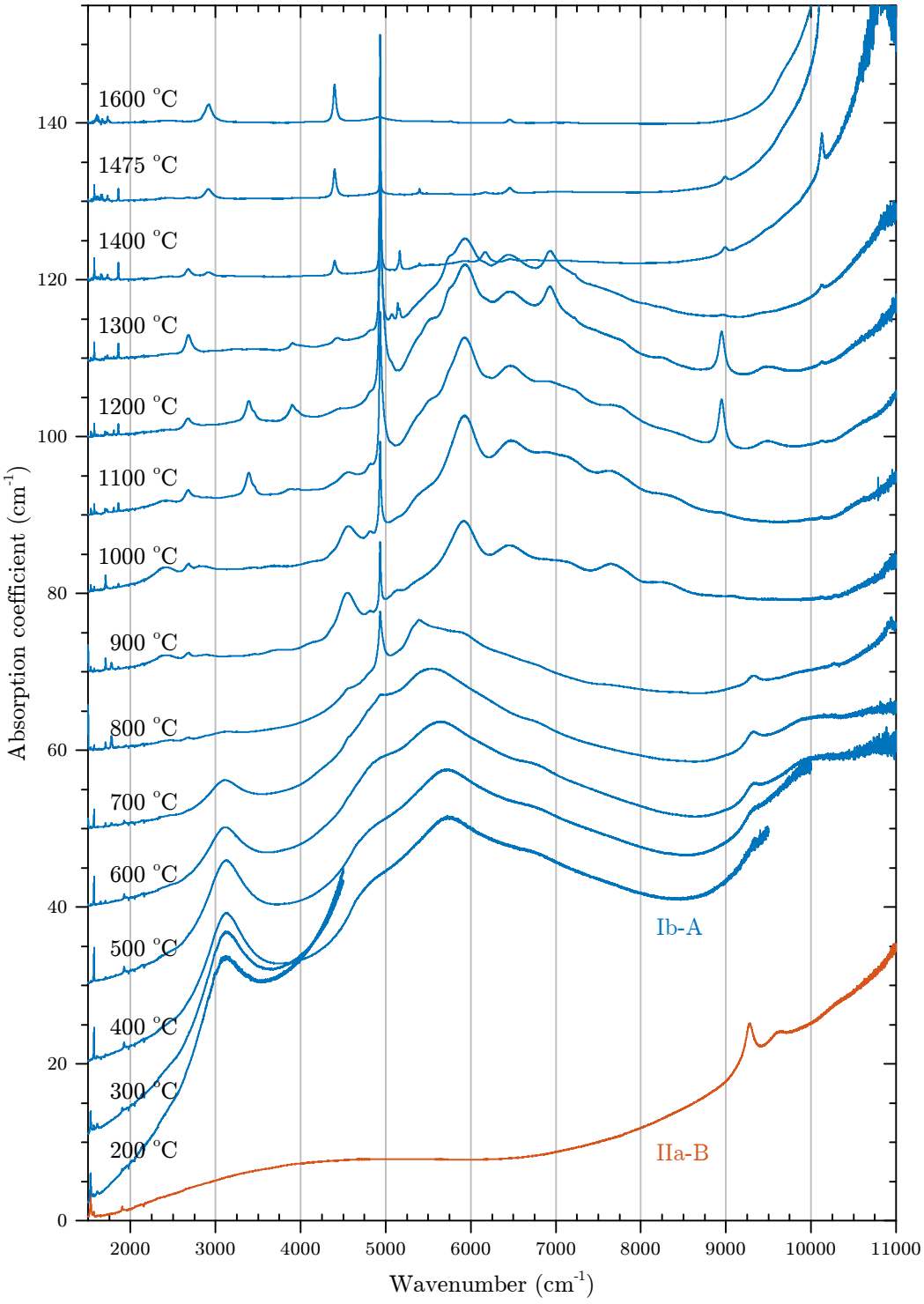

Figure 7-9 NIR absorption spectra for sample Ib-A at RT after successive 4 h anneals from 200–1600 °C in 100 °C intervals and sample IIa-B after irradiation for comparison (bottom). The intrinsic diamond spectrum has been subtracted. Notable features are the decrease in the large radiation induced absorption, the annealing in and out of H1b at 4935 cm^{-1} and the annealing in of N_2V^- at 10 130 cm^{-1}.

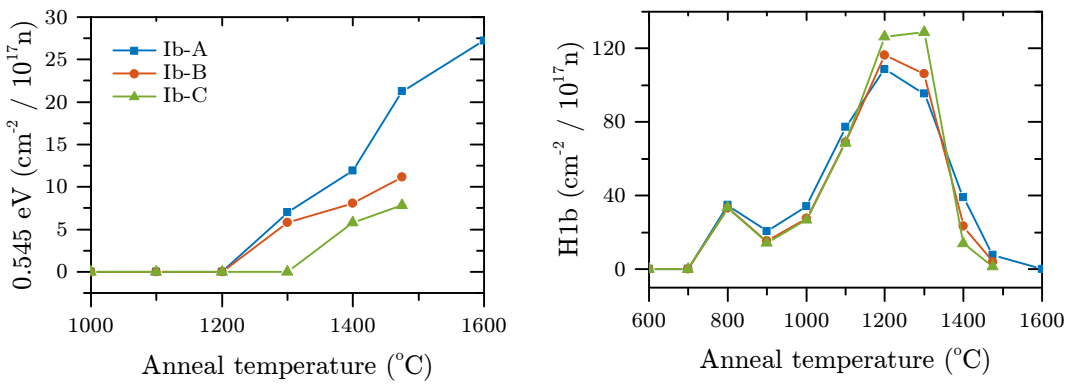

(a) 0.545 eV **(b)** H1b

Figure 7-10 Annealing curves for (a) 0.545 eV (4399 cm^{-1}) and (b) H1b (4935 cm^{-1}) zero-phonon lines at room temperature. Both lines have been normalised to the neutron dose. The rise in (b) after annealing at 800 °C could be a different absorption in the same location.

increased N_S^0 implying the charge transfer

$$(0.545\,\text{eV})^n + N_S^+ \rightleftharpoons (0.545\,\text{eV})^{n+1} + N_S^0\,. \tag{7-2}$$

Correlating the 24 % decrease in 0.545 eV with the 4.6(10) ppm increase in N_S^0, the maximum possible concentration of 0.545 eV was 19(4) ppm making the calibration constant $1.3(3) \times 10^{-17}$ meV cm^2. This assumes no charge transfer involving other species - although no other significant charge transfer was observed this cannot be ruled out. One of the charge states of the 0.545 eV defect should be paramagnetic. EPR spectra were recorded with and without simultaneous 3.061 eV illumination but no signals were observed.

A number of other smaller lines can be seen annealing in and out, notably at 2681 cm^{-1}, 2912 cm^{-1}, 3392 cm^{-1}, 4550 cm^{-1}, 6459 cm^{-1}, 8949 cm^{-1}, 8987 cm^{-1} and 9321 cm^{-1}. The 2912 cm^{-1} and 6459 cm^{-1} have been investigated with uniaxial stress by Liggins [15]. The splitting could not be resolved from 2912 cm^{-1} suggesting the defect to be hard; the 2912 cm^{-1} line seemed to show monoclinic behaviour, but low intensity made interpretation difficult.

The absorption from N_2V^- dominates the spectra after the highest annealing temperatures. Interestingly there is evidence, albeit small, of the N_2V^- ZPL at 1.256 eV (10 130 cm^{-1}) after annealing at 900 °C.

7.4.2 EPR

7.4.2.1 Defect quantification

After each anneal centre- and half-field spectra were recorded for each sample with $\boldsymbol{B}$ orientated along ⟨0 0 1⟩ at RT. The centre-field spectra were used for quantification of N_S^0 and N_2V^-, while half-field spectra were used for quantification of NV^-. The quantification for each sample, normalised to the neutron dose, of NV^- is shown in figure 7-11a and of N_2V^- is shown in figure 7-11b.

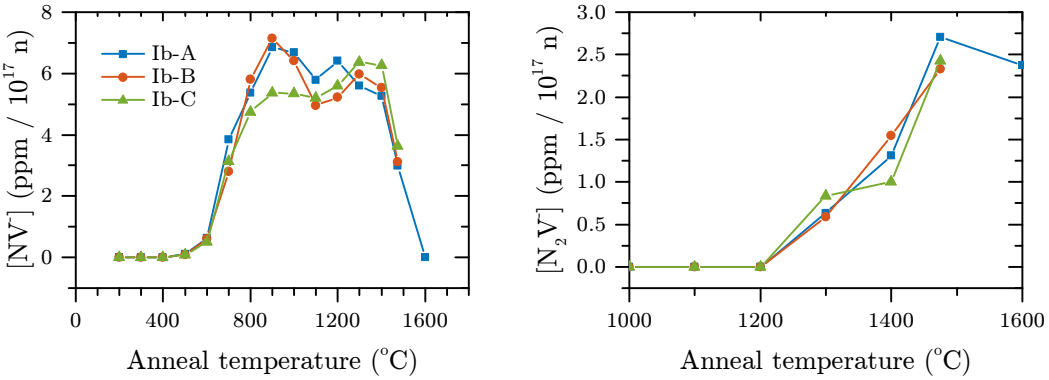

(a) NV^- **(b)** N_2V^-

Figure 7-11 Concentration of NV^- (a) and N_2V^- (b) determined by EPR. NV^- was quantified by the $\Delta m_s = \pm 2$ transitions. The concentrations have been normalised to the neutron dose to illustrate the dose dependence.

NV^- started annealing in at about 500 °C and scaled well to neutron dose as expected with nitrogen in excess. The highest measured NV^- concentration (without the correction discussed later) was 69(7) ppm in sample Ib-A after annealing at 900 °C. Although it could be within error, it is interesting that $[NV^-]$ was maximal in samples Ib-A and Ib-B at 900 °C, but not until 1300 °C for sample Ib-C. NV^- started annealing out in the 1475 °C anneal and had almost completely annealed out by the 1600 °C anneal. NV^- was found to be stable over a very broad range of temperatures, being at near maximum concentration from 800 °C to 1400 °C.

From the results of chapter 6 it is now possible to quantify N_2V^-. Since the spectrum of N_2V^- overlaps with that of N_S^0 in diamond of natural isotopic abundance, and is relatively featureless with the line broadening in these diamonds, care was

required in quantifying it. Reassuringly its annealing in agrees well with the ZPL at 1.256 eV (10 130 cm^{-1}) in figure 7-9. In the one sample annealed to 1600 °C the concentration has decreased. The maximum concentration of N_2V^- is less than half of NV^-.

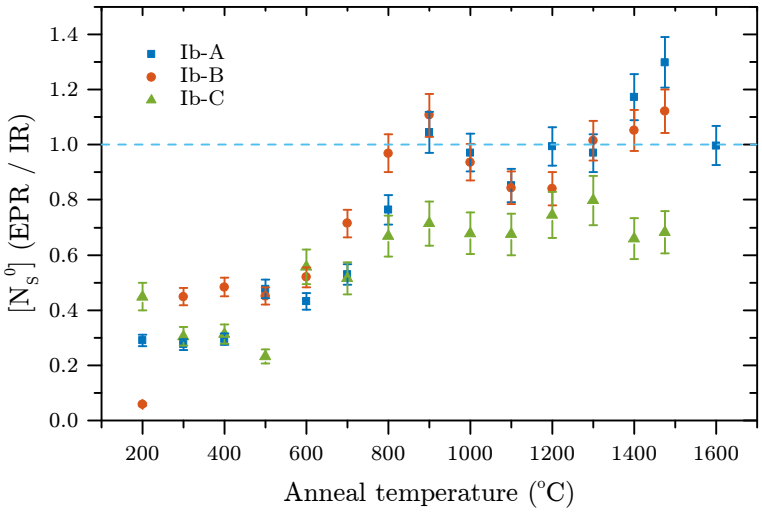

Figure 7-12 Comparison between quantification of N_S^0 by EPR and IR spectroscopy after each annealing stage. The error bars originate from a 5 % error on each measurement. EPR significantly underestimates the N_S^0 concentration before annealing to approximately 800 °C.

The quantification of N_S^0 from the IR absorption has already been shown in figure 7-5c. Figure 7-12 shows the ratio of N_S^0 measured by EPR spectroscopy to that measured by IR absorption spectroscopy. Both measurements are of the same defect and so the ratio of the two should be 1. Instead, a large underestimate of the spin concentration relative to the IR absorption measurement was observed until the samples were annealed to approximately 800 °C. It was noticed that the Q-factor of the microwave cavity reduced with the samples loaded. It seems that dielectric absorption in the samples lowered the Q-factor relative to that for the reference sample (the EPR signal is proportional to Q – see §5.2.1). The cause could be the very large concentration of paramagnetic species created by the neutron irradiation, giving rise to dielectric loss; in other words, the sample conductivity has been increased by neutron irradiation.

Sample Ib-C shows a systematic offset, most likely caused by different N_S^0 concentrations in different sectors of the diamond; the EPR measurement was on the entire sample while the IR measurement was through the centre. This can also

explain the different shape of the NV^- annealing curve for sample Ib-C to Ib-B and Ib-A in figure 7-11a. The neutron damage was homogeneous over the samples so if $N_S^0 > V$ the production of NV^- should be homogeneous, however if there was a sector with $N_S^0 < V$ the production of NV^- would be reduced.

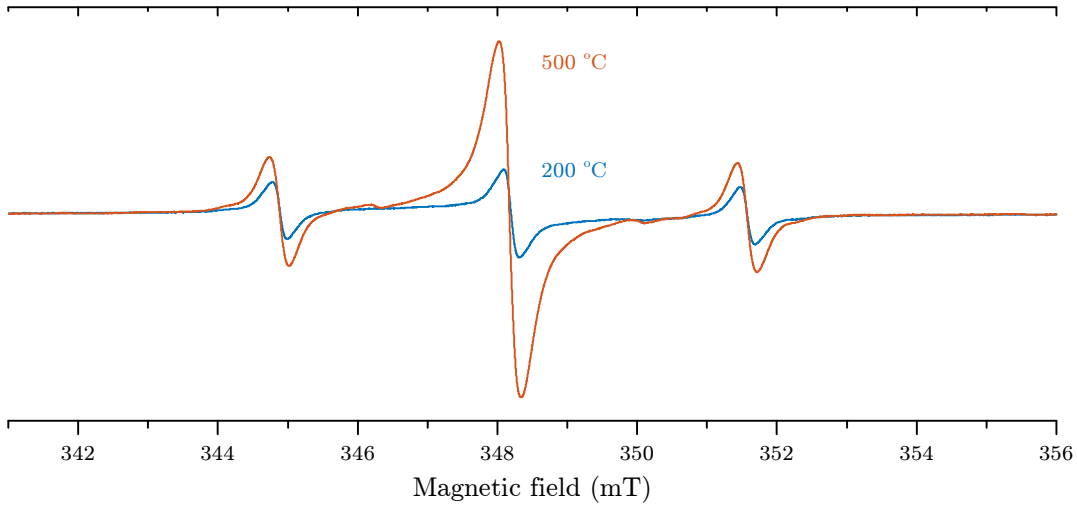

Figure 7-13 EPR spectra of sample Ib-A after 200 °C and 500 °C anneals. Intensity is proportional to spin concentration. No corrections have been made to the spectra.

Figure 7-13 shows EPR spectra of sample Ib-A after the 200 °C and 500 °C anneals. The spectra are both on the same scale, that is, they have the same proportionality to spin concentration. The spectra are comprised of N_S^0, V^- and a rather broad feature at approximately $g = 2.0027$. N_S^0 increases as is also seen in the IR data. Unexpectedly V^- increases dramatically. The temperature of this change corresponds with that of the change in charge balance between N_S^+ and N_S^0 seen in figure 7-5.

It would be expected that the concentration of V^- before NV^- anneals in is similar to, or more than, that of the NV^- which anneals in. Using normal procedure, the quantification of V^- after the 500 °C anneal put the concentration at only 19(2) ppm, significantly lower than $[NV^-]_{max}$. Referring to the previous discussion about EPR underestimating concentrations prior to annealing at 800 °C, a correction can be made (see §7.5.2). This doubles the concentration to approximately 44(4) ppm. Further more, up to two thirds of the signal might not be accounted for due to strain broadening of the $S = \pm\frac{1}{2} \rightarrow S = \pm\frac{3}{2}$ transitions (See

§7.6.1). The actual concentration of V^- could in fact be a factor of up to ~ 5 higher than measured.

7.4.2.2 NV^- production efficiency

The maximum possible NV^- concentration is determined by the requirement for one N_S incorporated in the defect and another to donate an electron. Therefore

$$[NV^-]_m = \frac{1}{2}[N_S]_i \,, \tag{7-3}$$

where $[NV^-]_m$ is the maximum possible concentration of NV^- and $[N_S]_i$ is the concentration of N_S before irradiation.

The dose dependence of highest concentration of NV^- attained in each sample is shown in figure 7-14, where $[NV^-]_m$ is indicated for the highest $[N_S]_i$ by a dashed line. For comparison, results are overlaid from a separate study by Mita [21], where type-Ib samples were neutron irradiated and subsequently annealed to 900 °C. The results were determined, using the calibration constant for NV^- deduced in chapter 6, from the optical absorption intensities given for the 1.945 eV ZPL. A good agreement in production versus neutron dose is observed between the two studies.

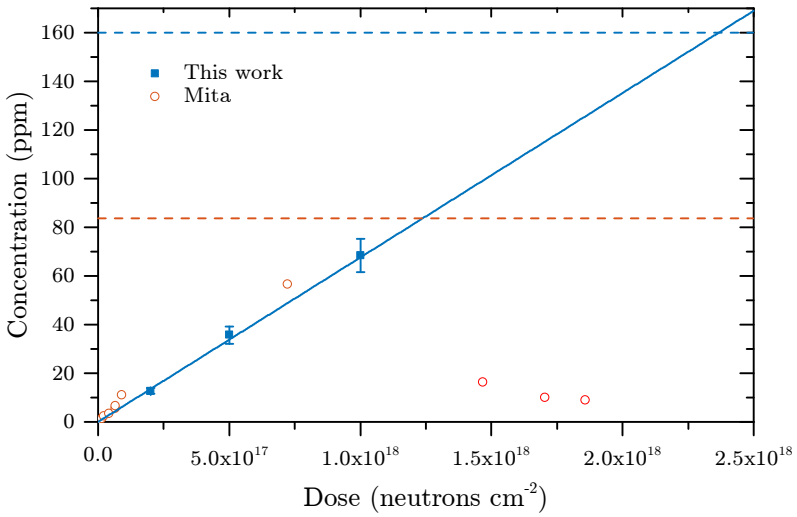

Figure 7-14 Maximum NV^- concentration attained from isochronal annealing. The dashed lines represents $[NV^-]_m$ defined in equation (7-3). Also displayed are equivalent data from [21].

In this study the neutron dose was insufficient to enable $[NV^-]_m$ to be reached. Mita however used samples with an initial N_S concentration around 100 ppm and irradiated to higher neutron doses. When the dose was sufficient for $[NV^-]$ to exceed $\frac{1}{2}[N_S]_i$, rather than level off, the NV^- concentration decreased. This was interpreted as there not being enough N_S^0 available to contribute an electron, causing the production of NV^0.

7.4.2.3 EPR linewidth

In EPR of diamond, homogeneous line broadening is caused by the spin-spin relaxation. In diamonds showing predominantly N_S^0, the relaxation rate $(1/T_2^*)$ is proportional to the spin concentration [22]. Figure 7-15 shows the linewidth of N_S^0 and NV^- after each anneal for sample Ib-A. The calculated linewidth from the concentration of paramagnetic defects (N_S^0, NV^-, N_2V^- and V^-) using the relationship in [22] is also shown with and without V^-. The very broad feature in figure 7-13 was included in the V^- quantification.

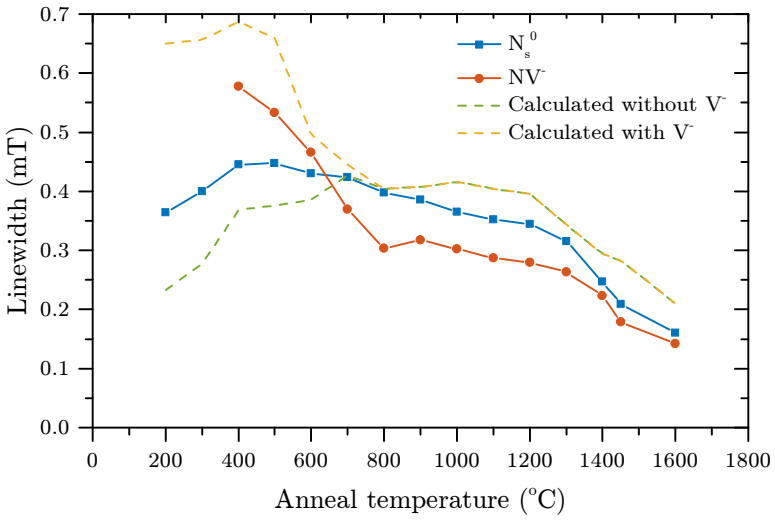

Figure 7-15 EPR linewidth (FWHM) of N_S^0 and NV^- measured after successive annealing in sample Ib-A. The NV^- linewidth is measured from the $\Delta m_s = \pm 2$ transitions. Values calculated from the spin concentration are also shown using the relationship by Van Wyk et al. [22].

The linewidths for NV^- were measured from the $\Delta m_s = \pm 2$ transitions (since the $\Delta m_s = \pm 1$ transitions are also broadened by the strain sensitive zero-field

splitting). Since the spin concentration is large the main broadening mechanism for N_S^0 and the $\Delta m_s = \pm 1$ transitions of NV^- is spin-spin broadening (evidenced by a Lorentzian lineshape) and the linewidth is a good indicator of T_2^*. It is expected that the measured linewidth of NV^- is smaller than N_S^0 because of the frequency-field conversion factor (see §3.1.8.3).

Before any NV^- annealed in, the linewidth of N_S^0 increased to a maximum at 500 °C. This corresponds to the increase in concentration of N_S^0 related to a charge transfer (as seen in figure 7-5). After this initial increase, the N_S^0 linewidth slowly decreased at a constant rate, until the spin concentration was reduced by the production of N_{2S} starting at 1200 °C causing the linewidth to fall significantly. The linewidth of N_S^0 is consistent with that calculated from a homogeneous distribution of paramagnetic defects, but excluding V^- (N_S^0, NV^- and N_2V^-).

The NV^- linewidth changes differently to N_S^0. As it anneals in there is a significant fall from 0.6 mT to 0.3 mT. The linewidth of NV^- is consistent with that calculated from a homogeneous distribution of paramagnetic defects, including V^- (N_S^0, NV^-, N_2V^- and V^-). The difference in behaviour of the N_S^0 and NV^- lineshapes indicates a difference in the distribution of defects. It is expected that NV^- forms around the cascade damage, so dipolar coupling with nearby paramagnetic defects will have a strong influence on linewidth; N_S^0 is spread more evenly through the diamond and is broadened by dipolar coupling with other N_S^0.

7.5 Nitrogen aggregation

7.5.1 Nitrogen assay

IR absorption spectroscopy has provided a quantification of N_S^0, N_S^+, and N_{2S}, while EPR spectroscopy has provided quantification of NV^- and N_2V^-. Together these defects represent the majority of nitrogen incorporation after each annealing stage; the defects which are not accounted for, which are potentially significant, are the nitrogen interstitials. Although we do not have a reliable quantification of N_{2I}, we do have its annealing curve. Figure 7-16 compares the annealing curves

for sample Ib-A for each of these defects, but with the simplification of N_S^0 and N_S^+ being summed into N_S. The annealing curve for N_{2I} is included but has been tentatively scaled to fit the missing nitrogen from N_S +N_{2S} +NV^- +N_2V^-.

The first loss of N_S corresponds well with the annealing in of NV^- as expected, and probably N_{2I}. The second loss in N_S corresponds well with the annealing in of N_{2S}. This occurs before the annealing out of NV^- and the annealing in of N_2V^-.

The recovery of nitrogen as N_{2S} anneals in suggests that nitrogen was trapped in interstitial forms, most likely N_I and N_{2I}, and is finally released at the same temperatures that N_{2S} anneals in. This is corroborated by N_{2I} annealing out at the same time. The obvious conclusion is that N_{2S} is created by the dissociation

$$N_{2I} \rightarrow N_{2S} + C_I \, . \tag{7-4}$$

The released C_I can then be recycled, analogous to the recycling of V in the vacancy mediated migration, in the process

$$C_I + N_S^0 \rightarrow N_I \tag{7-5}$$

$$N_I + N_S^0 \rightarrow N_{2I} \, , \tag{7-6}$$

thus providing a mechanism to aggregate N_S into N_{2S}. This is the same mechanism originally proposed by Kiflawi, Kanda and Mainwood [23] and more recently supported by Jones et al. [24]. This interstitial mediated aggregation does not mean vacancy mediated aggregation is incorrect, but provides a route to nitrogen aggregation at lower temperatures.

If the concentration of 40 ppm of nitrogen in N_{2I}, based on the nitrogen assay, is correct then the interstitial concentration after irradiation must have been at least 20 ppm. This is corroborated by the quantification of the $\langle 0\,0\,1 \rangle$-split self interstitial by EPR in the type-IIa neutron irradiated samples. In sample IIa-B, which was irradiated to the same dose as sample Ib-A, the concentration of R2 was measured to be 82(8) ppm after irradiation. It is expected that some interstitial defects would be lost on annealing from vacancy-interstitial recombination.

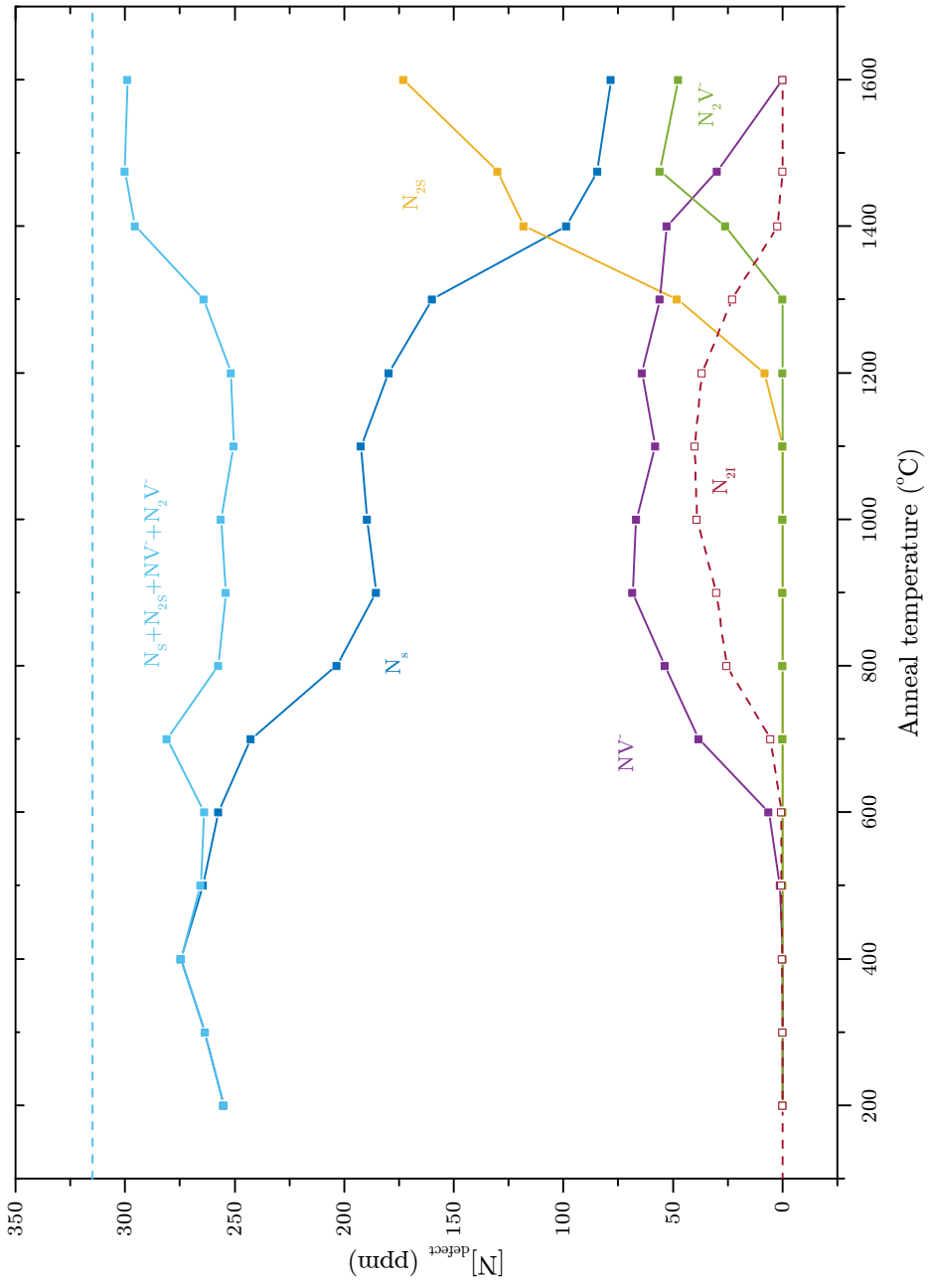

Figure 7-16 Annealing curves of N_S (N_S^0 + N_S^+), NV^-, N_{2I}, N_{2S} and N_2V. N_{2I} has been scaled to account for the missing nitrogen. The dashed line represents the quantification of N_S^0 before irradiation. The vertical scale is the concentration of nitrogen in the form of each defect – the concentrations of the N_{2I}, N_{2S} and N_2V^- defects are half of what is shown.

7.5.2 Charge assay

As well as accounting for all of the nitrogen in the sample the charge should also balance. The only ionised donor defect verified to exist in the samples is N_S^+, which can be quantified by the one-phonon absorption. Negatively charged defects which have been identified are V^-, NV^- and N_2V^-. In §7.4.2 it was shown that there were errors in the EPR quantification before annealing to approximately 800 °C. In an attempt to account for this to allow quantification of V^-, all EPR derived concentrations have been scaled by the ratio $[N_S^0]_{IR}/[N_S^0]_{EPR}$ and are shown in figure 7-17.

The initial corrected V^- concentration is only 6(2) ppm, however it increases significantly to 48 ppm on annealing to 400 °C. Before V^- anneals in there is a large concentration of negatively charged defect(s) not accounted for, which anneal out on annealing at 400 °C. The change corresponds well with the annealing out of the broad EPR feature (figure 7-13), and the annealing in of V^-. After NV^- anneals in there is too much negative charge by a factor of approximately 1.5. This is also seen for samples Ib-B and Ib-C. There are several reasons which could potentially cause this: an under estimate of N_S^+, an over estimate of NV^-, or a positive defect which has not been accounted for. The calibration constant for N_S^+ is 5.5(1) ppm cm^{-1}. Although the error given is nearly 20 %, the correction required here is much larger. Such a large discrepancy seems unlikely, particularly given that the calibration has given good results elsewhere.

7.5.3 Annealing models

A model of the annealing processes can be created using chemical kinetics theory (§3.5), forming a system of coupled differential equations. Only considering the processes involving vacancies provides a good starting model: the migration of V to N_S to create NV; the migration of NV to allow vacancy mediated aggregation to create N_2V; and ultimately the dissociation of N_2V to leave behind N_{2S} [25]. The processes and their activation energies used are described under the Vacancy processes heading in table 7-2, with the addition of a trap for vacancies (V → traps)

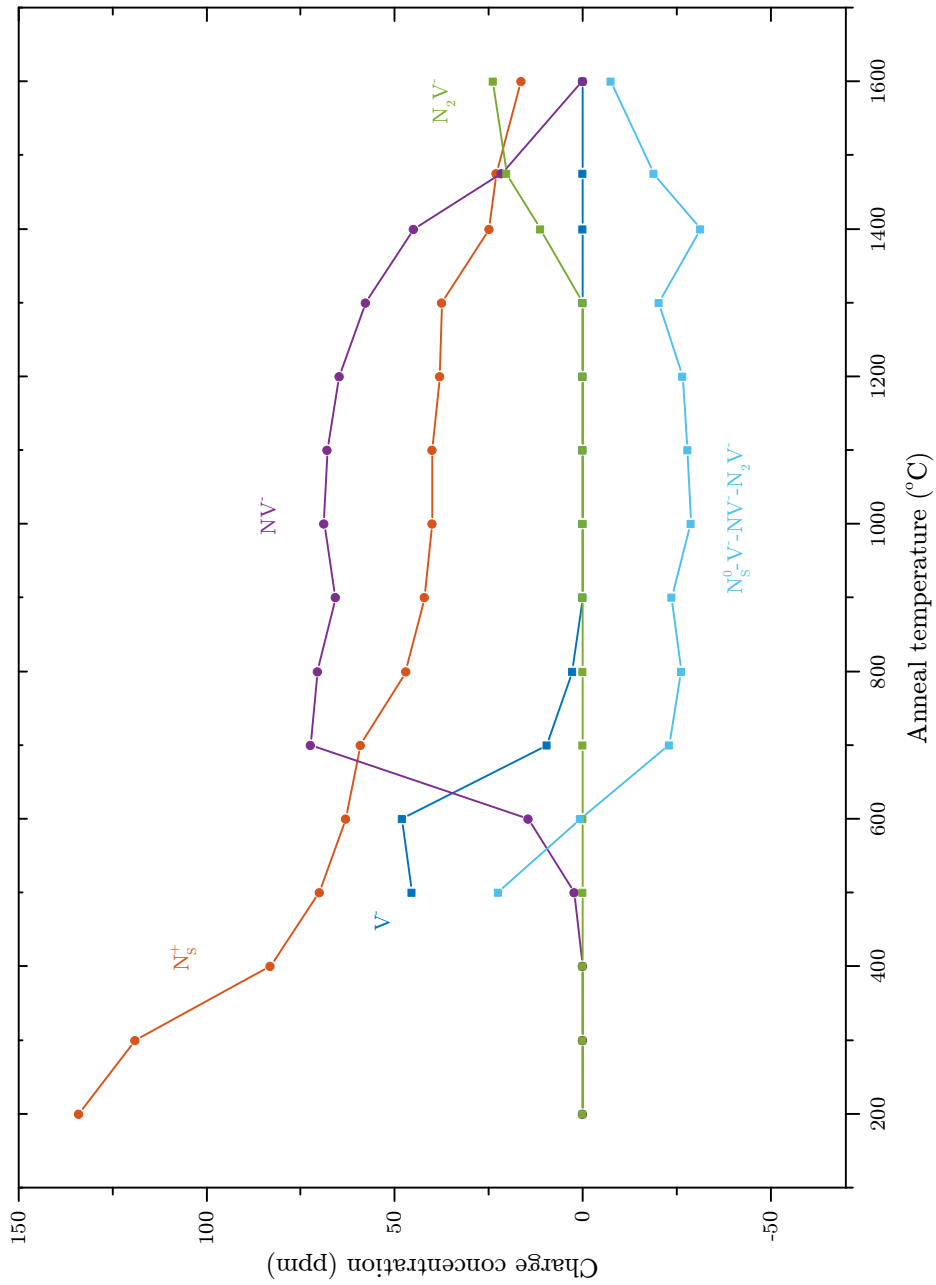

Figure 7-17 Quantification of charge in sample Ib-A after each anneal. To approximate the V^- concentration the EPR concentrations have been corrected by the ratio $[N_S^0]_{EPR}/[N_S^0]_{IR}$.

with activation energy 6.0 eV.

Process	Mechanism	Activation energy (eV) Here	Previous
Vacancy processes			
$N_S + V \rightarrow NV$	V migration	2.3	2.3 [26]
$N_{2S} + V \rightarrow N_2V$	V migration	2.3	
$N_S + NV \rightarrow N_2V$	NV migration	4.0	4.9 [27]
$NV \rightarrow N_S + V$	NV dissociation	5.8	5.8 [27]
$N_2V \rightarrow N_{2S} + V$	N_2V dissociation	5.7	6.5 [27]
Interstitial processes			
$N_S + C_I \rightarrow N_I$	C_I migration	1.6	1.6 [28]
$N_S + N_I \rightarrow N_{2I}$	N_I migration	2.4	2.4 [29]
$N_{2I} \rightarrow N_{2S} + C_I$	N_{2I} dissociation	4.7	
Interstitial-vacancy processes			
$V + C_I \rightarrow C$	C_I migration	1.6	
$NV + C_I \rightarrow N_S$	C_I migration	1.6	
$N_2V + C_I \rightarrow N_{2S}$	C_I migration	1.6	
$N_{2S} + C_I \rightarrow N_{2I}$	C_I migration	1.6	
$N_I + V \rightarrow N_S$	V or N_I migration	2.3/2.4	
$NV + N_I \rightarrow N_{2S}$	N_I migration	2.4	

Table 7-2 Equations used in simulating annealing of radiation damage in type-I diamond. The process driving each reaction is given along with the activation energy used here and activation energies previously in the literature for each mechanism. The migration energies from reference [27] are calculated assuming $\nu = 1 \times 10^{13}\,s^{-1}$. In all simulations here $\nu = 1 \times 10^{11}\,s^{-1}$.

The resulting set of coupled differential equations is as follows:

$$\frac{d[N_S]}{dt} = -k_{V_{mig}}[N_S][V] - k_{NV_{mig}}[NV][N_S] + k_{NV_{dis}}[NV]$$
$$\frac{d[V]}{dt} = -k_{V_{mig}}[N_S][V] + k_{N_2V_{dis}}[N_2V] + k_{NV_{dis}}[NV] - k_{V_{mig}}[N_{2S}][V] - k_{V_{mig}}[V]$$
$$\frac{d[NV]}{dt} = +k_{V_{mig}}[N_S][V] - k_{NV_{mig}}[NV][N_S] - k_{NV_{dis}}[NV]$$
$$\frac{d[N_2V]}{dt} = +k_{NV_{mig}}[NV][N_S] - k_{N_2V_{dis}}[N_2V] + k_{V_{mig}}[N_{2S}][V]$$
$$\frac{d[N_{2S}]}{dt} = +k_{N_2V_{dis}}[N_2V] - k_{V_{mig}}[N_{2S}][V]$$

where k is the rate constant defined in equation (3-46). To simulate isochronal

anneals the computing environment MATLAB was used to find the solution to this system of equations after each anneal. The resulting concentrations were used as starting parameters for the next temperature. The system of coupled equations is stiff and consequently the standard 'ode45' MATLAB solver gave unstable solutions. Instead, solver 'ode23s' was used providing stable solutions. A simulation of this model is shown in figure 7-18 where anneals were for 4 h at every 100 °C. Starting concentrations have been chosen to represent sample Ib-A.

For simplicity the different charge states of defects have been combined together. Because of the large excess of nitrogen in these samples the charge states of acceptors are believed to have been stable and so the approximation has been made that $NV^{total} \approx NV^{-}$ and $N_2V^{total} \approx N_2V^{-}$. If the irradiation damage concentrations had been close to, or exceeded, the nitrogen concentrations this approximation would not be valid. The vacancy model is a good starting point but it does not account for any production of N_{2S} before N_2V as clearly seen in figure 7-16.

In light of the evidence in figure 7-18 for the importance of interstitials in the annealing, and the results from [24], the interstitial processes in table 7-2 were added to the simulation. In addition, rather than using a generic V → traps mechanism, the combination of vacancy defects with interstitial defects were added as a means to switching off the aggregation. The resulting simulation using all of the processes in table 7-2 is shown in figure 7-19.

Comparing the simulated results in figure 7-19 with the experimental results in figure 7-16, the agreement is remarkable. The dissociation of N_{2I} reproduces the production of N_{2S} at the temperatures it was seen in the experiment and before N_2V. After N_2V is produced N_{2S} increases further by the vacancy mediated mechanism. Thus it seems that both interstitial and vacancy mediated aggregation mechanisms are important.

The production mechanism for N_I is believed to be by $C_I + N_S \rightarrow N_I + C$ [30]. If this occurs on annealing and migration of $C_{I_{001}}$ the associated activation energy would be 1.6 eV, however radiation-enhanced interstitial migration has also been reported [28]. The starting concentration of C_I was chosen to cause the correct loss in N_S from the production of N_{2I} and the initial creation of N_{2S}. At 28 ppm it

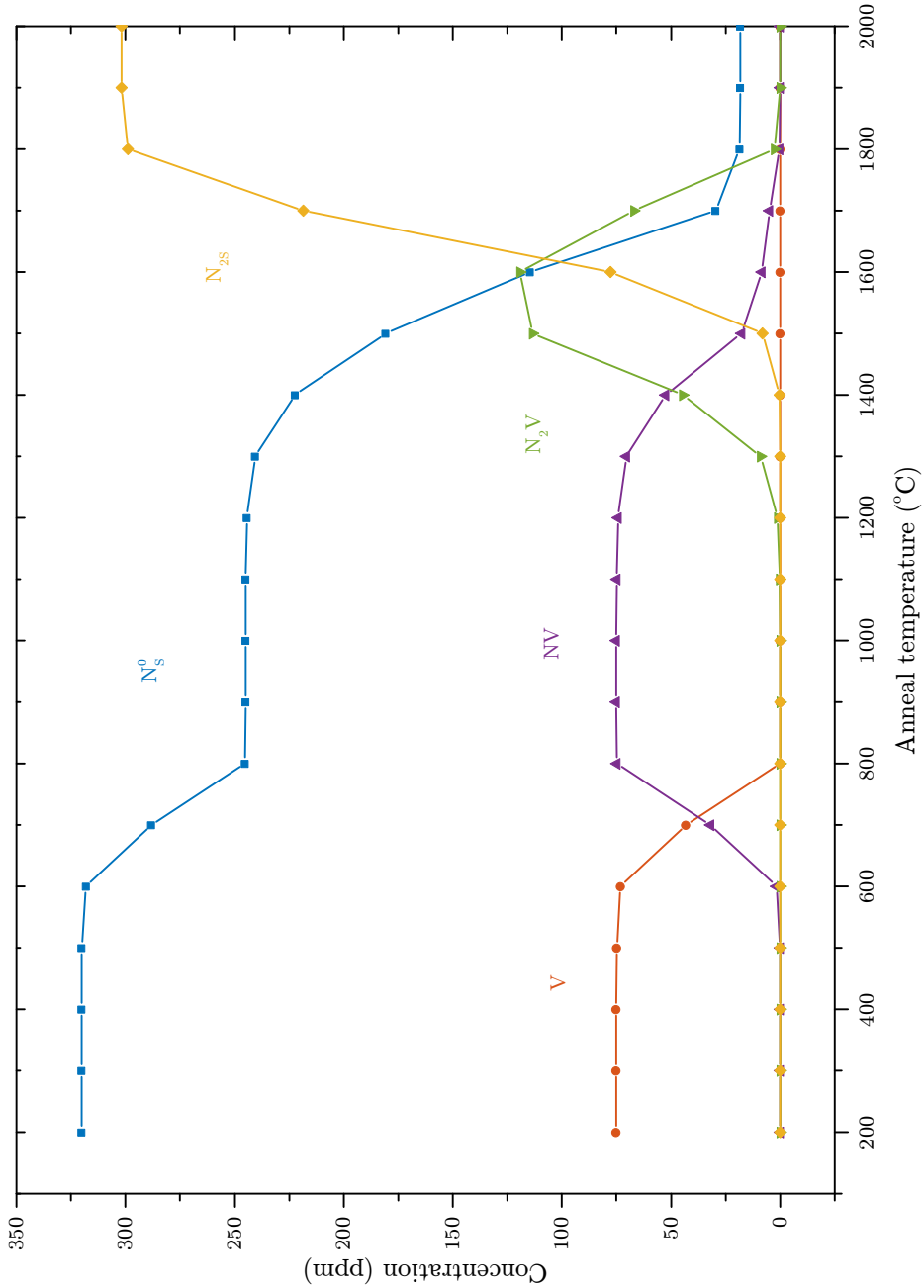

Figure 7-18 Simulation of isochronal annealing in 100 °C intervals using the vacancy processes in table 7-2, with starting concentrations [N_S] = 320 ppm and [V] = 70 ppm. Each simulated anneal was 4 h long. For defects containing nitrogen, the concentration of nitrogen in the form of that defect is used.

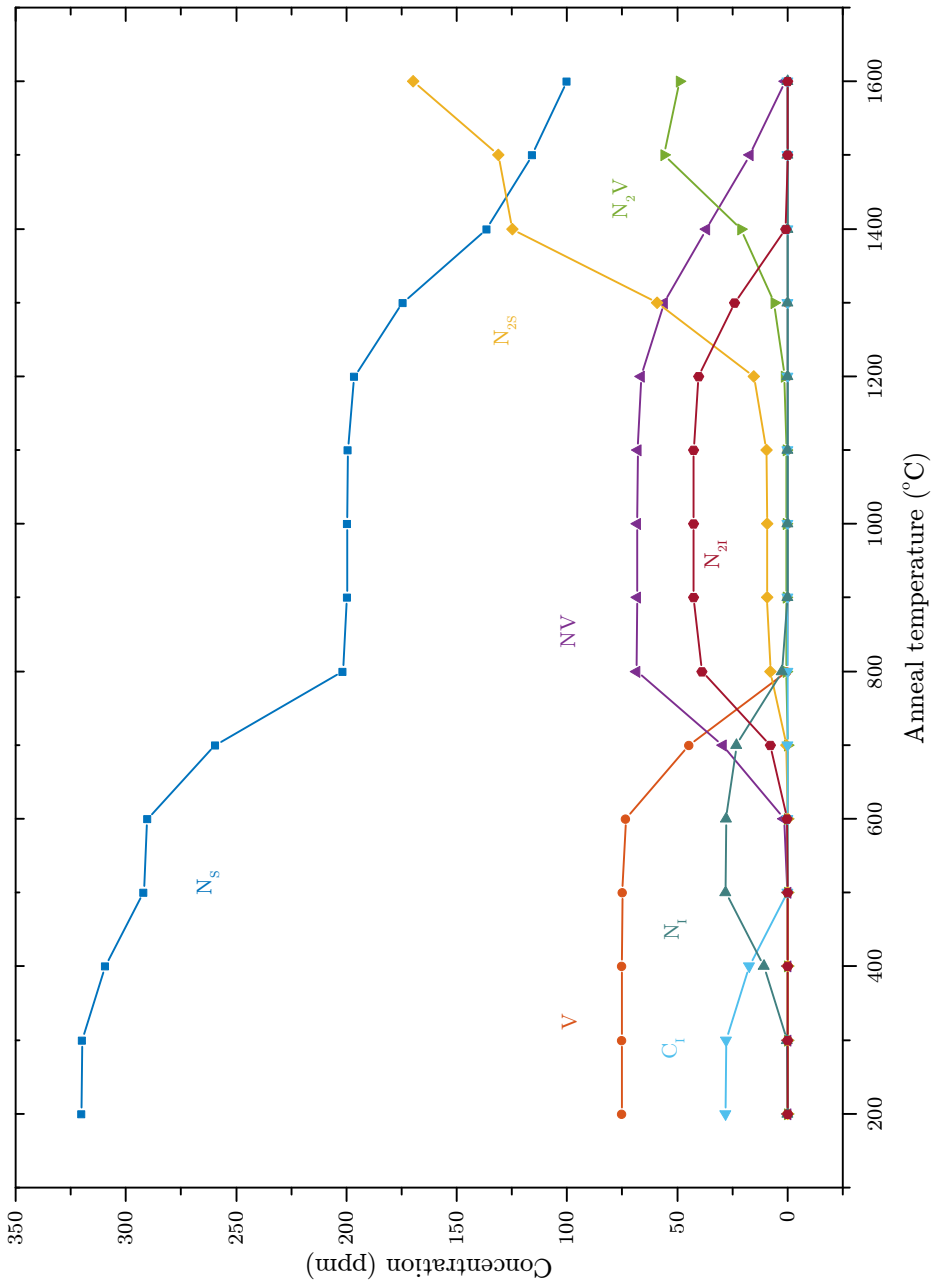

Figure 7-19 Simulation of isochronal annealing in 100 °C intervals using the model in table 7-2. The starting concentrations were $[N_S] = 320$ ppm, $[V] = 75$ ppm and $[C_I] = 28$ ppm. For defects containing nitrogen, the concentration of nitrogen in the form of that defect is used.

is in reasonable accord with the 20 ppm predicted from the nitrogen assay (§7.5.1).

For completeness a simulation was made with the same model but with starting concentrations $[N_S] = 0$ ppm and $[N_{2S}] = 160$ ppm to represent irradiated type-IaA diamond. The resulting simulated annealing curves are shown in figure 7-20. N_2V and N_{2I} are created at lower temperatures as expected with a corresponding loss in N_{2S}. The model shows that as N_{2I} and N_2V dissociate, N_{2S} returns.

7.6 Discussion

7.6.1 V^- quantification

Figure 7-13 shows an apparent large increase in V^- with the annealing curve in figure 7-17. As V^- annealed in, two other processes were observed. There was a large decrease in N_S^+, corresponding to an approximate halving of its initial concentration, and the broad feature in the centre of the EPR spectrum decreased in intensity. In addition, although $C^0_{I_{001}}$ was not quantified here, it is known to increase in concentration on annealing up to 400 °C in irradiated type-Ib diamond [31].

The simulations of neutron damage predicted that 85(11) ppm of vacancies were created on irradiation; From the NV^- production at least 72(7) ppm of vacancies must have been created. For samples annealed at $\lesssim 600$ °C either the vacancies are in a different charge state, incorporated into other complexes, or not visible due to strain broadening. Each of these possibilities will be discussed.

It is possible that vacancies are doubly charged in the state V^{2-}. This could explain both the annealing in of V^- and the corresponding charge transfer with N_S^+. However, for charge to transfer from N_S^0 to V^-, N_S^0 must be higher than V^{2-} in the band gap. The band gap is 5.5 eV, and N_S^0 is 1.7 eV below the conduction band. The ground state of V^- is at least 3.15 eV below the conduction band leaving at most 1.45 eV above the V^- ground state for V^{2-}.

That vacancies are incorporated into di-vacancies and larger complexes, perhaps

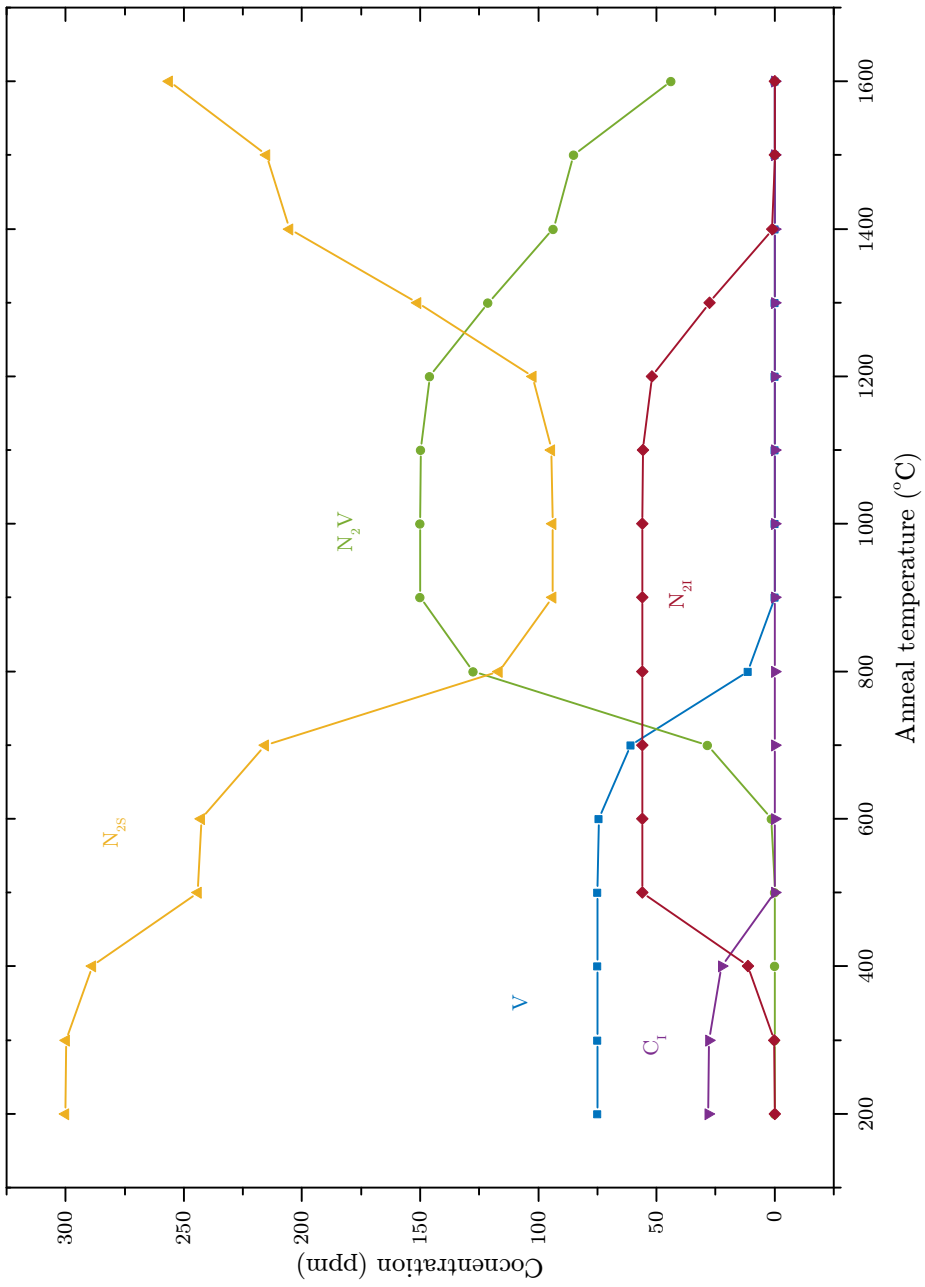

Figure 7-20 Simulation of isochronal annealing of irradiation damage in type-IaA diamond using the model in table 7-2. The starting concentrations were $[N_{2S}]$ = 160 ppm, [V] = 75 ppm and $[C_I]$ = 28 ppm. Each anneal is for 4 h. For defects containing nitrogen, the concentration of nitrogen in the form of that defect is used.

with interstitials, is not hard to believe given their formation in cascade damage. It is possible that such complexes then release defects on annealing.

V^- has $S = \frac{3}{2}$ but has $D = 0$ since it has $\mathscr{T}_d$ symmetry. The Zeeman splitting on the $S = \frac{3}{2}$ causes a shift in energy of the $m_S = \pm\frac{1}{2} \rightarrow \pm\frac{3}{2}$ transitions. If this symmetry is lifted, for instance by strain, a D term will be introduced. This is demonstrated in figure 7-21a. The effect is to lift the degeneracy of the three transitions creating a spectrum with three lines, decreasing the intensity of the centre line. If there is a distribution of strain there will be a distribution of D. This will cause a broadening of the two outer lines but not affect the centre line. The result can manifest as a relatively narrow line with a very broad line underneath as shown in the simulation in figure 7-21b; this is exactly what is seen in figure 7-13.

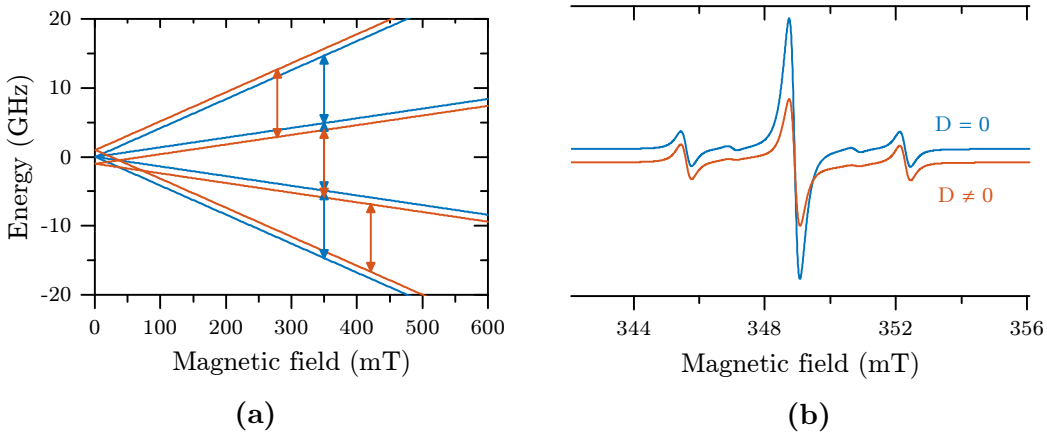

Figure 7-21 (a) Comparison of energy levels of V^- with and without a D term (D = 1 GHz has been used for clarity) with corresponding transitions at 9.8 GHz. (b) Simulated spectrum showing effect of a distribution of D about zero with FWHM 35 MHz. The total intensity of V^- is the same in both cases. N_S^0 is included to demonstrate the effect on the experimental spectrum.

Given the excellent agreement between the figure 7-13 and figure 7-21b, strain broadening is almost certainly causing and/or contributing to the broad EPR line and also accounts for part or all of the under quantification of V^-. The release of vacancies from complexes during annealing also seems likely.

7.6.2 Charge balance

From figure 7-17 there are clearly unaccounted for defects with non-zero charge. At low annealing temperatures there is negative charge missing. The majority of this is probably from an underestimate of the V^- concentration because of strain broadening. If the $m_S = \pm\frac{1}{2} \rightarrow \pm\frac{3}{2}$ transitions broaden out and are not observed the apparent intensity will be one third of the total intensity. Additionally it is likely that different charge states of interstitials exist, such as N_I^- and C_I^-, explaining the annealing in of $C_{I_{001}}$ [31].

When an NV^- anneals in there is unaccounted for positive charge. N_{2I} anneals in at the same temperature and could present in the positive charge state, however in the charge study in chapter 6 N_{2I} was one of the few defects that did not show any photochromic behaviour. Although it couldn't be measured in this study because of the strength of the absorption, the 594 nm defect reaches maximum intensity at approximately 800 °C and its annealing out complements the annealing in of H1b [19]. Both defects were found in chapter 6 to be photochromic suggesting different charge states exist. The nitrogen assay would suggest that there is at most 20 ppm of these defects, however, although they are only observed in type-I diamond, there is no direct evidence that either defect definitely incorporates nitrogen. In this study charge transfer was observed between N_S^0 and the 0.545 eV defect, indicating its presence in more than one charge state. The 0.545 eV defect started annealing in at 1300 °C with a concentration after 1600 °C estimated at up to 19 ppm. As such it could have a significant contribution to charge in the later annealing stages.

7.6.3 EPR linewidth

In figure 7-15 the measured linewidths of N_S^0 and NV^- are compared with that calculated from the relationship given by Van Wyk et al. [22] from the total spin concentration, including and excluding V^-. The linewidth of NV^- was measured from the $\Delta m_S = \pm 2$ transitions in the half field spectrum, thus it is not so sensitive to strain broadening. The NV^- linewidth approximately follows the calculation

including V^- and the N_S^0 linewidth follows the calculation without. This is consistent with the cascade damage caused by neutron irradiation and NV^- forming near it. It is of course expected as the cascade is a source of vacancies for the NV^-.

After annealing to 800 °C the discrepancy between the N_S^0 and NV^- linewidth disappears. Either the cascade damage has healed, or the activation energy for forming NV near cascades is lower causing it to be created there first.

7.6.4 N_{2I} calibration constant

The results from this chapter and also from chapter 6, provide data on the production of N_{2I} from which the calibration constant for the 1450 cm^{-1} LVM can be estimated. From the nitrogen assay, between 800–1400 °C approximately 40(10) ppm of N_S was not accounted for between N_S^0, N_S^+, and NV^-, but returned as N_{2I} annealed out. If this was incorporated in N_{2I} then the maximum N_{2I} concentration was 20(5) ppm. This agrees well with the concentration estimated from the annealing simulations (figure 7-19) of 28 ppm, required to correctly model the annealing in of N_{2S}. It is also consistent with the interstitial production measured in a type-IIa sample subjected to the same irradiation. In that sample a concentration of 82(8) ppm of $C_{I_{001}}^0$ was measured after irradiation. We would expect a proportion of interstitials to be lost to interstitial-vacancy recombination in early annealing stages. Taking the concentration of 24(4) ppm and the 1450 cm^{-1} intensity as 142 cm^{-2}, the calibration constant is calculated as $f_{1450} = 3.4(5) \times 10^{-17}$ cm.

As further corroboration of the calibration constant for N_{2I}, its production in type-IaA diamond will be considered. The annealing in of N_{2I} in irradiated type-IaA diamond is arguably simpler than in type-Ib diamond with fewer steps required in the mechanism. We can determine the vacancy concentration after irradiation, which gives an absolute upper limit to the interstitial concentration. The interstitial production in HPHT-grown type-IIa diamond is ≈ 10 % of vacancy production [32]. This can be used as a lower bound since in type-I diamond interstitial production should be higher due to strain and other nitrogen interstitials [16].

From the results of chapter 6, where a type-IaA diamond was electron irradiated and annealed, the vacancy production was approximately 3.4 ppm (determined by the NV and N_2V production after annealing to 800 °C) and the 1450 cm^{-1} absorption was 11.0 cm^{-2}. This gives bounds on the calibration constant of 1.8×10^{-17}–2.6×10^{-16} cm – consistent with $f_{1450} = 3.4(5) \times 10^{-17}$ cm.

7.7 Conclusions

Neutron irradiation of diamond has been modelled with SRIM resulting in a predicted damage rate of 15(2) V n^{-1} cm^{-2}, corresponding to a vacancy concentration of 85(11) ppm in the sample irradiated to the highest dose. This is in agreement with the highest NV^- concentration of 72(7) ppm, but lower than the N_S^+ concentration of 134(20) ppm, which in electron irradiated diamond is often presumed a good measure of vacancy production. The V^- concentration measured by EPR was only 6(2) ppm after irradiation but increased to 48(5) ppm after annealing to 500 °C. The lack of observed signal from V^- can in part be accounted for by a broadening of its $m_S = \pm\frac{1}{2} \rightarrow \pm\frac{3}{2}$ transitions due to strain, potentially reduces the apparent signal by two thirds. It is also likely that some vacancies are involved in complexes.

A large 0.545 eV absorption was created by annealing from 1200–1600 °C enabling its previously reported photochromism to be investigated. Charge transfer between N_S and the 0.545 eV defect were correlated allowing the calibration for 0.545 eV to be determined as $f_{0.545} = 1.3(3) \times 10^{-17}$ meVcm^2 at 80 K. The determination of the calibration constant assumes that there were no other significant charge transfers between N_S and other defects. Using the calibration constant its maximum concentration was estimated to be 19(4) ppm after annealing at 1600 °C. A small photochromic change of H1b was also observed.

Several approaches have been used to estimate a calibration constant for the 1450 cm^{-1} LVM of N_{2I}, including a nitrogen assay, chemical kinetics simulations and the production of $C_{I_{001}}$ in type-IIa diamond. All methods were in good accord, estimating maximum N_{2I} concentrations of 20–28 ppm, giving a calibration

constant of $f_{1450} \sim 3.4 \times 10^{-17}\,\mathrm{cm}$. A large number of additional LVMs were observed, all of much smaller intensity than $1450\,\mathrm{cm}^{-1}$. This includes the $1424\,\mathrm{cm}^{-1}$ LVM which has the correct annealing curve for the N_I precursor of N_{2I}, however no further conclusions could be drawn.

EPR allowed quantification of V^-, NV^- and N_2V^-. The highest concentrations of NV^- and N_2V^- produced were 72(7) ppm and 24(2) ppm respectively. The production of NV^- and N_2V^- were both dose limited, therefore higher concentrations would be possible with heavier irradiation. NV^- started annealing out at approximately 1400 °C and nearly completely annealed out after annealing at 1600 °C. N_2V^- was did not increase by annealing at 1600 °C. V^- was observed to anneal in at 400 °C, with a corresponding decrease in N_S^+. Several mechanisms responsible for this have been discussed. The likely explanation is that strain reduces the symmetry of V^-, inducing a small zero-field splitting, broadening components of the line leading to an estimate in intensity.

The majority of nitrogen was accounted for in the defects N_S^+, N_S^0, NV^-, N_2V^- and N_{2S}. Irradiation decreased the concentration of N_S, implying that a quantity was trapped in other defects, likely N_I, the precursor to N_{2I}. From the nitrogen assay the remaining concentration of nitrogen not accounted for is $< 10\,\%$.

The initial production of N_{2S} at 1300 °C was proportional to neutron dose but subsequent production was not, occurring at similar rates for all three samples. N_{2S} was produced before N_2V^- and increased at two separate rates. The experimental evidence strongly supports the production of N_{2S} by multiple methods, namely the dissociation of N_{2I} and interstitial mediated aggregation and the dissociation of N_2V and vacancy mediated aggregation. A model of the significant annealing processes has been proposed, including mechanisms for interstitial and vacancy mediated aggregation. Simulations of the model agree very well with the experimental data.

References

1. M. W. Doherty et al., *Physics Reports* **528**, 1–45 (July 2013).
2. R. Schirhagl et al., *Annual review of physical chemistry* **65**, 83–105 (Jan. 2014).
3. B. K. Ofori-Okai et al., *Physical Review B* **86**, 081406 (Aug. 2012).
4. B. Naydenov et al., *Applied Physical Letters* **96**, 163108 (2010).
5. L. Cranberg et al., *Physical Review* **103**, 662–670 (Aug. 1956).
6. A. Mainwood, *Diamond and Related Materials* **7**, 504–509 (1998).
7. C. D. Clark, P. J. Kemmey, E. W. J. Mitchell, *Discussions of the Faraday Society* **31**, 96 (1961).
8. J. C. Bourgoin, B. Massarani, *Physical Review B* **14**, 3690–3694 (1976).
9. J. Koike, D. M. Parkin, T. E. Mitchell, *Applied Physics Letters* **60**, 1450–1452 (1992).
10. B. Campbell et al., *Nuclear Instruments and Methods in Physics Research A* **476**, 680–685 (2002).
11. *T-2 Nuclear Information Service*.
12. B. Campbell, A. Mainwood, *physica status solidi (a)* **181**, 99–107 (2000).
13. J. Ziegler, *The Stopping and Range of Ions in Solids* (Wheaton and Co, Oxford, 1985).
14. G. H. Kinchin, R. S. Pease, *Reports on Progress in Physics* **18**, 1 (1955).
15. S. Liggins, PhD thesis, The University of Warwick, 2010.
16. A. T. Collins, A. Dahwich, *Journal of Physics: Condensed Matter* **15**, L591–L596 (2003).
17. I. Kiflawi et al., *Physical Review B* **54**, 16719–16726 (1996).
18. G. S. Woods, *Philosophical Magazine Part B* **50**, 673–688 (1984).
19. A. T. Collins, G. Davies, G. S. Woods, *Journal of Physics C: Solid State Physics* **19**, 3933 (1986).
20. Y. Mita, H. Kanehara, Y. Nisida, *Diamond and Related Materials* **6**, 1722–1725 (1997).
21. Y. Mita, *Physical Review B* **53**, 11360–11364 (May 1996).

22. J. A. Van Wyk et al., *Journal of Physics D: Applied Physics* **30**, 1790–1793 (1997).
23. I. Kiflawi, H. Kanda, A. Mainwood, *Diamond and related materials* **7**, 327–332 (1998).
24. R. Jones et al., *Diamond and Related Materials* **53**, 35–39 (2015).
25. A. T. Collins, *Journal of Physics C: Solid State Physics* **13**, 2641–2650 (1980).
26. S. Lawon et al., *Journal of Physics: Condensed Matter* **4**, L125–131 (1992).
27. H. Pinto et al., *Physica Status Solidi (A) Applications and Materials Science* **209**, 1765–1768 (2012).
28. M. E. Newton et al., *Diamond and Related Materials* **11**, 618–622 (2002).
29. J. Goss et al., *Physical Review B* **70**, 235208 (2004).
30. S. Liggins et al., *Physical Review B* **81**, 085214 (Feb. 2010).
31. K. Iakoubovskii et al., *Physica B* **340-342**, 67–75 (Dec. 2003).
32. D. J. Twitchen et al., *Physica B* **273-274**, 628–631 (1999).

8

Irradiation under uniaxial stress

8.1 Introduction

If a point defect has lower symmetry than its host crystal, there are a number of orientations, or sites, which it can occupy. For example, the symmetry of $C_{I_{001}}$ is $\mathscr{D}_{2d}$ allowing three distinct sites with its symmetry axis oriented along the [1 0 0], [0 1 0] and [0 0 1] directions, depicted in figure 8-1. If these sites are not equally populated we refer to the defect as being preferentially oriented.

When a defect is incorporated during growth, or introduced by a subsequent treatment, it is usual for all of the sites to be equally populated as there is nothing to distinguish them. In CVD growth, if a defect is incorporated on the growth surface, then during growth the different sites are no longer necessarily all equivalent

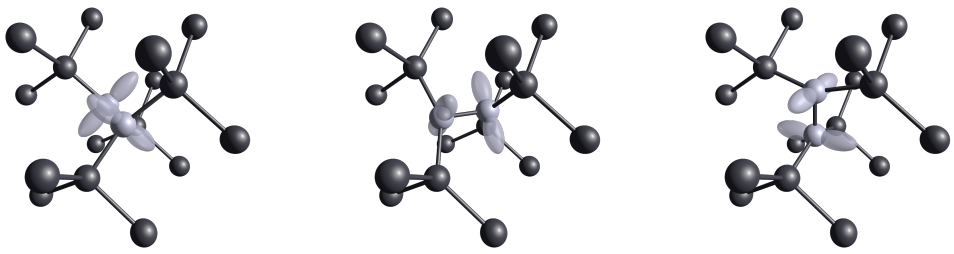

[1 0 0] [0 1 0] [0 0 1]

Figure 8-1 Models of the ⟨001⟩-split interstitial on its three distinct lattice sites. Interstitial atoms are indicated in dark blue.

and the probability of creating defects on them differs.

The NV centre, for example, as well as being created by trapping of mobile vacancies at nitrogen impurities during growth is believed to grow in as a unit. A nitrogen atom is incorporated into the surface but it is energetically unfavourable to bond a carbon atom above it due to the N-C antibonding orbital. This results in an increased probability of creating a vacancy above the nitrogen, creating an NV pointing out of the surface [1]. Significant success has been made growing diamond with oriented NV centres on {0 0 1} [2], {1 1 0} [1] and {1 1 1} [3, 4] substrates. The preferentially oriented NV grown on the {0 0 1} substrate were grown in to {1 1 0} surfaces resulting from step-flow growth [2]. On the (1 1 1) substrates the degrees of preferential orientation were determined as 94 % and 97 % along [1 1 1] [3, 4].

Growing-in defects has the disadvantage of a lack of control over their position and the relatively low nitrogen concentrations that can currently be achieved with CVD growth. Defects can be made in large concentrations (see chapter 7) and in specific locations by irradiation (and subsequent annealing where appropriate) [5–8]. To engineer defects we must be able to control their orientation as well as position. Defects created by annealing are orientationally degenerate within the restriction of their symmetry allowed sites. This degeneracy can be lifted by the application of stress [9].

8.2 Experimental details

8.2.1 Samples

The samples used were cut from type-IIa diamond grown by CVD on a {0 0 1} substrate. The details of the samples as prepared are given in table 8-1. Ten samples were prepared with pairs of (0 0 1) faces, polished for stress, and with areas in the range 1.39–2.02 mm^2. The remaining four faces were all {1 1 0} faces. The N_S^0 concentration was determined by EPR to be near to 100 ppb for all samples. The lengths of the samples were in the range 1.52–2.53 mm providing a good com-

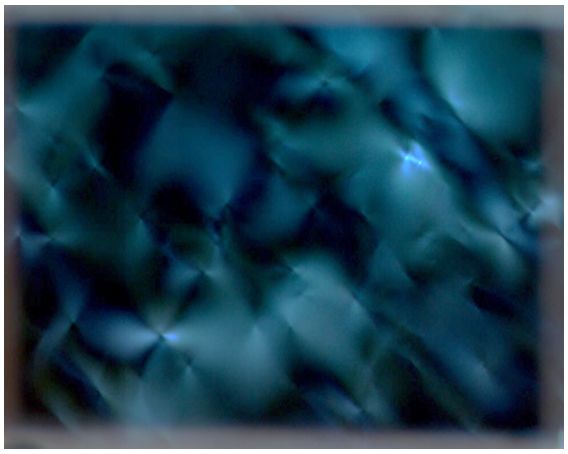

Figure 8-2 A {0 0 1} face of sample D viewed through crossed polarisers when illuminated with white light. The photo was taken after the sample was irradiated under stress.

promise between sample size for spectroscopy and face size for obtaining sufficient stress.

Sample	Mass (mg)	Stress ∥ [0 0 1] (GPa)	Dose (10^{17} e$^-$ cm^{-2})	$[N_S^0]_{initial}$ (ppb)
A	13.9	0.00	5.34	96(5)
B	11.5	0.00	5.34	107(6)
C	17.5	1.00	8.26	113(6)
D	11.2	1.45	8.26	93(5)
E	9.9	2.00	5.34	106(6)
F	8.6	2.10	5.34	101(6)
G	10.0	2.92	7.08	137(7)
H	12.9	3.00	7.08	116(6)

Table 8-1 List of samples referred to in this chapter. The N_S^0 concentration was determined by EPR prior to irradiation.

Figure 8-2 shows the birefringence in sample D when viewed down a [0 0 1] axis with crossed polarisers. The birefringence is caused by strain in the diamond, in turn caused by bundles of dislocations parallel to the growth axis [10]. A strain free diamond would appear completely dark. Such strains are common in diamond grown by CVD.

8.2.2 Irradiation

The electron irradiations were carried out at the Takasaki Advanced Radiation Research Institute, Japan Atomic Energy Agency. The accelerator employs a Cockcroft-Walton generator to create a voltage of up to 2.0 MeV. Electrons created by an electron gun are accelerated by this voltage through the evacuated beam tube and rastered back and forth by a beam scanner before exiting the evacuated beam tube through a titanium foil window. A beam current of up to 15 mA is produced giving a power output of 30 kW. Water cooling is used to prevent heating of apparatus.

The stress was applied to the samples using the optical stress probes previously described in §4.3.1. The probes were modified with water cooling to prevent heating of the samples. The cooling was a simple design consisting of a copper sleeve which made a slip fit the to end of the probe, with copper tubing wrapped around it and brazed in place 8-3b. A thermally conductive paste was applied between the probe and the sleeve when mounting it. During irradiation the probe temperature was measured with a thermocouple to not exceed 35 °C. All stresses were applied along a $\langle 0\,0\,1 \rangle$ axis, defined as $[0\,0\,1]$.

The beam width at the sample height was 120 cm allowing the use of two optical stress probes to be configured in parallel under the beam. An illustration of the setup with the probes configured in parallel is shown in figure 8-3. An additional water cooled plate with an aperture was positioned between the probes and the beam window to block unwanted flux.

10 µm aluminium foil was used as a gasket between the sample and the anvils to fill irregularities between the two surfaces. Great care was taken when mounting and unmounting samples to not apply a torque. Once samples were mounted the apparatus was positioned under the beam window and the gas pressure slowly increased to the desired value. Both probes were supplied gas by the same regulator; the gas pressure was therefore the same in each and the relative sample pressures were determined by differences in sample area.

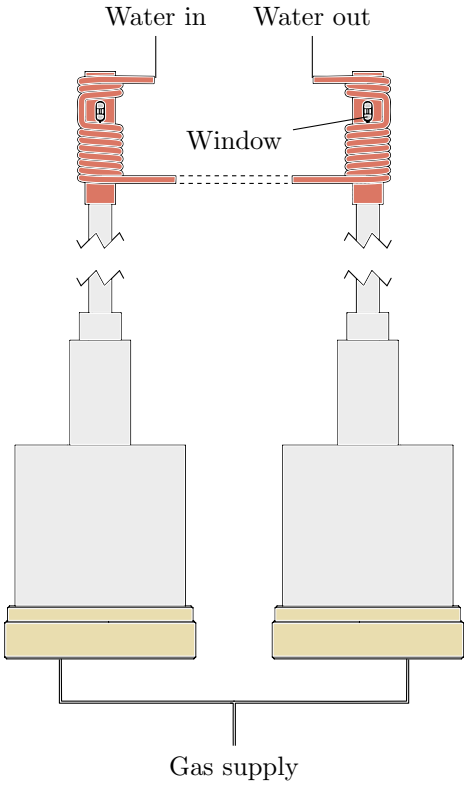

(a) Configuration

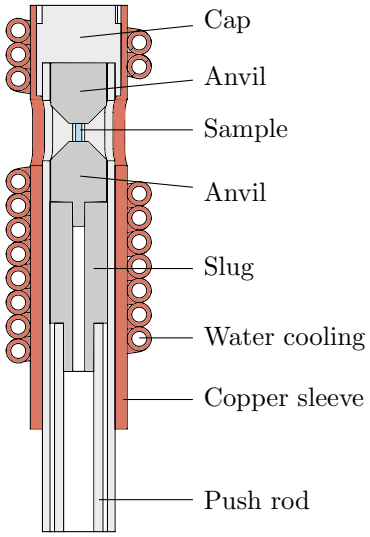

(b) Probe head cross section

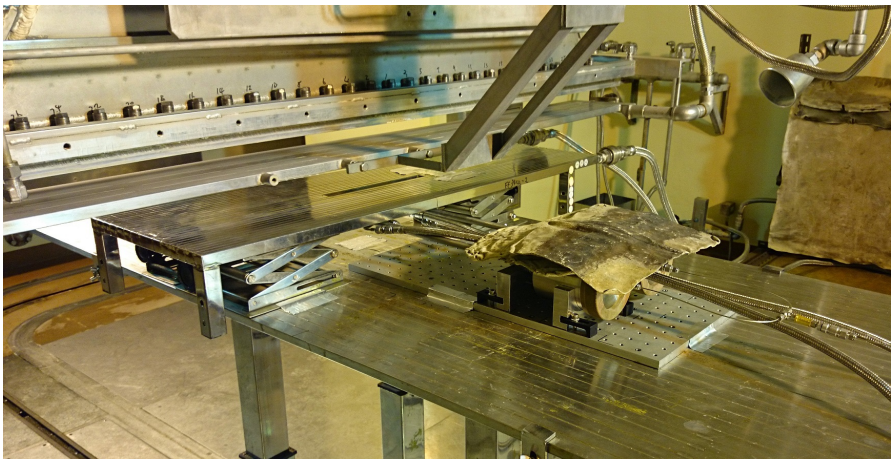

(c) Photo of probes in situ

Figure 8-3 Diagrams of modified uniaxial stress probes. Figure (a) shows a diagram of the optical stress probes modified with water cooling and connected in parallel, (b) shows a detailed cross-section of the water cooled probe head and (c) is a photo of the stress probes in situ.

8.2.3 EPR spectroscopy

X-band EPR measurements were made on a Bruker EMX-E spectrometer set up with a Bruker ER041X microwave bridge and Bruker ER4122SHQ spherical resonator. Samples were mounted in a dual axis goniometer allowing aligning to any specified crystal axes. Quantitative measurements were made by comparing the signal intensity to that of a diamond reference with a previously characterised spin concentration by FT-IR spectroscopy (see §4.2.2). Q-band EPR measurements were performed on a Bruker EMX spectrometer set up with a Bruker E41-KQ microwave bridge and Bruker cylindrical TE_{011} resonator. The sample was affixed to a Rexolite® rod on a known crystal face and aligned to a specified orientation with a single axis goniometer.

8.2.4 UV-visible absorption spectroscopy

A Perkin Elmer UV-vis Lambda 1050 dispersive spectrometer was used for UV-visible absorption spectroscopy. The samples were mounted in indium in an Oxford Instruments exchange gas cryostat and cooled to 77 K. The beam was depolarised with a Hanle depolariser before being split into sample and reference beams. The sample beam was then linearly polarised with a Glan-Thomspon polariser. Samples were all mounted such that the stressed [0 0 1] axis was vertical and with the {1 1 0} face normal to the beam.

8.2.5 Photoluminescence spectroscopy

Photoluminescence measurements were made on a Renishaw inVia Reflex Raman spectrometer. Samples were cooled to 77 K in a Linkam THMS600 microscope stage. A HeNe laser at 1.956 eV (632.8 nm) and a HeCd laser at 2.808 eV (441.6 nm) were used for excitation, focused to a spot size on the sample of ≈ 15 µm. The polarisation of the laser was rotated from $E_{\parallel}$ to $E_{\perp}$ using a half-wave plate. All spectra were normalised to the intensity of the Raman line at 1332 cm^{-1} and a correction made for the polarisation dependent detection efficiency.

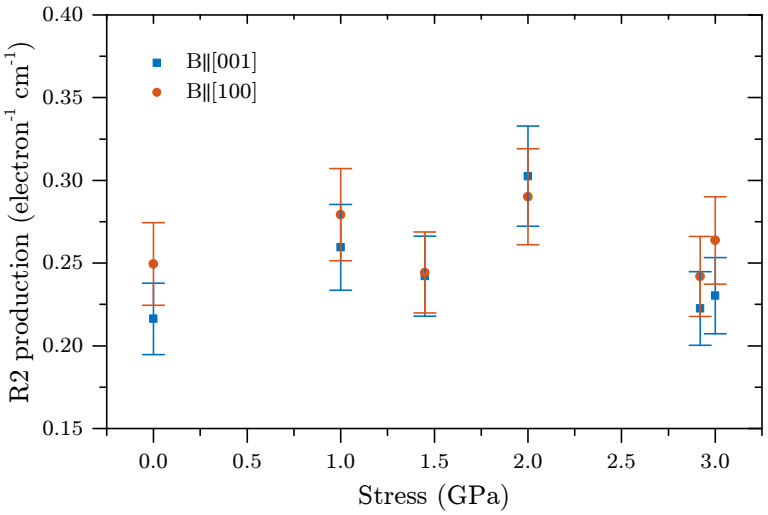

Figure 8-4 Production rate of R2 measured by the intensity of the inner high field line, with $\boldsymbol{B} \parallel [0\,0\,1]$ and $\boldsymbol{B} \parallel [1\,0\,0]$ directions. Preferential orientation of R2 would cause the $\boldsymbol{B} \parallel [1\,0\,0]$ measurement to overestimate the production of R2 while $\boldsymbol{B} \parallel [0\,0\,1]$ would underestimate it. A microwave power of 3.2 mW was used.

8.3 Results

A total of six samples were irradiated under stress across three runs with stresses ranging from 1.0–3.0 GPa. Of the six samples one (sample F) broke, cleaving after being irradiated under stress at 2.1 GPa. It is likely that the sample broke as it was removed from the stress probe rather than during the irradiation.

8.3.1 EPR

8.3.1.1 R2

The EPR of R2 arises from a thermally excited spin triplet state determined to be $\Delta E = 50(2)$ meV above the spin singlet ground state [11]. The intensity of the signal as a function of temperature can be derived from the Boltzmann distribution for two states

$$\frac{I(T)}{I(0)} = \left[1 + \frac{g_1}{g_2} \exp\left(\frac{\Delta E}{k_B T}\right)\right]^{-1}, \tag{8-1}$$

where $\frac{g_1}{g_2} = \frac{1}{3}$ is the ratio between the multiplicity of the lower and upper levels. At the lab temperature the correction is $I(0) = 3.40 \cdot I(294\ \mathrm{K})$.

The very broad lines of R2 significantly reduce the signal height for a given intensity compared with other defects in diamond, reducing the concentration sensitivity. With $\boldsymbol{B} \parallel \langle 0\,0\,1 \rangle$ the width of the inner high field line is about 3 mT, compared to 8 mT for the outer lines. This causes its signal height to be relatively high and thus the error is smaller when fitting to it. With $\boldsymbol{B} \parallel [0\,0\,1]$ the inner lines originate from the [1 0 0] and [0 1 0] sites and the outer lines from the [0 0 1] site. With $\boldsymbol{B} \parallel [0\,0\,1]$ the inner lines originate from the [0 1 0] and [0 0 1] sites and the outer lines from the [1 0 0] site. By comparing scans with $\boldsymbol{B} \parallel [0\,0\,1]$ and $\boldsymbol{B} \parallel [1\,0\,0]$, the relative site populations can be determined. In favour of concentration sensitivity of R2 it is difficult to saturate the R2 spin transitions and a relatively high microwave power can be used – EPR signal increases with the square root of the power.

Figure 8-4 shows the quantification of R2, normalised to the electron dose, for each sample with $\boldsymbol{B} \parallel [0\,0\,1]$ (the stress axis) and with $\boldsymbol{B} \parallel [1\,0\,0]$. If a preferentially oriented population of R2 had been created the two measurements would differ with one overestimating the total concentration and the other underestimating it. Despite the gain in signal to noise from measuring only the inner high field line it is not possible to determine any degree of preferential orientation. Considering the errors, the upper limit on preferential orientation of R2 was put at 25 % (from 33 %) in the [0 0 1] site and 75 % (from 67 %) in the [1 0 0] and [0 1 0] sites. The stress did not have any apparent effect on the production rate of R2.

To determine the degree of preferential orientation of R2 to a higher accuracy, EPR measurements were made at Q-band on sample G and sample A (irradiated without stress) for reference. At Q-band the smaller resonator size results in a larger filling factor and hence bigger signal. In addition the larger external magnetic field increases the spin polarisation at thermal equilibrium. Sample G had been irradiated under 2.92 GPa of stress and the resulting concentration of R2 was determined by quantitative EPR at X-band to be 0.9(2) ppm. Similar scans on all samples would have been impractical as the data for each sample took approximately six days to acquire.

The resulting spectra of sample G are shown in figure 8-5. By comparing the

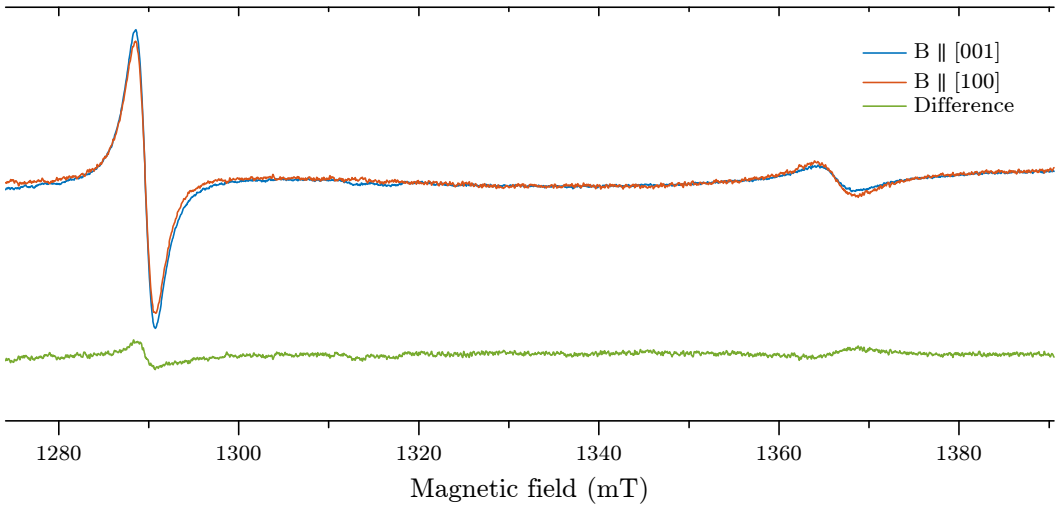

Figure 8-5 EPR spectra of high field R2 lines with $\boldsymbol{B} \parallel [0\,0\,1]$ and $\boldsymbol{B} \parallel [1\,0\,0]$ using a microwave frequency of 34.2 GHz and power of 0.85 mW. The sample was previously electron irradiated under a 2.92 GPa [0 0 1] stress. Fits to the spectra found 27(2) % of R2 population in the [0 0 1] site and 73(6) % in the [1 0 0] and [0 1 0] sites.

relative intensities of the lines for the two scans it is apparent that the inner line is largest in the $\boldsymbol{B} \parallel [0\,0\,1]$ spectrum and the outer line is largest in the $\boldsymbol{B} \parallel [1\,0\,0]$ spectrum. This is clear evidence that a small degree of preferential orientation was created. From fitting the inner and outer lines it was determined that the populations of R2 were 27(2) % in the [0 0 1] site (parallel to stress) and 73(6) % in the [1 0 0] and [0 1 0] sites (perpendicular to stress). At equilibrium the populations would be 33 % and 67 % respectively.

8.3.1.2 R1

In contrast to R2, the lines of R1 in irradiated type-IIa samples are very narrow (< 10 µT) making a good signal to noise ratio easily obtainable. The narrow lines however, together with a large zero field splitting, make alignment of R1 spectra very tedious (misalignment of ≈ 0.01° split the spectrum into many lines). R1 was therefore quantified from its $\Delta m_S = \pm 2$ transitions analogous to how NV^- was quantified in this thesis (§5.2.7.3). Being far less sensitive to crystal alignment and saturation, this significantly reduces errors to the region of 10 %.

A diagram of R1 is shown in figure 2-2a. The defect has $\mathscr{C}_{1h}$ symmetry hence there

are twelve distinct lattice sites. The additional carbon atom over R2 reduces the symmetry, splitting each of the ⟨0 0 1⟩ sites into four. The interstitial atoms of R1 cause a distortion in the [0 0 1] direction hence we would expect its behaviour to be the same as for R2: a stress along [0 0 1] would decrease the populations of the four [0 0 1] sites and increase the populations of the four [1 0 0] and [0 1 0] sites.

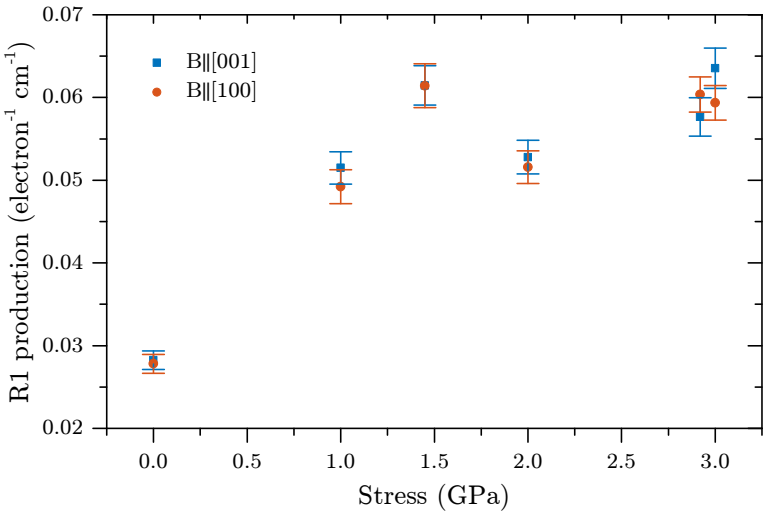

Figure 8-6 Production rate of R1 with $\boldsymbol{B} \parallel [0\,0\,1]$ and $\boldsymbol{B} \parallel [1\,0\,0]$. With $\boldsymbol{B} \parallel [0\,0\,1]$ the measurement was of the [1 0 0] and [0 1 0] groups of sites, whereas with $\boldsymbol{B} \parallel [0\,0\,1]$ quantification was of the [1 0 0] and [0 1 0] groups of sites. Therefore if R1 was preferentially oriented we would see a difference in the two measurements. A microwave power of 13 µW was used.

The production rate of R1 measured with $\boldsymbol{B} \parallel [0\,0\,1]$ and $\boldsymbol{B} \parallel [1\,0\,0]$ for each sample is shown in figure 8-6. With $\boldsymbol{B} \parallel [0\,0\,1]$ the measurement was of the [1 0 0] and [0 1 0] sets of sites; with $\boldsymbol{B} \parallel [1\,0\,0]$ the measurement was of the [0 1 0] and [0 0 1] sets of sites. The lack of any clear difference in the respective measurements indicates that there was no preferential orientation of R1. The production rate however appears to double from no stress to 3.00 GPa stress. This interpretation should be made with caution since it is based on one sample.

8.3.1.3 Other EPR defects

From the Q-band measurements it became evident that stress had affected a number of other defects. Q-band spectra of sample G with $\boldsymbol{B} \parallel [0\,0\,1]$ and $\boldsymbol{B} \parallel [1\,0\,0]$ are shown in figure 8-7. The central group of lines is attributed to the R3 and R14

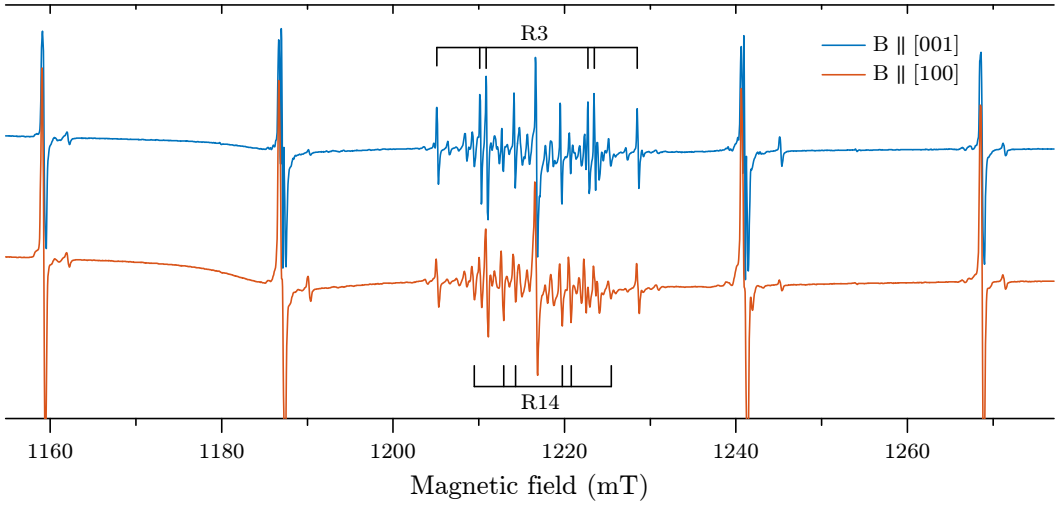

Figure 8-7 EPR spectra with $\boldsymbol{B} \parallel [0\,0\,1]$ and $\boldsymbol{B} \parallel [1\,0\,0]$ using a microwave frequency of 34.2 GHz and power 0.85 mW. The sample was previously electron irradiated under a 2.92 GPa [001] stress. The clipped lines are R1.

defects (indicated in the figure) amongst others. Comparing the intensities of the R3 and R14 lines in the two spectra it is clear that there is significant preferential orientation of the defects. A set of lines are seen to the high field side of R1 with an apparently similar zero field splitting. The relative intensities of the high and low field lines is different in the two scans. These lines were visible in sample A but were much weaker and with no apparent anomalies in intensities. A small O3 (tri-interstitial [12]) signal was seen in sample G but not in A.

8.3.2 Optical absorption

UV-vis absorption spectra were recorded over the range 200–800 nm for all samples with light linearly polarised with $\boldsymbol{E} \parallel [0\,0\,1]$ and $\boldsymbol{E} \parallel [1\,1\,0]$ – parallel and perpendicular to the [0 0 1] stress axis respectively. A diagram illustrating the orientation of the sample relative to stress and light polarisation is give in figure 8-8. Example spectra of sample H, which was irradiated under 3.0 GPa, are shown in figure 8-9. As expected in an irradiated type-IIa diamond the largest absorption is from GR1 with smaller absorptions seen from $C^0_{I_{001}}$, 3H, TR12, GR2-8 and ND1. The only absorption which shows a clear polarisation dependence is 3H, being largest with $\boldsymbol{E} \parallel [0\,0\,1]$, visible as a small peak in the difference spectrum in figure 8-9.

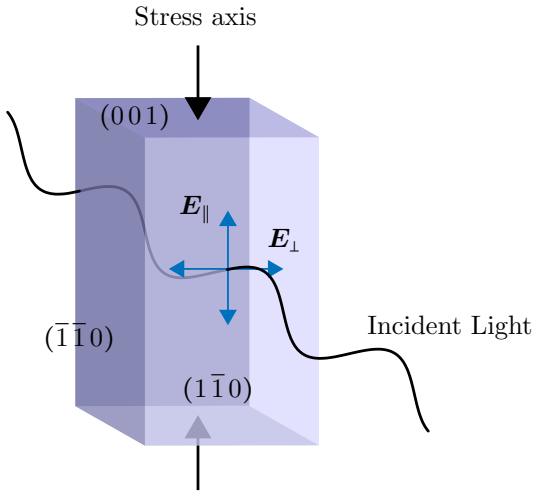

Figure 8-8 Diagram of orientation of sample relative to stress and polarisation of light in optical experiments. $\boldsymbol{E}$ is indicated parallel and perpendicular to the stressed [0 0 1] axis.

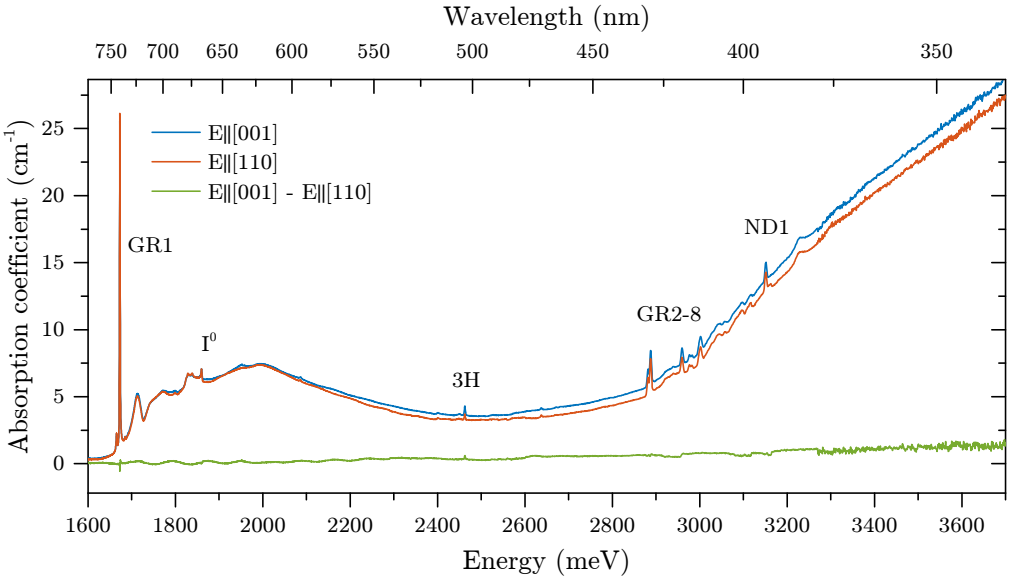

Figure 8-9 Absorption spectra of sample SF1 at 77 K with light linearly polarised with $\boldsymbol{E} \parallel [1\,1\,0]$ and $\boldsymbol{E} \parallel [0\,0\,1]$. The sample was irradiated whilst held under a 3.00 GPa [0 0 1] uniaxial stress.

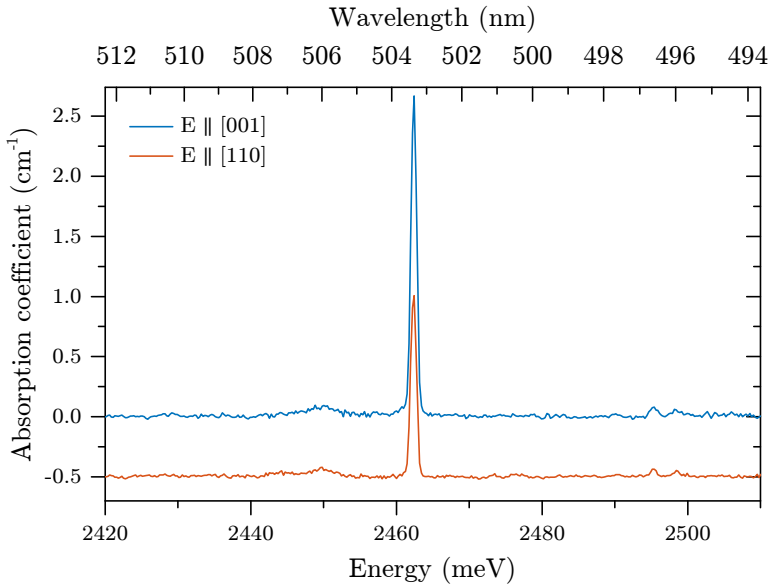

Figure 8-10 Absorption spectra of 3H defect at 77 K in sample H with light linearly polarised with $\boldsymbol{E} \parallel [1\,1\,0]$ and $\boldsymbol{E} \parallel [0\,0\,1]$. The sample was stressed irradiated whilst held under a 3.00 GPa [0 0 1] uniaxial stress. Spectra are offset for clarity.

8.3.2.1 3H

Since the 3H absorption was of small intensity, spectra of it were recorded about a narrow range to increase the signal to noise ratio, again with light linearly polarised with $\boldsymbol{E} \parallel [1\,1\,0]$ and $\boldsymbol{E} \parallel [0\,0\,1]$. The resulting spectra from sample H, irradiated under a 3.00 GPa [0 0 1] stress, are shown in figure 8-10. The intensity of the absorption is seen to be roughly twice as strong with $\boldsymbol{E} \parallel [0\,0\,1]$ compared to with $\boldsymbol{E} \parallel [1\,1\,0]$.

The intensities of the 3H absorptions with both polarisations are shown in figure 8-11a and the ratios of the polarisations in figure 8-11b. The intensity of the 3H absorption, normalised to electron dose, was increased by a factor of approximately six by the 3.00 GPa stress. The increase in absorption with dose was however somewhat erratic. Despite the variation in absorption intensity the ratio of the absorptions with the two polarisations are consistent.

The sample irradiated without an applied stress does not show a polarisation dependence as expected; those with stress all show a strong dependence. The ratio of the two measurements is approximately 1.7(1) for all stressed samples,

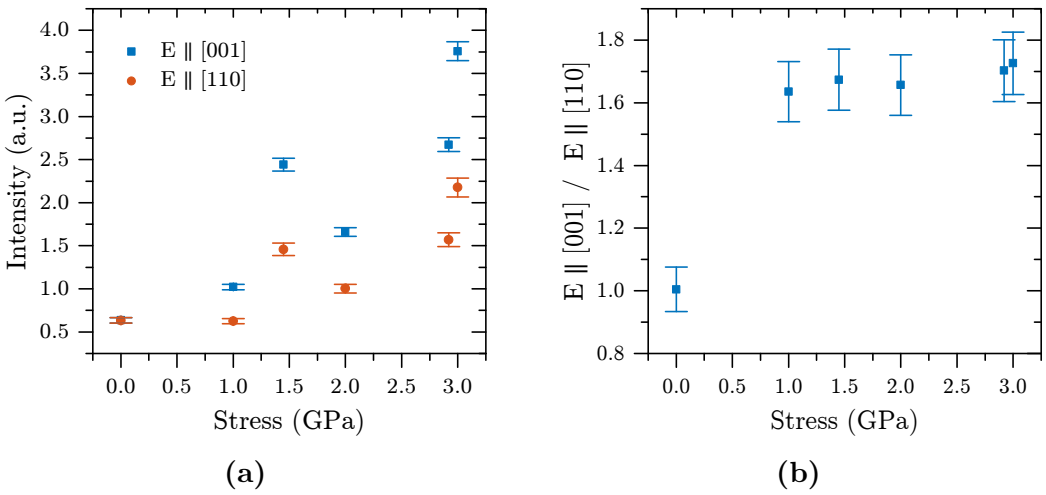

Figure 8-11 3H absorption measurements made at 77 K for all samples. Spectra were recorded with light linearly polarised with $\boldsymbol{E} \parallel [0\,0\,1]$ and $\boldsymbol{E} \parallel [1\,1\,0]$. Figure (a) shows the intensity of 3H with the two polarisations of light, normalised to the electron dose and (b) shows the ratio of the two measurements.

however a small increase is observed to higher stress. There is clearly a dramatic change with a stress < 1 GPa but unfortunately no samples were stressed within this range.

The symmetry of 3H has previously been determined to be $\mathscr{C}_{2v}$ with a $\langle 1\,1\,0 \rangle$ dipole [13] and it has been argued to correspond to the Humble form of the di-interstitial [14]. The six lattice sites of the Humble defect are shown in figure 8-12. Take for example a stress along the $[0\,0\,1]$ axis. The $[1\,1\,0]$ and $[\bar{1}\,1\,0]$ sites have their C_2 axes parallel to $[0\,0\,1]$ and the remaining four have their C_2 axes perpendicular to $[0\,0\,1]$. If the interstitial atoms cause a distortion along the C_2 axis then a stress along $[0\,0\,1]$ will increase the energy of the $[1\,1\,0]$ and $[\bar{1}\,1\,0]$ sites over the others. Thus $[0\,\bar{1}\,1]$, $[0\,1\,1]$, $[1\,0\,1]$ and $[1\,0\,\bar{1}]$ will be created preferentially.

The interaction of light with an electric dipole is given by $\hat{\mathscr{H}}_{opt} = -\boldsymbol{p} \cdot \boldsymbol{\epsilon}$, where $\boldsymbol{p}$ is the dipole moment, and $\boldsymbol{\epsilon}$ is a plane wave (§3.2.1). For linearly polarised light the relative intensities of the absorptions from each site for 3H can be calculated as $\boldsymbol{p} \cdot \boldsymbol{E} / |\boldsymbol{p}|\,|\boldsymbol{E}|$ and are given in table 8-2.

For an equal population over all sites the ratio of the absorption intensities would

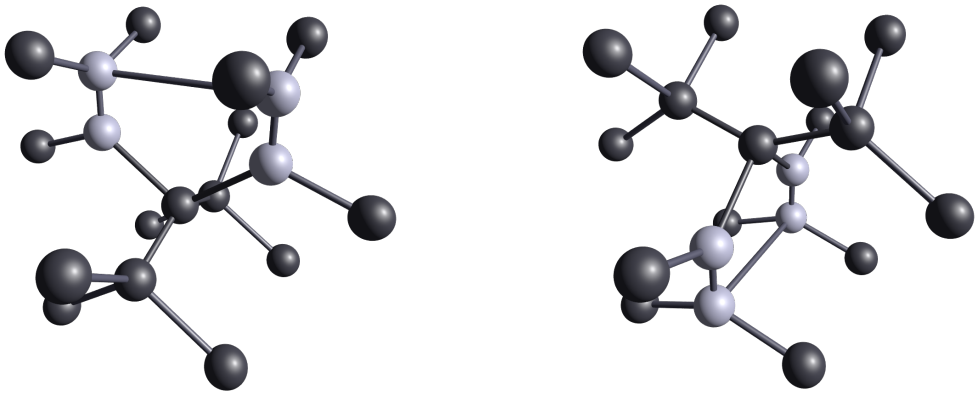

[1 1 0]

[$\bar{1}$ 1 0]

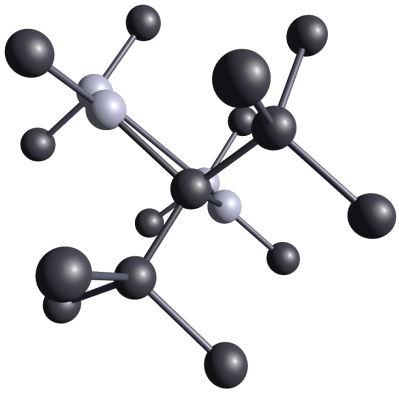

[0 $\bar{1}$ 1]

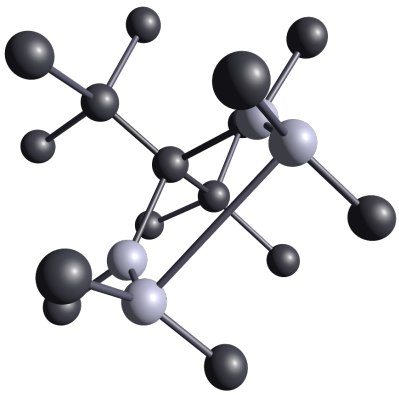

[0 1 1]

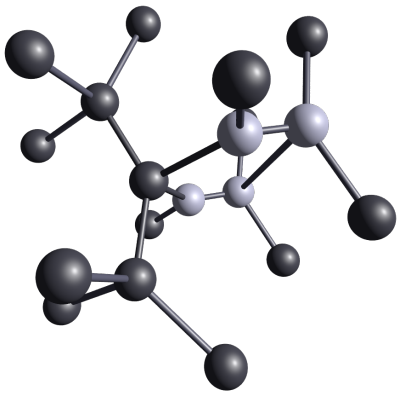

[1 0 1]

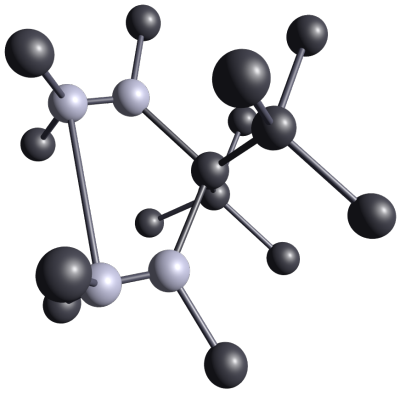

[1 0 $\bar{1}$]

Figure 8-12 The six sites of the Humble di-interstitial defect, consisting of two [0 0 1]-split interstitials at next neighbour sites. The [0 0 1]-split interstitials are indicated in light grey.

Site	Dipole axis	Intensity	
		$\boldsymbol{E} \parallel [0\,0\,1]$	$\boldsymbol{E} \parallel [1\,1\,0]$
1	$[1\,1\,0]$	0	1/2
2	$[\bar{1}\,1\,0]$	0	0
3	$[0\,\bar{1}\,1]$	1/4	1/8
4	$[0\,1\,1]$	1/4	1/8
5	$[1\,0\,1]$	1/4	1/8
6	$[1\,0\,\bar{1}]$	1/4	1/8

Table 8-2 Relative intensities for different sites of a $\mathscr{C}_{2v}$ defect with a $[1\,1\,0]$ dipole moment with $\boldsymbol{E} \parallel [0\,0\,1]$ and $\boldsymbol{E} \parallel [1\,1\,0]$.

be

$$\frac{I(E_\parallel)}{I(E_\perp)} = 1\,, \tag{8-2}$$

and for a 100 % preferential population into the perpendicular sites

$$\frac{I(E_\parallel)}{I(E_\perp)} = 2\,. \tag{8-3}$$

In figure 8-11b the ratio of 1.7(1) indicates a significant degree of preferential population. In reality the ratio will be reduced by the efficiency of the linear polarisation, birefringence in the sample and any errors in alignment between the sample and the polarisation. That the ratio in figure 8-11b is approximately constant for stress greater than 1 GPa suggests near 100 % preferential population.

8.3.2.2 Vacancies

GR1 was quantified using the calibration constant $f_{GR1} = 1.2(3) \times 10^{-16}\,\mathrm{meV\,cm^2}$ [15]. Figure 8-13 shows the production of GR1 against stress, along with the production of $C^0_{I_{001}}$ for comparison. The production rate is given in the conventional units of number of defects $\mathrm{e^{-1}\,cm^{-1}}$, however, it should be noted that the penetration depth of 2 MeV electrons in diamond is ≈ 3 mm [16]. The interaction up to the penetration depth is reasonably constant with a sharp drop at the penetration depth. The samples in this study were in the range 0.80–1.13 mm thick, thus approximately two thirds of electrons passed through the sample. If we assume the effective dose is one third of the incident dose then the vacancy production rate with no stress is increased to $1.4\,\mathrm{V\,e^{-1}\,cm^{-1}}$, close to the value of $1.53(10)\,\mathrm{V\,e^{-1}\,cm^{-1}}$ given in [11].

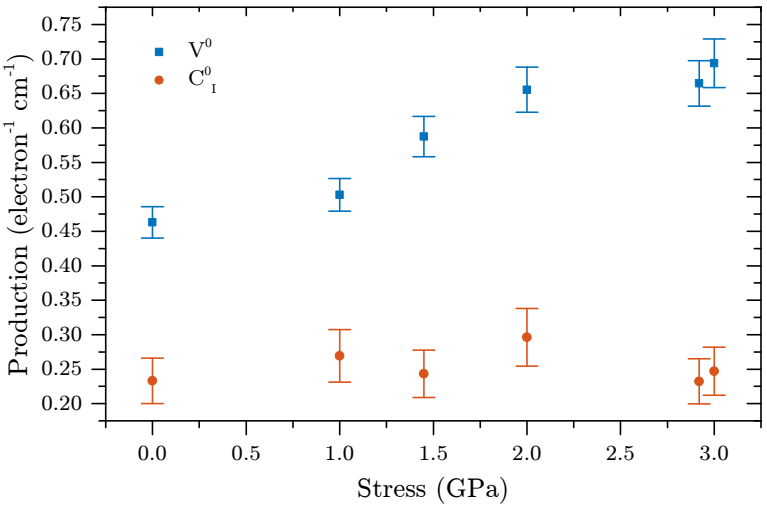

Figure 8-13 Production rate of V^0 determined from the GR1 ZPL at 1.673 eV, compared with that for $C^0_{I_{001}}$ from EPR of R2.

There is a clear positive correlation between the applied stress and vacancy production with the latter increasing by a factor of 1.5(1) between 0 GPa and 3.00 GPa, in contrast to constant production of $C^0_{I_{001}}$. ND1 was also quantified from figure 8-9 (using the calibration constant $f_{ND1} = 4.8(2) \times 10^{-16}$ meV cm^2 [15]) to be 85(9) ppb, in line with the starting N^0_S concentration and the condition $[V] \gg [N^0_S]$.

8.3.3 Photoluminescence

The spectra recorded with 1.956 eV excitation were dominated by GR1 luminescence. Since GR1 has $\mathscr{T}_d$ symmetry, no dependence on the excitation polarisation was expected, as seen in the UV-vis absorption measurements. A large number of lines were observed with 2.808 eV excitation. The largest of which were at 2.156 eV (NV^0), 2.437 eV (TR12 LVM), 2.463 eV (3H), 2.519 eV, 2.527 eV, 2.536 eV and 2.637 eV (TR12).

Since the light was focused to a 15 µm spot, the measurement is not a bulk measurement and variations across the sample can lead to misleading results. Therefore averages were made of measurements with both polarisations at three different locations on the sample. The standard deviation from these measurements is given as the error. From figure 8-14a and figure 8-14c there was significant variation in the intensities of both 3H and TR12 across the sample for those stressed at the

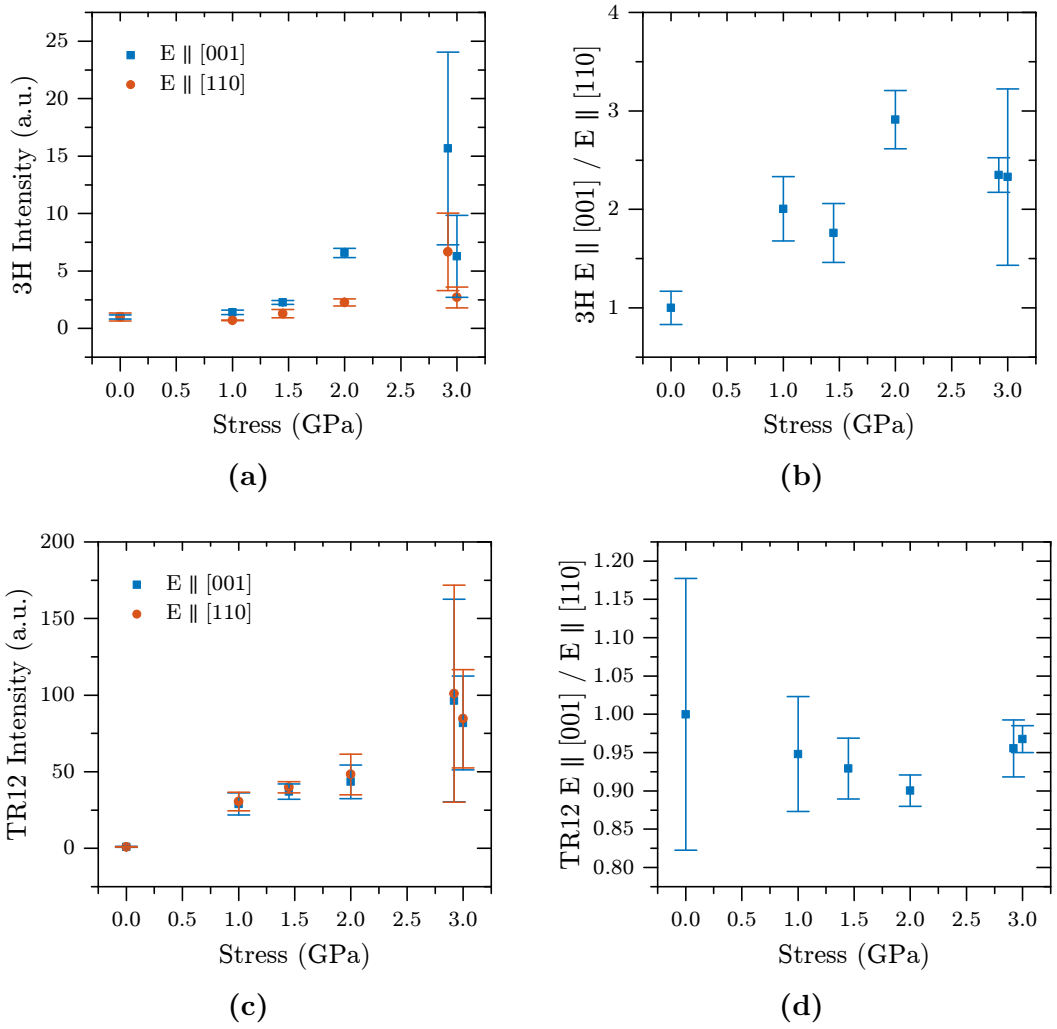

Figure 8-14 PL measurements of the TR12 line at 2.637 eV and the 3H line at 2.464 eV made at 77 K with 2.808 eV excitation. Spectra were recorded with the laser polarised with $\boldsymbol{E} \parallel [0\,0\,1]$ and $\boldsymbol{E} \parallel [1\,1\,0]$. Intensities are normalised to the Raman line and a correction has been made for the polarisation dependent detector efficiency. Averages have been made from a number of measurements over each sample, the standard deviation of which is given by the error bars. Figures (a) and (c) show the intensity of 3H and TR12 under the two polarisation for each stress and (b) and (d) show the ratios between them.

highest stress.

The NV was present before irradiation (although irradiation will have caused the charge transfer $NV^- \rightarrow NV^0$ since $[V^-] \approx [N_S]$) and as expected showed no polarisation or stress dependence. The lines at 2.519 eV, 2.527 eV and 2.536 eV are unidentified but did not show any dependence on polarisation or stress. The 3H and TR12 lines were both found to increase in intensity with stress; 3H increased

by a factor of up to ≈ 25 (figure 8-14a) and TR12 by a factor of up to ≈ 170 (figure 8-14c) between 0 and 3.00 GPa. The 3H intensity was dependent on the laser polarisation. With $\boldsymbol{E} \parallel [0\,0\,1]$ the intensity was a factor of ≈ 2 greater than with $\boldsymbol{E} \parallel [1\,1\,0]$ (figure 8-14b), consistent with the absorption data. The intensity of TR12 did not change with laser polarisation (figure 8-14d).

8.4 Discussion

In type-IIa diamond, for irradiation at room temperature, the production of the single interstitial $C^0_{I_{001}}$ is much lower than the vacancy production [11]. Lattice displacements create Frenkel pairs and so the total number of interstitials and vacancies must add up; clearly there are a large number of interstitials in other forms. A number of other forms have been identified such as the R1 di-interstitial and O3 tri-vacancy and more tentatively assigned such as the Humble di-interstitial (3H). The production of R1 is approximately 10 % of R2 production [17], therefore defects such as 3H might exist in large concentrations.

For interstitials to aggregate into interstitial or interstitial-vacancy complexes requires that they are mobile during the irradiation. The thermal activation energy required for the migration of $C^0_{I_{001}}$ however has previously been determined as 1.6(2) eV [18, 19], requiring temperatures of several hundred degrees and so is not possible in a temperature controlled irradiation. It has been proposed that during electron irradiation the interstitials exists in the more mobile form C^*_I, and are able to migrate with a much lower activation energy of 0.3 eV [20]. Either C^*_I is an excited state with a lower migration energy, or it occupies different lattice sites with different charge states, allowing it to migrate as it changes charge state.

In chapter 9 the orientation of $C^0_{I_{001}}$ was found to depend strongly on stress, with high degrees of preferential orientation at stresses of 1.0 GPa for temperatures at which it is mobile. In this study, even up to stresses of 3.0 GPa, there was very little preferential orientation of $C^0_{I_{001}}$. This is consistent with it being immobile at the irradiation temperature and the interstitial complexes being formed by its migration as C^*_I. We do not know the symmetry of C^*_I and so can only speculate

on its behaviour under stress. The very small amount of preferential orientation of $C^0_{I_{001}}$ observed could be accounted for by some local heating and Boltzmann statistics giving a low reorientation rate.

Figure 8-13 shows an increase in vacancy production with stress whist $C^0_{I_{001}}$ production remains constant within error. Possible explanations are that:

1. stress causes a reduction in the displacement energy T_d,
2. potential barriers associated with forming complexes are changed,
3. potential barriers to interstitial-vacancy recombination are increased.

Since the stress causes a small compression of the lattice, it seems unlikely that any potential barriers will be decreased, and so the latter reason seems most probable. If the interstitials do not recombine with vacancies their probability of forming complexes is increased, leading to the increased production of the di-interstitials R1 and 3H, TR12 and O3, as observed.

The energetically favourable structure of the di-interstitial is calculated to be the diamagnetic Humble configuration at 0.7 eV lower in energy than R1 [14]. R1 and the Humble configuration could both form by the combination of two C^*_I or the combination of one C^*_I with $C^0_{I_{001}}$. In both R1 and 3H, the component $C^0_{I_{001}}$ interstitials are aligned parallel to each other. However, it is found that only 3H is preferentially oriented when a uniaxial stress is applied; such preferential alignment of the interstitials away from the [0 0 1] applied stress seems plausible. However, this new finding, taken in combination with the fact that R1 anneals out at lower temperatures than $C^0_{I_{001}}$, and that the concentration of 3H can be increased by annealing (at temperatures where $C^0_{I_{001}}$ is mobile) raises questions about the production mechanism of both, and potential interconversion between them.

The formation of di-interstitials should be a second order process, thus a higher concentration of C^*_I will cause a larger percentage conversion. This could explain the lack of an observed increase in $C^0_{I_{001}}$ production as large as the increase in vacancy production. An increase in $C^0_{I_{001}}$ would still be present but it would be smaller than that seen with vacancies. Similar results might be found by changing

the beam current.

The production of all observed interstitial complexes increased with stress. That all (observed) interstitials increased, rather than some increasing at the expense of others, implies that there is a common cause. This is consistent with an increased interstitial concentration from a decrease in the probability of interstitial-vacancy recombination.

The samples used in this study were grown by CVD and exhibited birefringence originating from strain. The birefringence of one sample after irradiation is shown in figure 8-2. Since the production rates of interstitial complexes has been found to be effected by the uniaxial stress it is very likely that the strain in the diamond does the same, explaining some conflicting interstitial production rates. For example in this study the production without stress was measured to be $0.23(3)\,\mathrm{eV}^{-1}\,\mathrm{cm}^{-2}$. Correcting for the effective dose gives a rate of approximately $0.6\,\mathrm{eV}^{-1}\,\mathrm{cm}^{-2}$ compared to a rate of $0.1\,\mathrm{eV}^{-1}\,\mathrm{cm}^{-2}$ measured in HPHT-grown samples [17]. This also potentially explains why for the local PL measurements large variations in spectra were seen with the location of the measurement, corresponding to variations in strain over the diamond.

8.5 Conclusions

Samples were successfully irradiated under [0 0 1] uniaxial stresses up to 3.0 GPa. The samples have subsequently been characterised by EPR, UV-Vis and PL spectroscopies. Typical irradiation damage products were observed such as the EPR defects R1, R2 and smaller signals from R3, R14 and O3 amongst others and the optical centres GR1, 3H and TR12. The production rates and preferential orientations of defects, where applicable, have been characterised.

Stress affected the production rates of a number of defects, most notably increasing the production of the interstitial aggregates, 3H, TR12 and tentatively R1. The production of V^0 also increased with stress however no change in the production rate of $C^0_{I_{001}}$ was detected. The implication is that the stress increases the barrier to interstitial-vacancy recombination, enhancing the vacancy production.

The corresponding enhanced interstitial production increases the production of interstitial complexes.

Only a small preferentially orientated population of $C^0_{I_{001}}$ resulted from irradiating samples under a [0 0 1] stress. The only defect for which a significant preferential orientation was measured was 3H. That $C^0_{I_{001}}$ did not preferentially orientate is consistent with the existence of single interstitials in an excited state C^*_I, which migrates with a low activation energy, unimpeded by the stress. On returning to the ground state it becomes locked-in to whichever position it was in. The preferential orientation of 3H but not of R1 indicates an important difference in their production mechanisms.

PL measurements varied quite considerably across the sample suggesting that strain had a significant effect on damage rates and the formation of complexes. This is consistent with the increased production of complexes with stress.

8.6 Further work

As the first experiment of its kind there are many further experiments that could be done. Firstly, now we have an idea of what to expect, it would be of benefit to repeat the experiment but with higher irradiation doses of order $10^{18}\,\mathrm{eV\,cm^{-2}}$ and stresses in the range 0.0–1.0 GPa. The higher doses would significantly reduce the errors in the difficult EPR measurements and lower stresses would investigate the dose dependence of R1 and orientation dependence of 3H.

Stress was only applied along [0 0 1]. A [1 1 0] stress for example should orientate the Humble di-interstitial into two of its six sites rather than four for the [0 0 1] stress and would potentially give more insight into the formation trajectories of 3H and R1.

As an extension, it would be interesting to investigate the response of defect production with stress at low temperatures. At low temperatures of approximately 100 K the interstitial production approaches the vacancy production [17] as the migration of C^*_I is switched off. At temperatures where it is just able to migrate

($\approx$ 200 K) the stress perturbation will potentially be able to affect it, providing insight into its properties and symmetry.

Another parameter which is worth investigating is the type of sample irradiated. It would be interesting to see whether differences would be observed in irradiation of low strain HPHT samples. So far we have only considered type-IIa diamond; there are a host of additional processes to explore in type-Ib diamond. In particular, if nitrogen interstitials are formed during irradiation it is very likely that stress will be able to alter their formation.

References

1. A. M. Edmonds et al., *Physical Review B* **86**, 035201 (2012).
2. L. M. Pham et al., *Physical Review B* **86**, 121202 (2012).
3. J. Michl et al., *Applied Physics Letters* **104**, 102407 (Mar. 2014).
4. M. Lesik et al., *Applied Physics Letters* **104** (2014).
5. B. Naydenov et al., *Applied physics letters* **95**, 181109 (Nov. 2009).
6. J. O. Orwa et al., *Journal of Applied Physics* **109**, 083530 (2011).
7. B. K. Ofori-Okai et al., *Physical Review B* **86**, 081406 (Aug. 2012).
8. S. Sangtawesin et al., *Applied Physics Letters* **105**, 063107 (2014).
9. T. Karin, S. Dunham, K.-M. Fu, *Applied Physics Letters* **105**, 053106 (Aug. 2014).
10. H. Pinto, R. Jones, *Journal of Physics: Condensed Matter* **21**, 364220 (2009).
11. D. C. Hunt et al., *Physical Review B* **61**, 3863–3876 (Feb. 2000).
12. D. C. Hunt et al., *Physical Review B* **62** (2000).
13. H. E. Smith, PhD thesis, King's College London, 2004.
14. J. P. Goss et al., *Physical Review B* **63**, 195208 (Apr. 2001).
15. D. Twitchen et al., *Diamond and Related Materials* **8**, 1572–1575 (Aug. 1999).
16. B. Campbell et al., *Nuclear Instruments and Methods in Physics Research A* **476**, 680–685 (2002).
17. D. J. Twitchen et al., *Physica B* **273-274**, 628–631 (1999).
18. L. Allers, A. T. Collins, J. Hiscock, *Diamond and Related Materials* **7**, 228–232 (1998).
19. D. Hunt, PhD thesis, University of Oxford, 1999.
20. M. E. Newton et al., *Diamond and Related Materials* **11**, 618–622 (2002).

9

Annealing under uniaxial stress

9.1 Introduction

As discussed in chapter 8, applying stress to a sample can lift the orientational degeneracy of a defect. When there is sufficient thermal energy for it to overcome the barrier to reorientation it can preferentially orientate. Whereas in that chapter the focus was on defects which are mobile as they are created during irradiation, here we are concerned with manipulating defects; this is achieved by providing sufficient thermal energy for reorientation with the diamond under stress, causing the defect to preferentially orientate away from the stress.

There are significant challenges with simultaneous heating of a sample and application of stresses large enough to sufficiently lift degeneracy. Diamond has a large bulk modulus of 443 GPa [1], requiring a 4.43 GPa pressure for a 1 % volume change. For comparison the bulk modulus of silicon is 97.8 GPa [2]. For GPa pressures to be applied successfully (without the sample breakage) the force must be applied to parallel faces and torque minimised. Typically, metal anvils and apparatus are used to apply large uniaxial forces. Heating of the metal softens it and causes thermal expansion, resulting in non-uniaxial forces and torque.

Experiments were successfully made by Ammerlaan and Burgemeister on the reorientation of N_S^0, for which the barrier to reorientation is sufficiently low for it to occur at room temperature [3]. The sample was cooled whilst held under stress

to freeze in preferential orientation and then transferred whilst cold to an EPR spectrometer for investigation. Although the experiment did not involve heating, it did demonstrate the successful preferential orientation of defects. In a promising experiment by Hunt et al. an irradiated sample was annealed under 0.6 GPa [0 0 1] stress at 247 °C in a tube furnace to investigate the preferential orientation of the ⟨0 0 1⟩-split self interstitial ($C^0_{I_{001}}$) [4]. After the anneal $C^0_{I_{[0\,0\,1]}}$ was found to have decreased by about 30 %, while $C^0_{I_{[1\,0\,0]}}$ and $C^0_{I_{[0\,1\,0]}}$ had increased by 15 % each. The total concentration of R2 had not changed within error. The sample was then subjected to the same anneal but without stress. Again the total concentration did not change but the site populations returned to equilibrium.

In this chapter results of further experiments on the preferential orientation of $C^0_{I_{001}}$ are presented. The problems associated with heating the apparatus were overcome by heating the sample directly with a CW laser. The apparatus is still heated indirectly by thermal conduction through the sample, but can be kept at a constant temperature by appropriate cooling, creating a large temperature gradient between it and the sample. The temperature of the diamond was easily maintained at 200–300 °C above the temperature of the apparatus.

9.2 Experimental details

9.2.1 Samples

Critical to the success of the experiment was a high concentration of R2. Samples were prepared from a type-IIa {0 0 1} grown plate, of thickness 0.8 mm, previously irradiated with fast neutrons to a dose of 1×10^{18} n cm^{-2} (sample IIa-A from chapter 7). The sample was subsequently laser cut into four samples, each of dimension 1.50 mm by 1.50 mm and polished to remove graphitisation from the cutting process. The R2 concentration after the irradiation, but before laser cutting, was determined to be 66(7) ppm. Unfortunately heat from the laser cutting annealed out a varying amount of R2 in the four samples. The samples with the largest remaining concentrations of $C^0_{I_{001}}$ at 47(5) ppm and 14(2) ppm were used for the

experiments here.

9.2.2 Annealing

A LIMO Lissotschenko Mikrooptik solid state diode CW laser capable of delivering 40 W of output power at 983 nm was used as a heat source. The laser was coupled directly into an armoured fibre optic cable, the output of which was focussed with a lens with a working distance of 55 mm to a spot of approximately 1 mm. As the maximum annealing temperature used was 350 °C, graphitisation of the sample was not a concern and the annealing was performed in atmosphere.

The samples were mounted in the optical stress probe previously described in §4.3.1 with their largest faces against the anvils. Aluminium foil of thickness 10 µm was used as a gasket between the sample and the anvils to fill irregularities in the mating surfaces. The laser was focussed on the sample through one window in the probe and a small type K thermocouple positioned on the sample through the other opposite window. A diagram of the set-up is shown in figure 9-1a. A small amount of silicone thermal grease was used to thermally contact the thermocouple to the sample.

Tests were carried out with and without the water cooling used in chapter 8 for the stressed irradiation experiments (see figure 8-3). Although the tests with the water cooling successfully demonstrated a thermal gradient between the sample and apparatus, the temperatures reached at the sample were not quite sufficient for interstitial reorientation. Annealing was therefore performed without it. With small modifications to the design sufficient temperatures could be achieved with the water cooling, increasing temperature stability and reducing thermal expansion of the apparatus.

Gas pressure was increased in the stress probe slowly to obtain the desired stress. Once the pressure was stable the sample was heated whilst the temperature was monitored with the thermocouple. The laser power was adjusted to maintain the desired temperature. After approximately 5 min heating a stable temperature was reached of ±2 °C. Once the anneal was complete the probe was allowed to cool to

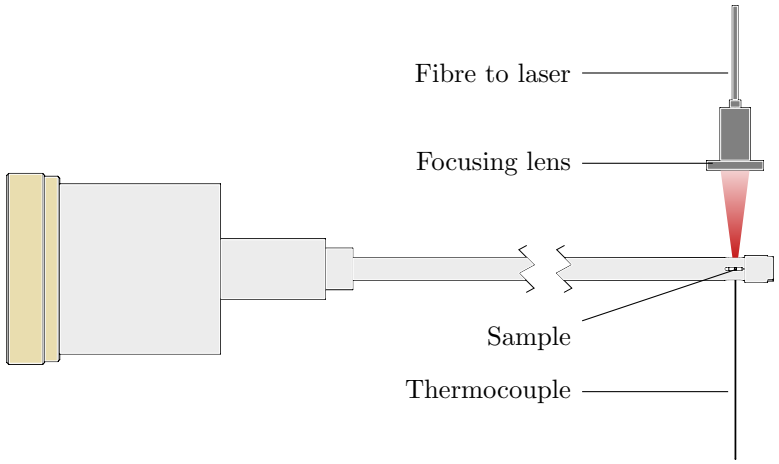

(a) Diagram of apparatus layout

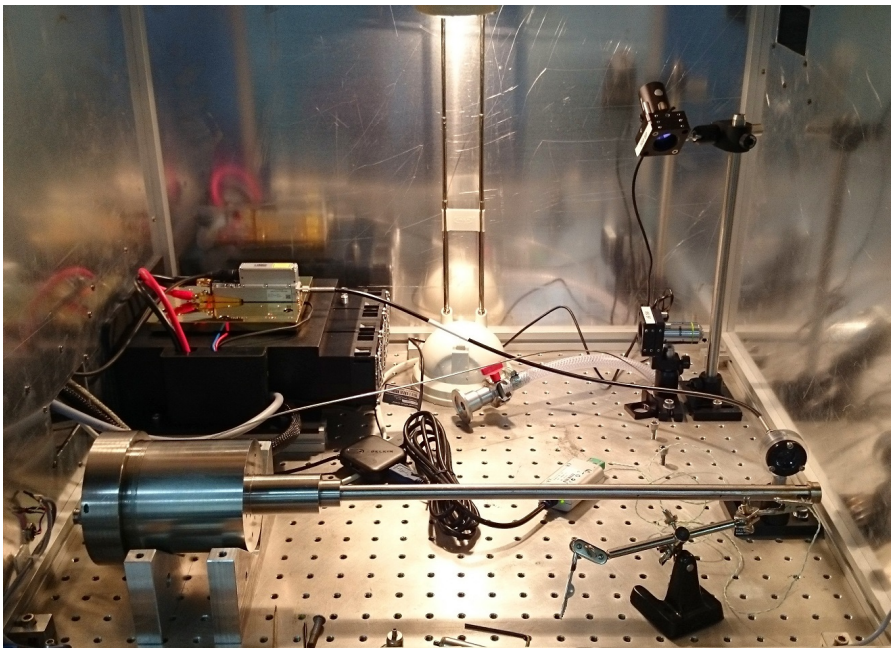

(b) Photo of apparatus

Figure 9-1 Diagram and photo of the configuration of the apparatus for annealing under stress. The laser was focused to a spot of approximately 1 mm on one side of the sample. A thermocouple was adhered to the opposite side.

room temperature before the gas pressure was slowly reduced.

Isothermal annealing in situ in an EPR cavity was performed using a Bruker variable temperature system. Nitrogen gas was heated by flowing past a hot filament in a quartz tube before flowing over the sample in a quartz insert in the cavity. The sample was fixed on a ledge in the end of a quartz rod. A thermocouple was situated just below the resonator, approximately 2 cm below the sample. Inconsistencies were found in the temperature measurement and so the temperature was calibrated at the same settings with a second 300 µm thermocouple in place of the sample on the quartz rod.

9.2.3 EPR measurements

The degree of preferential orientation of $C^0_{I_{001}}$ was determined by measurements of the R2 EPR signal at X-band. A Bruker EMX CW-EPR spectrometer was employed with a Bruker ER041XG microwave bridge coupled to a Bruker ER4119HS cylindrical cavity. All measurements (at high temperature and at room temperature) were made with the sample in the quartz insert of the variable temperature system as it increases the mircowave power density at the sample, increasing the size of the sample signal over that of the cavity background.

The significantly higher concentrations of $C^0_{I_{001}}$ in the samples here than in the samples in chapter 8 made measurements much simpler and more accurate. The increased signal meant that the intensity of both the inner and outer high field lines of the $\langle 0\,0\,1\rangle$ R2 spectrum could be determined, and the preferential orientation found from their ratio. This significantly reduces errors as it does not require the comparison of the intensity in one scan to another taken at a different time.

9.2.4 Temperature profiles

When focussed to a small spot the power density of a laser can be very high. At constant pressure and at room temperature the heat capacity of diamond is $0.51\,\mathrm{J\,g^{-1}\,K^{-1}}$ and rises with higher temperatures [5]. A $1\,\mathrm{mm^3}$ diamond has mass

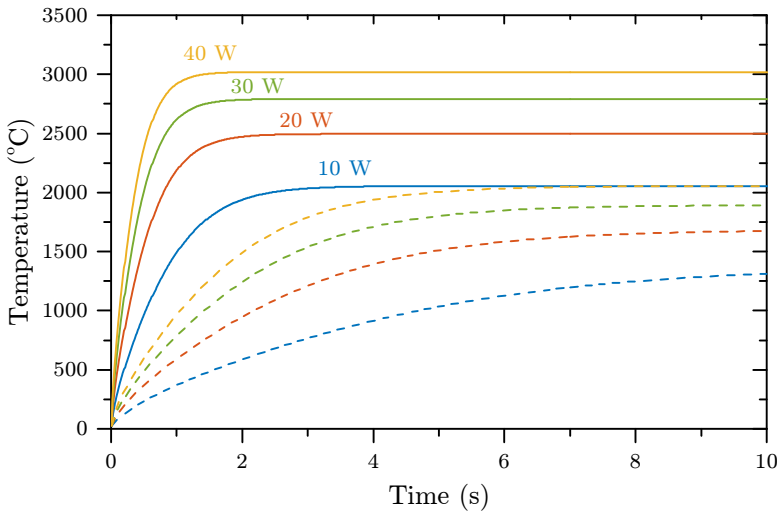

Figure 9-2 Calculated temperature profiles from continuous heating with 10 W, 20 W, 30 W and 40 W and radiative losses according to the Stefan-Boltzmann law. The solid and dashed lines are for cubes with sides of length 1 mm and 2 mm respectively.

3.5 mg, therefore if it absorbs 40 W of power from the laser, and does not lose energy, it would heat at a rate of approximately 22 000 $\mathrm{K\,s^{-1}}$. The primary mechanism for heat loss at very high temperatures is thermal radiation, significantly limiting the maximum temperature. The Stefan-Boltzmann law describes power radiated as a function of temperature

$$P = \epsilon\sigma A T^4 \,, \tag{9-1}$$

where ϵ is the emissivity, σ is the Stefan-Boltzmann constant and A is the surface area. For a 1 mm cube radiating from every face with $\epsilon = 1$, the radiative power reaches 40 W at 3020 °C; although the initial heating rate is fast the temperature quickly stabilises. The result of a simple model using the finite difference method and considering energy absorbed and energy radiated is shown in figure 9-2 for a range of laser powers and for a cube with lengths 1 mm and 2 mm. The temperature is seen to increase quickly, stabilising in a few seconds at temperatures up to 3000 °C.

Of course when the sample is heat sunk by contact with two anvils and not in a vacuum, the losses from thermal conductivity are significant and reduce the maximum temperature. To test the heating potential of the laser a sample was heated with a range of powers and the temperature monitored with a thermocouple. This

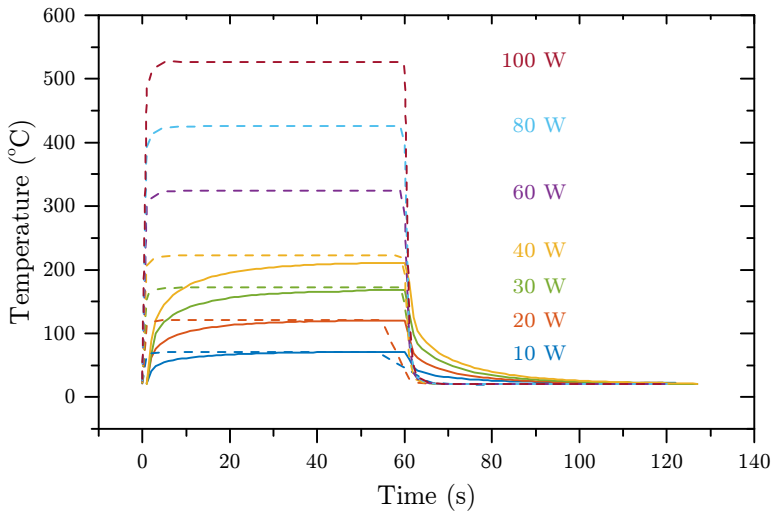

Figure 9-3 Comparison between experimental and simulated temperatures for a sample laser heated whilst held in the optical uniaxial stress probe. The sample had dimensions $1.5 \times 1.3 \times 0.7\,\mathrm{mm}^2$ and was mounted with the smallest face contacting the anvils.

was performed with and without water cooling. The purpose of water cooling the probe is to keep its temperature stable preventing expansion and twisting which could easily crack the sample.

In addition to experimentally determining the sample temperature a model was constructed in COMSOL finite element analysis software.[1] The model had the same geometry as in figure 4-6. The thermal conductivity of the steel was found to be critical in determining the temperature reached. Standard values of 16.3 and $44.5\,\mathrm{W\,mA^{-1}\,K^{-1}}$ were used for the stainless steel construction of the probe and high carbon steel anvils respectively. Water cooling was simulated by fixing the temperature of the outside of the probe at room temperature. The experimental and simulated temperature profiles for the water cooled probe are shown in figure 9-3. The sample was of dimension $1.5 \times 1.3 \times 0.7\,\mathrm{mm}^3$ and mounted with the smallest face on the anvils.

The maximum temperature reached in the simulation and experiment are in good accord, however there is significantly more thermal lag in the experiment. This could be a result of a thermocouple being used for temperature measurement. The thermal mass of the thermocouple is significant compared to that of the

[1] COMSOL Multiphysics version 5.1, COMSOL Ltd, 2015

diamond. To obtain a better agreement either the simulation should include the thermocouple, or ideally a non contact temperature measurement method used such as a pyrometer.

Water cooling the exterior of the probe creates a large temperature gradient, limiting the maximum temperature. With the water cooling removed the temperature initially increased at a similar rate but then continued to increase slowly over a few minutes as the probe heated. With continuous heating at 40 W the temperature reached over 500 °C. Constructing anvils with a lower thermal conductivity to increase the thermal gradient could dramatically increase the maximum obtainable temperature with water cooling.

9.3 Results and analysis

The results can be divided into two sections. The first concerns annealing in a preferential orientation of $C^0_{I_{001}}$, investigating the effect of changing temperature and stress. The second investigates the annealing out of the preferential orientation allowing a measurement of the activation energy for the reorientation of $C^0_{I_{001}}$, a fundamental mechanism for its migration.

9.3.1 Annealing under stress

9.3.1.1 Isochronal annealing under constant stress

High field EPR spectra of the sample with $\boldsymbol{B} \parallel [0\,0\,1]$ after each stage of 1 h isochronal anneals under a 1.00 GPa [0 0 1] stress are shown in figure 9-4. The inner line at 416 mT is from the [1 0 0] and [0 1 0] sites, and the outer line at 498 mT is from the [0 0 1] site of $C^0_{I_{001}}$. It should be noted that the inner line has a linewidth of ~ 3 mT, whereas the outer line has a linewidth of ~ 8 mT; the broadening reduces the signal height and so the heights of the lines cannot be used for comparison. On annealing at 300 °C there is a noticeable increase in the inner line and decrease in the outer line corresponding to a movement of population away

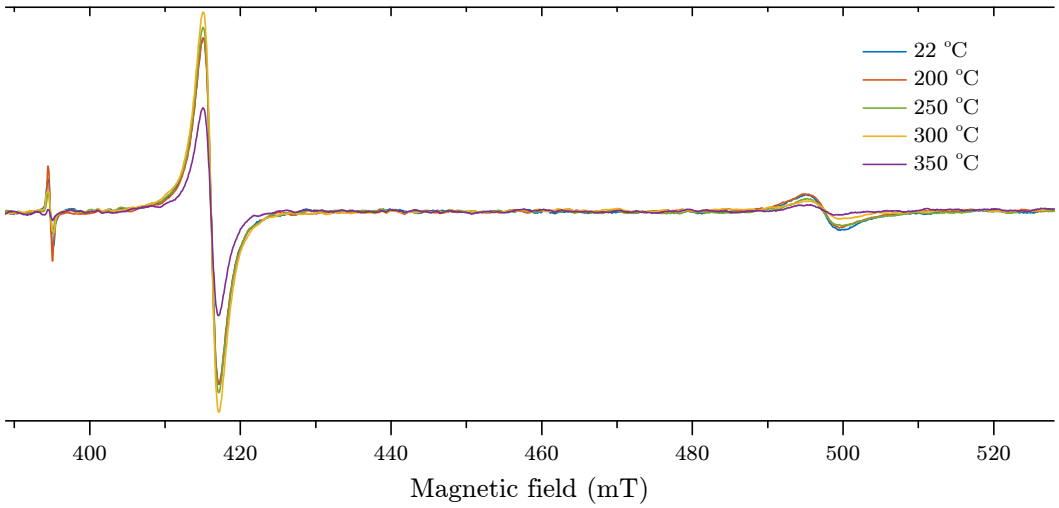

Figure 9-4 High field EPR spectra with $\boldsymbol{B} \parallel [0\,0\,1]$ after isochronal annealing with a 1.00 GPa [0 0 1] stress. The narrow line on the left is R1; the two wide lines are R2. The outer R2 line clearly decreases in intensity with a corresponding increase in the inner line. At the final temperature of 350 °C both lines decrease as R2 anneals out.

from the stressed [0 0 1] site into the [1 0 0] and [0 1 0] sites. After the anneal at 350 °C, both lines reduced in intensity indicating the defect is annealing out.

The population of $C^0_{I_{001}}$ in the [0 0 1] site is given in figure 9-5, along with the total concentration. With $\boldsymbol{B} \parallel [0\,0\,1]$, the degree of preferential population into the sites is given as the percentage population by

$$[C^0_{I_{[0\,0\,1]}}] = \frac{R2_{outer}}{R2_{outer} + R2_{inner}} \tag{9-2}$$

and

$$[C^0_{I_{[1\,0\,0]}}] + [C^0_{I_{[0\,1\,0]}}] = \frac{R2_{inner}}{R2_{outer} + R2_{inner}}\,. \tag{9-3}$$

At equilibrium each site will represent 33 % of the total population. A clear preferential population was created by annealing at 250 °C and a further increase at 300 °C, indicating enough thermal energy has been supplied to reorientate the interstitials under stress. No further increase in preferential orientation is seen from annealing at 350 °C, but the total concentration does start to decrease. The 300 °C anneal was the most effective at preferentially orientating $C^0_{I_{001}}$, halving the [0 0 1] site population and only annealing out a very small fraction of the total concentration.

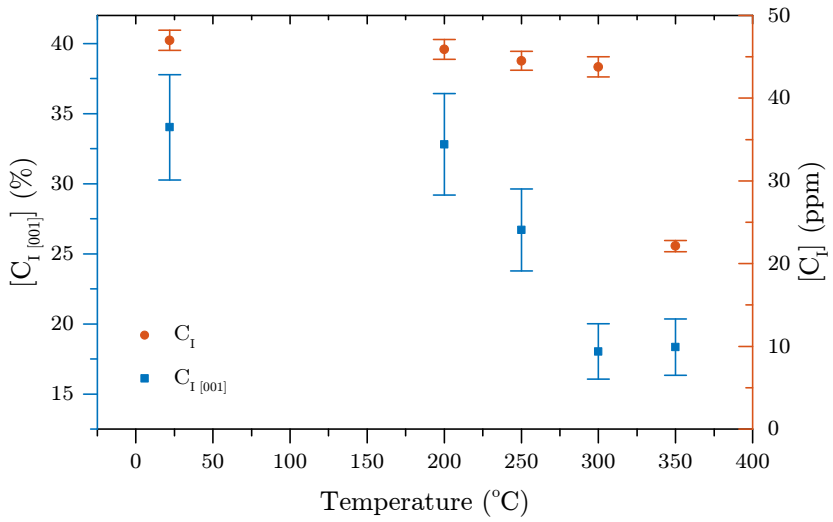

Figure 9-5 Isochronal annealing for 1 h in 50 °C intervals with 1.00 GPa [0 0 1] stress. R2 is clearly reorienting at 250 °C but only starts annealing out at 350 °C.

9.3.1.2 Increasing stress

Having determined the temperature required to create a preferentially orientated population of $C^0_{I_{001}}$, the effect of annealing at a constant temperature of 300 °C for 1 h over a range of stresses was investigated. Given that in figure 9-5 no further preferential orientation is seen between the 300 °C and 350 °C anneals, a 1 h 300 °C anneal is sufficient to reach the equilibrium state of preferential orientation. Annealing at higher temperatures would only have the unwanted effect of annealing out $C^0_{I_{001}}$.

Using the measures in equation (9-2) and equation (9-3) the site populations perpendicular and parallel to the stress were determined after each anneal and are given in figure 9-6. The degree of preferential population is seen to increase with every anneal up to 2.00 GPa. After the 2.00 GPa anneal the [0 0 1] population had decreased to 7(1) %, a preferential population of 93(1) % into the [1 0 0] and [0 1 0] sites. Exponential fits to the data are also shown in the figure as dashed lines; extrapolating the fit predicts that a 96(1) % preferential population would be achieved at 3.0 GPa and 98(1) % preferential population at 4.0 GPa.

EPR spectra of the highest degree of preferential orientation created are shown in figure 9-7 recorded with $\boldsymbol{B} \parallel [0\,0\,1]$ and $\boldsymbol{B} \parallel [1\,0\,0]$. With no preferential

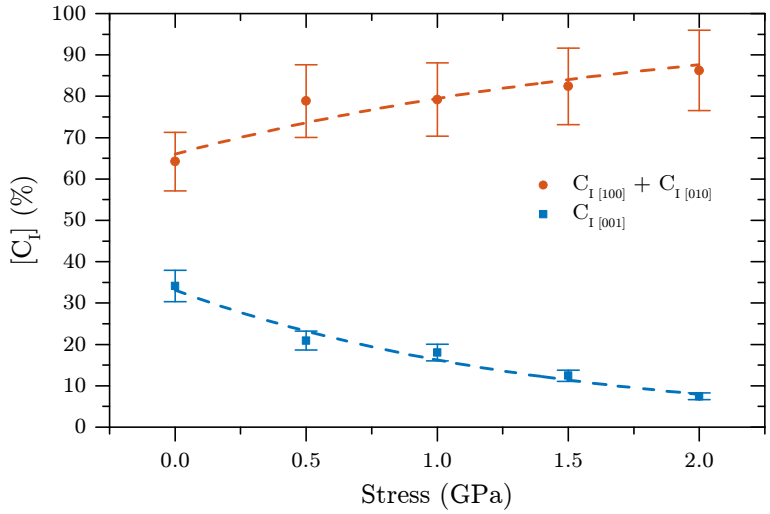

Figure 9-6 Population of R2 in the [0 0 1] and [1 0 0] sites, as percentage of total, after annealing for 1 h at 300 °C with a [0 0 1] stress. After annealing at 2.00 GPa there was 93(1) % preferential orientation into the [1 0 0] and [0 1 0] sites. The dashed lines are exponential fits to the data.

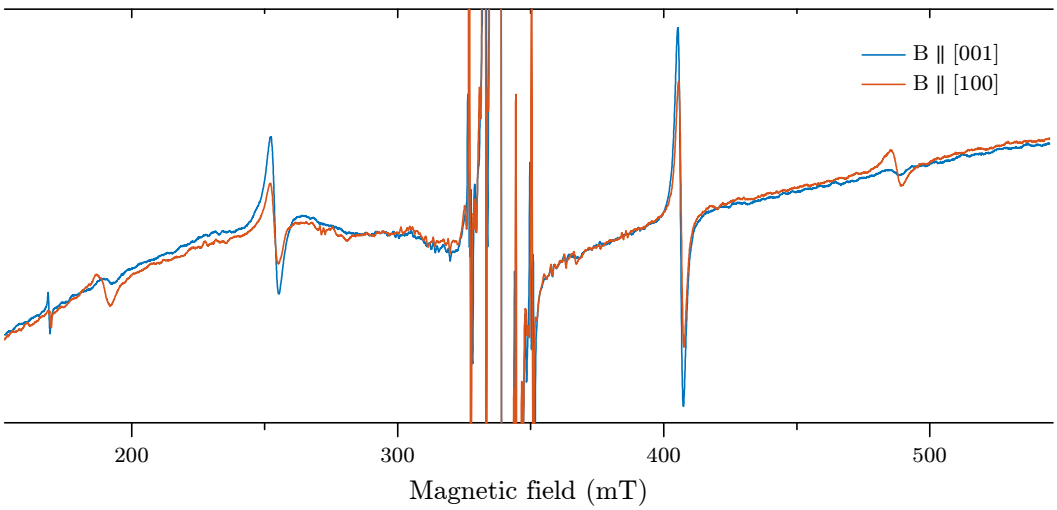

Figure 9-7 Full field EPR spectra of R2 with $\boldsymbol{B} \parallel [1\,0\,0]$ and $\boldsymbol{B} \parallel [0\,0\,1]$ after annealing under a 2.00 GPa [0 0 1] stress. A clear preferential population of $C^0_{I_{001}}$ is observed.

population all lines would have the same intensity in both measurements. Clearly the inner line is largest for $\boldsymbol{B} \parallel [0\,0\,1]$ and the outer line is largest for $\boldsymbol{B} \parallel [1\,0\,0]$.

9.3.2 Annealing of preferentially orientated populations

Once preferentially oriented populations of $C^0_{I_{001}}$ had been created, samples were isothermally annealed in an EPR cavity whilst simultaneously recording spectra of the two high field lines. Although this was repeated a number of times (after each uniaxially stressed anneal), the temperature measurement was determined to have been inaccurate and so only the results of the final anneal at 285 °C, for which the temperature was calibrated, will be presented.

Each spectrum recorded contained both the inner and outer high field lines and so allowed the determination of the preferential orientation. Since there was a very large number of spectra they were processed automatically by subtraction of an appropriate baseline and subsequent fitting of pseudomodulated Voigt profiles to each line. The baseline was a cubic spline fixed at one point either side of each of the two lines. To decrease errors the linewidth of the two lines were fixed. The automatic baseline subtraction procedure had the advantage of being systematic and removing human error. The resulting intensities were used to determine the preferential population in the $[0\,0\,1]$ site from equation (9-2), displayed in figure 9-8a. As evidence of the consistency of the technique, and the reorientation without annealing out of the defect, the total intensity of the two lines is shown in figure 9-8b.

9.3.3 Modelling the reorientation

At room temperature $C^0_{I_{001}}$ is immobile and fixed in orientation. For a defect to migrate, it must be given sufficient thermal energy to overcome a potential barrier, E_b. The activation energy associated with the migration of $C^0_{I_{001}}$ has been experimentally determined from the annealing out of its 1.859 eV transition to be 1.68(15) eV with an attempt frequency of $\nu = 4 \times 10^{13}$ Hz [6], and 1.6(2) eV with an attempt frequency of $\nu = 10^8$ Hz [7]. Whether this experimentally determined acti-

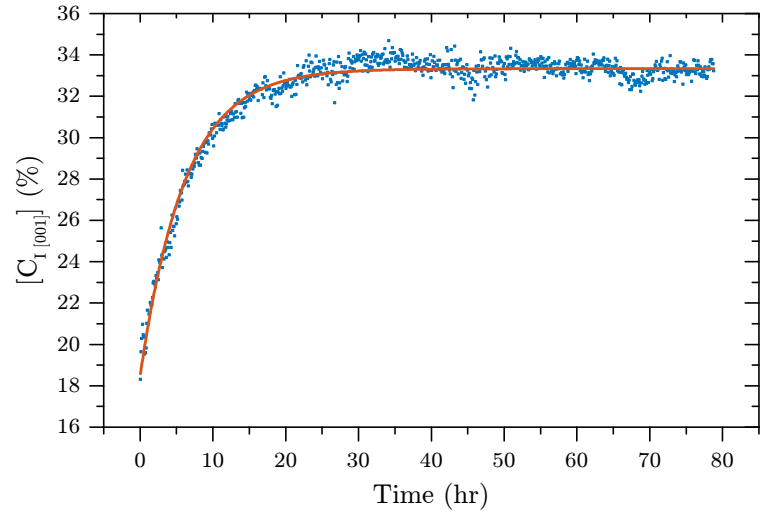

(a)

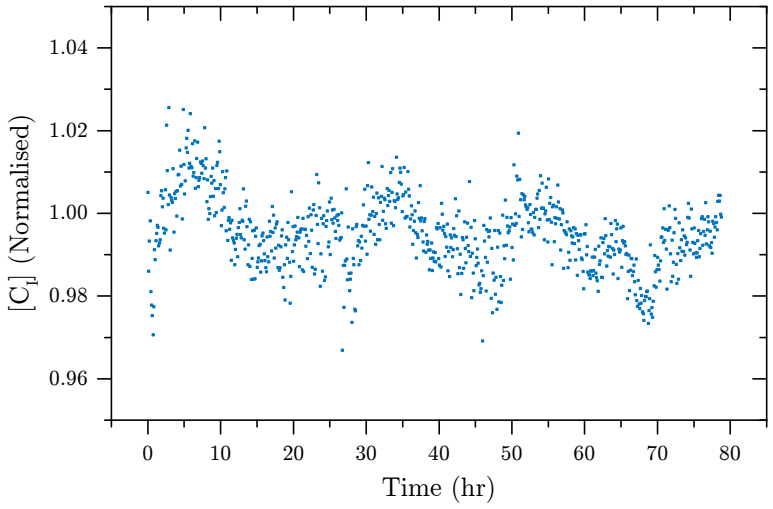

(b)

Figure 9-8 (a) Percentage of $C^0_{I_{001}}$ in the [0 0 1] site, measured by EPR, during an in situ 285 °C isothermal anneal and (b) total R2 over the same time range. Each data point is calculated from the fitted intensities of the high field inner and outer lines with $\boldsymbol{B} \parallel [0\,0\,1]$. The sample had previously been annealed at 300 °C for 1 h with a 1.00 GPa [0 0 1] stress. The solid line is a fit of equation (9-5) to the experimental data. The resulting activation energy is E = 1.42(2) eV using an attempt frequency of 10^8 Hz.

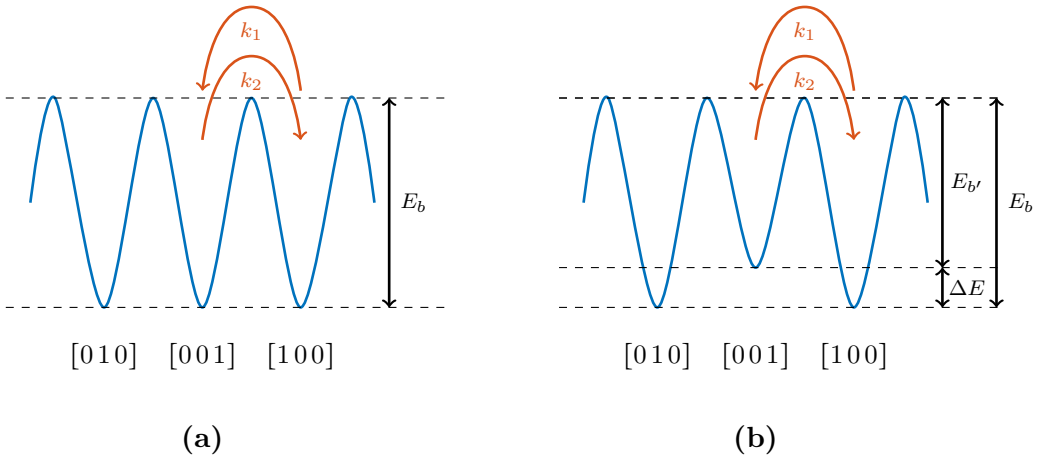

Figure 9-9 Representations of the potential wells for $C^0_{I_{001}}$ in its three orientations (a) without any applied stress and (b) with a large uniaxial stress (for illustrative purposes) of 6 GPa along [0 0 1]. In (a) the rate $k_1 = k_2$. In (b) $k_2 > k_2$.

vation energy originates solely from E_b or includes other barriers to trapping is not known. Ab initio calculations found that an energetically favourable mechanism for the migration of $C^0_{I_{001}}$ is its reorientation from one cube orientation to another [8]. For such a reorientation E_b was calculated to be 1.7 eV with $\nu = 4 \times 10^{13}$ Hz, agreeing well with experimentally determined activation energies.

Under normal circumstances the energy levels of the three sites of $C^0_{I_{001}}$ are degenerate and, as depicted in figure 9-9a, a reorientation from any one to either of the other two has equal probability. Applying a stress lifts this degeneracy creating an energy difference ΔE, as depicted in figure 9-9b. The degree of preferential orientation after an equilibrium has been reached can be used to determine ΔE by considering the Boltzmann distribution (equation (3-44)). For the situation in figure 9-9b, and taking the [1 0 0] and [0 1 0] sites to be degenerate at 0 eV, the population of the [0 0 1] site is given by

$$P_{[001]} = \frac{e^{-\beta\Delta E}}{e^{-\beta\Delta E} + 2}\,, \quad \text{with} \quad \beta = \frac{1}{k_B T}\,, \tag{9-4}$$

where k_B is the Boltzmann constant and T is the temperature. Using equation 9-4, ΔE has been calculated from the preferential population in figure 9-6 and is shown in figure 9-10. The stress induced splitting of the energy levels for the [0 0 1] stress is determined as $\frac{d\Delta E}{d\sigma} = 45(2)\,\text{meV GPa}^{-1}$.

To determine the activation energy required to reorientate $C^0_{I_{001}}$, a number of pro-

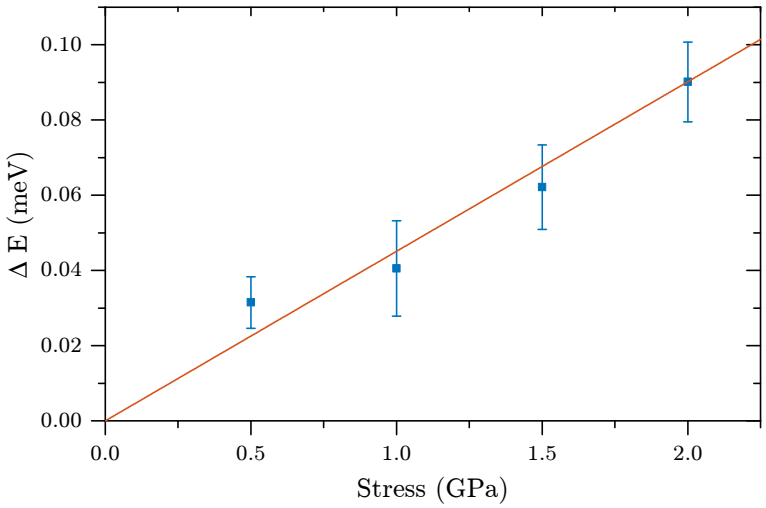

Figure 9-10 The lifting in energy of the [0 0 1] site of $C^0_{I_{001}}$ from the [0 0 1] stress, calculated from the preferential populations in figure 9-6 using equation (9-4). A linear fit gives the splitting rate as $\frac{d\Delta E}{d\sigma}$ = 45(2) meV GPa^{-1}.

cesses must be considered. As well as the probability of a defect in the [0 0 1] site reorienting to the [1 0 0] or [0 1 0] site, the reverse process must also be accounted for. The following set of coupled differential equations represent all of the possible reorientations:

$$\begin{aligned}\frac{d[I_{100}]}{dt} &= k_{I_{010}\to I_{100}}\cdot[I_{010}] + k_{I_{001}\to I_{100}}\cdot[I_{001}] \\ &\quad - k_{I_{100}\to I_{010}}\cdot[I_{100}] - k_{I_{100}\to I_{001}}\cdot[I_{100}]\end{aligned} \tag{9-5a}$$

$$\begin{aligned}\frac{d[I_{010}]}{dt} &= k_{I_{100}\to I_{010}}\cdot[I_{100}] + k_{I_{001}\to I_{010}}\cdot[I_{001}] \\ &\quad - k_{I_{010}\to I_{100}}\cdot[I_{010}] - k_{I_{010}\to I_{001}}\cdot[I_{010}]\end{aligned} \tag{9-5b}$$

$$\begin{aligned}\frac{d[I_{001}]}{dt} &= k_{I_{100}\to I_{001}}\cdot[I_{100}] + k_{I_{010}\to I_{001}}\cdot[I_{010}] \\ &\quad - k_{I_{001}\to I_{100}}\cdot[I_{001}] - k_{I_{001}\to I_{010}}\cdot[I_{001}]\end{aligned} \tag{9-5c}$$

where

$$k_{a\to b} = \nu e^{\frac{E_{a\to b}}{k_b T}}\ , \tag{9-6}$$

with ν the attempt frequency and $E_{a\to b}$ the energy barrier associated with the reorientation from site a to site b. Under the assumption that $C^0_{I_{001}}$ is not annealing out, nor is created by the dissociation of complexes, equation (9-5) can be used to model the kinetics of the reorientation. If no stress is applied $\Delta E = 0$ and $E_{a\to b}$ is equal for every reorientation. All rate constants are hence equal and the

populations will all remain at 33 %; if a [0 0 1] stress is applied then $E_{[0\,0\,1]\rightarrow[0\,1\,0]} = E_{[0\,0\,1]\rightarrow[0\,0\,1]} = E_b - \Delta E$ and the population will move from the [0 0 1] site to the [1 0 0] and [0 1 0] sites.

The model was fitted to the data in figure 9-8a to determine the energy barrier to reorientation, E_b, without stress. The solid line in the figure is the best fit with $E_b = 1.42(4)\,\text{eV}$ taking $\nu = 10^8\,\text{Hz}$. Using the upper value of the attempt frequency $\nu = 4 \times 10^{13}\,\text{Hz}$, corresponding to the Raman frequency of diamond, $E_b = 2.04(4)\,\text{eV}$. The error originates from a ±10°C error in temperature measurement. To accurately determine E_b and the attempt frequency the experiment needs to be repeated for a range of annealing temperatures. This will allow an Arrhenius plot to be constructed and the parameters determined (see §3.5).

9.4 Conclusions

An optical stress probe has been used for uniaxially stressing samples whilst simultaneously heating with a CW laser at up to 40 W of power. The effectiveness of laser heating has been characterised and compared with simulations of a model in finite element analysis software COMSOL. A good agreement in temperature reached was found between experiment and simulation. Experimental tests were performed with and without water cooling of the apparatus. With water cooling the maximum temperature reached for a $1.5 \times 1.3 \times 0.7\,\text{mm}^3$ sample with 40 W of power was 210 °C and without water cooling was 515 °C. The temperature depends on the sample size.

Samples have successfully been annealed at 300 °C under [0 0 1] uniaxial stresses up to 2.00 GPa and up to temperatures of 350 °C under a uniaxial stress of 1.00 GPa. The treatments successfully created preferentially oriented populations of $C^0_{I_{001}}$ with up to 93(1) % population in two sites (increased from 67 %). The degree of preferential orientation has been used to determine the splitting rate of the energy levels of $C^0_{I_{001}}$ under a ⟨0 0 1⟩ stress as $\frac{d\Delta E}{d\sigma} = 45(2)\,\text{meV GPa}^{-1}$.

Preferentially orientated populations of $C^0_{I_{001}}$ have been isothermally annealed in situ in an EPR spectrometer, allowing the site populations to be monitored over

time. A chemical kinetics model of the reorientation has been simulated and fitted to the experimental data. An energy barrier to the reorientation of $C^0_{I_{001}}$ of $\approx 1.4\,\text{eV}$ with the attempt frequency $\nu = 10^8\,\text{Hz}$ fits the experimental data presented, but to date there is insufficient data to determine E_b.

9.5 Further work

The progress in this work can easily be built upon with future experiments. Continuing the work on the $C^0_{I_{001}}$, higher degrees of preferential orientation could be achieved with larger $\langle 0\,0\,1\rangle$ stresses, but in particular it would be interesting to anneal under a $\langle 1\,1\,0\rangle$ stress. This would raise the energy of two sites, potentially allowing preferential orientation to just one. It is also possible that the stress affects the barrier to reorientation making it more difficult.

Having demonstrated the successful preferential orientation of $C^0_{I_{001}}$, other defects can be investigated, the most significant of which is arguably NV^-. The success of NV^- in certain quantum technologies requires that individual defects be identical and hence must have the same alignment. Progress has been made in growing-in preferentially oriented NV^- in CVD diamond [9–12] but is not suitable for creating large concentrations of arrays or preferentially oriented defects. The preferential orientation of NV^- by annealing under stress will be more challenging than for $C^0_{I_{001}}$ as it requires higher temperatures and probably higher stress [13]. The symmetry of NV^- is $\mathscr{C}_{3v}$ with its symmetry axis along the $\langle 1\,1\,1\rangle$ directions. Applying a $[1\,1\,0]$ stress will increase the energy of the $[1\,1\,1]$ and $[\bar{1}\,\bar{1}\,1]$ sites allowing preferential orientation into $[\bar{1}\,1\,\bar{1}]$ and $[1\,\bar{1}\,\bar{1}]$. With a $[1\,1\,\bar{2}]$ stress it might be possible to preferentially orientate into just the $[1\,1\,1]$ site.

Annealing under stress can potentially be used to change the annealing rates of some defects relative to others, potentially switching off certain mechanisms. For example, if a $\langle 1\,1\,0\rangle$ stress restricts $C^0_{I_{001}}$ to just one site, and its migration mechanism is through reorientation, then it would no longer be able to migrate. Thus interstitial related mechanisms could be reduced or switched off, whilst others continue.

References

1. H. J. McSkimin, *Journal of Applied Physics* **43**, 985 (1972).
2. M. A. Hopcroft, W. D. Nix, T. W. Kenny, *Physical Acoustics* **19**, 229–238 (2010).
3. C. A. J. Ammerlaan, E. A. Burgemeister, *Physical Review Letters* **47**, 954–957 (1981).
4. D. C. Hunt et al., *Physical Review B* **61**, 3863–3876 (Feb. 2000).
5. A. C. Victor, *The Journal of Chemical Physics* **36**, 1903–1911 (1962).
6. L. Allers, A. T. Collins, J. Hiscock, *Diamond and Related Materials* **7**, 228–232 (1998).
7. D. Hunt, PhD thesis, University of Oxford, 1999.
8. S. Breuer, P. Briddon, *Physical Review B* **51**, 6984–6994 (Mar. 1995).
9. J. Michl et al., *Applied Physics Letters* **104**, 102407 (Mar. 2014).
10. M. Lesik et al., *Applied Physics Letters* **104** (2014).
11. L. M. Pham et al., *Physical Review B* **86**, 121202 (2012).
12. A. M. Edmonds et al., *Physical Review B* **86**, 035201 (2012).
13. T. Karin, S. Dunham, K.-M. Fu, *Applied Physics Letters* **105**, 053106 (Aug. 2014).

10

Conclusions

In this thesis a variety of spectroscopies and uniaxial stress techniques have been employed for the production and study of defects in diamond. Software has been developed which has improved our ability to quantify defects by EPR and optical absorption spectroscopies (chapter 5). This has allowed a detailed study to be undertaken of the annealing of neutron irradiated type-Ib diamond, providing new insight into the role of interstitials in nitrogen aggregation (chapter 7). The effect of uniaxial stress on the creation and modification of defects has been investigated through electron irradiation (chapter 8) and annealing (chapter 9). The effect of a uniaxial stress on the production rates of defects and their preferential orientation (or lack thereof) has proved insightful. The preferential orientation of defects by annealing has allowed the investigation of fundamental annealing mechanisms and is a step towards creating other preferentially orientated defects.

10.1 Defect quantification in diamond

The development of new and improved software for the analysis and quantification of spectra was fundamental to the results of every subsequent chapter in this thesis. All fitting software has been written in the MATLAB[1] environment, providing access to a library of powerful functions.

[1]MATLAB version 8.5, The MathWorks, Inc., 2015

New software for general fitting of spectra has made analysis of IR and UV-Vis absorption spectra routine and fast, with automatic and repeatable calibration of spectra and deconvolution into their component spectra.

Improvements have been made in our ability to quantify defects from their EPR spectra. New fitting software for the quantification of paramagnetic species by comparison with a reference, specific to EPR spectroscopy of crystals, has been developed using the EasySpin[2] toolbox in MATLAB for fast and accurate computation of resonance positions and intensities. A normalised spectrum is created by convolution of the resonances with a normalised pseudomodulated Voigt lineshape. The use of a normalised lineshape removes the requirement to perform error prone numerical integration, significantly increasing the accuracy of subsequent quantification of defects. The software built upon software previously developed within the group [1].

The ability to quantify defects from misoriented spectra by fitting the orientation of the simulation to the experimental spectrum has been developed. This has reduced the lower limit of routine quantification of paramagnetic species in single crystals by removing the requirement to align the crystal.

The accuracy of quantifying $S \geq 1$ defects from their $\Delta m_S = \pm 2$ transitions using EasySpin to simulate resonances has been confirmed. This ability was critical for later results in the thesis.

10.2 Photo- and thermo-chromism

Defects in semiconductors often have levels in the band gap in more than one charge state. In diamond, photochromic and thermochromic processes can often drive charge between defects allowing their observation in their multiple charge states. The investigation of such processes is important for a number of reasons. Firstly, observation of such charge transfers can be used to relate one transition to another. Secondly if a defect is present in more than one charge state, at least one should be paramagnetic allowing EPR to be used to characterise the defect.

[2]EasySpin 4.5.5, www.easyspin.org

Finally, the stability of defects is also important. In diamond the charge state of defects depends not so much on the position of the Fermi level, but the proximity between donor and acceptor defects [2].

The enhancement of N_2V^- by thermochromism in ^{15}N doped diamond has been utilised to increase its recently reported EPR signal [3], allowing determination of ^{13}C hyperfine parameters. The observation of N_2V^- in diamond of natural isotopic abundance has allowed the quadrupole interaction in $^{14}N_2V^-$ to be characterised. The knowledge of the spin Hamiltonian parameters of $^{14}N_2V^-$ enabled its quantification in chapter 7.

The photochromism of NV and N_2V between neutral and negative charge states has been investigated in ^{15}N doped HPHT-grown diamond. Changes in the ZPLs of the defects have been correlated allowing their relative oscillator strengths to be determined. Combined with EPR quantification of NV^-, made accurate by the work in chapter 5, and EPR quantification of N_2V^- made possible in this chapter, calibration constants have been determined for NV^0, NV^-, N_2V^0 and N_2V^-.

Photochromism of the so far unidentified defects H1b and the 594 nm defects was also observed. With the assumption that the photochromism corresponds to a charge transfer with N_S, a lower bound for the H1b calibration constant was estimated. Despite the photochromism of both defects, no new EPR signals were observed.

10.3 Annealing of neutron irradiated type-Ib diamond

This chapter has primarily contributed to our understanding of two related topics. With the demand for arrays of defects and shallow defects in quantum information processing and sensing applications [4, 5], ion implantation is increasingly being used as a method for creating defects. There is however a lack of understanding of the nature of the damage caused by ion implantation and the properties of defects created by the method suffer from damage caused to their environment. Since the

volume of damage caused is small it is difficult to study. Neutron irradiation has provided a route to creating damage with the same characteristics but through the bulk of the diamond, facilitating its study. In addition our understanding of nitrogen aggregation in diamond has been furthered. Despite a significant body of research on the subject there still remain many questions about the aggregation of nitrogen in diamond. Vacancy mediated aggregation has long been recognised as an important process [6], however, although its role has previously been recognised [7, 8], the interstitial is less well understood.

The lattice damage caused by neutron irradiation was simulated with SRIM yielding damage rates of $77(10)\,\mathrm{V\,n^{-1}cm^{-1}}$ with a carbon atom displacement energy $T_d = 40\,\mathrm{eV}$ and $15(2)\,\mathrm{V\,n^{-1}cm^{-1}}$ for $T_d = 213\,\mathrm{eV}$. The additional energy in the second rate accounts for the requirement that atoms be displaced with sufficient energy that they do not immediately recombine with the vacancy.

Type-Ib HPHT-grown diamonds were neutron irradiated up to a dose of $10^{18}\,\mathrm{n\,cm^{-2}}$ with a corresponding predicted vacancy concentration of $85(11)\,\mathrm{ppm}$ using $T_d = 40\,\mathrm{eV}$. EPR of a sample after irradiation to $10^{18}\,\mathrm{n\,cm^{-2}}$ determined a concentration of $\mathrm{V^-}$ far lower than this, however, the $\mathrm{N_S^+}$ concentration, usually a good indicator of $\mathrm{V^-}$ concentration, was $134(20)\,\mathrm{ppm}$ and EPR on a type-IIa CVD-grown diamond irradiated at the same time found an $\langle 0\,0\,1\rangle$-split interstitial concentration of $82(8)\,\mathrm{ppm}$. An explanation for the discrepancy has been explained in terms of strain around the vacancies lowering their tetrahedral symmetry and introducing a D term. Simulations of the spectra with a Gaussian distribution of D about $D = 0$, show encouraging agreement with the experimentally observed EPR lineshape.

A further reduction in the measured $\mathrm{V^-}$ concentration originated from the large damage and spin concentration in the diamonds, causing dielectric losses lowering the effective Q-factor of the EPR resonator. Such losses are estimated to have reduced the signal by up to a factor of three. Considering these two effects the total concentration of $\mathrm{V^-}$ could have in fact easily been greater than the $\mathrm{N_S^+}$ concentration, with additional charge possibly donated by nitrogen interstitials.

The samples were annealed up to 1600 °C in 100 °C intervals and analysed after each anneal by IR absorption and EPR spectroscopies. An assay of nitrogen

throughout the annealing stages was able to account for nearly all of the nitrogen in the defects N_S^0, N_S^+, NV^-, N_2V^- and N_{2S}, which was present before irradiation. A shortfall in nitrogen which matched the presence of the H1a (di-nitrogen $\langle 0\,0\,1\rangle$-split interstitial) local vibrational mode was used to estimate its calibration constant as $f_{1450} = 3.4(5) \times 10^{-17}\,\mathrm{cm}$.

The annealing mechanisms were simulated considering vacancy related processes and interstitial related processes including interstitial mediated aggregation. The simulation was able to match the experimental data exceptionally well providing good support for the interstitial mediated mechanism in the production of N_{2S} at lower temperatures than that mediated by the vacancy assisted mechanism. The simulated annealing also gave excellent agreement to the estimated calibration constant for H1a.

10.4 Irradiation under uniaxial stress

Irradiation, and in particular electron irradiation, is frequently used to create damage to the intrinsic diamond lattice in the form of vacancies and interstitials. For every atom knocked out of the lattice an interstitial and vacancy defect must be created. Unless irradiating at low temperatures there is however a large discrepancy between the two, with the vacancy production being up to a factor of ten higher than $\langle 0\,0\,1\rangle$-split interstitial production [9]. The interstitials form complexes and are therefore mobile in some form during the irradiation. At room temperature the $\langle 0\,0\,1\rangle$-split interstitial is not mobile. An excited state of the interstitial (C_I^*) which is mobile at ~ 100 K has been proposed, although few details are known about it [10].

Electron irradiating diamond under uniaxial stress has allowed the migration of defects during the irradiation to be investigated. Samples were successfully irradiated at room temperature under [0 0 1] uniaxial stresses up to 3.0 GPa and subsequently characterised by EPR, UV-Vis and PL spectroscopies. Typical irradiation damage products were observed such as the EPR defects R1, R2 and the optical centres GR1, 3H and TR12.

The stress had minimal influence on the ⟨0 0 1⟩-split interstitial production with no measurable effect on the production rate and a very small preferential orientation. The lack of an effect of stress gives good support for the role of C_I^* during irradiation. Neither did the stress cause preferential orientation of the R1 defect (nearest neighbour di-interstitial), consistent with its production at low temperature and it being created by C_I^*.

The stress did however cause significant changes in the production of the 3H (next nearest neighbour di-interstitial) and TR12 (larger interstitial complex) defects. Variations in the production of defects across the samples as measured by PL spectroscopy was possibly a result of strain around dislocations in the CVD-grown diamond.

10.5 Annealing under uniaxial stress

The final chapter in this thesis has explored the annealing of samples with simultaneous uniaxial stress. The stress causes a perturbation to otherwise degenerate orientations of defects in the crystal. With sufficient thermal energy to overcome a barrier to reorientation the defects preferentially orientate into a subset of their possible orientations.

Neutron irradiated type-IIa CVD diamond was successfully annealed at 300 °C under [0 0 1] stresses of 2.00 GPa using a CW IR laser. Stress was applied with an optical stress probe which was not specifically designed for the purpose. There is therefore significant room for improvement in the mechanical and thermal properties of the equipment.

The treatment successfully oriented the single ⟨0 0 1⟩-split interstitial with up to 93(1) % preferential orientation into two out of its three sites in the diamond lattice, as measured by EPR spectroscopy. The degree of preferential orientation allowed the stress splitting of energy levels to be determined by considering the Boltzmann distribution of defects.

Subsequent preferentially oriented populations of defects have enabled the thermal

barrier to reorientation to be investigated. Samples with preferentially oriented interstitials were annealed in situ in an EPR spectrometer and the site populations of defects monitored over time, allowing the time constant associated with the recovery to be determined. With sufficient data it would be possible to determine the activation energy and attempt frequency for the mechanism with good accuracy; the mechanism is fundamental to the annealing of radiation damage in diamond.

The success of the experiment in engineering defects has important implications for the possibility of preferentially orientating NV centres. NV centres require more thermal energy for their reorientation and may not respond so well to the stress; thus significant challenges remain.

References

1. A. M. Edmonds, PhD thesis, 2008.
2. A. T. Collins, *Journal of Physics: Condensed Matter* **14**, 3743–3750 (Apr. 2002).
3. B. L. Green, PhD thesis, University of Warwick, 2013.
4. V. Dobrovitski et al., *Annual Review of Condensed Matter Physics* **4**, 23–50 (2013).
5. R. Schirhagl et al., *Annual review of physical chemistry* **65**, 83–105 (Jan. 2014).
6. A. T. Collins, *Journal of Physics C: Solid State Physics* **13**, 2641–2650 (1980).
7. I. Kiflawi, H. Kanda, A. Mainwood, *Diamond and related materials* **7**, 327–332 (1998).
8. R. Jones et al., *Diamond and Related Materials* **53**, 35–39 (2015).
9. D. J. Twitchen et al., *Physica B* **273-274**, 628–631 (1999).
10. M. E. Newton et al., *Diamond and Related Materials* **11**, 618–622 (2002).